Sodium-dependent multivitamin transporter: a potential novel cause of cardiomyopathy

Lauren Charlotte Phillips

Thesis submitted in accordance with the requirement for the degree of

Doctor of Philosophy

Biosciences Institute
Newcastle University

July 2021

Abstract

Cardiomyopathy is a heterogeneous disorder affecting adults and children and is a leading cause of death globally. Paediatric cardiomyopathies affect ~1:100,000 children, with around one third requiring a heart transplant or risk death within two years of diagnosis.

A homozygous missense mutation in the human Sodium Multivitamin Transporter (SMVT) gene, *SLC5A6*, was identified in sisters with paediatric cardiomyopathy. The transporter is a plasma membrane protein that transports biotin, pantothenic acid and lipoic acid throughout several tissues including the brain, intestine and heart. These substrates play an essential role in energy metabolism and homeostasis, suggesting reduced functionality of Slc5a6 within the heart could result in cardiomyopathy.

Mouse models were employed to conditionally delete *Slc5a6* within cardiomyocytes resulting in the development of cardiomyopathy markers throughout early adulthood leading to sudden death at five months of age. Cardiac functionality was assessed using electrocardiography (ECG) which showed atrioventricular block, and histological analysis demonstrated myocardial fibrosis and cardiomyocyte hypertrophy. Cardiac magnetic resonance imaging (CMR) revealed a reduction in ejection fraction, cardiac output and stroke volume, hallmarks of left ventricular dysfunction. Together, these changes confirm the presence of cardiomyopathy within the cardiomyocyte specific *Slc5a6* knockout model.

Gross abnormalities in mitochondrial structure and organisation were observed using electron microscopy, and quadruple immunofluorescence staining revealed a reduction in complex I of the mitochondrial electron transport chain. This suggests that loss of *Slc5a6* has a negative impact on energy metabolism through deficiency of complex I, causing excess stress upon the heart ultimately resulting in cardiomyopathy.

Preliminary data from vitamin supplementation to pregnant females and their *Slc5a6* knockout offspring shows a delay in the onset of cardiomyopathy markers including myocardial fibrosis and cardiomyocyte hypertrophy, as shown by ECG and histology.

Collectively this data suggests that *Slc5a6* is important for normal cardiac structure and function, with potential for therapeutic intervention in patients with variants in *SLC5A6.*

Acknowledgements

I would like to thank my supervisors Dr Helen Phillips, Dr Simon Bamforth and Dr Gavin Hudson for their help, support, and guidance throughout this project and for also providing me with the opportunity to undertake this research.

I would also like to thank Professor Sir John Burn and Professor Robert McFarland for their help and advice with the clinical aspects of this project. Thanks to my assessors, Professor Deborah Henderson and Dr Colin Miles, for their insightful knowledge and guidance with this project.

The animal care technicians: Steve Smith, Michael Robson, Brigid Griffin and other members of the FGU have been instrumental in helping with animal care, without which, this research would not have been possible.

Many thanks to Dr Gavin Richardson, Dr Anna Walaszczyk and Dr Simon Tual-Chalot for help with the MRI scan protocols and analysis. Thank you to Dr Kathryn White, Ross Laws and Tracey Davey for help with sample processing and advice on electron microscopy. Many thanks to Dr Amy Vincent and Dr Angela Pyle for their help and guidance with mitochondrial work within this project.

Thank you to the core technical staff at the Centre for Life; Lisa Hodgson, Debra Jones, Michelle Murray, Paul Sidney, Arron Scott and Tony Riley for your time, support, and friendship over the last 4 years.

A special thank you to my family; my grandparents, parents, brother and sister for their continuous support and for always encouraging me to always strive further, I am proud to share this with you.

Thank you to my friends; Emine Sage, Emily Dookun, Catherine Stothard, Laura Powell, Laura Devlin and Daniel Cooney thank you so much for your friendship over the years and your constant encouragement, kindness, and help has been invaluable.

Lastly, I want to thank John-Luke Wilkinson, for your never-ending patience, immeasurable support, and unwavering belief in my ability to complete this thesis.

This work was funded by the Borwick Charitable Trust.

Table of Contents

List of Abbreviations

2D	Two dimensional
3D	Three dimensional
A	Atria
Ab	Antibody
ACP	Acyl carrier protein
ADP	Adenosine diphosphate
αKGDH	αKetoglutarate dehydrogenase
AMP	Adenosine monophosphate
AngI	Angiotensin I
AngII	Angiotensin II
ACE	Angiotensin converting enzyme
ATP	Adenosine triphosphate
ATP6A	ATP synthase
AVC	Atrioventricular canal
AVN	Atrioventricular Node
BBB	Blood-brain barrier
BCAA	Branched chain amino acids
BLAST	Basic Local Alignment Search Tool
bmp	Beats per minute
bp	Base pairs
BSA	Bovine Serum Albumin
BTD	Biotinidase
Ca^{2+}	Calcium
$CaCl_2$	Calcium chloride
CDK	Cyclin-dependent kinase
cDNA	Complementary DNA
Ce	Cerebellum
CHD	Congenital heart defects
CI	Complex 1
CII	Complex 2
CIII	Complex 3
CIV	Complex 4
cLDH	Cytosolic lactate dehydrogenase
Cm	Cardiomyocyte
CMR	Cardiovascular Magnetic Resonance
CO	Cardiac Output
CO_2	Carbon dioxide
CoA	Coenzyme A
CPT-1	Carnitine palmitoyltransferase I
CPT-2	Carnitine palmitoyltransferase II
CRISPR	Clustered regularly interspaced short palindromic repeats

CS	Carnegie Stage
CV	Complex 5
CVD	Cardiovascular Disease
Da	Dalton
DAPI	4',6-diamidino-2-phenylindole
DCM	Dilated Cardiomyopathy
DEPC	Diethyl pyrocarbonate
dH_2O	Distilled water
dNTPs	Deoxynucleotide
DORV	Double outlet right ventricle
DSB	Double stranded break
dsDNA	Double stranded DNA
DTT	Dithiothreitol
E	Embryonic day
ECG	Electrocardiograph
ECG	Electrocardiogram
ECM	Extracellular matrix
EDTA	Ethylenediaminetetraacetic acid
EDTA	Ethylenediamine tetra-acetic acid
EDV	End Diastolic Volume
EF	Ejection Fraction
EMT	Epithelial-to-mesenchymal transition
ER	Endoplasmic reticulum
ES	Embryonic stem cells
ESV	End Systolic Volume
ETC	Electron transport chain
EtOH	Ethanol
eYFP	Enhanced yellow fluorescent protein
FA	Fatty acid
FACS	Fluorescence-activated cell sorting
FAO	Fatty acid oxidation
FAS	Fatty acid synthesis
FBS	Fetal bovine serum
FCS	Fetal calf serum
FGU	Functional genomics unit
FOV	Field of view
FLP	Flippase
GAPDH	Glyceraldehyde 3-phosphate dehydrogenase
GAPDH	Glyceraldehyde 3-phosphate dehydrogenase
GFP	Green fluorescent protein
GL	Granular layer
H&E	Hematoxylin and eosin
HCL	Hydrochloric acid
HCM	Hypertrophic Cardiomyopathy
HCS	Holocarboxylase synthase
HDR	Homologous directed repair
HF	Heart failure

HR	Heart rate
ICD	Inter canthal distance
IF	Immunofluorescent staining
IF	Immunofluorescence
IGL	Inner granular layer
IHC	Immunohistochemistry
IMF	Intermyofibrillar
IMM	Inner mitochondrial membrane
IMPC	International Mouse Phenotyping Consortium
Kb	Kilobase
kDa	Kilodalton
KO	Knockout
LA	Left Atria
LA	Lipoic Acid
LC-MS	Liquid chromatography–mass spectrometry
LDH	Lactate dehydrogenase
LM	Lamina propria
LS	Longitudinal section
LV	Left Ventricle
LVAD	Left Ventricular Assist Device
LVNC	Left ventricular non-compaction
MCC	3-methylcrotonyl-CoA carboxylase
MCD	Multiple carboxylase deficiency
MCG	Methylcrotonylglycinuria
Mc-Sq	Squamous cell mucosae
MI	Myocardial infarction
ML	Molecular layer
MM	Mean mass
MOM	Mouse on Mouse
ms	Milliseconds
MTCO1	Cytochrome c oxidase
mtDNA	Mitochondrial DNA
Mye	Myencephalon
NaCl	Sodium chloride
NADH	Nicotinamide adenine dinucleotide
NDUFB8	NADH dehydrogenase complex
NHEJ	Non-homologous end-joining
NO	Nitric oxide
NOS	Nitric oxide synthase
NPC	No primary control
NS	Non-significant
OCT	Optimal cutting temperature compound
OFT	Outflow tract

OMM	Outer mitochondrial membrane
OXPHOS	Oxidative phosphorylation
PA	Pantothenic acid
Pa	Propionic acidemia
PAM	Promoter adjacent motifs
PanK	Pantothenate kinase
PBS	Phosphate buffered saline
PC	Pyruvate Carboxylase
Pk	Purkinje layerl
PCC	4'Phospho N Pantothenoylcysteine
PCC	Propionyl-CoA carboxylase
pcd	Post Conception Days
PCR	Polymerase chain reaction
PDH	Pyruvate dehydrogenase
PFA	Paraformaldehyde
PHF	Primary heart field
PICU	Paediatric intensive care unit
PMF	Proton motive force
PPANT	4'Phosphopantetheine
PSCD	Primary systemic carnitine deficiency
PTM	Post transcriptional modifications
qRT-PCR	Quantitative Real Time Polymerase Chain Reaction
R	Argenine
RA	Right Atria
ROI	Region of interest
ROS	Reactive oxygen species
RT	Room temperature
RT-PCR	Reverse transcription polymerase chain reaction
RV	Right Ventricle
SAN	Sinoatrial Node
SBFSEM	Serial block face scanning electron microscopy
SD	Standard deviation
SD	Sudden death
SDHB	Succinate dehydrogenase complex
sGC-PKG	Soluble guanylate cyclase-cGMP-dependent protein kinase
SHF	Second heart field
SLC25A16	Solute Carrier family 25 Alpha 16
SLC5A6	Solute Carrier family 5 Alpha 6
SMVT	Sodium-dependent Multivitamin Transporter
SV	Stroke Volume
TAE	Tris base, acetic acid, EDTA
TBS	Tris-buffered saline
TBST	Tris-buffered saline and tween 20

TCA	Tricarboxylic Acid
TE	Echo time
TEM	Transmission electron microscopy
TnT	Troponin
TPN	Total Parenatal Nutrition
TPP	Thiamine pyrophosphate
TR	Repetition time
UQCRC2	Cytochrome b-c1 complex
V	Ventricle
VSD	Ventricle septal defects
W	Tryptophan
WES	Whole exome sequencing
WGS	Whole genome sequencing
WGA	Wheat germ agglutinin

List of Tables

List of Figures

Chapter 1 Introduction

1.1 Cardiovascular Disease

Cardiovascular disease (CVD) is one of the leading causes of death around the world. According to the World Health Organisation, 31% of global deaths are caused by CVD every year, equating to approximately 17.7 million people (Organisation, 2017). Of these, 353 700 were caused by cardiomyopathies (Roth *et al.*, 2017). Congenital heart defects are the most common congenital malformation in new-borns and occur in ~8 in every 1,000 live births (Olson and Srivastava, 1996; Knowles *et al.*, 2017). To determine how these defects arise it is important to understand normal heart development and function.

1.1.1 Formation of the heart

The heart is one of the first fully functional organs to develop during embryogenesis and is formed in a similar mechanism within vertebrates (Hamburger and Hamilton, 1951; Olson and Srivastava, 1996; Kuo *et al.*, 1997). The process is initiated on post conception day (pcd) 21 in humans and embryonic day (E) 6.5 in mice (Brand, 2003; Moorman *et al.*, 2003). Physiological pumping of the heart occurs at approximately 3 weeks post conception in humans and E8.0 in mice. This process continues while cardiac remodelling takes place to form the four chambers of the heart (Figure 1.1) (Brand, 2003). Within the cardiogenic fields, cardiac progenitor cells migrate bilaterally to the primitive streak. These fields travel to the midline of the embryo to form the cardiac crescent, which fuse to create the linear heart tube around E8.0 (Olson and Srivastava, 1996; Brand, 2003; Moorman *et al.*, 2003). Myocardial cells found within the linear heart tube differentiate into cardiomyocytes and begin to beat (Andrés-Delgado and Mercader, 2016). Following this, cardiac looping takes place, whereby the heart tube loops to the right and the ventricular regions expand. This causes all four chambers to align in the correct anatomical position. At this point, cells which later form the tricuspid and mitral valves begin to migrate and create endocardial cushions (Person *et al.*, 2005). During this process, extracardiac cells are recruited from the proepicardium organ, the second heart field (SHF) and neural crest cells to form the epicardium, ventricle, atria and, contribute to outflow tract development, respectively (Andrés-Delgado and Mercader, 2016). Tight regulation of the looping process is

carried out by two pathways which include *lefty* and *Pitx2* (Moorman *et al.*, 2003; Hill *et al.*, 2019). Upon completion of cardiac looping, the outflow tract extends into the pharyngeal arches allowing the formation of cardiac chambers (Moorman *et al.*, 2003). Septation and trabeculation then occurs by E14.5. During this, cardiomyocyte proliferation is responsible for the formation of the ventricular trabeculae and compact myocardium (Figure 1.1).

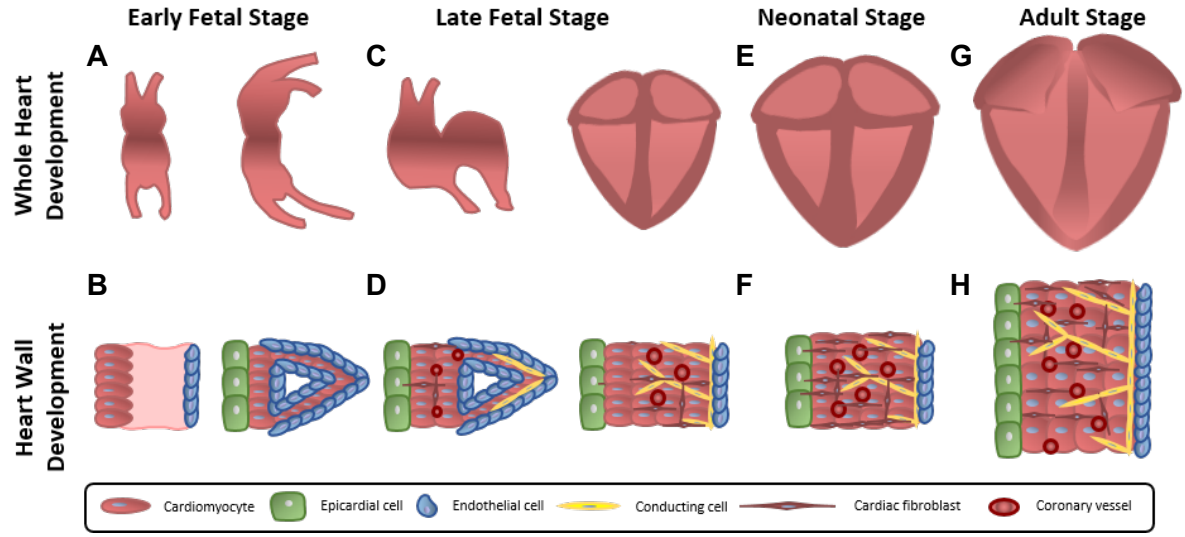

Figure 1.1. Overview of cardiac development and ventricle wall development. A) Formation of the heart tube and early cardiac looping encompasses the early fetal stage. B) During this stage fetal cardiomyocytes line the endocardium and begin to spontaneously beat. Throughout cardiac looping, trabeculations begin to form. C) The late fetal stage includes late cardiac looping and formation of the four chambers. D) Late cardiac looping consists of compaction of the myocardium and epicardial-derived progenitor cells undergoing epithelial to mesenchymal transition and migrating into the myocardium differentiating into cardiac fibroblasts. E) The neonatal stage (post birth) the heart grows in size to meet the workload demand (physiological hypertrophy). F) During this, cardiomyocytes hypertrophy as workload increases resulting in an increase in cardiomyocyte maturation. G) The adult heart is fully mature with an increased left ventricular wall thickness. H) The cardiomyocytes within the heart wall during this stage are mature aligned cells that possess high functional efficiency to meet demand of the grown body. Adapted from (Scuderi and Butcher, 2017).

Following birth, cardiomyocytes continue to mature (Figure 1.1). Cardiomyocytes contribute to the thickening of the heart through hypertrophy, whereby the cells enlarge but do not proliferate. Maturation is observed through definition of sarcomeres, binucleation of the cell and physiological cardiomyocyte hypertrophy (Jacot *et al.*, 2010a; Scuderi and Butcher, 2017). The thickening of the ventricular wall occurs in response to an increase in haemodynamic load following birth (Foglia and Poss, 2016). As previously mentioned, mature cardiomyocytes do not proliferate, and

therefore if injury to the heart occurs it compensates for a loss of cardiomyocytes by pathological hypertrophy resulting in dilative or concentric remodelling within the heart (Leone *et al.*, 2015). This is accompanied by fibrosis leading to ventricle wall stiffness, and continuous cardiomyocyte apoptosis.

This process is highly complex, and disruption often results in a cardiovascular disease phenotype. Animal models provide an invaluable tool in understanding heart development, with more than 150 mouse models reported to develop cardiac dysfunction through mutation of essential components of heart development (Brand, 2003). Mutations in zebrafish models have also been reported with cardiac dysfunction, therefore understanding the cardiac development at the molecular level provides vital insight into the pathomechanism of cardiovascular diseases.

1.1.2 Energy metabolism during heart development

Efficient cardiac function heavily relies upon a constant energy supply, to provide the body with oxygen and essential nutrients (Lopaschuk and Kelly, 2008). To maintain this high energy supply, cardiac processes have adapted to utilise any available substrate for ATP synthesis. When the heart becomes stressed, through starvation or overexertion, this substrate flexibility enables the heart to maintain its energy supply, short term (Kolwicz *et al.*, 2013). Throughout cardiac development the heart can use lipids, amino acids and carbohydrates as a source for energy metabolism (Doenst *et al.*, 2013).

During embryogenesis the fetal circulation contains high levels of lactate and glucose, while levels of fatty acids are low (Figure 1.2) (Stanley *et al.*, 2005). The heart utilises lactate and glucose rather than fatty acid oxidation (FAO) for energy production. At this stage the fetus exists within a hypoxic environment, and relies upon various transcription factors, such as hypoxia inducible factor 1 (*Hif-1α*), to regulate glycolysis; the conversion of glucose to pyruvate (Kolwicz *et al.*, 2013). Expression of these cofactors is high within fetal hearts, whereas expression of essential regulators of mitochondrial biogenesis and FAO is reduced. Once born, the neonatal heart is exposed to oxygen tension and an increase in haemodynamic load. This induces a metabolic transformation, increasing cardiac mass and mitochondrial biogenesis simultaneously. This metabolic switch reduces glucose dependency and increases the level of fatty acids within circulation, generating ATP through FAO. This process is driven by a reduction in the expression of metabolic enzymes including acetyl CoA

carboxylase 2 (*ACC2*) and glucose receptor 1 (*GLUT1*), and an increase in the expression of downstream proteins peroxisome proliferator activated receptor γ (PPARγ) and PPARα which play a key role in fatty acid metabolism (Lopaschuk and Kelly, 2008; Doenst *et al.*, 2013; Kolwicz *et al.*, 2013).

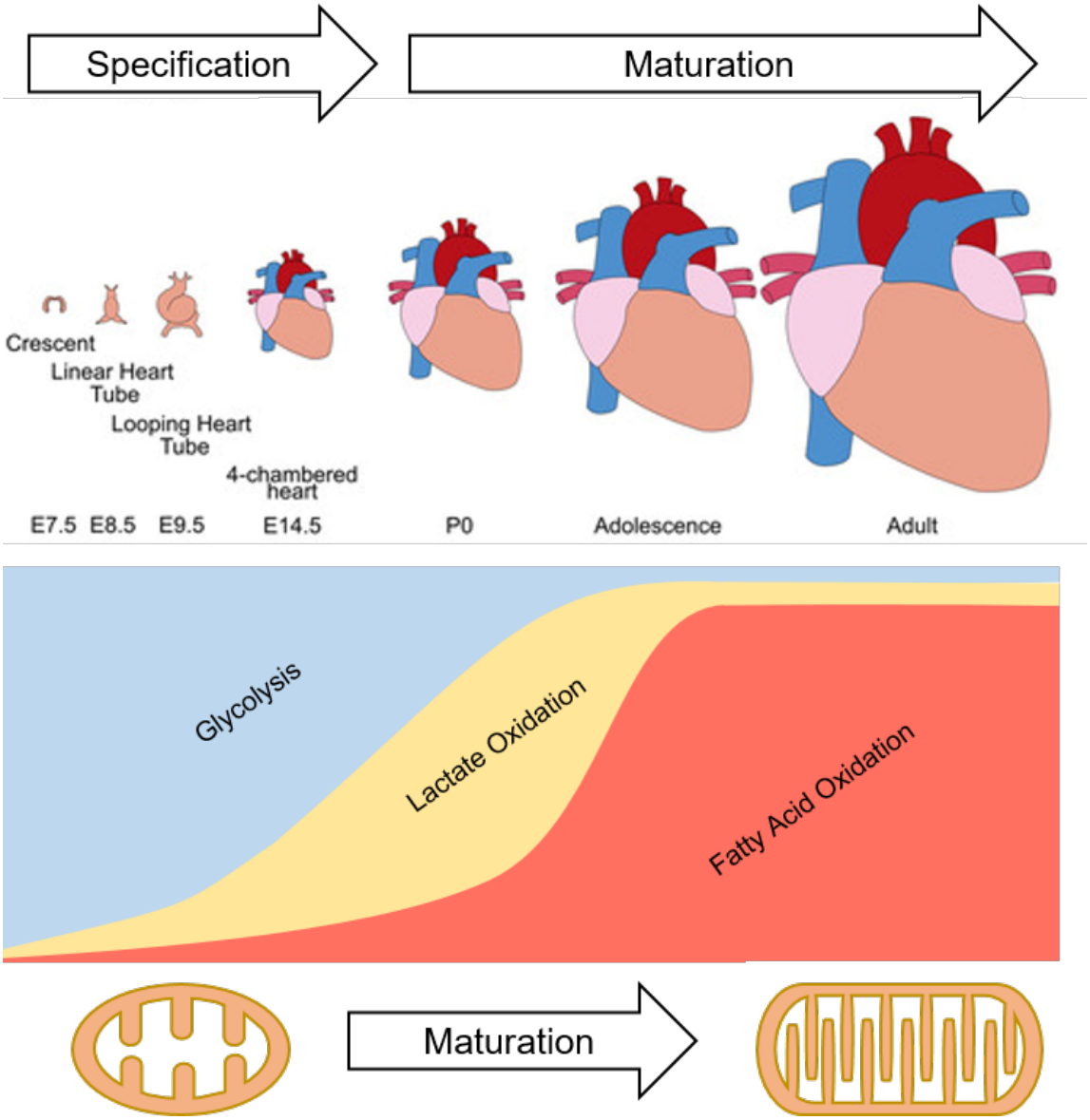

Figure 1.2. Schematic diagram of changes to energy metabolism and mitochondrial maturation throughout cardiac development.
Cardiac cell specification occurs during early embryogenesis E7.5-E14.5 with glycolysis as the main source of energy production while mitochondria are immature. As cardiac maturation continues there is an increase in lactate oxidation from E14.5 to adolescence, where FA oxidation dominates energy production in the matured adult heart which is facilitated by matured mitochondria. Adapted from Guo and Pu (2020) and Morita Y (2020).

Once the cardiomyocytes reach maturation and the neonate reaches adulthood, all metabolic changes are complete. The oxidative capacity for energy production is

increased, with the increased presence of mitochondria within the adult heart. During adulthood, oxidative phosphorylation produces 95% of the total ATP generated within the heart whereas only 5% is contributed from glycolysis (Kolwicz *et al.*, 2013).

1.2 Cardiomyopathy

Cardiomyopathies are a group of heterogeneous disorders, defined as a disease of the myocardium, resulting in a spectrum of clinical phenotypes. Cardiomyopathies can be divided into the following; hypertrophic and dilated cardiomyopathy (Figure 1.3), the most commonly diagnosed, followed by restrictive cardiomyopathy and left ventricular non-compaction, with the rarest form, arrhythmogenic right ventricular dysplasia (Lee *et al.*, 2017; Yuan, 2018). Cardiomyopathy can affect both adults and children and is further classified when considering if the patient has a primary cardiomyopathy; confined to heart muscle, or a secondary cardiomyopathy as a result of systemic disease such as mitochondrial or neuromuscular disorders (Jefferies and Towbin, 2010; Meyers *et al.*, 2013; El-Hattab and Scaglia, 2016b).

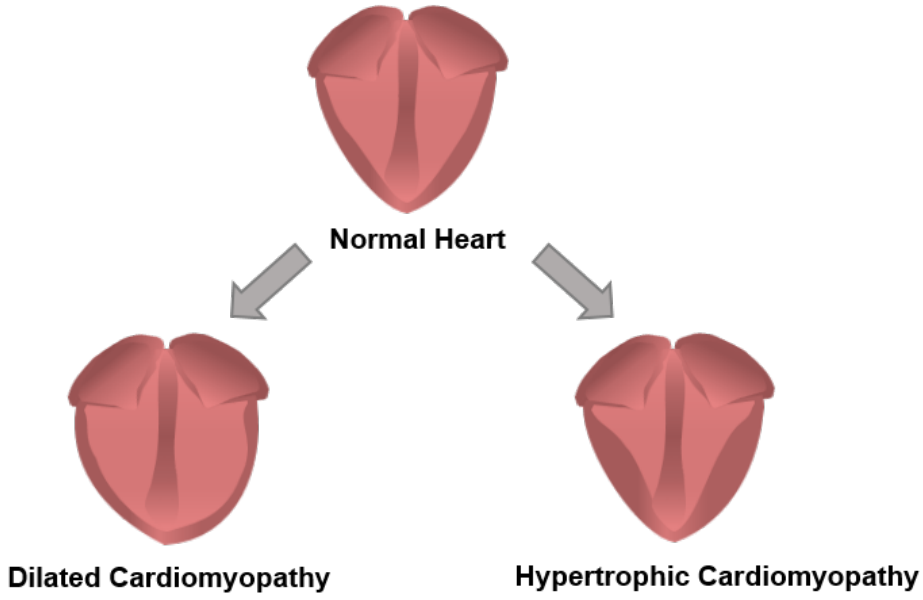

Figure 1.3. Schematic of cardiomyopathy morphology showing changes from normal heart morphology.
Dilated cardiomyopathy; thinning of the ventricle wall, and hypertrophic cardiomyopathy; thickening of ventricle wall.

1.2.1 Paediatric cardiomyopathy

Paediatric cardiomyopathies affect approximately 1 in 100,000 children worldwide, with over a third of symptomatic patients requiring heart transplantation or risk mortality within two years of life (Lipshultz *et al.*, 2013; Lee *et al.*, 2017; Yuan, 2018). Types of cardiomyopathies are subdivided into idiopathic; sporadic or unknown in origin and familial, defined as when two or more cases of idiopathic cardiomyopathy are identified in closely related family members. Clinical presentation can vary depending on the subtype of cardiomyopathy, ranging from completely asymptomatic to severe cardiac dysfunction leading to death, often observed in cases of dilated cardiomyopathy (Elliott, 2000; Yuan, 2018).

1.2.2 Dilated cardiomyopathy

Dilated cardiomyopathy (DCM) has a global incidence of 1 in 2,700 and is characterised by an increase in left ventricular volume and mass leading to systolic dysfunction, often defined by reduction in ejection fraction of the LV (Jefferies and Towbin, 2010; Sweet *et al.*, 2015; McNally and Mestroni, 2017; Schultheiss *et al.*, 2019b). Patients present a major risk factor of heart failure and death, as systolic dysfunction does not typically present with immediately obvious symptoms (McNally and Mestroni, 2017). However, when the left ventricle becomes dilated, ventricle wall stress in addition to reduced systolic function causes ventricular arrhythmias and changes to the conduction cycle of the heart, which can be detected by electrocardiography (ECG) (Jefferies and Towbin, 2010; McNally and Mestroni, 2017). The presence of conduction defects indicates that the cardiac conduction system plays a pathological role in DCM. As previously described, if DCM remains undetected, patients undergo heart failure with symptoms of breathlessness, abdominal pain and fatigue (Jefferies and Towbin, 2010). Paediatric cases often present with a reduced appetite, muscle weakness and wasting. Clinical diagnosis of DCM is confirmed with the presence of reduced ejection fraction (<40%) and fractional shortening, which are used as measures of muscle contractility using cardiac magnetic resonance imaging (CMR) and echocardiography respectively (Francone, 2014; Fatkin *et al.*, 2017; Mathew *et al.*, 2017; McNally and Mestroni, 2017).

With the advancement of next-generation technologies, genetic screening has become highly improved through the integration of whole exome (WES) and whole

genome sequencing (WGS) approaches within the clinical setting (Krier *et al.*, 2016; Marshall *et al.*, 2020). Many case studies have linked sarcomeric, nuclear and cytoskeletal genes to dilated cardiomyopathy. The sarcomere consists of myofilaments, thick and thin, and is known to be the basic structure required for contraction (Figure 1.4) (Dellefave and McNally, 2010). Muscle contraction occurs by myosin heads binding to thin actin filaments to form cross bridges. Contraction occurs by a series of hydrolysis reactions of adenosine triphosphate (ATP) to adenosine diphosphate (ADP) to adenosine monophosphate (AMP) to generate the energy required for the sliding of actin filaments (Squire, 2016). The regeneration of ATP causes the myosin heads to detach from the actin filaments, returning to a relaxed state ready for another contractile cycle. This process is known as Sliding Filament Theory, first described by Huxley and Hanson (1954). Most of the proteins which form the thin and thick filaments have been reported to cause autosomal recessive DCM characterised by conduction abnormalities (Dellefave and McNally, 2010; England and Loughna, 2013; Mestroni *et al.*, 2014). The sarcomeric protein most commonly associated with DCM is titin (*TTN)* (Dellefave and McNally, 2010; Mestroni *et al.*, 2014). *TTN* is the largest human protein known to be highly expressed within the heart and plays a key role in diastolic and systolic function (Hackman *et al.*, 2002; Dellefave and McNally, 2010). Although many cases of familial DCM have been diagnosed with mutations in proteins (Figure 1.4), a large proportion of cases remain undiagnosed. Therefore, sequencing projects investigating novel genetic causes of DCM are required to i) provide accurate diagnoses, ii) allow clinicians to give genetic counselling, iii) allow research to be carried out into novel therapeutic targets for treatment. Although the cost of individual sample sequencing is falling, it still remains a limiting factor in general medicine (Posey *et al.*, 2016; Mazzarotto *et al.*, 2020) .

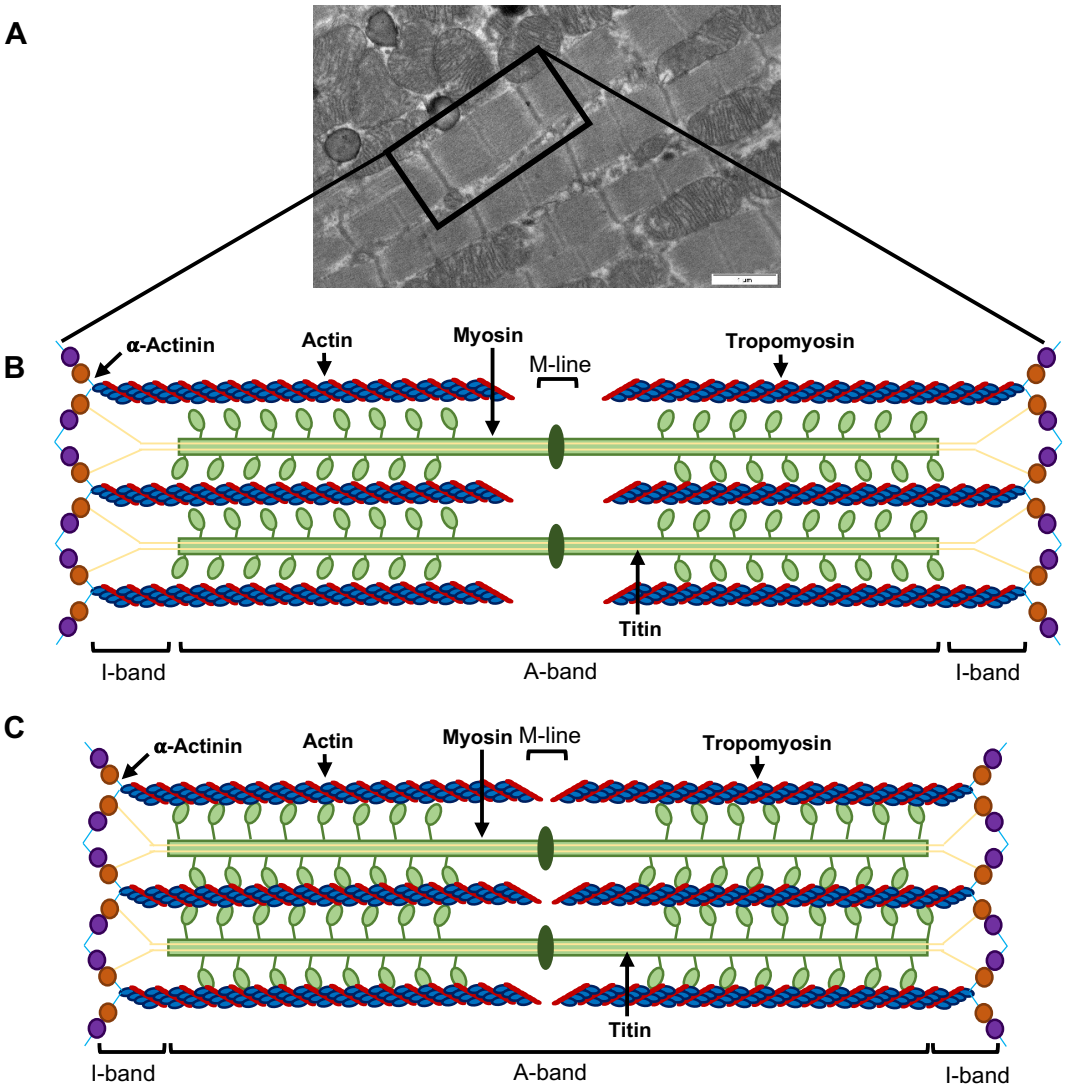

Figure 1.4. Sarcolemmal proteins and structure.
A) Transmission electron microscopy image of cardiac muscle (mouse). B) Sarcomeric structure consisting of thin and thick myofilaments in a relaxed state. Proteins associated with DCM are indicated. C) Contracted sarcomere with myosin heads bound to shortened (contracted) actin filaments. Dark blue = Actin, green = myosin, orange = titin cap, purple = myotilin, red = tropomyosin, turquoise = α-actinin, yellow = titin. Adapted from (Rahimov and Kunkel, 2013).

1.2.3 Diagnosis and treatment

To give an accurate diagnosis of cardiomyopathy, clinicians need to ascertain a full family history to access whether the case is sporadic or has potential to be caused by genetic factors (Elliott, 2000; Minoche *et al.*, 2019). Dilated cardiomyopathy is also known to be a secondary condition to several X-linked diseases such as Duchenne muscular dystrophy as well as metabolic and mitochondrial disorders, such as Barth syndrome and Friedreich ataxia, therefore a full family history must be as comprehensive as possible (El-Hattab and Scaglia, 2016a).

Cardiomyopathies can be confirmed using ECG, echocardiography, CMR and finally an endomyocardial biopsy (Elliott, 2000; Yuan, 2018). The use of ECG is usually the first line of screening for patients with suspected cardiac conduction abnormalities.

The cardiac conduction cycle is one of the most important mechanisms within the heart which coordinates blood flow by initiating cardiac contraction and relaxation in different areas within the heart. The cardiac conduction system comprises of the sinoatrial node (SAN), atrioventricular node (AVN), bundle of His and the left and right bundle branches (Figure 1.5A) (Anderson *et al.*, 2009; Ginoux and Rossetto, 2014). The cycle begins at the SAN where an electrical impulse (action potential) is passed to the AVN initiating atrial depolarisation and contraction, this is characterised on an ECG trace as the P wave. The action potential is held at the AVN, while blood flows from the atria into the ventricle, indicated by the PR interval. The action potential then travels through the bundle of His to the right and left bundle branches triggering ventricular depolarisation and contraction, expelling blood from the ventricles into the circulation, shown as the QRS complex. The ventricles then repolarise (T wave) and relax ready for another conduction cycle (Anderson *et al.*, 2009). The ventricular AP can be generalised to compose of 5 phases (Figure 1.5B); 0) depolarisation, sodium (Na^+) channels open allowing rapid Na^+ influx into the cell, this causes the membrane potential to increase from the resting potential (~ -80mV). 1) early repolarisation, K^+ channels open to allow K^+ efflux decreasing the membrane potential. 2) Plateau, Ca^{2+} channels open to allow Ca^{2+} influx at a similar rate to K^+ efflux, balancing the membrane potential. 3) final repolarisation, $Ca2^+$ channels begin to close whilst K^+ channels remain open continuing K^+ efflux and decreases the membrane potential to the resting state. 4) resting, membrane potential is maintained at ~ -80mV through open K^+ channels and closure of Ca^{2+} and Na^+ channels (Nerbonne and Kass, 2005; Joukar, 2021). Whilst in the slow action potential, the resting phase is less negative ~ -70mV, depolarisation peaks at ~ 0mV and early repolarisation does not occur (Joukar, 2021).

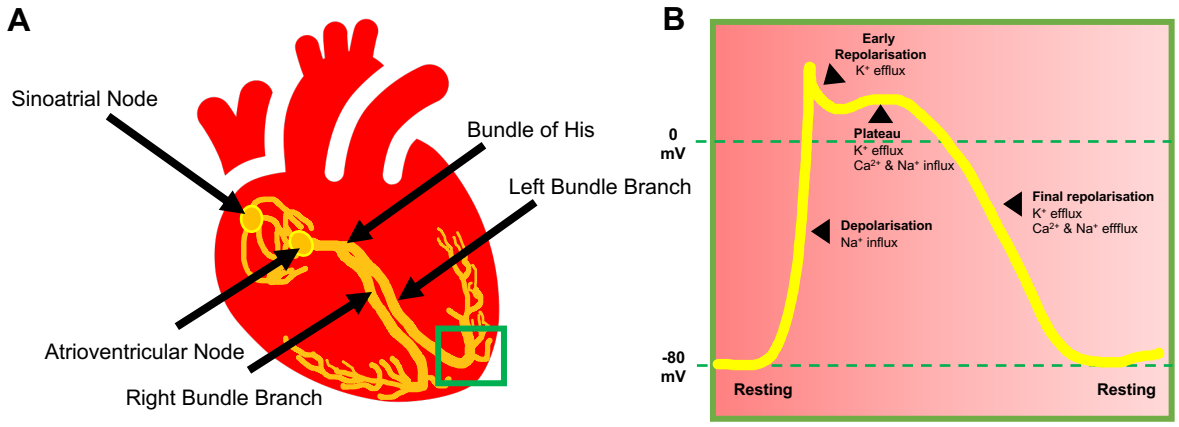

Figure 1.5 Cardiac conduction system and action potential.
A) Schematic representation of cardiac conduction system with key components labelled. Electrical impulses are received by the sinoatrial node, triggering atrial contraction (depolarisation). The impulse is passed and held at the atrioventricular node to allow blood to flow from the atria to the ventricle. Following this, the impulse is passed through the bundle of His, before splitting along both the left and right bundle branches, allowing contraction of the ventricles (depolarisation). The ventricles then relax (repolarisation), ready for another conduction cycle. Adapted from Ginoux and Rossetto (2014). B) Representation of a ventricular action potential. Ventricular cardiomyocytes are in a resting phase at ~80mV, until the electrical impulse triggers membrane depolarisation and rapid influx of Na+ (phase 0), the cell then undergoes early repolarisation and K+ efflux (phase 1). The action potential then plateaus with K+ efflux occurring in addition to Ca2+ and Na+ influx (phase 2). Ca2+ influx decreases with K+ efflux continuing to return the cell membrane potential back to the resting state. Adapted from Nerbonne and Kass (2005).

There are now many characteristics and patterns of an ECG trace which have been linked to cardiomyopathy. Specifically a review by Finocchiaro *et al.* (2020) summarised characteristic patterns of published DCM patients which included but are not limited to, atrioventricular block, abnormal QRS, left ventricular hypertrophy and T wave inversion and ST depression. Although indicative of DCM, follow up investigations by further functional imaging including CMR and echocardiography are used to provide more information on diastolic and systolic function, as well as determining the degree of myocardial fibrosis often observed in DCM patients using late gadolinium enhancement in CMR imaging (Kramer, 2015). Myocardial fibrosis occurs through many pathways, activation of the renin-angiotensin-aldosterone system (RAAS) is most associated with DCM and HF (Kong *et al.*, 2014). In this pathway, the enzyme renin, converts angiotensinogen to angiotensin I (AngI) and, in the presence of angiotensin converting enzyme (ACE), AngI is further converted to

angiotensin II (AngII), a stimulant for fibroblast proliferation (Jia *et al.*, 2018). In DCM and HF, once the heart becomes injured, fibroblasts and macrophages invade the myocardium producing renin and ACE, which in turn stimulates AngII production, fuelling fibroblast proliferation and enhancing collagen synthesis within the heart (Weber *et al.*, 2013; Jia *et al.*, 2018). Increased myocardial fibrosis results in myocardial stiffening contributing to systolic dysfunction observed by enhanced CMR. As a chronic disease, paediatric cardiomyopathies are typically progressive and pose a high economic burden (Nandi *et al.*, 2018). Early genetic screening and diagnosis, provides both the patient, family and medical research teams, with the most information and time to monitor the disease progression, and to allow further research to identify potentially beneficial interventions, such as genetic targets for gene therapies (Lipshultz *et al.*, 2013).

1.3 Consanguineous family with two children affected by DCM

1.3.1 Family history and clinical presentation

This project is based upon a consanguineous family with three daughters, two of whom presented with DCM (Figure 1.6). The family is of Pakistani ethnicity and parents are first cousins who conceived three children. The first child died at 24 months of age due to DCM. The mother's pregnancy and delivery of the second affected child was normal, with no need for resuscitation at birth.

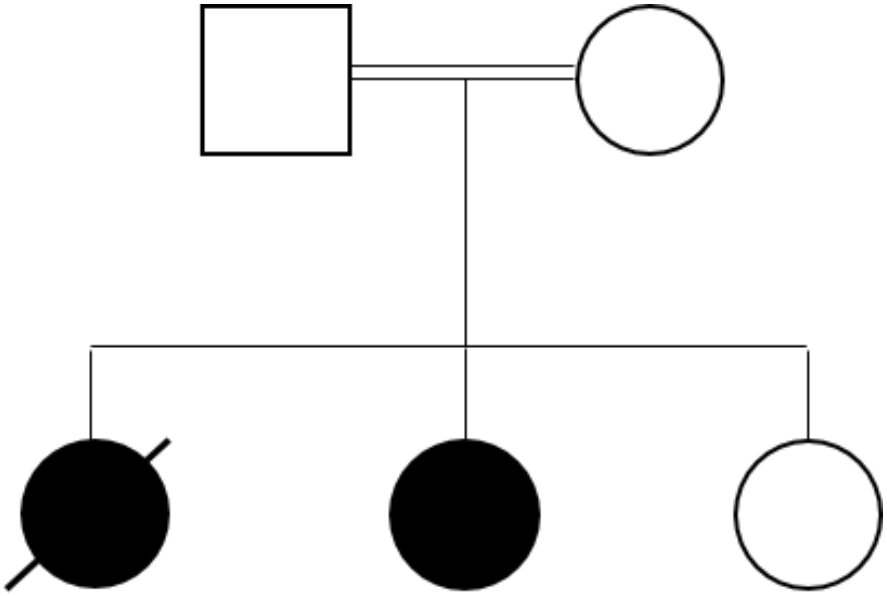

Figure 1.6. Family pedigree of consanguineous family.
Both consanguineous (double line) parents and third child are unaffected (white) with the first and second child affected by DCM (black). The first child died at 24 months with the second child receiving a heart transplant. Square = male, circle = female.

The child was healthy until 9 months where she developed an acute illness including low blood glucose and stupor, with rapid deterioration leading to admission to the paediatric intensive care unit (PICU). During this event, she was placed on a ventilator for two weeks, where total parenteral nutrition (TPN) was administered as part of standard care protocols and DCM was noted. TPN is administered intravenously when oral feeding is not possible, and provides essential nutrients such as vitamins, amino acids, glucose and lipids in addition to electrolytes ((NICE), 2021). The patient was removed from the ventilator after two weeks, discharged where she was remained well until the following year, where she developed a similar acute illness which required intropic support to regulate cardiac contraction. During this time, she was ventilated for 6 weeks and developed pneumonia, left sided paralysis and absent seizures. Mild developmental delay was noted, with continuous nasogastric feeding required due to gastroparesis (a chronic condition affecting movement of food through the stomach) and TPN was also given during ventilation. Once recovered the patient was discharged and remained well for two years.

Following this period, she again developed an acute illness and was transferred to the Freeman Hospital Newcastle upon Tyne Hospitals NHS Foundation Trust for the insertion of a left ventricular assist device (LVAD). At implantation, a biopsy of the LV was collected and revealed myocardial disarray (Figure 1.7A), signs of apoptosis

(Figure 1.7B) with “relatively preserved myocardial architecture’ and “enlarged myocytes with perinuclear halo” (Figure 1.7C), as well as “evidence of mild interstitial and perimyocyte fibrosis with mild subendocardial fibrosis” (Figure 1.7C) determined by the examining pathologist as “Cardiomyopathy with no morphological evidence as to cause”. Transmission electron microscopy (TEM) was also performed and showed localised sarcomeric wasting (Figure 1.8A), increased mitochondrial proliferation (Figure 1.8B) and some evidence of autophagy (Figure 1.8C). Additionally, oxidative enzyme histochemistry was performed on the biopsy which showed normal enzymatic activity, however, a slight decrease in complex IV was noted by Dr Robert W Taylor, Professor of Mitochondrial Pathology. The patient was also given vitamin supplementation of Riboflavin, Thiamine, Ascorbic acid, and Ubiquinone during this time. After 7 weeks, cardiac function was recovered, the VAD was removed, and the patient was discharged.

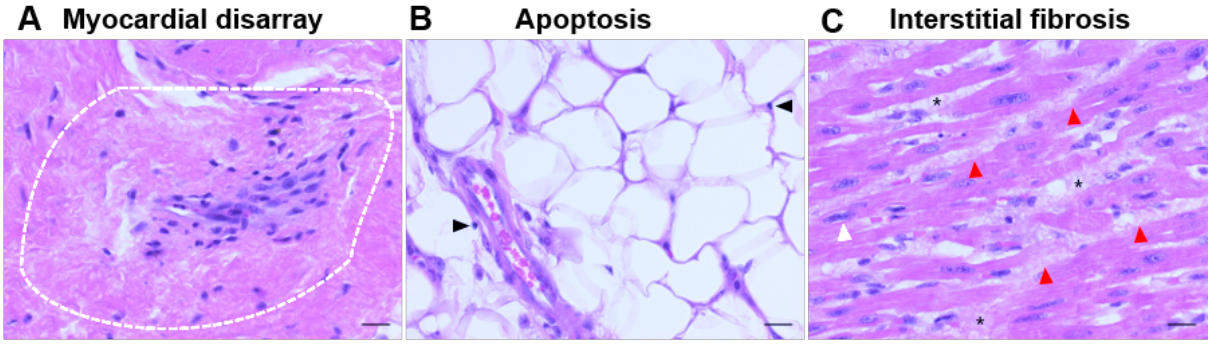

Figure 1.7. H&E staining performed on patient myocardial biopsy by examining pathologist.
A) Myocardial disarray highlight by white dashed box. B) Evidence of apoptosis with apoptotic cell debris indicated by black arrowheads. C) Widespread interstitial fibrosis (red arrowheads) with perinuclear halo observed (white arrowhead). Scale bar 20μm. Images provided by Dr Sian Hughes (REC 19/NE/0028).
.

The following year, another acute event triggered re-admission to the Freeman Hospital where a second LVAD was inserted and subsequently removed following recovery of LV function after 2 weeks, whilst receiving TPN.

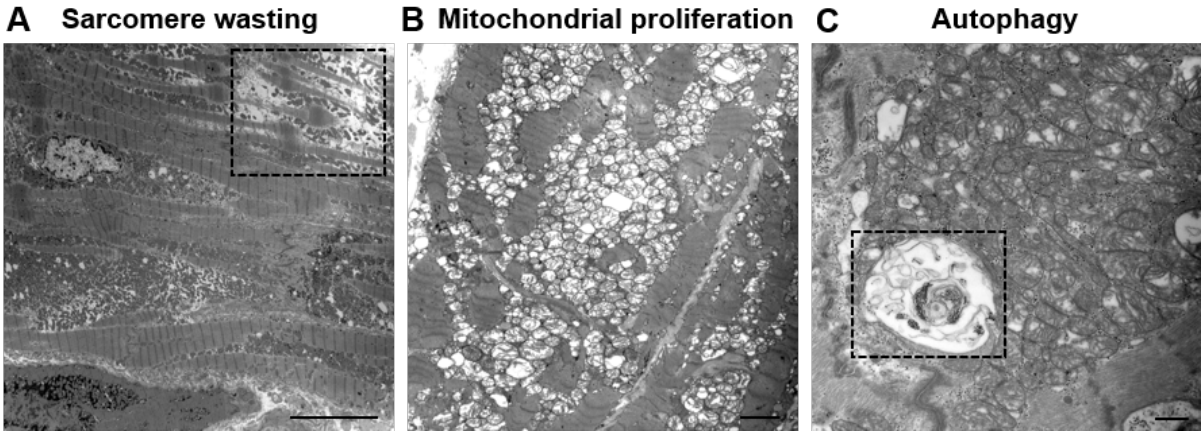

Figure 1.8. Micrographs of patient myocardial biopsy.
A) Localised region of sarcomeric wasting (dashed box). B) Evidence of increased mitochondrial proliferation. C) Autophagy apparent by presence of autophagosome shown (dashed box). Scale bar A 10μm, B 2μm, C 500nm. Images provided by Peter S. A. Rowley (REC 19/NE/0028).

Two years later, the patient was admitted to the Freeman Hospital with lethargy and cardiorespiratory insufficiency where a third LVAD was inserted as a bridge to cardiac transplant which was received the following week. During this time, the patient was administered TPN during admission and was discharged from hospital one month later with regular cardiovascular follow up appointments which detail no sign of rejection and good cardiac function. Assessment by Dr Robert MacFarland, Professor of Paediatric Mitochondrial Medicine, found that the development of the DCM phenotype was different to that of a typical mitochondrial disease found in children as the disease onset remained confined to the heart with some secondary events found to affect the brain including developmental delay.

Interestingly, within the extended family tree, there have been several deaths due to myocardial infarction (MI) as well as several miscarriages with the affected mother affected by haemochromatosis (iron overload) noted in the family history (Fleming *et al.*, 2005).

With the cause of cardiomyopathy unclear in this family, blood samples were collected for DNA extraction to be used for WES.

1.3.2 Whole Exome Sequencing

DNA samples from the two affected children were collected and whole exome sequencing (WES) was carried out at Newcastle University, with analysis performed by Dr Matthieu Miossec. This revealed no pathogenic mutations in any known genes

which cause cardiovascular defects and disease, however, a missense mutation (Chr2: 27427777 G>A), in a highly conserved amino acid residue (p.R253W) was identified within *SLC5A6* and was present on both alleles within both affected siblings (Figure 1.9B). Segregation analysis by Sanger sequencing confirmed that the homozygous mutations in *SLC5A6* were present in the affected children and the unaffected parents and sibling were heterozygous for the mutation, therefore segregating with disease within the family (Figure 1.9A).

SLC5A6 encodes the sodium-dependent multivitamin transporter, responsible for the transport of three essential substrates; biotin, pantothenic acid and lipoic acid. Studies have shown an adjacent amino acid residue, H254, plays an important role in the function of *Slc5a6* (Ghosal and Said, 2011). It was demonstrated that a reduction in sodium-mediated biotin transport was caused by a decrease of *Slc5a6* expression at the cell membrane induced by mutation of H254. Based upon this research, we propose R253W would result in a similar mechanism, reducing biotin uptake within the cell by reducing *Slc5a6* expression at the cell membrane.

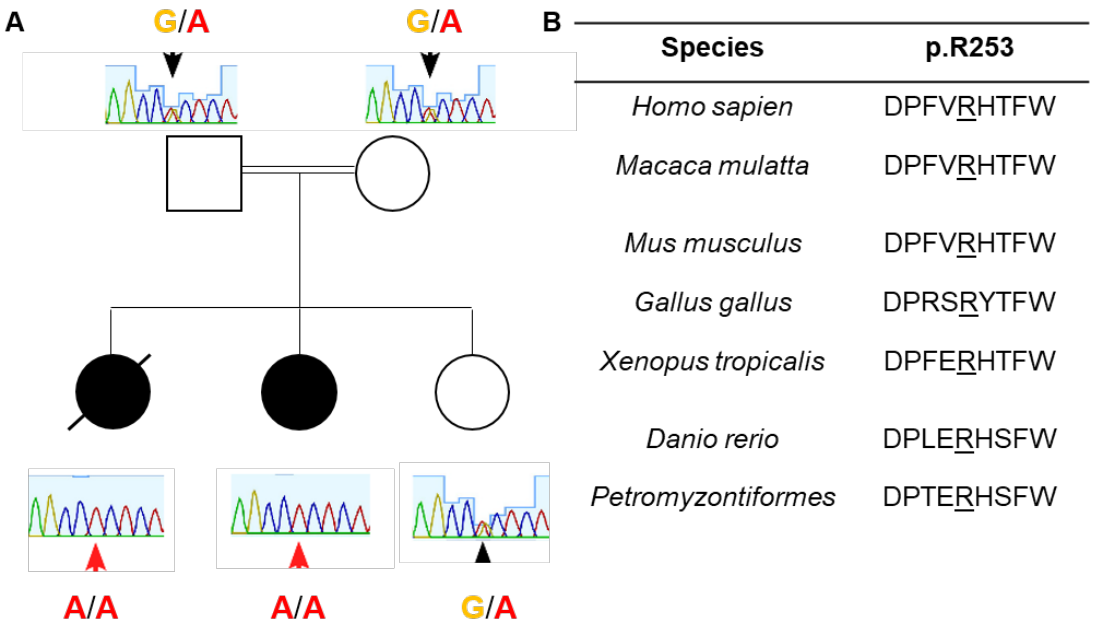

Figure 1.9. Variant analysis of the *SLC5A6* homozygous missense variant. Segregation analysis of the family showing the chromatograph featuring the homozygous mutation in both affected cases and the heterozygous mutation carried by the parents and unaffected sibling. B) Conservation of the amino acid sequence flanking the mutation site (p.R253) though evolutionary species.

In addition, *SLC5A6* was also highlighted as a novel candidate of interest by the referring clinician, through links with Barth syndrome whereby treatment with pantothenic acid proved successful in restoring myocardial function (Ostman-Smith *et al.*, 1994). *SLC5A6* was taken forward as the gene of interest for further functional investigation.

1.4 Sodium-dependent Multivitamin Transporter

SLC5A6 is an 18 exon transcript located on chromosome 2p23 (Prasad *et al.*, 1998). *SLC5A6* encodes the human sodium multivitamin transporter (SMVT), belonging to the amino acid-polyamine organocation superfamily (Jack *et al.*, 2000; Hediger *et al.*, 2013). This superfamily encompasses members which function as solute:cation symporters and solute:solute antiporter (Jack *et al.*, 2000; Wong *et al.*, 2012). SMVT belongs more specifically to the sodium/solute symporters (SSS) family which allow the unilateral transport of molecules across the cell membrane (Prasad *et al.*, 1998; Quick and Shi, 2015). Structurally and functionally unrelated, water-soluble vitamins share the responsibility of being essential for cellular growth, development, and function (Said, 2004; Said, 2011). Mammals cannot synthesise a number of vitamins and therefore rely upon the absorption of an external supply of nutrients via the gastrointestinal tract (Chatterjee *et al.*, 1999; Quick and Shi, 2015). Absorption through the intestine is facilitated by specialised carrier mediated transporters (Said, 2004).

SLC5A6 contains 13 transmembrane domains, with a LeuT fold at its core (Figure 1.10). It consists of two sets of 5 transmembrane domains which, when sodium is present, conformationally change to actively transport three essential substrates; biotin, pantothenic acid (PA) and lipoic acid (LA) into mammalian cells (Prasad *et al.*, 1998; Said, 2011; Ghosal *et al.*, 2012; Quick and Shi, 2015). This transport relies on sodium concentration gradient, whereby the concentration of sodium ions is higher outside of the cell (extracellular) than inside the cell (intracellular), this gradient is maintained through active transporters including the sodium/potassium pump which use ATP to facilitate transport (Bindels and Wagner, 2014). Energy from this process is released when sodium moves into the cell (down the sodium gradient) along with a substrate via a carrier protein, this is known as secondary active transport (Berg JM, 2002c; Forrest *et al.*, 2011). SMVT has also been reported to transport iodide in *Xenopus* oocytes using the same transport system (de Carvalho and Quick, 2011). These organic substrates play a vital role in cellular metabolism and homeostasis.

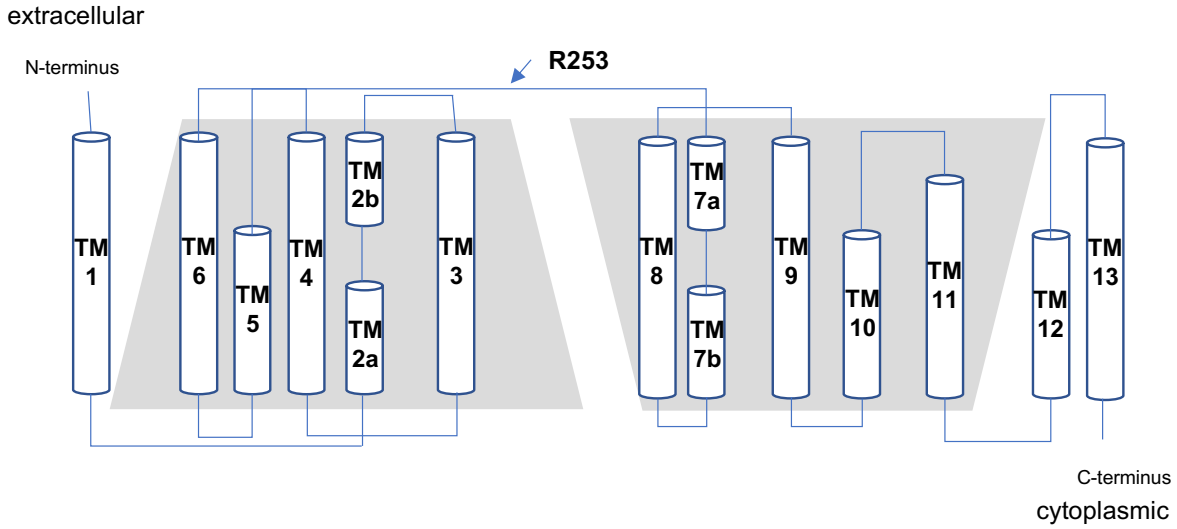

Figure 1.10. Transmembrane domains and LeuT fold structure of Slc5a6. Slc5a6 is comprised of 13 transmembrane domains with an extracellular N terminus and cytoplasmic C-terminus. The LeuT fold of the transporter includes two sets of five transmembrane (TM) domains; TM2a-TM6 and TM7a-TM11 (indicated within grey trapeziums), with a hinge region connecting the fold. The patient mutation is noted within the hinge region of the transporter.

Biotin, vitamin B7, is required for cell growth and development. The vitamin acts as a cofactor for several carboxylases required for essential metabolic pathways (Zempleni *et al.*, 2009; Said, 2012; Waldrop *et al.*, 2012). PA, vitamin B5, is a cofactor for coenzyme A synthesis, the main component of acetyl CoA, required for energy metabolism. PA uptake is essential in organisms which lack the ability to synthesise PA (Leonardi and Jackowski, 2007). LA is an essential cofactor for mitochondrial energy metabolism, specifically pyruvate dehydrogenase (PDH) and α-ketoglutarate dehydrogenase (αKGDH) complexes, and is also critical for regulation of AMPK signalling and transcription factors *PGC-1α*; however, LA is synthesised endogenously (Packer and Cadenas, 2010; Solmonson and DeBerardinis, 2018).

SLC5A6 is expressed throughout many tissues including brain, kidney, intestine and placenta (Prasad *et al.*, 1998; Quick and Shi, 2015; Uchida *et al.*, 2015; Subramanian *et al.*, 2017); however, little is known about its expression and involvement within the heart. Animal studies have been performed to investigate the effect of *Slc5a6* knockdown within the intestinal tract (Ghosal *et al.*, 2012). The Said group observed growth retardation, a reduction in bone density and length and reduction in villi length thought to contribute to the premature death of the knockout mice (Ghosal *et al.*, 2012; Ghosal *et al.*, 2013). Villi length plays a major role in absorption of nutrients throughout the intestinal tract and a decrease in length would therefore result in a reduction in

surface area to volume ratio, resulting in a decrease in vitamin absorption. Uchida *et al.* (2015) investigated the human sodium-dependent multivitamin transporter at the blood-brain barrier (BBB). They concluded it was the sole carrier for biotin and pantothenic acid across the BBB using a human cerebral microvascular endothelial cell line. This demonstrates the important role SLC5A6 plays in facilitating vitamin transport in multiple high energy dependent tissues.

Mutations in *SLC5A6* have been previously reported in patients with a neurodegenerative phenotype including developmental delay, immunodeficiency severe gastrointestinal defects and bone abnormalities (Subramanian *et al.*, 2017). Over-supplementation of biotin and pantothenic acid has been shown to rescue the phenotype observed in the intestinal specific knockout mouse model (Ghosal *et al.*, 2012; Ghosal *et al.*, 2013; Sabui *et al.*, 2018). Subsequently, the patient was given high pharmacological doses of biotin and pantothenic acid and responded well to treatment, suggesting the vitamin supplementation as a treatment for future patients with mutations in *SLC5A6* (Subramanian *et al.*, 2017). To date, there have been no publications linking mutations in *SLC5A6* to CVD; however, a recent study investigated biotinylation as a link between metabolism and circadian clocks (He *et al.*, 2016a). The group identified that cardiac expression of *Slc5a6* is reduced in two mouse models of cardiomyocyte-specific circadian clock disruption that present with cardiometabolic disease phenotypes. It is well established that energy homeostasis is maintained through fluctuation of several metabolic pathways which are triggered in response to exogenous and endogenous stimuli. The circadian clock has recently been described as a cell autonomous mechanism which gives organisms a selective anticipatory advantage to prepare for external stimuli before its onset (Bailey *et al.*, 2014; He *et al.*, 2016a). The circadian clock mechanism controls post transcriptional modifications (PTMs) such as phosphorylation, acetylation, ubiquitination and biotinylation. Downregulation of the PTMs has been linked to defects of mitochondrial energy metabolism such as fatty acid β oxidation (Peek *et al.*, 2013; Horton *et al.*, 2016). Almost all fatty acid oxidation defects affect skeletal muscle, heart and liver (Kilic *et al.*, 2011).

1.5 Biotin

Biotin is a water-soluble vitamin (B7) required for normal cell growth and development. The vitamin acts as a coenzyme for several carboxylases required for essential

metabolic pathways. Biotin plays a major role in regulating cell proliferation, gene expression and immune function (Kothapalli et al., 2005; Zempleni & Mock, 2001). A reduction in the availability of biotin would therefore negatively impact a wide range of cellular processes, including cellular respiration, which is essential for life. Biotin is composed of two-rings containing an ureido group known to facilitate the binding of biotin to avidin; the high binding affinity results in the reduction of biotin uptake within the intestine (Said, 2002; Said, 2012). This interaction is widely utilised in molecular biology for techniques including immunoassays, DNA hybridisation and immunohistochemistry (Diamandis and Christopoulos, 1991).

Mammals cannot synthesise biotin and rely upon an exogenous supply through diet, intestinal flora or through endogenous reutilisation of biotin (Healy et al., 2009; Rowland et al., 2018). Once absorbed within the intestine, biotin is transported across the epithelium via SLC5A6.

1.5.1 Biotin deficiency

Humans require a minimum level of biotin intake for the biotin cycle to continue efficiently to contribute to energy metabolism. The recommended intake of the vitamin is approximately 35 µg for children and up to 300 µg for adults; however, larger doses of biotin have been reported to be nontoxic (Said, 2012). Biotin deficiency is known to result in a spectrum of clinical phenotypes including growth retardation, neurological disorders and developmental delay (León-Del-Río, 2005; Quick and Shi, 2015). The deficiency can occur in patients on long-term anticonvulsant therapy, parenteral nutrition or patient with inborn errors of biotin metabolism (Morscher *et al.*, 2012; Said, 2012). A decrease in biotin levels has also been identified in pregnancy (Mock *et al.*, 2002), alcoholic-dependents (Subramanya *et al.*, 2011) and in patients suffering with inflammatory bowel disease. From this, biotin deficiency is a secondary effect, and the long-term decrease in biotin bioavailability has severe effects on downstream carboxylases; however, biotin supplementation is successful in reversing the phenotype (Dupuis *et al.*, 1999; Mock *et al.*, 2002; Zempleni *et al.*, 2008; Pindolia *et al.*, 2011).

1.5.2 Biotin dependent carboxylases

As previously described, biotin is essential for energy metabolism and homeostasis, however, biotin also plays a vital role in the regulation of gene expression. Both roles rely on the active form of biotin (biotinyl-AMP) which is transformed by holocarboxylase synthase (HCS). Once transformed biotinyl-AMP can be used to biotinylate carboxylases for energy metabolism. Investigation into biotin dependent carboxylases, first identified more than 50 years ago, revealed they have two distinct enzymatic activities and catalyse reactions in two stages. Initially, a biotin carboxylase component catalyses the carboxylation of the biotin cofactor using bicarbonate as a carbon dioxide donor (Zempleni *et al.*, 2009; Tong, 2013). In the second stage of the reaction, a carboxyltransferase component catalyses the carbon dioxide transfer from carboxybiotin to the acceptor of the carboxyl group (Tong, 2013). Finally, 1'-N-carboxybiotinyl carboxylase incorporates carboxylate into an organic acid, which is specific to each carboxylase (Zempleni *et al.*, 2009). Both Acetyl-CoA carboxylases, ACCα and ACCβ, propionyl-CoA carboxylase (PCC), 3-methylcrotonyl-CoA carboxylase (MCC) and pyruvate carboxylase (PC) contain the specific lysine residue which allows for covalent binding to biotin, catalysed by HCS (Knowles, 1989; Zempleni and Mock, 2001; Zempleni *et al.*, 2008; Zempleni *et al.*, 2009). Alternatively, biotinyl-AMP can be used to regulate gene expression by triggering the soluble guanylate cyclase-cGMP-dependent protein kinase (sGC-PKG) signal transduction pathway (Pacheco-Alvarez *et al.*, 2005). This pathway regulates genes involved in biotin homeostasis such as *SLC5A6* and *HCS* (Pacheco-Alvarez *et al.*, 2005; Vlasova *et al.*, 2005). When biotinylated carboxylases are used in the TCA cycle they replace other intermediates, such as succinyl CoA, which are required for downstream synthesis of key metabolites such as amino acids or heme groups (Owen *et al.*, 2002; Atamna, 2004; Atamna *et al.*, 2007).

PC localises to the mitochondria and is key to gluconeogenesis, the conversion of non-carbohydrate carbon substrates to glucose. Mitochondrial PCC catalyses an essential step in amino acid, cholesterol side chain and odd-chain fatty acid metabolism. 3-MCC catalyses an essential step in leucine metabolism and ACC catalyses acetyl CoA to malonyl CoA (Figure 1.11).

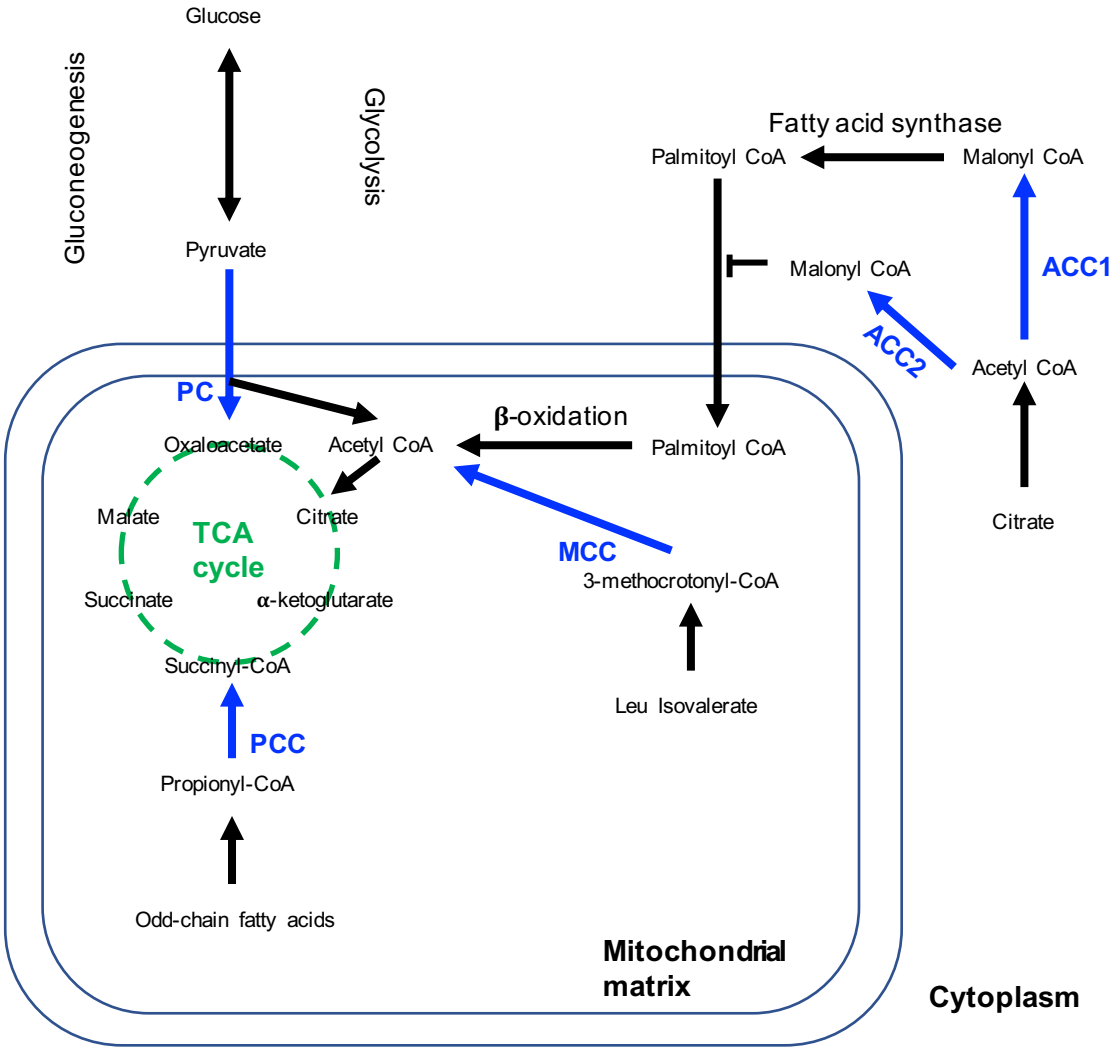

Figure 1.11. Role of biotin dependent carboxylases.
Each carboxylase reaction is highlighted in blue. Adapted from (Tong, 2013).

1.5.3 Pyruvate Carboxylase (PC)

PC is an essential enzyme in the intermediary metabolism responsible for the catalysis of pyruvate to oxaloacetate, and is localised to the mitochondrial matrix (Figure 1.11). Additionally, PC is required for the replenishment of intermediates of the TCA cycle which have been utilised for the synthesis of fatty acids, glucose and amino acids.

PC deficiency is a rare disorder with three different forms of the disorder, each of varying severities (Tong, 2013). The first form results in a chronic lactic acidemia and mental retardation, with patients dying in the first few years of life (Bartlett *et al.*, 1984). The second form is linked with severe lactic acidosis, convulsions, hypoglycaemia, hyperammonemia and interestingly mitochondrial CIV deficiency, with patients dying within the first months of life (Habarou *et al.*, 2015). The third form is the mildest form

of the disorder, with patients showing mild neurological symptoms and mild lactic acidosis. Mutations reported for each form vary between missense mutations and insertion/deletions.

1.5.4 Propionyl CoA Carboxylase (PCC)

PCC is responsible for the conversion of propionyl CoA to methylmalonyl CoA, is crucial for the catabolism of β-branched amino acids (BCAA) and is localised to the mitochondrial matrix (Figure 1.11). More than 50 mutations have been identified in *PCCA* and *PCCB,* including missense, nonsense, insertions/deletions and splicing mutations (Ugarte *et al.*, 1999; Schrick and Lingrel, 2001; Tong, 2013). These mutations are known to cause inborn errors of metabolism, specifically propionic acidemia, a metabolic disorder causing patients to present with ketoacidosis, cardiomyopathy, delayed growth and mental retardation with onset around the neonatal period (Ugarte *et al.*, 1999). This disorder is extremely rare worldwide, and is often fatal (Schrick and Lingrel, 2001). Defects in PCC cause an accumulation of propionyl CoA, this resulting in high levels of propionic acid which promotes toxic effects on organ systems and tissues. Cardiomyopathy has been reported in association with this disorder, however, such incidences are rare. A published case study reports on a 23-year-old female with propionic acidemia (Pa) at neonatal onset; she subsequently developed seizures resulting in delayed milestones, typical symptoms of Pa. She was also investigated for cardiac involvement, and displayed a severe reduction in systolic dysfunction and cardiac chamber enlargement, suggestive of dilated cardiomyopathy (Bhan and Brody, 2001). The cause of the cardiomyopathy is not yet known but is thought to be secondary to Pa (Massoud and Leonard, 1993).

1.5.5 3-Methylcrotonyl CoA carboxylase (MCC)

3-MCC is composed of two subunits; the alpha subunit, encoded by *MCCC1* gene containing the biotin carboxylase domain and biotin carboxyl carrier protein domain whereas, the beta subunit contains carboxyltransferase domain encoded by *MCCC2,* (Grünert *et al.*, 2012; Morscher *et al.*, 2012; Fonseca *et al.*, 2016). There have been 81 mutations in *MCCC1* and 89 mutations in *MCCC2* reported resulting in MCC deficiency (Fonseca *et al.*, 2016). The deficiency results in methylcrotonylglycinuria (MCG), an autosomal recessive disorder first described by Eldjarn *et al.* (1970). Leucine catabolism is inhibited due to the deficiency of the 3-MCC enzyme, responsible for the catalysis of the conversion of 3-methylcrotonyl CoA to 3-

methylglutaconyl CoA and ultimately acetyl CoA (Figure 1.11) (Darin *et al.*, 2007). This is a reversible reaction dependent on ATP concentration, and uses bicarbonate as a source of carboxyl groups.

3-MCC deficiency is one of the most common inborn errors of metabolism, with an incidence of 1 in 36, 000 new-born children many, of which are asymptomatic (Grünert *et al.*, 2012; Morscher *et al.*, 2012). Patients with this deficiency undergo normal growth and development until an acute episode of metabolic decompensation and failure to thrive at 2-3 years of age (Morscher *et al.*, 2012). This episode is usually triggered by an infection or increase in protein intake (Grünert *et al.*, 2012). Patients may also have a secondary carnitine deficiency due to carboxylase pathways (Darin *et al.*, 2007). Primary systemic carnitine deficiency (PSCD) is a fatal disorder with clinical presentation including skeletal myopathy, and progressive cardiomyopathy, as well as hypoglycaemia and hyperammonemia (Kilic *et al.*, 2011). PSCD is the only fatty acid oxidation defect which results in cardiac failure and arises from mutations in *OCTN2* (*SLC22A5*), which encodes the carnitine transporter (Kilic *et al.*, 2011). In addition to growth and developmental issues, dilated cardiomyopathy has also been reported in patients with 3-MCC deficiency (Visser *et al.*, 2000).

1.5.6 Acetyl CoA carboxylase (ACC)

ACC is key for many functions, including the catalysis of acetyl CoA to malonyl CoA (Figure 1.11). Acetyl-CoA carboxylase has two isoforms which catalyse the binding of bicarbonate to acetyl CoA generating malonyl-CoA (Saggerson, 2008; Tong, 2013). This carboxylase provides the two-carbon basis for fatty acid and polyketide biosynthesis (Abu-Elheiga *et al.*, 2001). *ACC1* (ACCα) is cytoplasmic and catalyses the rate-limiting step of the long-chain fatty acid biosynthesis in liver, adipose and other lipogenic tissues (Das *et al.*, 2010). It is known to interact with *BRCA1* in a phosphorylation dependent manner, reducing the activity of *ACC1*. This process is regulated by the cell cycle through protein kinases, such as cyclin-dependent kinase (CDK). The second isoform, *ACC2* (ACCβ), is highly conserved with *ACC1*. It is associated with the outer mitochondrial membrane by the N-terminus which is absent in *ACC1* with the C-terminus facing the cytosol. This isoform is primarily expressed within the heart and skeletal muscle (Abu-Elheiga *et al.*, 2001). The malonyl CoA product is an inhibitor of the carnitine palmitoyltransferase I (CPT-1), which is the

crucial enzyme for the transport of long-chain fatty acyl-CoA into mitochondria for β-oxidation (Figure 1.11) (McGarry and Brown, 1997; Saggerson, 2008).

Mutations in *ACC1* and *ACC2* are known to cause hypertriglyceridemia and hypercholesterolemia in patients taking antipsychotic drugs. The crucial role ACCs play in fatty acid metabolism make them attractive targets for drug discovery against metabolic syndromes (Tong, 2013). This was first validated by the *ACC2* knockout mice, which exhibited elevated fatty acid oxidation, increased energy expenditure, reduced body fat and had a smaller heart size but with no effect on function, life span or fertility compared to controls (Tong, 2013). Comparatively, the *ACC1* null mutation cause embryonic lethality in mice.

1.6 Pantothenic Acid

PA, also known as vitamin B_5, was first described as a growth factor for yeast (Williams *et al.*, 1933). It was later isolated as an accessory factor for lactic acid bacteria, which led to the use of the bacterium in an assay for the detection of PA, however, the biochemical role of PA was not yet defined (Snell *et al.*, 1937). The discovery of coenzyme A (CoA) along with the accidental occurrence of PA as a constituent of CoA allowed the biochemical function to be elucidated. PA acts as a precursor for the biosynthesis of CoA which is an essential component for the TCA cycle and fatty acid oxidation (Di Meo *et al.*, 2019). The biosynthesis of CoA consists of 5 stages once PA is transported across the plasma membrane by SLC5A6 (Figure 1.12). The process is initiated by the phosphorylation of PA by pantothenate kinase (PanK) to 4'Phosphopantothenate. The process continues, with the addition of a cysteine to form 4'Phospho N Pantothenoylcysteine (PCC). Decarboxylation then occurs, resulting in the formation of 4'Phosphopantetheine (PPANT). An adenyl group is transferred to PPANT, producing dephospho coenzyme A, which is dephosphorylated to form coenzyme A. This can then be utilised as an intermediate within the cytosol, as well as be transported into the mitochondrial matrix by the mitochondrial carrier, *SLC25A16* for conversion to acetyl CoA within the mitochondrial matrix. Modulation of CoA synthesis occurs through feedback inhibition of PanK by CoA; however, this inhibition may be reversed by the availability of free carnitine within the cytosol, which has been found to also modulate PanK activity.

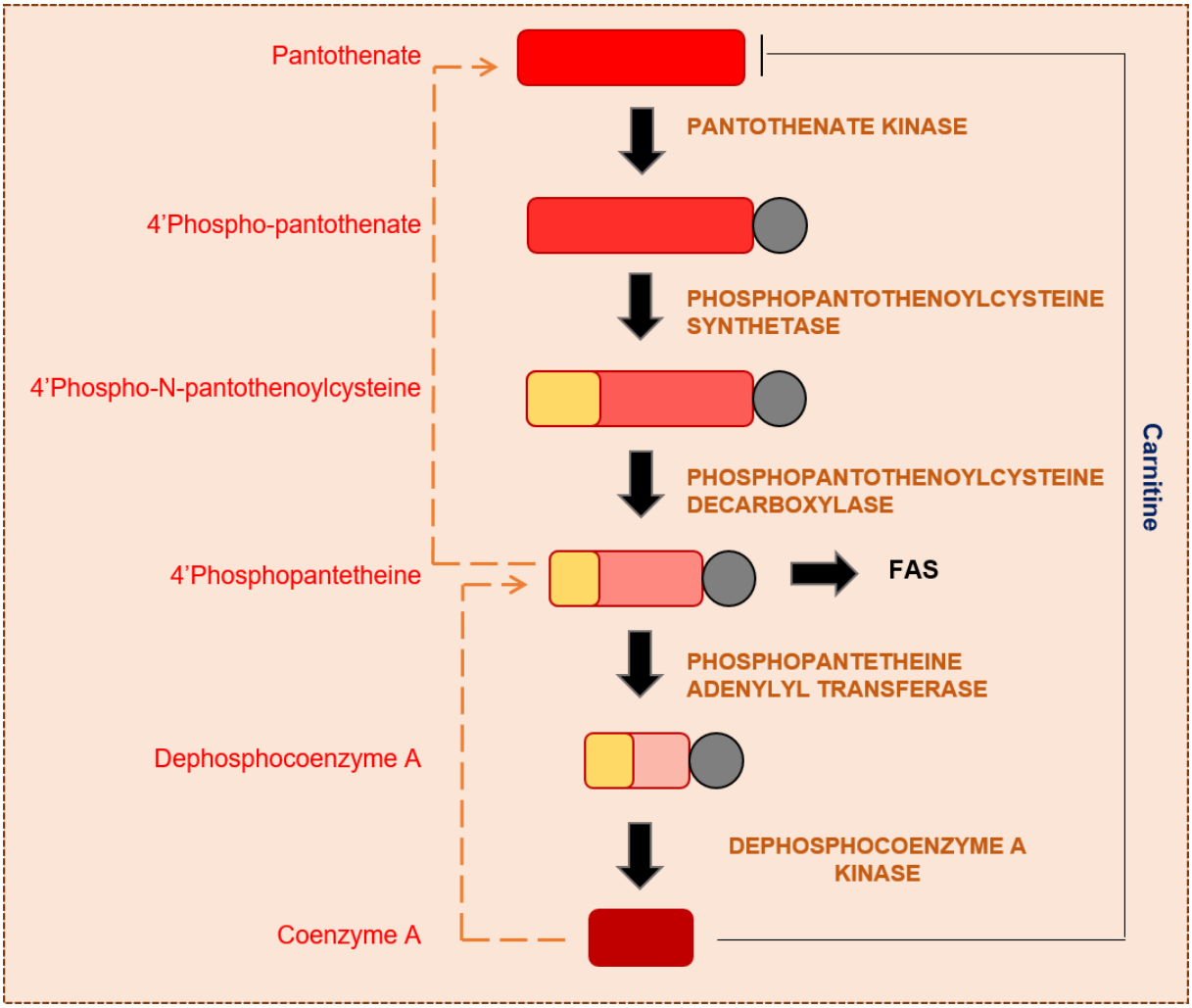

Figure 1.12. Conversion of pantothenate to coenzyme A.
Pantothenate (PA) is converted by pantothenate kinase (PanK) to 4'Phosphopantothenate. Next cysteine is added to form 4'Phospho N Pantothenoylcysteine. Decarboxylation occurs forming 4'Phosphopantetheine. An adenyl group is transferred to produce dephospho coenzyme A, and dephosphorylated to coenzyme A. Coenzyme A synthesis modulation occurs through feedback inhibition of PanK by Coenzyme A. However, this can be reversed by free carnitine. FAS = Fatty acid synthesis.

As previously described, PA is a precursor to coenzyme A, a key component in acetyl CoA used in the TCA cycle to generate succinyl CoA. PA deficiencies are well known to result in anaemia caused by reduced heme synthesis (Schulman and Richert, 1957; Di Pierro and Granata, 2020). Heme, unlike biotin and PA, must be synthesised within the cell and cannot be recycled or supplied from external food sources (Atamna, 2004). Interestingly, complex IV is the only mitochondrial complex which contains a heme group, heme-α. In the assembly of complex IV, the initial step is the incorporation of heme-α into COX-I subunit followed by assembly of the remaining subunits (Atamna *et al.*, 2001; Atamna *et al.*, 2007).

1.6.1 Pantothenic Acid deficiency

PA deficiency is rare in humans and results in varied clinical presentations including irritability and fatigue due to impaired energy production from reduced CoA production (Bean *et al.*, 1955). Patients can also display neurological symptoms such as parathesia and muscle cramps due to acetylcholine synthesis impairment (Bean *et al.*, 1955). Hypoglycemia, adrenal insufficiency and hepatic encephalopathy are also reported in some patients within this study.

1.7 Lipoic acid

LA is an organosulfur compound from octanoate which contains a ditholane ring (cyclic disulfide) (Packer and Cadenas, 2011; Salehi *et al.*, 2019). It is an essential component of four enzymes involved in energy metabolism within the mitochondria including pyruvate dehydrogenase (PDH), oxoglutarate dehydrogenase, branched chain dehydrogenase and α-ketoglutarate dehydrogenase (αKGDH) complexes (Cronan, 2014). Each complex is made of multiple copies of 3 enzymes (E1/E2/E3) (Figure 1.15). E1 catalyses a reaction in which the substrate is attached to the LA cofactor and is decarboxylated. During this reaction, the cofactor is reduced to dihydriolipoate. E2 catalyses an acyl transfer step, and the product is released. Finally, E3 catalyses the oxidation of the dihydrolipoyl cofactor back to lipoyl form, with NAD+ being the ultimate electron acceptor (Solmonson and DeBerardinis, 2018).

LA is universally conserved across all phylogenetic kingdoms. In mammals it is biosynthesised *de novo* in the mitochondrial matrix from octanoyl acyl carrier protein, produced during fatty acid synthesis (FAS), therefore it does not rely upon exogenous supply from dietary sources in contrast to PA and biotin. However, defects in the synthesis of LA have similar detrimental metabolic effects as described for biotin and PA, including mitochondrial dysfunction (Smith *et al.*, 2012). The effect of reduced LA synthesis has a negative downstream effect on PDH, αKGDH, oxoglutarate dehydrogenase and branched chain dehydrogenase, with symptoms including hypotonia, seizures and lactic acidosis (Burr *et al.*, 2016; Solmonson and DeBerardinis, 2018).

1.8 Energy metabolism

Cellular respiration occurs ubiquitously throughout nature. Glucose metabolism for energy production occurs through three reaction pathways, i) Glycolysis and pyruvate oxidation, conversion of glucose-pyruvate-acetyl CoA, ii) TCA cycle, produces electron carriers NADH and FADH, and iii) oxidative phosphorylation (OXPHOS), consumes oxygen to produce ATP (Figure 1.13) (Hroudová and Fišar, 2013; Hill, 2014). In addition to glucose, lactate, delivered into the cytosol of the cell via the circulation can be used to generate pyruvate by cytosolic lactate dehydrogenase (cLDH), which is then shuttled to the mitochondrial matrix for acetyl CoA conversion (Brooks *et al.*, 1999; Young *et al.*, 2020). The conversion also supplies intermediates NADH and NAD+ to the mitochondria for utilisation within the TCA cycle, contributing to ATP production by OXPHOS. Alternatively, lactate can be shuttled directly into the mitochondrial matrix for pyruvate conversion by mitochondrial LDH (Young *et al.*, 2020). The efficiency of these processes determines the amount of ATP production, as well as the amount of toxic reactive oxidative species (ROS) produced (Hill, 2014). Energy production is triggered in response to energy demand and therefore the yield of ATP varies between cell types. The heart has one of the highest metabolic demands in the human body, and therefore any defects in the respiratory pathway can result in detrimental effects on the heart, leading to heart failure (Allard *et al.*, 1994; Stanley *et al.*, 2005; Das *et al.*, 2010; Nathania *et al.*, 2017; Ritterhoff and Tian, 2017; Zhou and Tian, 2018).

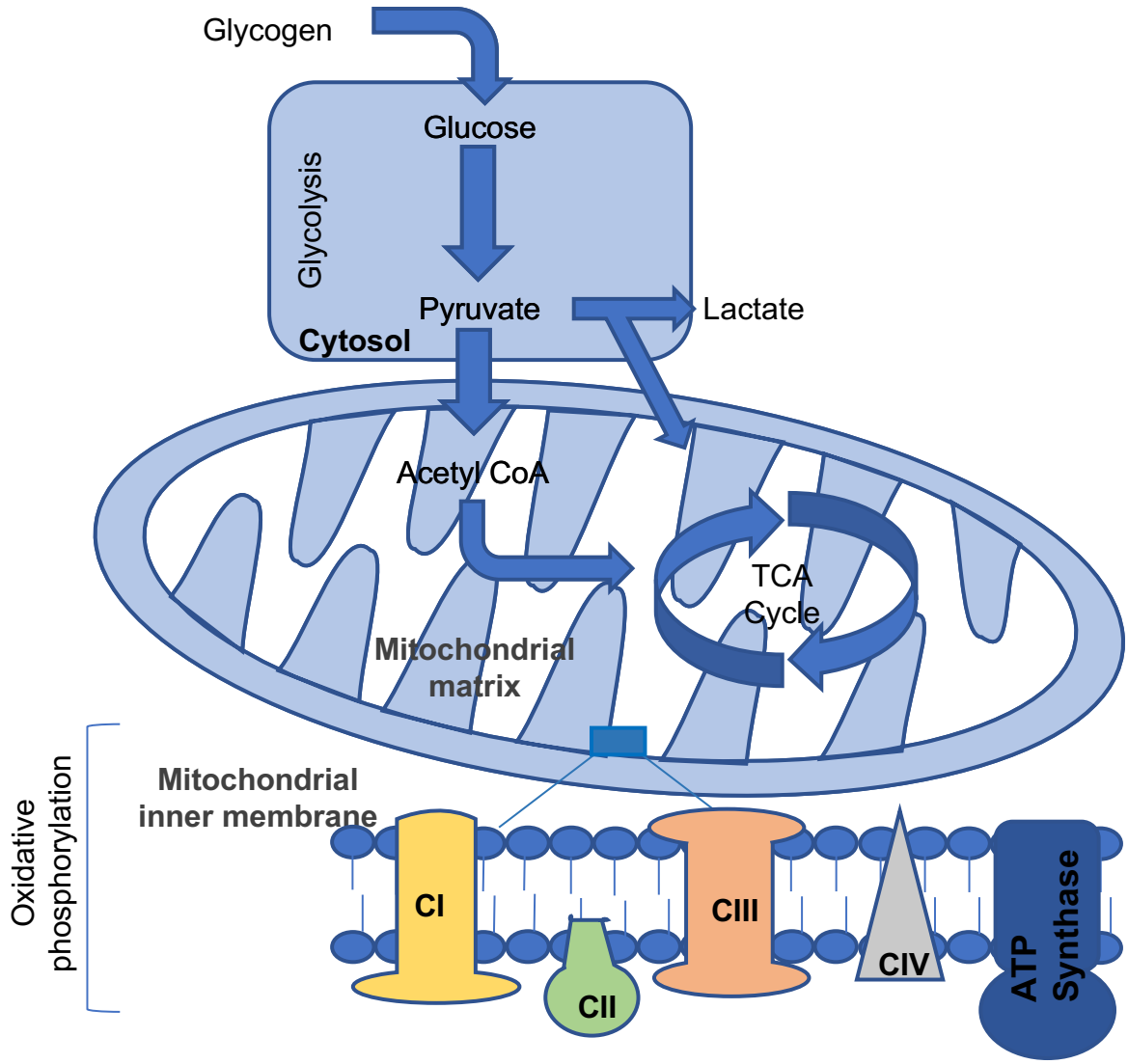

Figure 1.13. Overview of key processes of energy metabolism.
Glycogen is transported into the cytosol and converted into glucose. Through the process of glycolysis, glucose is converted to pyruvate which can be i) translocated into the mitochondrion to be processed into acetyl CoA, ii) converted to lactate by lactate dehydrogenase which provides intermediates, NAD+ and NADH. The intermediates and acetyl CoA are utilised in the TCA cycle to generate ATP molecules, additional NADH and FADH, which are transported to the mitochondrial inner membrane for oxidative phosphorylation.

1.8.1 Glycolysis

Glycolysis is a pathway for glucose metabolism, producing energy and providing biosynthesis precursors for cellular components (Rogatzki *et al.*, 2015). Glycolysis takes place within the cytoplasm and produces two molecules of ATP in addition to pyruvate. Pyruvate can then be utilised in a number of different ways under numerous conditions; during aerobic respiration 1) conversion of CoA to acetyl CoA via PDH complex, which ultimately produces ~30 ATP by oxidative phosphorylation (OXPHOS) and 2) synthesis of oxaloacetate (component of TCA cycle) via biotinylated PC, during anaerobic respiration 3) conversion to lactate via lactate dehydrogenase (LDH), producing ~2 ATP, and during starvation 4) conversion back to glucose (gluconeogenesis) via biotinylated PC (Figure 1.14) (Lopaschuk and Kelly, 2008; Zheng, 2012). Once pyruvate is synthesised during aerobic respiration, pyruvate is shuttled into the mitochondrial matrix for acetyl CoA formation.

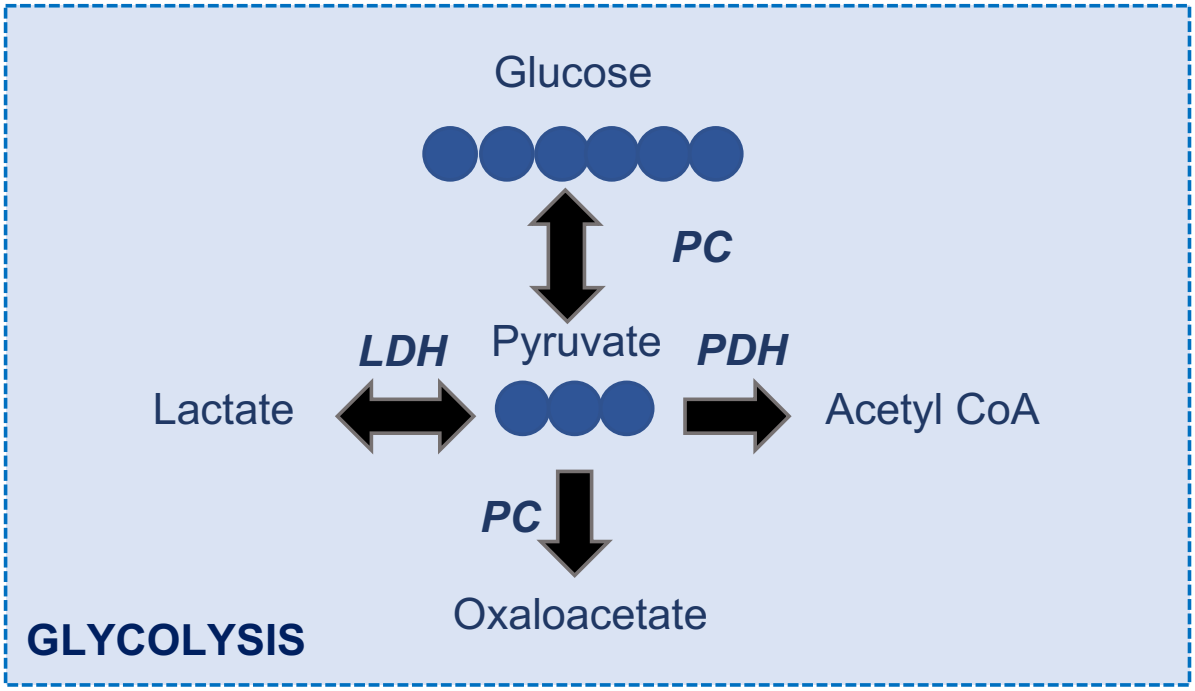

Figure 1.14. Overview of the glycolysis pathway.
Glucose (6 carbon molecule) is converted to pyruvate (3 carbon molecule) in a 10 step reaction process. Once produced, pyruvate can be converted to lactate by LDH, oxaloacetate by PC, acetyl CoA by PDH complex or be converted back to glucose (gluconeogenesis) by PC.

1.8.2 Acetyl CoA formation

The synthesis of CoA, which is an essential component of the TCA cycle and fatty acid β-oxidation, requires pantothenic acid (PA) as a precursor (Cooper, 2000a).

Biosynthesis of CoA once PA is transported across the plasma membrane was previously described (Figure 1.12). Briefly, the process is initiated by the phosphorylation of PA to 4'Phosphopantothenate, ending with the de-phosphorylation of dephospho-CoA to form CoA (Leonardi and Jackowski, 2007). If PA supply is reduced, then CoA can be converted back to 4'Phosphopanteteine for further conversion back to PA in a concentration dependent mechanism (Leonardi and Jackowski, 2007; Czumaj *et al.*, 2020).

Carboxylation of pyruvate occurs via PDH complex, which consists of three subunits (E1/2/3), to generate acetyl CoA (Figure 1.15). Pyruvate and thiamine pyrophosphate (TPP) are catalysed, irreversibly, by pyruvate dehydrogenase (E1). The acetyl group is transferred to lipoic acid by a thioester bond. Transacylation of acetyl group occurs via dihydrolipoyl transacetylase (E2) from lipoic acid to CoA producing acetyl CoA. The resultant FAD then oxidises dihydrolipoamide back to lipoic acid via dihydrolipoyl dehydrogenase (E3) (Figure 1.15) (Shi and Tu, 2015; Czumaj *et al.*, 2020). The same process is utilised during acetyl CoA formation from branched chain amino acids (BCAA) where the branched chain α-keto dehydrogenase complex is used, and succinyl-CoA formation by α-ketoglutarate dehydrogenase (αKGDH) complex, both of which are comprised of similar subunits as described above.

Once acetyl CoA is generated from pyruvate, this can be used as an intermediate for the TCA cycle as well as being transported out of the mitochondria and into the cytosol for fatty acid synthesis.

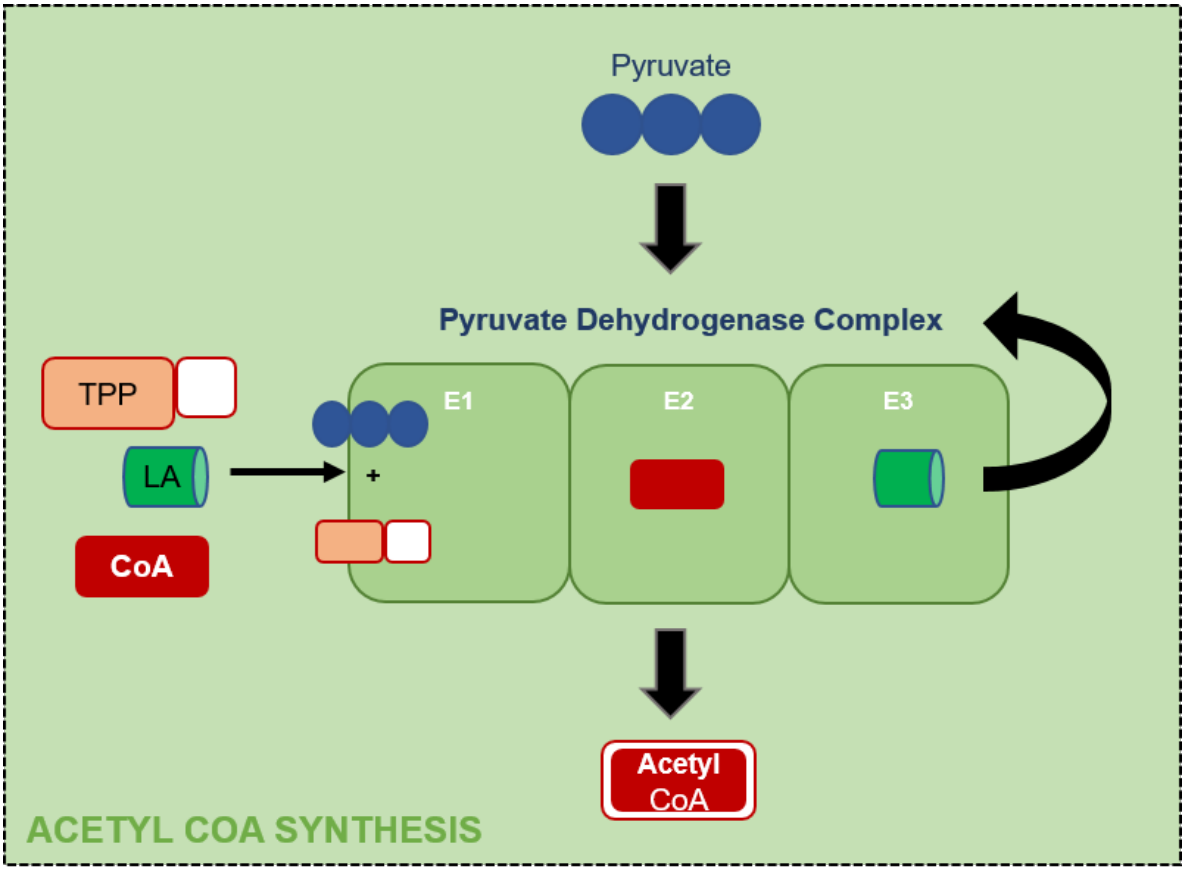

Figure 1.15. Synthesis of acetyl CoA.
Pyruvate and thiamine pyrophosphate (TPP) are catalysed by E1 subunit of PDH and the acetyl group is transferred to LA. Transacylation of the acetyl group occurs from lipoic acid to CoA producing acetyl CoA via E2. LA is recycled by E3.

1.8.3 Tricarboxylic acid (TCA) cycle

The TCA cycle is relied upon in aerobic organisms to produce NADH and $FADH_2$ from the acetyl CoA generated by glycolysis (Mailloux *et al.*, 2007). The TCA cycle takes place within the mitochondrial matrix, where acetyl CoA transfers an acetyl group to oxaloacetate to produce citrate (Figure 1.16). Citrate is then converted to isocitrate before becoming decarboxylated forming α-ketoglutarate. α-ketoglutarate then undergoes oxidative decarboxylation via α-KGDH using TPP, LA and coenzyme A to generate succinyl-CoA and NADH. Succinyl CoA is then hydrolysed to succinate and release coenzyme A. Succinate is converted to fumarate by succinate dehydrogenase which then becomes hydrated to form malate. Following this reaction oxaloacetate is generated by malate dehydrogenase or by pyruvate conversion via PC. (Martínez-Reyes and Chandel, 2020).

In addition to providing essential intermediates for energy metabolism, a novel role of this cycle has been reported, suggesting the TCA cycle helps to modulate the cell's

redox state by detoxifying reactive oxygen species (ROS) as well as generating ROS, therefore reducing oxidative stress (Sawa *et al.*, 2017).

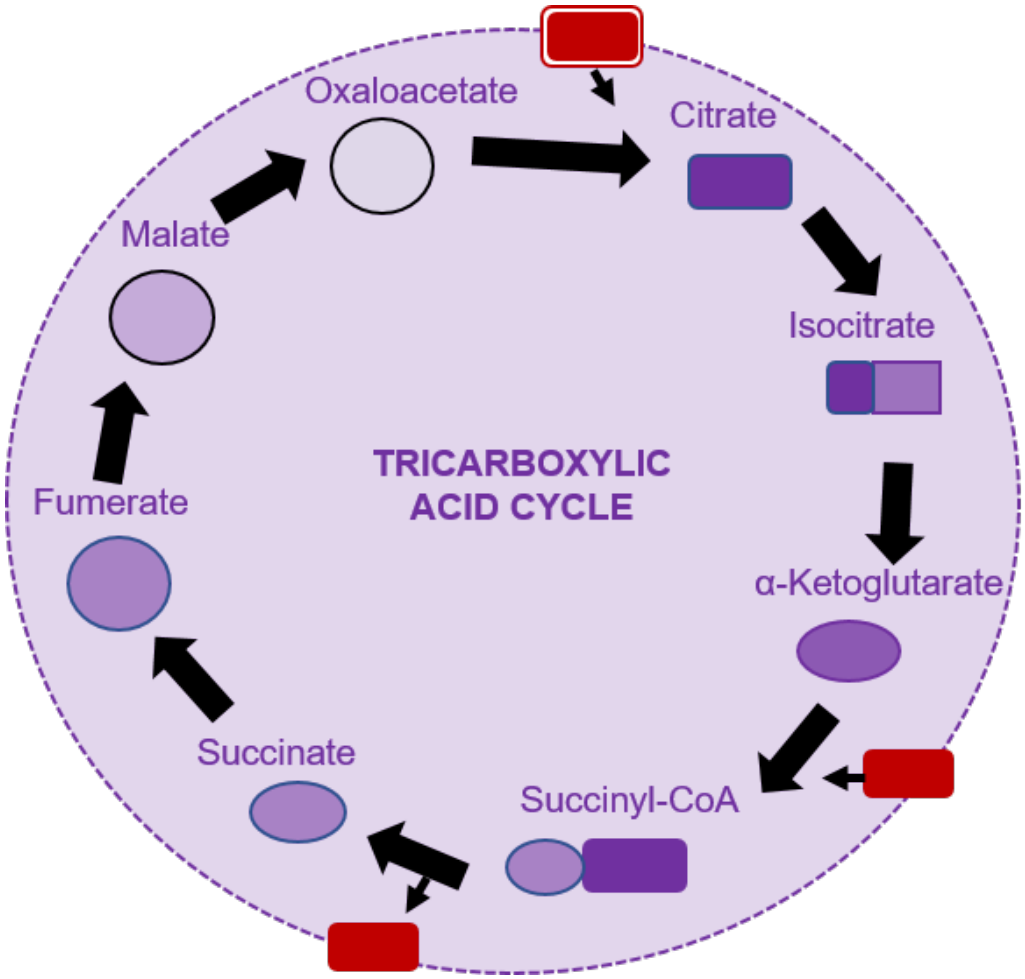

Figure 1.16. Overview of the tricarboxylic acid cycle.
Oxaloacetate combines with acetyl CoA (white outlined red box) to form citrate. This is converted to isocitrate and broken down to generate α-ketoglutarate, which is used by α-KGDH along with coenzyme A (red box) to produce succinyl CoA. This is broken down to form succinate and coenzyme A. The cycle continues to produce fumerate which is converted to malate and back to oxaloacetate, ready to begin the cycle again.

1.8.4 Fatty acid synthesis and β-oxidation

Fatty acid synthesis utilises acetyl CoA and NADPH to produce fatty acids. For the acetyl CoA to be utilised in this process, it must first be transported out of the mitochondria. This occurs through the formation of citrate from the TCA cycle, which is removed from the cycle and transported across the inner mitochondrial membrane (IMM) to the cytosol (Berg JM, 2002a). ATP citrate lyase then breaks down citrate to oxaloacetate, which can be transported back into the mitochondria for TCA cycle, and

acetyl CoA which becomes carboxylated by ACC to form malonyl CoA and generates acetyl CoA acyl carrier protein (ACP). Malonyl CoA is used to generate malonyl ACP which combines with acetyl ACP to form palmitonyl ACP. The fatty acid then undergoes elongation reactions to generate palmitate. Once generated, palmitate is transported into the mitochondria by the carnitine shuttle, which includes carnitine palmitoyltransferase 1 (CPT1), carnitine palmitoyltransferase 2 (CPT2) and carnitine;acylcarnitine translocase (Lopaschuk *et al.*, 1994). Once transported into the mitochondrial matrix, the fatty acid undergoes β-oxidation (Figure 1.17). β-oxidation occurs through four enzymatic reactions converting fatty acyl-CoA to acetyl CoA and acyl CoA in addition to donating electrons to the electron transport chain in OXPHOS (Lopaschuk *et al.*, 1994). Acetyl CoA is then used in the TCA cycle to generate intermediates for ATP production by OXPHOS (Berg JM, 2002a).

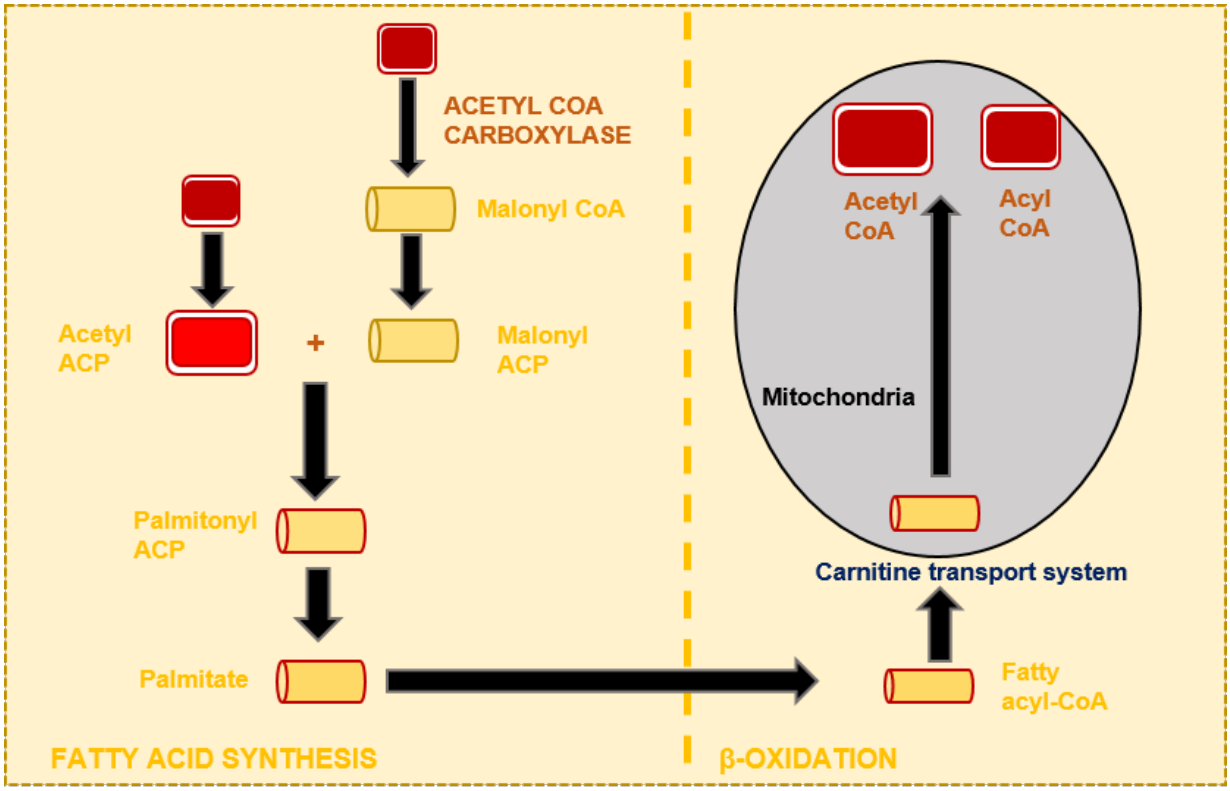

Figure 1.17. Fatty acid synthesis and β-oxidation overview.
Fatty acid synthesis utilises acetyl CoA generated from broken down citrate from the TCA cycle which is transported to the cytosol. Once in the cytosol acetyl CoA is converted to malonyl CoA by ACC. This is then converted to malonyl ACP as acetyl CoA is also converted to acetyl ACP. Malonyl and acetyl ACP combine to form palmitonyl ACP and ultimately palmitate. This is then transported into the mitochondrial matrix by the carnitine transport system. Once inside the mitochondrial matrix fatty acyl-CoA is converted to acetyl CoA for the TCA cycle and acyl CoA by β-oxidation.

1.8.5 Oxidative phosphorylation

Once intermediates, including NADH, $FADH_2$ and succinate, are generated from the TCA cycle they are utilised by OXPHOS. The heart primarily relies upon OXPHOS as it generates more ATP than glycolysis (Lopaschuk *et al.*, 1994; Zheng, 2012). This process occurs within the IMM and utilises the electron transport chain (ETC) which consists of five complexes; NADH-Q oxidoreductase (CI), Succinate Q reductase (CII), Q cytochrome c oxidoreductase (CIII), cytochrome c oxidase (CIV) and ATP synthase (CV) (Figure 1.18). The subunits of each complex are encoded by both nuclear and mitochondrial genes. OXPHOS also involves electron carrier's ubiquinone and cytochrome c. Utilising the production of NADH and $FADH_2$ from glycolysis, they reduce molecular oxygen to produce water. The energy produced from this process is then used by CI, CIII and CIV to pump protons across the IMM to the intermembranal space resulting in an electrochemical proton gradient (Chung and Kang, 2015). This gradient is known as proton motive force (PMF) and is employed by CV to convert ADP to ATP with the addition of inorganic phosphate (Figure 1.18) (Hanna and Nelson, 1999; Berg JM, 2002b; Mailloux *et al.*, 2007). Mitochondrial ATP is then exchanged across the IMM for cytosolic ADP by adenosine nucleotide translocator (Graham *et al.*, 1997). This exchange produces reactive oxidative species (ROS), which when generated in excess, are known to impair cell function if respiratory chain dysfunction occurs (Hanna and Nelson, 1999; Zhou and Tian, 2018).

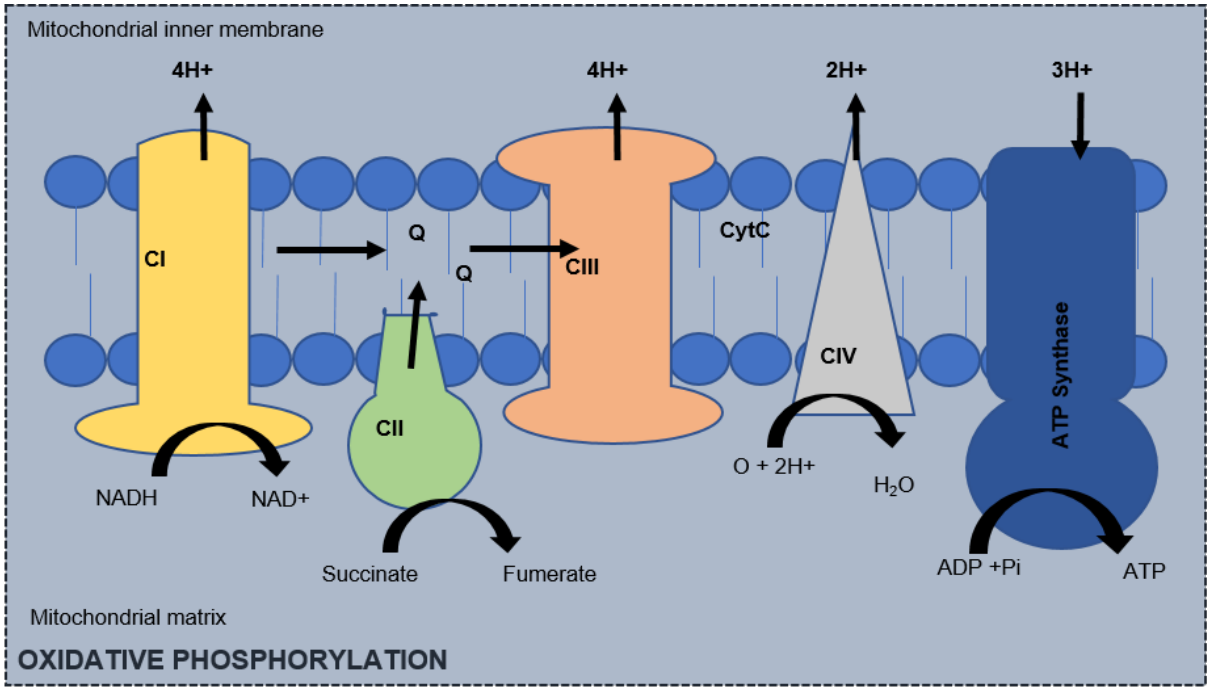

Figure 1.18. Overview of oxidative phosphorylation.
Intermediates generated by glycolysis, the TCA cycle and β oxidation are reduced by complex I and II to create a proton gradient (PMF) across the IMM. This gradient is used by ATP synthase to convert ADP to ATP. Adapted from (Kikusato et al., 2016).

1.9 Hypothesis and aims

1.9.1 Hypothesis

It is hypothesised that the homozygous missense mutation (p.R253W) in *SLC5A6* is the disease-causative gene in two siblings with DCM. Thus, it is proposed that the mutations in *SLC5A6* have altered cardiac function within the siblings leading to DCM.

1.9.2 Aims

Very little is known about *Slc5a6* within the heart and its role within cardiac function remains undetermined. The aim of this project is to further the understanding of the role *Slc5a6* plays within the developing and adult heart. To investigate this, mouse models in which the function of *Slc5a6* is targeted will be generated for extensive cardiac assessment. A potential link between vitamins, energy metabolism and heart morphology and function will start to be investigated.

Aim 1) To determine the expression of Slc5a6 within cardiac development. A developmental series of murine hearts will be collected from E9.5 to E17.5, P0 to P21 and adult. Immunohistochemistry and qPCR analysis will be carried out to identify cellular expression of Slc5a6 in the heart throughout the lifespan of a mouse. In addition, the expression of genes involved in the regulation of energy metabolism and mitochondrial biogenesis will be determined to understand the changes in metabolic pathways during normal embryonic and postnatal heart development.

Aim 2) To investigate the effect of the patient p.R253W mutation on the murine heart. A CRISPR-Cas9 generated *Slc5a6*^{R252W} mouse model has been generated. Phenotypic analysis will be carried out through histology, immunohistochemistry, ultrastructural imaging, and ECG to determine any structural and functional changes within the transgenic mice.

Aim 3) To generate and characterise a global conditional *Slc5a6* knockout mouse line. Phenotypic analysis will be carried out throughout development and adulthood by histology and ultrastructural imaging including transmission electron microscopy to examine the structure of mitochondria within the heart.

Aim 4) To investigate the role of *Slc5a6* on cardiac function by generating a cardiomyocyte specific *Slc5a6* knockout mouse line. ECG and CMR imaging

will be performed to determine cardiac function within the transgenic mice. Histological and immunofluorescent staining will be carried out to investigate any structural changes to the heart. Transmission electron microscopy will also be performed to characterise any changes to the cardiac mitochondria, which will be further investigated by quadruple immunofluorescence to determine the expression of mitochondrial complexes within cardiomyocytes.

Aim 5) To characterise the effect of vitamin supplementation as a potential therapeutic treatment for DCM. Vitamins will be supplied to transgenic mice to investigate the effect on the development of DCM. Phenotypic assessment, as described in aim 4, will be performed to determine the effect of supplementation on cardiac function and structure, including the effect on mitochondrial complex expression.

Chapter 2 Materials and Methods

2.1 Animal models

2.1.1 Animal care and husbandry

All animals used within this study were kept under controlled conditions (25°C, 12 hour light:dark cycle) with food and water supplied *ad libitum.* All experiments conformed to the Guidance of Care under the Animals (Scientific Procedures) Act 1986 (ASPA), approved by the UK Home Office. The animals were housed within the Functional Genomics Unit (FGU) as part of the Newcastle University establishment licence. All animal procedures were carried out by a personal licence holder (PILA/B or C) under the project licence P118131E3 held by Dr Helen Phillips. The animal work carried out within this project was granted ethical approval by the Animal Welfare and Ethical Review Board (AWERB) at Newcastle University. All transgenic mouse models used within this project were generated on a C57Bl6 genetic background, unless otherwise stated.

2.1.2 Generation of Slc5a6^{R252W} mouse model

To assess the effect of the patients' homozygous p.Arg253Trp mutation within a mouse model, CRISPR-Cas9 technology was utilised. In the mouse genome the amino acid equivalent to the mutation site was p.Arg252. The mouse model was generated by Dr Colin Miles using the methodology described by Ittner and Götz (2007) with the construct shown in Figure 2.1. Here, the codon sequence at 252 is mutated from CGT (arginine) to TGG (tryptophan). In addition to mutating the target site, the promoter adjacent motifs (PAM), recognised by Cas9 proteins cleavage, are mutated from a TGG and CCT codon to TCG and CGT, respectively. The alteration of the PAM sites allows for identification of genotype by PCR and *BamHI* digest rather than Sanger sequencing to confirm the presence/absence of the mutation in each *Slc5a6*^{R252W} mouse.

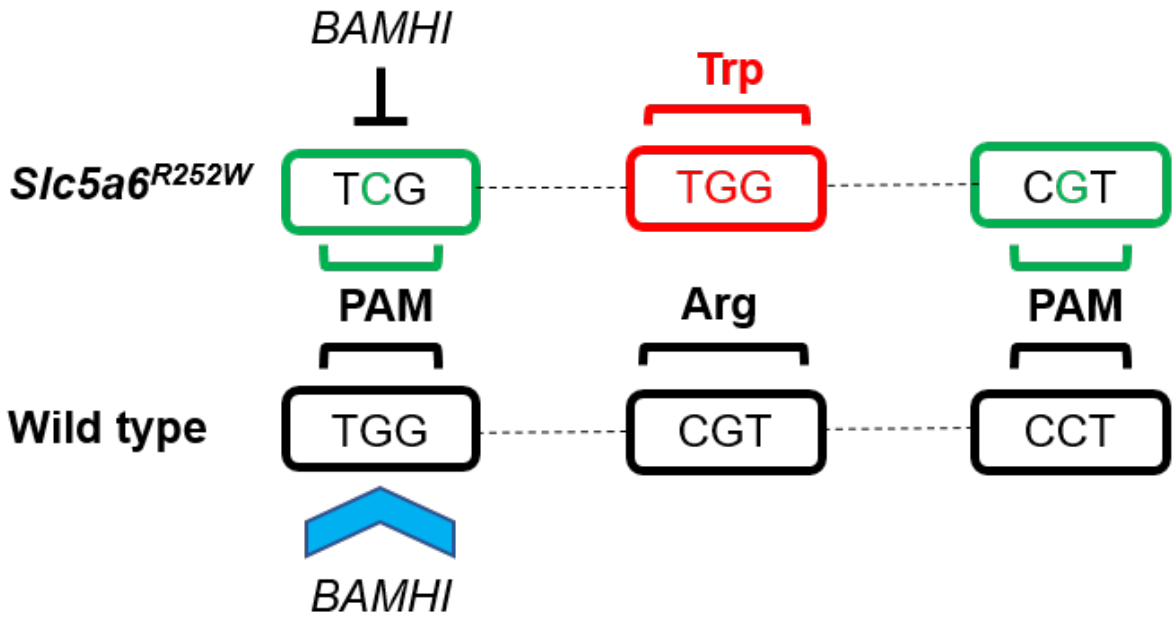

Figure 2.1. Generation of *Slc5a6^{R252W}* construct.
Slc5a6 is encoded on the reverse DNA strand, and in mouse to induce an amino acid change from arginine to tryptophan, C>T and T>G (red) are introduced at p.R252 shown in the Slc5a6^{R252W} allele. Additionally, a point mutation, G>C, introduced to the first PAM site and C>G in the following PAM site (green), this allows for offspring to be routinely genotyped without need for Sanger sequencing.

Transgenic mice were generated on a mixed background of CBA/CA and C57BL/6N (F1) mice. Eggs were collected and the construct injected to generate Slc5a6^{R252W} offspring. The offspring were backcrossed onto a C57BL/6N background to generate heterozygote (Slc5a6$^{+/R252W}$) mice, which were crossed to produce three genotypes; wild type (Slc5a6$^{+/+}$), Slc5a6$^{+/R252W}$ and homozygous mutant (Slc5a6$^{R252W/R252W}$) offspring for analysis (Figure 2.2).

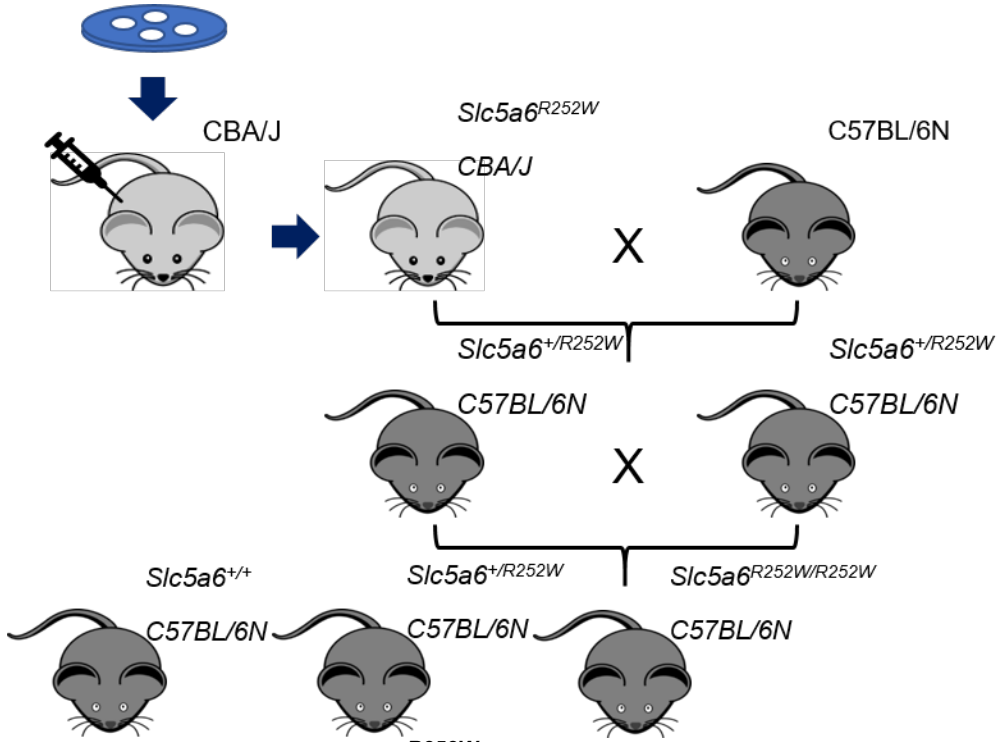

Figure 2.2. Insertion of *Slc5a6*^{R252W} construct and breeding strategy to generate Slc5a6$^{R252W/R252W}$ mice.
The construct was injected into CBA/J dams by Dr Colin Miles. The offspring were crossed with C57BL/6N mice to generate Slc5a6+/R252W mice which were then used to generate three genotypes including Slc5a6$^{R252W/R252W}$ for analysis.

2.1.3 Generation of Slc5a6 conditional knockout mouse models

To investigate the loss of *Slc5a6* on the model system, a *Slc5a6* transgenic mouse line was obtained from EUCOMM/IMPC consortium. The *Slc5a6*^{Tm1a} allele, consisted of a neomycin lacZ cassette flanked by frt sites as well as LoxP sites that flank exons 7-10 of *Slc5a6* (Figure 2.3). Heterozygous *Slc5a6*$^{+/Tm1a}$ mice were generated and crossed to produce homozygous *Slc5a6*$^{Tm1a/Tm1a}$ mice; however, no homozygotes were found after E10.5. At E9.5 homozygote *Slc5a6*$^{Tm1a/Tm1a}$ embryos were small and were in the process of being reabsorbed. It was concluded that this line was embryonic lethal.

To generate tissue specific *Slc5a6* knockout mice, *Slc5a6*$^{+/Tm1a}$ mice were crossed with a *Flp* recombinase line to remove the LacZ-neomycin cassette, producing the conditional *Slc5a6*^{Tm1c} allele, referred to as *Slc5a6*^{F} from this point forward (Figure 2.3).

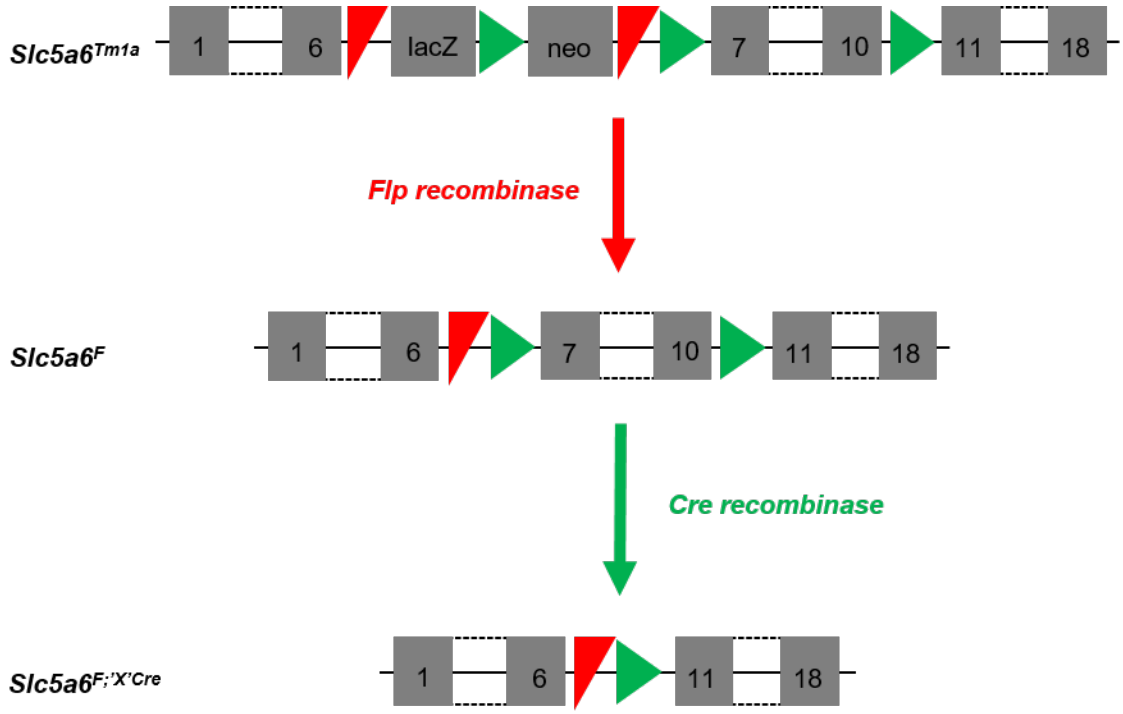

Figure 2.3. Schematic diagram for the generation of *Slc5a6* transgenic alleles for promoter specific knockout models.
The *Slc5a6*^{Tm1a} allele produced by MRC Harwell. The *Slc5a6*^{Tm1a} allele contains a lacZ-neomycin cassette flanked by FRT sites (red) which enable the generation of the conditional (*Slc5a6*^{F}) allele when crossed with a Flp recombinase mouse line, removing the lacZ-neomycin cassette. The *Slc5a6*^{F} allele can then be crossed with a Cre recombinase mouse line to remove the targeted region (exons 7-10) flanked by loxP sites (green) specifically within target cells.

The floxed allele can then be crossed with a *Cre* recombinase line to create a conditional knockout (Table 2.1).

Table 2.1. Tissue expression of *Cre* recombinase lines. Embryonic day in which promoter is expressed is noted for each gene.

Expression	***Sox2Cre***	***TnTCre***
Embryonic day	6.5	7.5
Tissue	Epiblasts	Cardiomyocytes
Reference	(Hayashi *et al.*, 2002)	(Jiao *et al.*, 2003)

To generate conditional knockout mice, *Slc5a6*$^{F/F}$ female mice were crossed with *Slc5a6*$^{+/F;'X'Cre}$ (heterozygous) males to generate four genotypes (Figure 2.4). For the purpose of this project, *Slc5a6*$^{+/F}$ and *Slc5a6*$^{F/F}$ mice are grouped as Slc5a6$^{+/+}$ mice as they are phenotypically normal, and homozygous mutants *Slc5a6*$^{F/F;'X'Cre}$.

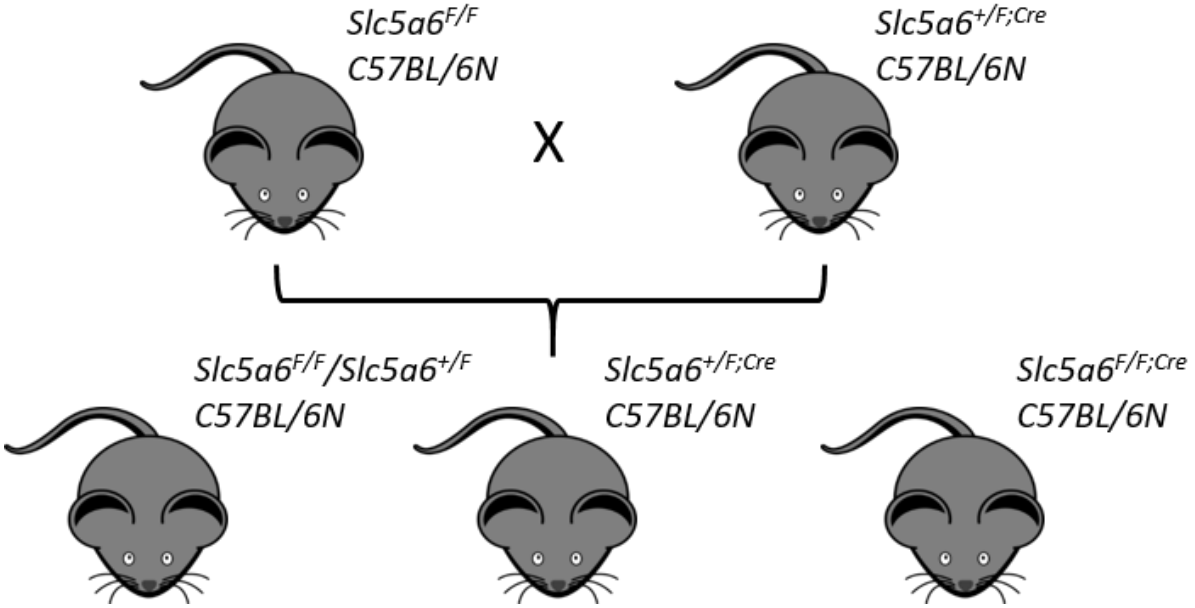

Figure 2.4. Breeding strategy for generating *Slc5a6* conditional knockout mice. *Slc5a6*$^{F/F}$ female mice were crossed with *Slc5a6*$^{+/F;'X'Cre}$ males to generate four genotypes depicted. Controls Slc5a6$^{+/F}$/Slc5a6$^{F/F}$ (*Slc5a6*$^{+/+}$), heterozygote (*Slc5a6*$^{+/F;'X'Cre}$) and mutant (*Slc5a6*$^{F/F;'X'Cre}$) mice for analysis.

2.1.4 Vitamin supplementation

Cardiomyocyte specific *Slc5a6* knockout mice were given vitamin supplementation to investigate the effect on the cardiac phenotype. Breeding trios were setup (two *Slc5a6*$^{F/F}$ dams and one *Slc5a6*$^{+/F;TnTCre}$ stud) and supplied with a custom diet (TD. 200233, ENVIGO UK) with additional biotin and pantothenic acid supplementation. One water-soaked pellet per mouse was supplied directly into the cage whilst, non-soaked custom pellets were placed into the food hopper. Biotin and pantothenic acid were also supplied through drinking water at 1 mM concentration. Both the supplemented food and water were supplied *ad libitum* by animal care technicians. This enabled vitamin supplementation through embryonic and fetal development into early adulthood. Once offspring were weaned, vitamin supplementation continued as described above, until harvest at 20 weeks. All animals under vitamin supplementation were closely monitored for adverse effects and weighed weekly.

2.2 General reagents

Many reagents, buffers and solutions are common to multiple applications. Table 2.2 describes the components of each solution. Any deviations from these standard protocols are described in the appropriate section.

Table 2.2 Breakdown of chemicals used to make general reagents

Solution	Components	Applications	Supplier
Phosphate buffered saline (PBS) (10X stock solution, 1X working solution)	1 L of ddH_2O (= 10X stock), autoclaved. 100 mL of 10X stock dissolved in 1 L of ddH_2O (1X).	Dissection, sample preparation, IHC, IF	Sigma Aldrich P4417
RNase-free PBS (1X working solution)	1 mL Diethyl Pyrocarbonate (DEPC) dissolved in 1 L of 1X PBS. Autoclaved	Dissection	Sigma Aldrich D5758
RNase-free dH_2O	1 mL DEPC dissolved in 1 L of 1X PBS. Autoclaved	Dissection, RNA extraction	Sigma Aldrich D5758
4% paraformaldehyde (PFA)	40 g of PFA dissolved in 1 L PBS at 56°C (pH adjusted to 7 with 5M NaOH)	Sample preparation, IHC, IF	Sigma Aldrich P6148
Tris-Acetate-EDTA buffer (50X stock solution, 1X working solution)	242 g Trizma base, 18.6 g EDTA, 57.1 g glacial acetic acid dissolved in 1 L ddH_2O (= 50X stock solution), autoclaved. 20 mL of 50X stock diluted in 1 L ddH_2O	Gel electrophoresis	Sigma Aldrich T1503, E9884 Fisher chemicals A/0400/PB17
Tris buffered saline (TBS) (10X stock solution, 1X working solution)	24.23 g of Trizma HCL and 80.06 g NaCl dissolved in 1 L ddH_2O (pH adjusted to 7.6 with 5M NaOH) (= 10X stock	IHC	Sigma Aldrich T3253

	solution), autoclaved. Dilute 100 mL of 10X stock in 1 L ddH_2O for 1X working solution.		
TBS-Tween20 (TBST)	1 mL Tween-20 dissolved in 1 L of 1X TBS	IHC	Sigma Aldrich P1379
Proteinase K DNA lysis buffer	50mM KCL, 1.5mM $MgCl_2$, 10mM Tris pH8.5, 0.45% NP40, 0.45% Tween-20 with proteinase K (20mg/ml)	DNA extraction	All chemicals from Sigma Aldrich. Proteinase K from Roche
Hot shot DNA lysis buffer	1 mL 5M NaOH and 80 µL 0.5M EDTA pH8 diluted in 198.9 mL ddH_2O	DNA extraction	All chemicals from Sigma Aldrich
Hot shot DNA neutralisation buffer	1.26g Trizma HCL dissolved in 198.7 mL ddH_2O	DNA extraction	Sigma Aldrich T3253
Citrate buffer (0.01M)	192 g citric acid dissolved in 1 L ddH_2O (pH adjusted to 6.3 with 5M NaOH)	IHC	Sigma Aldrich 27109

2.3 Standard molecular techniques

2.3.1 Genomic DNA extractions

Limbs and tail tips were collected from embryos, and ear-clips were taken from mice at weaning (~ 3 weeks old). Limbs and tail tip samples were lysed using proteinase K DNA lysis buffer (Table 2.2). Samples were incubated at 56°C for 2 hours before heat inactivation was carried out at 95°C for 10 minutes followed by centrifugation at 15,000 rpm for 60 seconds. DNA was stored at 4°C. Ear-clip samples were denatured at 95°C for 1 hour in DNA lysis buffer (Table 2.2). Samples were allowed to cool at room temperature (RT) before denaturation was inactivated by addition of DNA neutralisation buffer (Table 2.2). This was followed by centrifugation at 15,000 rpm for 3 minutes. DNA stored at 4°C.

2.3.2 RNA extractions

RNA was extracted from tissue using the RelipPrep RNA Tissue Miniprep System (Promega). Lysis solution volumes were adjusted for tissue type and weight (Table 2.3).

Table 2.3. Reagent volumes required per tissue mass for lysis solution.

Tissue	**Lysis buffer (µl)**	**100% Isopropanol (µl)**	**Nuclease-free water (µl)**
≤ 5 mg	250	85	15
> 5 mg	500	170	30

Tissue was disrupted using a tissue homogeniser (Qiagen) for large tissues or a 5mL syringe with 19G needle for small tissues followed by shearing using P1000 and P200 pipette. All centrifugation steps were carried out at RT. Centrifugation at 14,000 xg for 3 minutes was carried out to clear homogenates before transferring to a clean tube. Isopropanol was added and mixed by vortex before lysate was transferred to a minicolumn in a collection tube and centrifuged at 14,000 xg for 60 seconds. Flowthrough was discarded and 500 µl of RNA wash solution was added to the minicolumn and centrifuged at 14,000 xg for 30 seconds.

DNase I incubation mix (Table 2.4) was added to the minicolumn membrane and incubated at RT for 15 minutes. Following incubation 200 µl of column wash solution was added to the minicolumn and centrifuged at 14,000 xg for 15 seconds followed by the addition of 500 µl of RNA wash solution and centrifuged at 14,000 xg for 30 seconds. Flowthrough was discarded and the RNA was washed with 300 µl of RNA wash solution and centrifuged at high speed for 2 minutes. The RNA was eluted into a microcentrifuge tube with nuclease-free water added to the minicolumn and centrifuged at 14,000 xg for 60 seconds. RNA concentration was measured using NanoDrop ND-8000 (Thermo Fisher) before storage at -80°C.

Table 2.4. Volume of reagents required for DNase I incubation mix.

Solution	**Volume per reaction (µl)**
Yellow core buffer	24
$MnCl_2$ (0.09M)	3
DNase I	3

2.3.3 cDNA synthesis

For expression analysis, cDNA was synthesised from RNA extracted from tissue and cells using high capacity cDNA reverse transcription kit (Applied Bioscience). The master mix was multiplied by number of samples and added to each sample before incubation within a thermocycler (Applied Biosystems) for the period listed in Table 2.5.

Table 2.5. Master mix and cycle conditions for high-capacity cDNA reverse transcriptase.

Solution	**Volume per reaction (µl)**	
10x buffer	2.2	
10x random primers	2.2	
25x dNTPs	0.88	
Reverse transcriptase	1	
RNase inhibitor	1	
DEPC water	3.72	
1 µg RNA	11	
Cycle	25°C 37°C 85°C	10 minutes 2 hours 5 minutes

2.3.4 Nucleic acid concentration measurement

DNA and RNA concentrations were measured utilising ultraviolet-visible spectrophotometry technology within the NanoDrop ND-8000 8-sample spectrophotometer (Thermo Scientific).

2.3.5 Polymerase chain reaction (PCR)

Genotyping of mice and embryos was carried out using PCR. The genomic region of interest was amplified using primers listed in Table 2.6.

Table 2.6. Primer sequences designed for genotyping.

Primer	Sequence	Annealing Temperature (°C)
CRISPR_fwd	GCACCTGAGCCTTGGCAGAC	58
CRISPR_rev	GGGAGAAAGGTGATGGGTGG	
*Slc5a6*LoxP2F	CCTGTCTCTTGAGAAGCCA	58
*Slc5a6*LoxP2R	GGCTGTTGGGAAGCTGAGAT	
Slc5a6 5'arm WTF	AACTTCCATCCTTGGCAGAC	
Cre_fwd	GCATAACCAGTGAAACAGCATTGCTG	55
Cre_rev	GGACATGTTCAGGGATCGCCAGGCG	
ROSA_YFP_1	GGAGCGGGAGAAATGGATATG	58
ROSA_YFP_2	AAAGTCGCTCTGAGTTGTTAT	
ROSA_YFP_3	AAGACCGCGAAGAGTTTGTC	

A master mix of buffer, 10mM dNTPs, ddH_2O, primers and Taq polymerase was assembled based upon the reaction and sample numbers needed (Table 2.7). Samples were placed into a thermocycler (Applied Biosystems) for the appropriate cycle.

Table 2.7. PCR master mix and cycle conditions for genotyping.

	Slc5a6^{R252W}	*Slc5a6*^{Tm1c}	*Cre*	*YFP*
5x Go Taq Buffer	4 µl	4 µl	4 µl	4 µl
10mM dNTPs	0.25 µl	0.25 µl	0.25 µl	0.2 µl
ddH_2O	11.55 µl	10.65 µl	11.55 µl	7.7 µl
Primer	1 µl	1 µl	1 µl	2 µl
Go Taq G2 DNA polymerase	0.1 µl	0.1 µl	0.2 µl	0.1 µl
Genomic DNA	2 µl	2 µl	2 µl	2 µl
Cycle	95 C 2 mins 95 C 30 secs 58 C 30 secs. 72 C 30 secs } x 30 72 C 4 mins	95 C 60 secs 95 C 30 secs 58 C 30 secs. 72 C 30 secs } x 30 72 C 30 secs	95 C 2 mins 95 C 30 secs 55 C 30 secs. 72 C 30 secs } x30 72 C 4 mins	94 C 3 mins 94 C 30 secs 58 C 60 secs. 72 C 60 secs } x 30 72 C 10 mins
Expected product size	Wt = 97 bp +244 bp Ht = 97 bp + 244 bp + 341 bp Hm = 341 bp	Wt = 244 bp Ht = 244 bp + 293 bp Hm = 293 bp	Cre +ve = 280 bp	Wt = 600 bp Ht = 600 bp + 320 bp Hm = 320 bp

2.3.6 BamHI restriction digest

Slc5a6^{R252W} samples underwent restriction digest with *BamHI* reagents (Invitrogen, IVGN0056). To each 5 µl PCR product, 2 µl 10X ANZA buffer, 1 µl *BamHI* restriction enzyme, 12 µl nuclease free water was added. Samples were incubated at 37°C for 1 hour.

2.3.7 Reverse-Transcriptase PCR (RT-PCR)

RT-PCR was used to detect the amount of RNA from cDNA synthesis of all samples. The master mix was prepared, and samples placed into a thermocycler (Table 2.8). RT-PCR was also used to test primers (Table 2.9) and reaction conditions prior to qRT-PCR.

Table 2.8. RT-PCR reagents and reaction conditions.

Reagent	**Volume per reaction**	
5x Go Taq Buffer	4 µl	
10mM dNTPs	0.25 µl	
ddH_2O	11.55 µl	
Primer	1 µl	
Go Taq G2 DNA polymerase	0.1 µl	
cDNA	2 µl	
Cycle	95°C	2 mins
	95°C	30 secs
	58°C	30 secs. x 35
	72°C	30 secs
	72°C	4 mins

2.3.8 Gel electrophoresis

All PCR products were passed through a 2 % agarose (NBS biologicals) gel with the addition of 2.5 µl ethidium bromide (VWR) per 100 ml. Once set and samples were run at 100 V for 30 mins in a gel dock (Fisher Scientific) and imaged using a GelDoc-It 310 imaging system (UVP).

2.3.9 Quantitative real-time PCR (qRT-PCR)

To investigate gene expression in tissue qRT-PCR was carried out using Quant 7 Flex real time system (Applied Biosystems). Primers were designed to generate products between 80-120 bp with annealing temperatures of 58-60ºC (Table 2.9

Primer	**Sequence**	**Product size (bp)**
GAPDH F	TGTGCAGTGCCAGCCTCGTC	80
GAPDH R	TGACCAGGCGCCCAATACGG	
B-ACTIN F	CCCGCGAGCACAGCTTCTTTG	90
B-ACTIN R	CGACCAGCGCAGCGATATCGT	
hACTB F	AGCCTCGCCTTTGCCGATCC	104
hACTB R	TTGCACATGCCGGAGCCGTT	
hSMVT-RT-F-2-P6	TCCGTTGTCCTGTCAGAAGC	200
hSMVT-RT-R-2-P6	CCATGGCCTCCTTGTCTCTG	
Slc5a6ex6F	AGAGACAGGCAACGAAGAGC	590 (if deleted 96)
Slc5a6ex11R	ACCATCCTTGGCCCTCAATG	
Slc5a6ex9F	AGTGAATCAGGCTCAGGTGC	124
Slc5a6ex10R	CAGACCAATGAGGCAGCTCA	
Slc5a6ex16F	GGCCTGATTGTCAGTCTGCT	92
Slc5a6ex17R	AGTGCTAGGAGCTTTGGCAG	
Vimentin F	CTGCCTCTGCCAACCTTTTC	119
Vimentin R	CCATCTCTGGTCTCAACCGTC	
cTroponinT F	CTTAAAGCTCTCCCCATGCCC	100
cTroponinT R	CTCGGCTCTCCCTCTGAACA	
Acadvl F	GGTGGTTTGGGCCTCTCTA	82
Acadvl R	GGGTAACGCTAACACCAAGG	
Mfn1 F	AAGCATAAAGCTCAGGGGATG	60
Mfn1 R	TGCTTGAAATCCTTCTGCAA	
Lpl F	GCTGGTGGGAAATGATGTG	75
Lpl R	TGGACGTTGTCTAGGGGGTA	

).

Table 2.9. Primers designed for qRT-PCR.

Primer	Sequence	Product size (bp)
GAPDH F	TGTGCAGTGCCAGCCTCGTC	80
GAPDH R	TGACCAGGCGCCCAATACGG	
B-ACTIN F	CCCGCGAGCACAGCTTCTTTG	90
B-ACTIN R	CGACCAGCGCAGCGATATCGT	
hACTB F	AGCCTCGCCTTTGCCGATCC	104
hACTB R	TTGCACATGCCGGAGCCGTT	
hSMVT-RT-F-2-P6	TCCGTTGTCCTGTCAGAAGC	200
hSMVT-RT-R-2-P6	CCATGGCCTCCTTGTCTCTG	
Slc5a6ex6F	AGAGACAGGCAACGAAGAGC	590 (if deleted 96)
Slc5a6ex11R	ACCATCCTTGGCCCTCAATG	
Slc5a6ex9F	AGTGAATCAGGCTCAGGTGC	124
Slc5a6ex10R	CAGACCAATGAGGCAGCTCA	
Slc5a6ex16F	GGCCTGATTGTCAGTCTGCT	92
Slc5a6ex17R	AGTGCTAGGAGCTTTGGCAG	
Vimentin F	CTGCCTCTGCCAACCTTTTC	119
Vimentin R	CCATCTCTGGTCTCAACCGTC	
cTroponinT F	CTTAAAGCTCTCCCCATGCCC	100
cTroponinT R	CTCGGCTCTCCCTCTGAACA	
Acadvl F	GGTGGTTTGGGCCTCTCTA	82
Acadvl R	GGGTAACGCTAACACCAAGG	
Mfn1 F	AAGCATAAAGCTCAGGGGATG	60
Mfn1 R	TGCTTGAAATCCTTCTGCAA	
Lpl F	GCTGGTGGGAAATGATGTG	75
Lpl R	TGGACGTTGTCTAGGGGGTA	

Primer	Sequence	Product size (bp)
mt-Atp6 F	CCATAAATCTAAGTATAGCCATTCCAC	75
mt-Atp6 R	AGCTTTTTAGTTTGTGTCGGAAG	
mt-Co2 F	GCCGACTAAATCAAGCAACA	99
mt-Co2 R	CAATGGGCATAAAGCTATGG	
mt-Cytb F	GAGGTTGGTTCGGTTTTGG	72
mt-Cytb R	GTTTTGAAAGGGTGGGTGAC	
mt-Nd1 F	ACACTTATTACAACCCAAGAACACAT	66
mt-Nd1 R	TCATATTATGGCTATGGGTCAGG	
Klf4 F	CGGGAAGGGAGAAGACACT	62
Klf4 R	GAGTTCCTCACGCCAACG	
Ppara F	CTGAGACCCTCGGGGAAC	74
Ppara R	AAACGTCAGTTCACAGGGAAG	
Ppargc1a F	GAAAGGGCCAAACAGAGAGA	63
Ppargc1a R	GTAAATCACACGGCGCTCTT	
Cpt2 F	CCAAAGAAGCAGCGATGG	94
Cpt2 R	TAGAGCTCAGGCAGGGTGA	
Tfam F	CAAAGGATGATTCGGCTCAG	92
Tfam R	AAGCTGAATATATGCCTGCTTTTC	
Ulk1F	GGATCCATGGTGTCACTGC	72
Ulk1R	CAAGGGCAGCTGATTGTACC	
Hif1a F	CCACAGGACAGTACAGGATG	150
Hif1a R	TCAAGTCGTGCTGAATAATACC	

cDNA samples were diluted 1/10 in DEPC water and ran in triplicate (performed with at least three biological replicates per genotype) with 2 µL added to a 384-well optical plate (Applied Biosystems) and 8 µL of master mix (Table 2.10). The plate was sealed and protected from light and centrifuged at 1200 xg for 2 minutes at RT. The program was set to produce comparative Ct and melt curve with SYBR green FAST reagents using QuantStudio software (Applied Biosystems). The primer efficiency for each

primer set was determined using the amplification data generated and DART-PCR (Peirson *et al.*, 2003).

Table 2.10. qRT-PCR master mix components and reaction conditions.

Reagent	**Volume per reaction**
SYBR Green	5 µL
Forward primer (10 µM)	0.5 µL
Reverse primer (10 µM)	0.5 µL
DEPC ddH_2O	2 µL
cDNA	2 µL
Cycle	95°C 20 seconds — Hold stage 95°C 1 second 60°C 20 seconds — PCR stage 95°C 15 seconds 60°C 60 seconds — Melt curve stage 95°C 15 seconds

2.4 Bioinformatic analysis

2.4.1 In silico prediction tools

To determine the potential effect of a genetic variation, *in silico* tools can be utilised to analyse the predictive effect at the functional protein level (Tang *et al.*, 2020). In this project, 5 *in silico* prediction tools were used to determine the effect of our patient mutation, R252W, in addition to previously reported mutations in *SLC5A6.* Sorting intolerant from tolerant (SIFT) (available at https://sift.bii.a-star.edu.sg) assesses whether protein function may be affected by amino acid substitution based on conservation (Sim *et al.*, 2012). MutationTaster (available at https://www.mutationtaster.org) utilises multiple biomedical databases to assess the impact of the variation using conservation, potential loss of protein effects and changes to the mRNA levels (Schwarz *et al.*, 2010). PolyPhen is a tool which predicts amino acid substitution from the effect on protein structure in addition to conservation. Combined annotation dependent depletion (CADD) (available at https://cadd.gs.washington.edu/score) uses data from 63 variant annotations

databases to predict the pathogenicity of genetic variations (Kircher *et al.*, 2014). Functional analysis through hidden markov models (FATHMM) (available at http://fathmm.biocompute.org.uk) also predicts the consequences of variants on protein function using amino acid conservation (Shihab *et al.*, 2013).

2.4.2 Protein homology

To identify the degree of protein homology between species for Slc5a6, the FASTA sequence for human and mouse Slc5a6 was attained from national centre for biotechnology information (NCBI) database. The sequences were then entered into EMBOSS Needle tool (available at https://www.ebi.ac.uk/Tools/psa/emboss_needle) to perform pairwise sequence alignment using the Needleman-Wunsch algorithm (Needleman and Wunsch, 1970).

2.4.3 Allele frequency within control population

The presence of human variation within a control population can be found using freely available databases of WES and WGS data from Big Data projects. In this project, *SLC5A6* variants were searched for within the genome aggregation database (GnomAD) (available at https://gnomad.broadinstitute.org). This database lists all variations found within a control population of 141,456 samples and determines their frequency within the population which was noted for each *SLC5A6* variant reported.

2.5 Sample preparation

2.5.1 Paraffin wax embedding

Embryos were collected at various stages of development, aged with E0.5 defined as noon of the day the copulation plug was detected. Neonates, juveniles and adults were euthanised by cervical dislocation. Hearts and intestines were dissected and processed into wax blocks according to parameters listed in Table 2.11.

Table 2.11. Processing conditions for wax embedding mouse tissue.

Conditions listed for E10.5 and E15.5 are noted for whole embryo processing. E17.5, P0 and adult conditions are listed for heart processing.

	E10.5	E15.5	E17.5	P0	Adult
4% PFA	1 Night	2 Nights	2 Nights	2 Nights	2 Nights
PBS wash	2 x 5 mins				
50% EtOH	30 mins	3 hours	4 hours	4 hours	5 hours
70% EtOH	30 mins	3 hours	4 hours	4 hours	5 hours
70% EtOH	30 mins	3 hours	4 hours	4 hours	5 hours
95% EtOH	30 mins	3 hours	4 hours	4 hours	5 hours
100% EtOH	30 mins	3 hours	4 hours	4 hours	5 hours
100% EtOH	1 hour	Overnight	Overnight	Overnight	Overnight
Histoclear	10 mins	15 mins	15 mins	15 mins	30 mins
Histoclear	10 mins	15 mins	15 mins	15 mins	30 mins
Histoclear-wax	20 mins	1 hour	1 hour	1 hour	2 hours
Wax	1 hour 30 mins	4 hours	Overnight	Overnight	24 hours

2.5.2 Paraffine wax sectioning

Paraffin embedded embryos and tissues were sectioned coronally at 8 µm using a Leica RM2135 microtome. Sister sections were collected onto water coated slides at 37°C to allow sections to expand. Water was removed from the slides and allowed to dry before being placed into an incubator at 37°C overnight.

2.5.3 Cryo-embedding

Adult hearts were dissected and washed in 1x PBS. Hearts were placed into 7.5% sucrose in PBS solution for 1 hour, followed by immersion into 15% sucrose solution for 1 hour. This cryoprotects the tissue throughout the freezing process by removing water from the heart. Hearts were then rolled in OCT, to reduce the presence of air bubbles, and embedded coronally within a mould filled with OCT. Moulds were then placed on dry ice until OCT solidified and were stored at -80°C until required.

2.5.4 Cryo-sectioning

Hearts were coronally sectioned at 10 µm using a Leica CM1860 cryostat. Once cut, sections were placed onto StarFrost slides (Knittel-Glass) and air dried for at least 1 hour at room temperature. Slides were then stored at -80°C until use

2.6 Histology

2.6.1 Haematoxylin and Eosin

Paraffin embedded sections were dewaxed in Histoclear for 20 minutes and rehydrated through a descending alcohol series of ethanol for 2 minutes. Sections were washed in dH_2O for 2 minutes, stained with haematoxylin for 10 minutes followed by a 5 minute wash in running H_2O. Sections were then dipped in 1% HCL (hydrochloric acid diluted in 70% ethanol), rinsed in H_2O and immersed in Eosin for 5 minutes. Sections were dehydrated through an ascending ethanol series (50%-70%-90%-100%) for 2 minutes each and placed in Histoclear for 20 minutes before being mounted using Histomount. Cryosections were air dried for 15 minutes at RT and immersed in haematoxylin for 5 minutes. Sections were washed in running tap water for 60 seconds and dipped in acid alcohol three times before repeating the tap water wash. Samples were placed into eosin for 30 seconds and dehydrated through an ethanol series (50%-70%-90%-

100%) for 2 minutes each before immersion in Histoclear for 10 minutes. All sections were mounted in Histomount and allowed to dry overnight.

2.6.2 Masson's Trichrome

Paraffin sections were dewaxed in Histoclear for 10 minutes, rehydrated through 100%, 90%, 70% and 50% ethanol. Sections were washed in dH_2O for 5 minutes and fixed in Bouin's solution overnight. A H_2O wash was carried out before staining in Weigert's iron haematoxylin for 10 minutes. Sections were washed in dH_2O for 10 minutes and stained with Biebrich Scarlet-Acid Fucshin solution before rinsing in dH_2O for 5 minutes. Differentiation was carried out using a 1:1:2 solution of phosphotungstic acid, phosphomolybdic acid and dH_2O before staining with Aniline blue solution for 10 minutes before rinsing in dH_2O. Sections were immersed in 1% acetic acid for 2 minutes, washed in dH_2O and quickly dehydrated through an ethanol series (50%-70%-90%-100%) for 2 minutes each before mounting in Histomount and drying at RT overnight.

2.6.3 Picro-Sirius Red

Cryosections were dried at room temperature for 30 minutes and fixed in 4% PFA in 90% ethanol for 45 seconds. Sections were washed in running tap water for 5 minutes and immersed in haematoxylin for 15 minutes. Slides were removed, washed in running tap water for 10 minutes before staining in Sirius red (0.1% direct red 80; 1% picric acid) for up to 15 minutes. All sections were dehydrated through an ethanol series, 50-100%, cleared using Histoclear reagent and mounted in Histomount.

Paraffin sections were immersed in Histoclear for 10 minutes, rehydrated through an ethanol series (100%-90%-70%-50%) for 2 minutes each and washed in dH_2O for 10 minutes. Sections were placed in 0.2% phosphomolybolic acid for 5 minutes, washed in dH_2O then rinsed in 0.01% hydrochloric acid. All sections were washed in dH_2O and dehydrated through an ethanol series of 50-100% before immersion in Histoclear in 10 minutes and sections mounted in Histomount.

2.7 Immunofluorescence

2.7.1 Immuno-labelling

Paraffin wax was cleared from sections in Histoclear for 2 cycles of 10 minutes. Sections were rehydrated for 2 minutes through a series of ethanol washes (50%-70%-90%-100%) for 2 minutes each before equilibrating in PBS for 5 minutes. Antigen retrieval was performed dependent upon the antibody used (Table 2.12). Slides were placed into a pressure cooker at 80kPa with 600 mL of citrate buffer (0.01M, pH 6.3) for 5 minutes or high pH tris buffer (Vector) for 1 minute. Slides were allowed to cool at RT for 10 minutes then washed for 5 minutes in dH_2O or PBS for citrate buffer or high pH retrieval respectively. Samples then underwent 3 cycles of 5 minute PBS washes before placement in 10% FCS:PBS to block non-specific epitope binding for 30 minutes. The primary antibodies were prepared in the concentration required (Table 2.12) in a 2% FCS:PBS solution and applied to the slides. Parafilm coverslips were placed on top of the slides to ensure equal distribution across all samples. Slides were placed in a humidified chamber overnight at 4°C. The antibody solution was removed the following morning and slides washed in 3 cycles of PBS. Secondary antibodies were prepared to concentration (Table 2.12) in a 2% FCS:PBS solution and applied to sections. Parafilm coverslips were applied and sections incubated at RT for 2 hours in a humidified chamber. To remove the secondary antibody solution the slides were washed in 3 cycles of PBS in covered chambers to avoid bleaching. Sections were mounted in Vectashield with DAPI (Vector Laboratories, H-1200) and stored at 4°C before imaging.

Cryosections were air dried at RT for 15 minutes before fixing in 4% PFA for 5 minutes. Sections were washed in PBS for 10 minutes before placement in non-specific epitope binding block (10% FCS:PBS) for 30 minutes. The required concentration of primary antibody (Table 2.12) was prepared in a 2% FCS:PBS solution and applied to sections. Slides were incubated at 4°C overnight in a humidified chamber. The following morning the antibody solution was removed, and slides washed in 3 cycles of PBS. The secondary antibody was prepared in a 2% FCS:PBS solution in the appropriate concentration (Table 2.12) and applied to the sections. Slides were placed in a humidified chamber at RT for 2 hours. The secondary antibody solution was removed, and samples were washed in PBS for 15 minutes before mounting in Vectashield with DAPI (Vector Laboratories, H-1200). All slides were stored at 4°C before imaging.

Table 2.12. Antibodies used for fluorescence labelling.

Antibody	Description	Concentration	Supplier	Product number
Slc5a6	Rabbit polyclonal	1:50	Santa Cruz	Sc-134522
Slc5a6	Rabbit polyclonal	1:50	ProteinTech	26407-1-AP
GFP	Rabbit polyclonal	1:100	Torrey Pines	TP401
Wheat Germ Agglutinin	Alexa Fluor™ 594 conjugate	1:200	Life Technologies	997854
Alexa Fluor™ 488	Donkey anti-rabbit	1:200	Life Technologies	A21206
Alexa Fluor™ 594	Donkey anti-rabbit	1:200	Life Technologies	A21207

2.7.2 Quadruple immunofluorescence

Adapted from (Rocha *et al.*, 2015b) with help from Dr Amy Vincent. Cryosections were air dried for 1 hour, isolated by a hydrophobic pen and fixed in 10% formalin for 10 minutes. TBS-T was used to wash sections for 5 minutes followed by permeabilization through a gradient of methanol (70%-95% for 10 minutes-100% for 20 minutes-95%-70% for 10 minutes). Sections were then washed in TBS-T and blocked in 10% normal goat serum (NGS:TBST) for 1 hour. Endogenous biotin blocking was carried out by incubation in Avidin D solution for 15 minutes, washed in TBS-T for 10 minutes and blocked in Biotin for 15 minutes before washing in TBS-T for 10 minutes. Sections were then further blocked in Mouse on Mouse (MOM) for 2 hours at RT before primary antibodies were diluted in MOM dilutent (Table 2.13) and added to sections and incubated overnight at 4°C.

Table 2.13. Antibodies used for quadruple immunofluorescence.

Antibody	Description	Concentration	Excitation/ Emission (nm)	Supplier	Product number
NDUFB8	Mouse (IgG1)	1:100	-	Abcam	ab110242
MTCO2	Mouse (IgG2a)	1:100	-	Abcam	ab110258
VDAC	Mouse (IgG2b)	1:100	-	Abcam	ab14734
Laminin	Rabbit polyclonal	1:50	-	Abcam	ab11575
Biotin	Goat Anti-Mouse (IgG1)	1:200	-	Life Technologies	A10519
Alexa 488	Goat Anti-Mouse (IgG2a)	1:200	BP450-490 – BP515-565	Life Technologies	A21131
Alexa 546	Goat Anti-Mouse (IgG2b)	1:200	BP546/12 – BP575-640	Life Technologies	A21143
Alexa 405	Goat Anti-Rabbit (IgG)	1:100	G365 – BP445-450	Life Technologies	A31556
Alexa 647	Streptavidin conjugated	1:100	BP575-625 – BP660-710	Life Technologies	S32357

Sections were washed in TBS-T for 15 minutes before incubation with secondary antibodies (Table 2.13) in a dark, humidified chamber for 2 hours at 4°C. Following this, sections underwent a TBS-T wash for 15 minutes before addition of streptavidin conjugated secondary antibody (Table 2.13) for 2 hours at 4°C. Samples were washed in TBS-T covered for 15 minutes before mounting in ProLong Gold Antifade (Life Technologies, P36930).

2.8 Image acquisition

2.8.1 Brightfield/fluorescence microscopy

Whole embryos and hearts were imaged using a Leica MZ6 stereomicroscope at 0.63x magnification. Histological sections were imaged on Zeiss Axio Imager motorised microscope fitted with a Zeiss Axiocam camera (Carl Zeiss Germany Ltd.) using brightfield at 2.5x and 20x magnification. Immunofluorescent sections were visualised on Zeiss Axio Imager using ApoTome using the 20x, 40x and 63x objectives. An average exposure time was taken for 405 nm, 488 nm, 546 nm 594 nm and 647 nm channels using the no primary control sections then applied to all relevant images. All Zeiss acquired images were processed using the Zen 3.1 blue software (Carl Zeiss Germany Ltd.)

2.8.2 Image analysis

Image analysis software ImageJ (NIH, Bethesda, USA) was used for the following IHC/IF methods. Cardiac fibrosis was quantified by applying a colour threshold to each image to generate an area measurement of fibrosis (μm). The total area of the image was measured to determine the percentage area of fibrosis. Measurements were calculated for four images taken at three regions of interest throughout the LV and RV wall. Measurements were acquired for three technical and at least three biological replicates per genotype.

Quantification of cardiomyocyte hypertrophy using WGA within the heart was determined by manually tracing the area of cardiomyocytes adjacent to a capillary to ensure an equivalent cross-section was counted per image. Four images taken at 20x magnification were analysed in three regions of interest per ventricle with three technical and, at least three biological repeats included.

Quadruple immunofluorescent stained sections were imaged throughout the LV of one experimental and one no primary control section per mouse, with at least three biological replicates analysed per genotype. Segmentation of cardiomyocytes was performed randomly using IMARIS (Bitplane). Intensity mean was obtained for each channel per cardiomyocyte, at least 150 cardiomyocytes were analysed per section. Values were analysed following protocols described (Rocha *et al.*, 2015b).

All image analysis was performed blind without prior knowledge of genotype. Samples were coded with a litter and mouse ID, the genotype of each sample was then correlated to the sample code after images were acquired.

2.9 Western blotting

2.9.1 Sample collection

E15.5 embryos were collected in ice-cold PBS with protease and phosphatase inhibitor cocktails (Sigma) added at a 10µl/ml concentration. The head, heart and a limb were collected into eppendorfs and snap frozen in liquid nitrogen and stored at -80°C until use.

2.9.2 Protein extraction

Samples were homogenised and lysed in cellytic buffer (Sigma) containing 10µl/ml of protease and phosphatase inhibitors. The heart and limb were lysed in 300µl of buffer whereas the heads were lysed in 500µl of buffers. Tissue was ruptured using a 2ml syringe and passed through a 19G and 27G needle five times. Samples were then placed onto an orbital shaker at 4°C for 1 hour before centrifugation at 12,000rpm for 20minutes at 4°C. Following centrifugation, the supernatant was transferred to a new Eppendorf and the concentration measured by Bradford assay. Protein lysates were stored at -20°C until use.

2.9.3 Bradford assay

The concentration of protein lysates was measured using a colorimetric assay, which allows quantification of protein using a dye which binds to proteins producing a colour change from 470nm to 595nm. A series of bovine serum albumin protein standards (Pierce) were used to create a standard curve for analysis, from 0µg/ml up to 2000µg/ml. All samples were measured in duplicate.

2.9.4 SDS-PAGE and western blotting

20µg of protein lysates were mixed with 2x Laemmli buffer (Sigma) and heated at 95°C for 5minutes. Samples were removed from the heat block and centrifuged for 5minutes at 14,000rpm. 4µ of ProteinPlus pre-stained ladder (Thermofisher Scientific) and 30µl of lysate was loaded into a well in a 4-12% Bis-Tris NuPAGE gel (Life Technologies) in a mini-blot tank system filled with MOPS running buffer (Life Technologies). Gels were run at 80V for 15minutes and then 100v for 1 hour 15minutes. Proteins were then transferred to a nitrocellulose membrane (Thermofisher Scientific) in transfer buffer for 1 hour at 10V. Protein transfer was confirmed by Ponceau staining (Sigma) for 5minutes at RT. Membranes were then de-stained using dH_2O before blocking the membrane in 5% milk;TBST for 1 hour RT. Membranes were then incubated in primary antibodies (Table 2.14) diluted in 5% milk;TBST for 1 hour at RT. Primary antibodies were removed and the membranes washed three times in

1xTBST for 5 minutes each. After washing, secondary antibodies were added to the membranes (Table 2.14) diluted in 5% milk;TBST for 1 hour at RT covered. Following incubation, the secondary antibodies were removed, and the membranes washed three times in 1xTBST for 5 minutes each. Chemiluminescent substrate (Licor) was added to the membranes (1:1 solution A and solution B) for 5 minutes before imaging on the c-digit developer (Licor).

Table 2.14. Antibodies used for western blot detection.

Antibody	**Description**	**Concentration**	**Supplier**	**Product number**
Slc5a6	Rabbit polyclonal	1:500	ProteinTech	26407-1-AP
Gapdh	Rabbit	1:10,000	Abcam	Ab22555
HRP	Goat anti-Rabbit	1:10,000	Dako	P0448

2.10 Electron microscopy

An apex section of mouse heart (~2x2x2mm) was fixed with 2% glutaraldehyde at 4°C for minimum of 12 hours. Tissue processing was carried out by the Electron Microscopy Research Service (EMRS) at Newcastle University. Samples were submitted for heavy metal staining protocol before embedding in 100% resin (Cocks *et al.*, 2018). The resin block is then sectioned at 70 nm using a diamond knife, placed on a copper grid and imaged with CM100 TEM (FEI). Images were acquired blindly (without prior knowledge of genotype) in longitudinal sections (LS) to capture intermyofibrillar (IMF) mitochondria, and were taken at four magnifications; 3000x, 8000x, 15000x and 30,000x.

2.10.1 Morphometric analysis

ImageJ (NIH, Bethesda, USA) software. Within each genotype three hearts were used for analysis. For each heart, 50 IMF mitochondria were randomly selected and analysed from three spatially distant cardiomyocytes; 8 images acquired per cardiomyocyte. Mitochondrial size descriptors and measurements were captured and used to calculate; area and perimeter (μm)

$$\text{Form factor (indicates branching and complexity)} = [(\text{perimeter}^2)/(4\pi \cdot \text{area})]$$

$$\text{Aspect ratio (length-width ratio)} = [(\text{major axis})/(\text{minor axis})]$$

$$\text{Circularity} = [4\pi \cdot (\text{area}/\text{perimeter}^2)]$$

$$\text{Roundness } [4\cdot(\text{area})/(\pi\cdot\text{major axis}^2)]$$

Additionally, Ferert's diameter (μm), the largest distance between two points within any mitochondrion was determined (Koopman *et al.*, 2006; Picard *et al.*, 2013). Data was exported into, and graphs generated using GraphPad Prism v.8.4.3 (GraphPad Software, La Jolla, USA).

2.11 Electrocardiography (ECG)

To characterise electrophysiological changes *in vivo*, electrocardiography (ECG) was carried out on mice anaesthetised using isoflurane (3% isoflurane/97% oxygen) (Abbott, USA) for 3 minutes, or until no response from tail pinch (maximum time allowed 5 minutes). Using a published protocol (Sysa-Shah *et al.*, 2015) as point of reference, an amended procedure was established. Anaesthesia was maintained at 2% isoflurane/98% oxygen with body temperature maintained using a heated mat throughout the recording. Three electrode probes were inserted into each mouse as shown in

Figure 2.5A. ECG was recorded for 3 minutes using the PowerLab data acquisition system (ML866, ADInstruments, CO) and animal bio amp (FE136, ADInstruments, CO). Software provided by ADInstruments, LabChart, was used to record electrical activity and average each reading using QRS maximum for alignment. Following recording, anaesthesia was removed and mice recovered between 40-90 seconds whilst still placed on heated mat.

2.11.1 ECG analysis

The averaged reading from the ECG readings were used for analysis. The time intervals (RR, PR and QT) and waves (P, QRS and T) were, in most recordings, detected by the LabChart software automatically (

Figure 2.5B). In recordings where this was not detected, the parameters would be defined manually. To minimise any effects from anaesthetic acclimatisation, data recorded between 60-120 seconds was used for analysis.

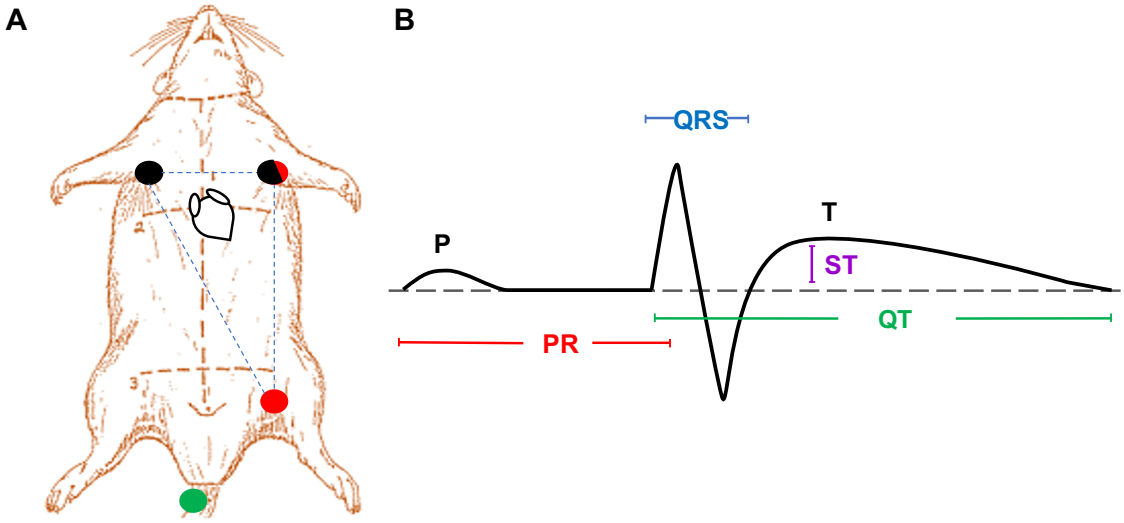

Figure 2.5. Parameters for electrocardiography.
A) Representative schematic of probe placement for ECG readings. Negative electrode (black), positive electrode (red) and ground electrode (green). B) Schematic of ECG reading, indicating P wave and QRS complex as well as the PR and QT intervals. Each parameter is measured during the recording to determine efficiency of the cardiac conduction system.

2.12 Cardiac Magnetic Resonance (CMR) Imaging

2.12.1 Data acquisition

CMR images were acquired using 7.0T horizontal bore Varian microimaging system (Varian Inc., Palo Alto, CA, USA) with a 12 cm microimaging gradient insert (40 gauss/cm). Mice were anaesthetised with 4% isoflurane (Abbott, USA) and placed on a custom-built sled (Dazai Research Instruments, Toronto, Canada) accompanied with electrographic, respiratory and cutaneous temperature monitoring. A warm air device (SA Instruments) was used to maintain body temperature at 37°C with anaesthesia maintained at 1.5% Isoflurane and oxygen levels set to 0.5 L/min delivered via nose cone. For physiological monitoring and gating, a SA Instruments Inc (Edison, NJ, USA) small animal system was used. To transmit and receive the MR signal, a 30mm quadrature birdcage coil (Rapid Biomedical, GmbH) was inserted and used as a radiofrequency transceiver for CMR imaging. Training provided by Dr Anna Walaszczyk.

2.12.2 Imaging parameters

Imaging performed by Dr Anna Walaszczyk. The long and short axes of the LV were orientated using scout images. The following parameters were used to measure cardiac function with an ECG triggered, respiratory gated gradient echo (FLASH) cine MR sequence, echo time (TE) = 1.36 ms, repetition time (TR) = 5 ms, flip angle 15°. Matrix (MTR) = 12 x 128, field of view (FOV) = 25.6 x 25.6 mm^2, number of averages = 4. Continuous 1 mm thick short axis slices were taken, with 3 averages, to cover the whole LV (Figure 2.6A).

2.12.3 CMR image analysis

Short axis images acquired during CMR were analysed blind using ImageJ analysis software (NIH, Bethesda, USA). The epicardial and endocardial borders were manually drawn to measure the area between each cardiac layer at end-diastole and end-systole, determining myocardial area (Figure 2.6B). Myocardial volume (mm^3) was measured by multiplying myocardial area per slice x total number of slices x slice thickness (1mm/slice). Mass of the left ventricle was calculated, multiplying myocardial volume by myocardial specific gravity (1.05mg/mm^3). To ensure accuracy of the measurements, 2 parameters were considered i) a limit of 5% variance in myocardial mass is maintained, ii) ensuring calculated mass correlated well with actual mass when harvested. Analysis training received from Dr Emily Dookun.

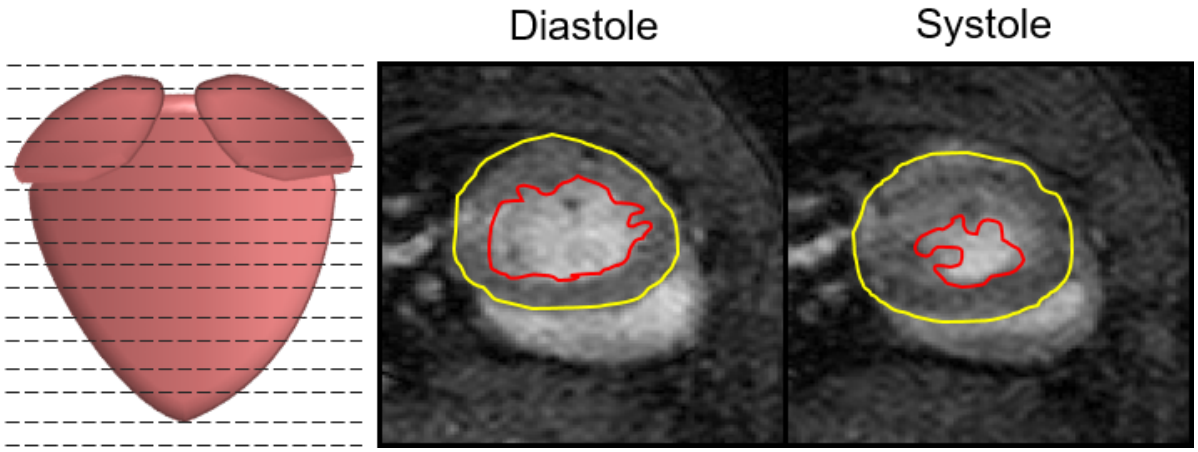

Figure 2.6 Defining LV endocardial and epicardial layers for CMR image analysis. A) Schematic of whole heart indicating 1 mm short axis slices taken during MR imaging. B) Image slices of the LV in diastole and systole with the endocardium marked in red and the epicardium outline in yellow.

Cardiac function was determined by measuring left ventricular chamber area x slice thickness. Stroke volume, cardiac output, mean mass and ejection fraction was calculated using the following formulae;

Stroke volume, SV (μl) = left ventricular end diastolic volume (LV-EDV) - left ventricular end systolic volume (LV-ESV)

Cardiac output, CO (μl) = (SV (μl) x mean HR (bpm)) /1000

Ejection fraction, EF (%) = (SV/LV-EDV) x 100

Mean Mass, MM = (left ventricular end diastolic mass (LV-EDM) + left ventricular end systolic mass (LV-EDM)) / 2

2.13 Skeletal analysis

2.13.1 Radiograph acquisition

Radiographs (X-Ray images) were acquired on the MX-20 Cabinet X-Ray system (Faxitron, Tuscon, USA) by Dr Ella Dennis. Mice were anaesthetised using 4% isoflurane (Abbott, USA) and X-rays acquired at 23 kV for 5 seconds (Dennis *et al.*, 2020). Mice were laid prone to allow for longitudinal bone measurements at 5 weeks.

2.13.2 Radiograph analysis

Bone length measurements were acquired blindly using ImageJ (NIH, Bethesda, USA). In addition to the long bones; femur and tibia, the cranial bones were assessed by measuring the inner canthal distance (ICD) (Dennis *et al.*, 2020).

2.14 Statistical analysis

Statistical analysis was performed using GraphPad Prism 8.4.3 (GraphPad Software, La Jolla, USA). All datasets were subject to normality testing using Shapiro-Wilk, if the data was normally distributed, parametric testing was then performed. Non-parametric testing was carried out where the *n* number was too small. Where 3 datasets are compared, a one-way ANOVA with repeated measures using Bonferroni correction was performed. A student's t-test was carried out to compare 2 datasets.

Chapter 3 Expression of SLC5A6 and markers of energy metabolism during mammalian cardiac development

3.1 Introduction

3.1.1 Cardiac development

Cardiac development is described in 1.1.1. Briefly, the heart is one of the first fully functional organs to develop during embryogenesis and is formed in a similar manner in all vertebrates (Kuo *et al.*, 1997; Sakabe *et al.*, 2005). This process is initiated in the third week of development in humans and E6.5 in mice (Brand, 2003; Moorman *et al.*, 2003) when gastrulation occurs. The first cardiac progenitors, the PHF, are derived and form the primary cardiac crescent. The structure then fuses at the midline to produce the linear heart tube (Rosenquist, 1970). Physiological pumping of the heart occurs once the heart tube forms and continues while cardiac remodelling takes place to form the four chambered heart (Christoffels *et al.*, 2000; Brand, 2003). Meanwhile, cells of the PHF proliferate and, with the addition of cells from the SHF, contribute to the growth of the linear heart tube (De La Cruz *et al.*, 1989; Waldo *et al.*, 2001).

The heart tube then loops rightwards where the atrial and ventricular regions of the heart become separated by the formation of the atrioventricular canal (AVC). These regions balloon due to cellular proliferation, and become re-orientated into the correct alignment prior to septation (Moorman and Christoffels, 2003). The myocardium also undergoes morphological changes to aid in contraction and septation; trabeculation and compaction. Following birth, cardiomyocytes continue to mature displaying clearly defined sarcomeres (Jacot *et al.*, 2010b; Foglia and Poss, 2016). Once cardiomyocytes mature, they lose their proliferative properties and, in response to an increase in haemodynamic load, further contribute to the thickening of the myocardium by physiological hypertrophy (Foglia and Poss, 2016).

3.1.2 Energy metabolism during cardiac development

During embryogenesis, the fetus exists within a hypoxic environment and relies upon various transcription factors, such as hypoxia inducible factor 1 (*Hif-1α*), to regulate glycolysis (Kolwicz *et al.*, 2013). Expression (mRNA) of these cofactors is high within fetal hearts, whereas expression of essential regulators of mitochondrial biogenesis and fatty acid oxidation (FAO) is low. The fetal circulation contains high levels of lactate

and glucose while levels of fatty acids are low (Stanley *et al.*, 2005). As a result, the developing heart utilises lactate and glucose for energy production rather than FAO. This level of substrate flexibility is beneficial, as it allows the heart to meet the high energetic demand generated by physiological changes during development (Ritterhoff and Tian, 2017). As the cardiac progenitors differentiate into immature cardiomyocytes, the reliance on glycolysis decreases as mitochondrial biogenesis occurs increasing the capacity for oxidative generation of ATP (Morita Y, 2020). As previously described, from birth the heart is exposed to an increase in haemodynamic load, which triggers a transformation in energy metabolism (Ritterhoff and Tian, 2017). At this point, although the postnatal heart still relies on glycolysis, oxidative phosphorylation (OXPHOS) also occurs to a lesser degree. This balance shifts over the first week of life; as glucose and lactose levels drop, the availability of fatty acids increase resulting in oxidative phosphorylation becoming the main provider of ATP through fatty acid oxidation. This remains the primary source throughout adulthood (Allard *et al.*, 1994; de Carvalho *et al.*, 2017; Zhao *et al.*, 2019).

3.1.3 Sodium-dependent multivitamin transporter (SMVT)

As previously described, a homozygous missense mutation within *SLC5A6* was identified as the potential cause of disease in siblings affected by DCM. *SLC5A6* encodes the human sodium-dependent multivitamin transporter (SMVT), which is responsible for the transport of pantothenic acid (PA), biotin and lipoic acid (LA) across the plasma membrane. As an essential vitamin transporter, it is strongly expressed within the intestine, specifically at the intestinal mucosa enabling absorption of each substrate from external food sources (Said, 2004; Said, 2011; Quick and Shi, 2015). Each substrate is essential for energy metabolism, therefore SLC5A6 is reported to be ubiquitously expressed in organs including the brain, liver, kidneys and placenta (Prasad *et al.*, 1998; Quick and Shi, 2015; Uchida *et al.*, 2015; Subramanian *et al.*, 2017). However, very little is known about SLC5A6 expression within one of the highest energy-dependent organs in the human body, the heart. There have been no studies published to date, which investigate the expression of *Slc5a6* during embryogenesis, and to date no studies have been performed to determine expression throughout cardiac development, both in *utero* and postnatally.

3.1.4 Aims of the chapter

The aim was to determine SLC5A6 expression in human cardiac development at both the RNA and protein level, in addition to characterising the expression of *Slc5a6* within the murine heart and investigating its role throughout cardiac development.

As *Slc5a6* is solely responsible for the transport of essential substrates; PA, biotin and LA, required for aerobic energy metabolism, it is hypothesised that *Slc5a6* will be expressed throughout the heart when reliance on aerobic energy metabolism is highest. Consequentially, the normal expression pattern of genes involved in energy metabolism and mitochondrial biogenesis will be characterised.

3.2 SLC5A6 expression throughout human development and adulthood

3.2.1 Confirmation of SLC5A6 expression within human tissue

As very little is known about the role of *SLC5A6* within the heart, the initial aim was to establish if and when SLC5A6 is expressed within the heart. To investigate *SLC5A6* expression throughout different human cell types, heart cDNA was obtained from the Human Developmental Biology Resource (Newcastle University, 18/NE/0290) at two developmental stages CS13 (*n*=1) and CS17 (*n*=1), where the heart has looped to form distinct cardiac chambers. Additionally, the research group had access to control human cDNA which was synthesised from primary human myoblast and fibroblast cells, obtained from the MRC Centre for Rare Neuromuscular Diseases Biobank (Newcastle University). A human ventricular cardiomyocyte cell line, AC10 (*n*=1), was also used to determine *SLC5A6* expression as a potential use for *in vitro* experiments. Using the cDNA synthesised, RT-PCR was performed as described in 2.2.7. Figure 3.1 suggests *SLC5A6* is present within the heart at CS13 and CS17 during human development, and is also present in primary control myoblasts, however, *SLC5A6* appears absent from primary control fibroblast cells. From investigation into *SLC5A6* expression within the AC10 cells, a ventricular cardiomyocyte cell line, only a faint band is detected. As SLC5A6 was suggested to be expressed within CS13 and CS17 hearts, preliminary investigation into SLC5A6 expression within the developing human heart was performed using IHC.

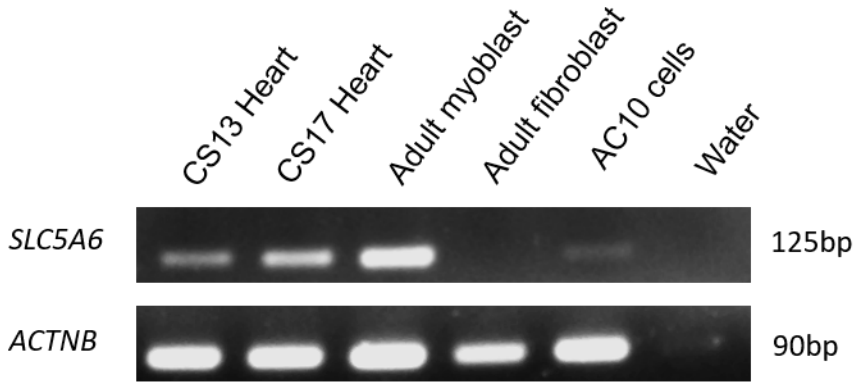

Figure 3.1. *SLC5A6* expression in human samples by RT-PCR.
SLC5A6 was detected at 125 bp in all samples but adult fibroblasts and shows very faint expression in AC10 cells. *ACTNB* was used as a housekeeping control and was found in all samples. *n* = 1.

3.2.2 SLC5A6 is expressed within the heart during human embryonic development

Paraffin sections of human embryonic tissue were used in the initial IF to detect SLC5A6 at CS14 (equivalent to E11.0 in the mouse embryo), CS19 (equivalent to E12.5 in mouse embryo) and CS23 (equivalent to E14.5 in mouse embryo). Previous studies have shown that SLC5A6 is expressed in both the brain and gut, and therefore both tissue types were included as positive controls for the initial use of the SLC5A6 antibody.

At CS14, the human embryonic heart is undergoing cardiac looping, whereby the ventricular compartment of the primary heart tube loops rightwards. SLC5A6 staining was performed on sections of the heart (Figure 3.2A-D), brain (Figure 3.2G-H) at CS14 (*n* =1). SLC5A6 expression appears to be confirmed in the midline of the brain (Figure 3.2G) and the myelencephalon and granular layer surrounding the midline region (Figure 3.2H). Initial investigation into the expression of SLC5A6 within the heart by IF indicated some positive SLC5A6 staining in the developing ventricle (Figure 3.2A-B). Although distinct membrane localisation was expected within the cardiomyocytes, it was not clearly apparent in the cardiac staining performed within this study. However, from higher powered imaging some possible evidence of membranal localisation of SLC5A6 in cardiomyocytes may be present within the endocardium (Figure 3.2C) and pericardium (Figure 3.2D). The low degree of SLC5A6 staining within the heart, may correlate with the RT-PCR data (Figure 3.1) which shows a low level of *SLC5A6* within whole heart cDNA; however, staining should be repeated to confirm initial findings.

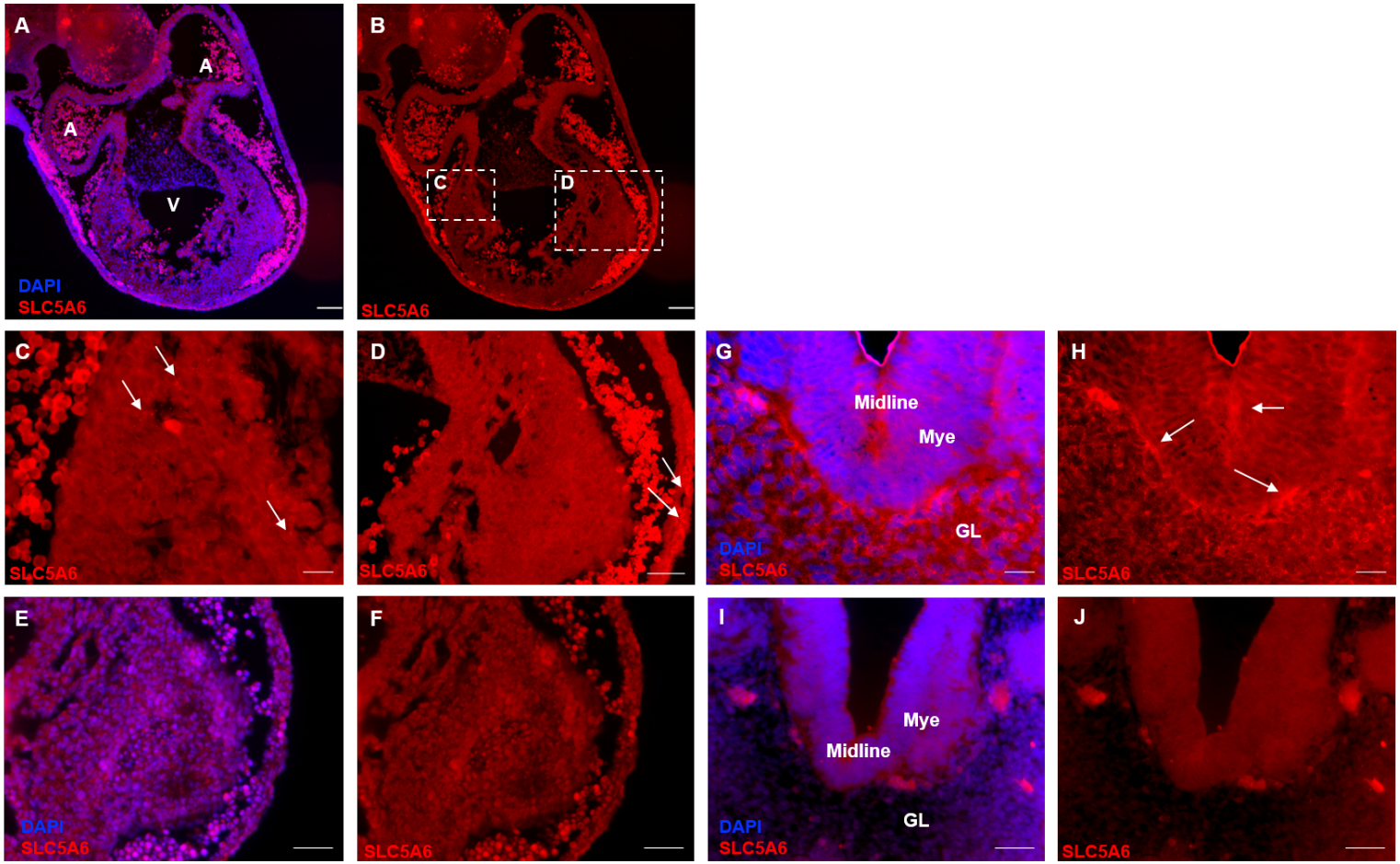

Figure 3.2. SLC5A6 is expressed in the brain, heart and gut at CS14 shown by IHC.
Human embryonic sections obtained from HDBR stained with SLC5A6 antibody (red), nuclei stained with DAPI (blue). A-B) Some SLC5A6 staining may be observed within the atria and ventricle. Higher magnification of the ventricles reveals very small areas of possible cardiomyocyte membrane staining of SLC5A6 within the myocardium (C) and pericardium (D) indicated by arrows. G-H) SLC5A6 expression is confirmed in the brain used as a positive control, with strong expression shown at the midline and within the GL (H) indicated by arrows. No primary controls shown for heart (E-F) and brain (I-J). A Atria, GL granular layer, LM lamina propria, Mye myelencephalon, V ventricle. *n* = 1 for each tissue stained. Scale bar = 100μm (A,B,E), 50μm (D,F), 20μm (C).

At CS19, the myocardium becomes thicker and ventricular septation can be observed, forming the two ventricle chambers. Further investigation into SLC5A6 expression was performed on sections collected at CS19. This too indicated some positive SLC5A6 expression within the heart, but not the distinct membrane localisation expected. Again small areas of SLC5A6 staining can be observed, however at CS19, this appears more pronounced in the myocardial and epicardial layer (Figure 3.3C-D), when compared to staining at CS14 (Figure 3.2C-D). Staining should be repeated to confirm initial findings.

Additionally, SLC5A6 expression was confirmed within the cerebellum (Figure 3.3G), specifically within the inner granular layer (Figure 3.3H). SLC5A6 was also confirmed to be expressed within the gut (Figure 3.3I), with strong staining shown within the LM at CS19 (Figure 3.3J).

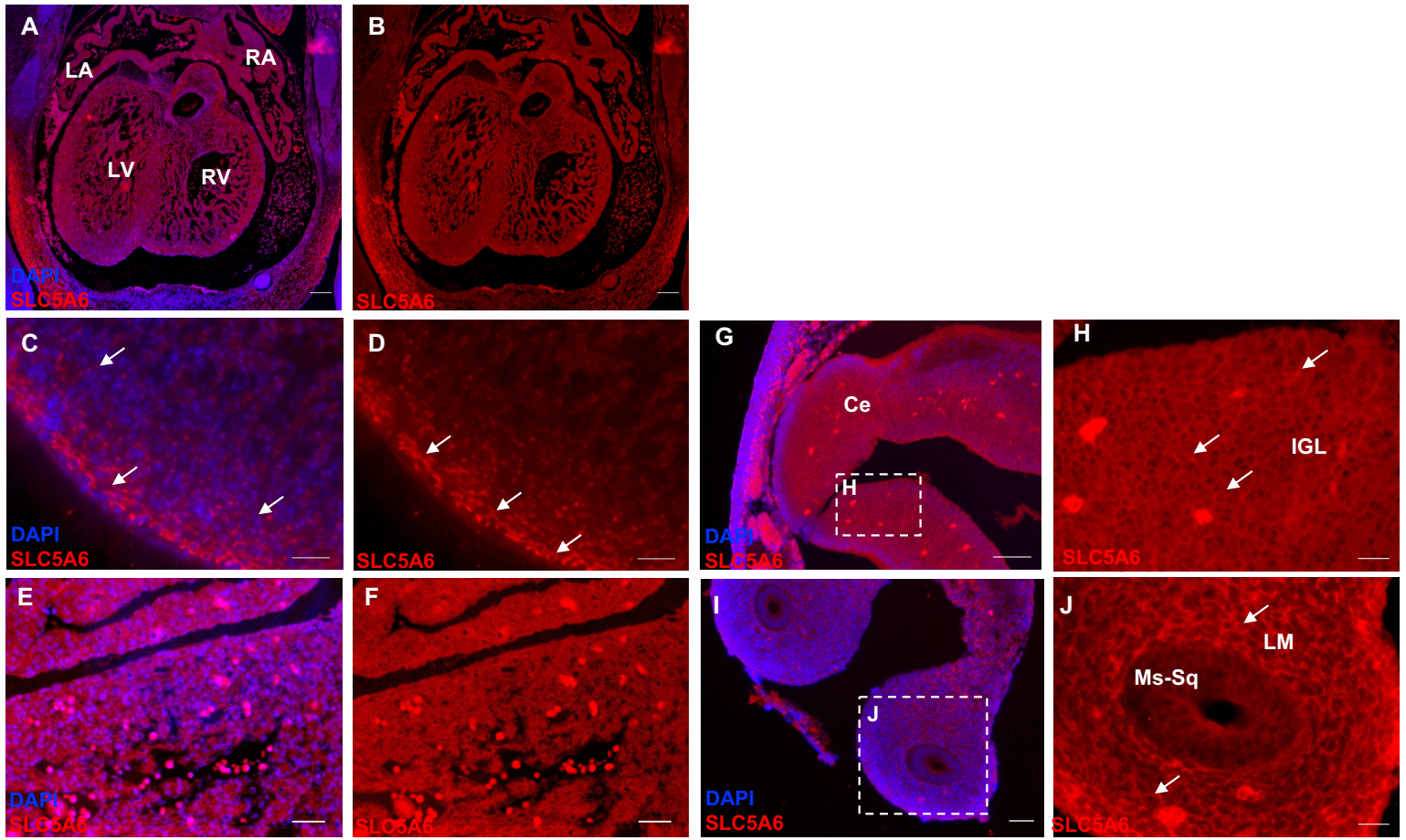

Figure 3.3. Detection of SLC5A6 expression in human tissues at CS19.
Human embryonic sections stained with SLC5A6 antibody (red), nuclei stained with DAPI (blue). A-B) Some evidence of SLC5A6 staining is present within the heart at CS19. Higher magnification suggests evidence of SLC5A6 expression within the myocardial and epicardial layer (C-D) indicated by arrows. G-H) Expression was also confirmed throughout the cerebellum (G), specifically within the IGL (H). I-J) SLC5A6 was also confirmed within the gut (I), with strong membranal expression within the LM (J). E-F) No primary control images of heart. LA left atria, RA right atria, Ce cerebellum, IGL inner granular layer, LM lamina propria, Mc-Sq squamous cell mucosae, LV left ventricle, RV right ventricle. *n* = 1 for each tissue stained. Scale bar =100μm (A,B,E,G), 50μm (C), 20μm (D,F,H).

By CS23 all the major structures of the heart are complete, including ventricular septation which occurs last. At this stage of cardiac development, the expression of SLC5A6 continues to be low throughout the heart (Figure 3.4A-B). The potential expression pattern observed at the myocardial and epicardial layers at CS19 does not appear to be replicated at CS23. Higher magnification of the upper ventricle suggested some positive staining within the trabeculae layer (Figure 3.4C) and myocardium (Figure 3.4D) but not as pronounced as staining shown at CS19 (Figure 3.2C-D).

At CS23, the myelencephalon continues to show SLC5A6 expression (Figure 3.4G-H), with staining present at the purkinje layer (Figure 3.4H). SLC5A6 also continues to be expressed within the gut (Figure 3.4E-F); however, expression appears to become localised to the Ms-Sq (Figure 3.4F), where nutrients will be absorbed through the internal membrane.

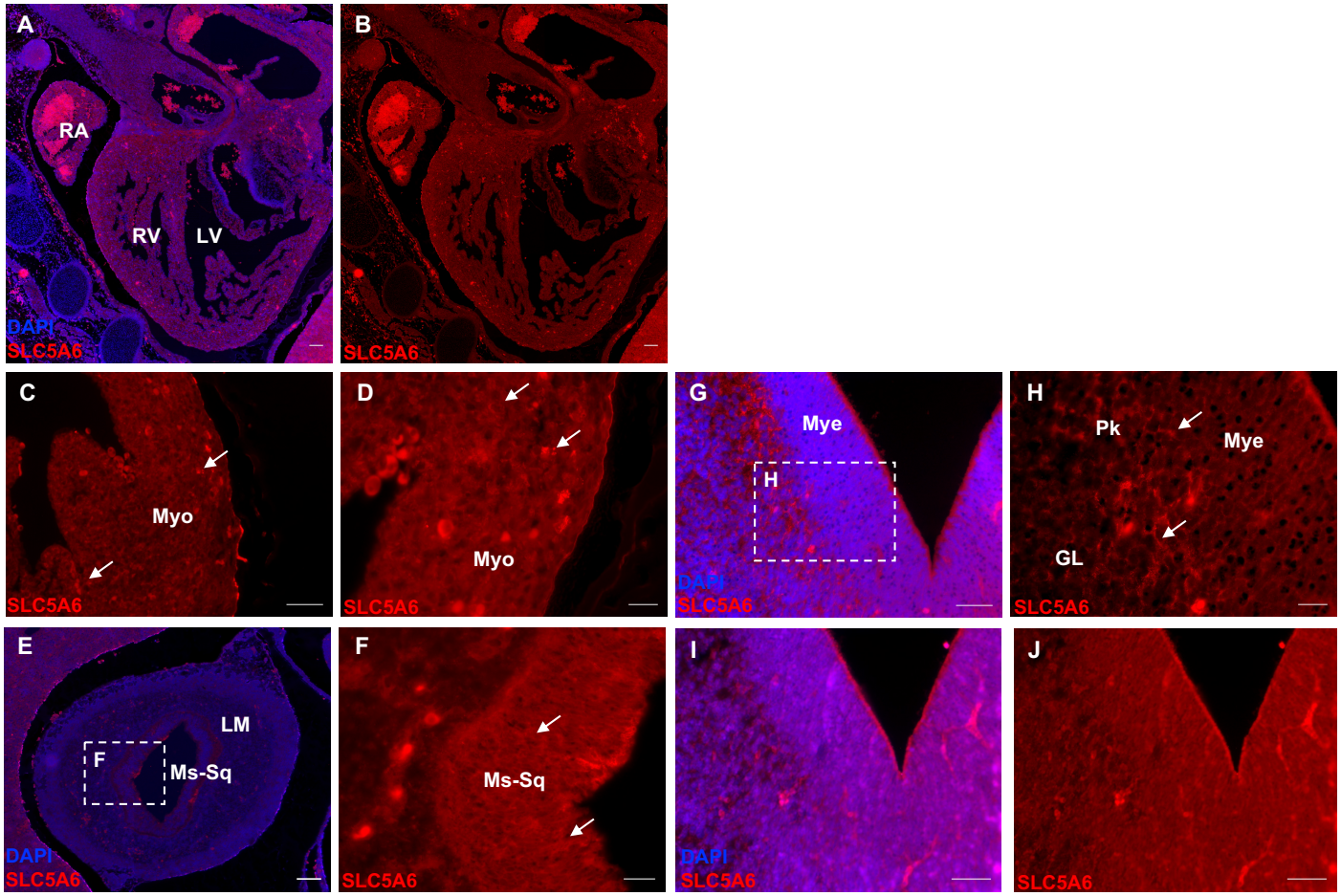

Figure 3.4. IHC to detect SLC5A6 in brain, heart and gut at CS23.
SLC5A6 (red) staining of human embryonic sections, nuclei stained with DAPI (blue). A-B) Some level of SLC5A6 staining may be observed within the heart. Higher magnification also suggests some positive staining at the myocardium (C,D). E-F) SLC5A6 staining in the gut, with strong membrane staining within the Ms-Sq layer (F). G-H) SLC5A6 expression in the brain, specifically at the Pk layer between the Mye and GL (H) indicated by arrows. I-J) No primary control image of brain. RA right atria, C cerebellum, GL granular layer, LM lamina propria, Mye myelencephalon, Myo myocardium, Ms-Sq squamous cell mucosae, Pk purkinje layer, LV left ventricle, RV right ventricle. *n* = 1 for each tissue stained. Scale bar = 100μm (A,B,G), 50μm (E,H), 20μm (D,F).

From the investigation into SLC5A6 expression in developing human embryos, preliminary experiments performed in this study have suggested that *SLC5A6* is expressed at CS13 and CS17 by RT-PCR. In addition, initial investigation into expression within the heart by IHC at CS14, CS19 and CS23 revealed inconsistent findings relating to the expression of cardiac SLC5A6. From this, it is suggested further investigation should be performed to increase the number of sections included in the analysis in addition to use of alternative techniques such as *in-situ* hybridisation, to determine the localisation of SLC5A6 within the developing human heart.

3.3 *Slc5a6* expression throughout murine cardiac development

Following the novel investigation into SLC5A6 expression within human cardiac development, the expression pattern of *Slc5a6* was established in murine cardiac development.

3.3.1 Slc5a6 expression within different murine cell types

In the human heart, SLC5A6 was clearly expressed within the cell membrane of cells within the myocardium. To establish if Slc5a6 is expressed specifically in the cardiomyocytes, the mouse model was used as this allowed the isolation the cardiomyocyte population. To do this a *TnTCre;YFP*$^{+/F}$ mouse line was utilised which fluorescently labels cardiomyocytes through *Cre*-mediated eYFP expression. Embryos were harvested at E10.5 and cells were dissociated from the heart and flow-sorted via fluorescence-activated cell sorting (FACS). Cardiac cells positive (+) for eYFP represent cardiomyocyte cell populations and the negative (-) population contain non-cardiomyocyte mixed cell types including cardiac fibroblasts, epicardial and endocardial cells. At E10.5, *Slc5a6* is expressed in the whole heart and appears to be expressed in both the cardiomyocytes and non-cardiomyocyte cardiac cells; however, this appears reduced in both cell samples (**Figure 3.5**). This may be due to the contribution of multiple cell types found within the developing heart such as endothelial cells, smooth muscle cells and atrial cardiomyocytes, which may represent the remaining Slc5a6 expression level observed in the whole heart cDNA collected from E10.5 embryos.

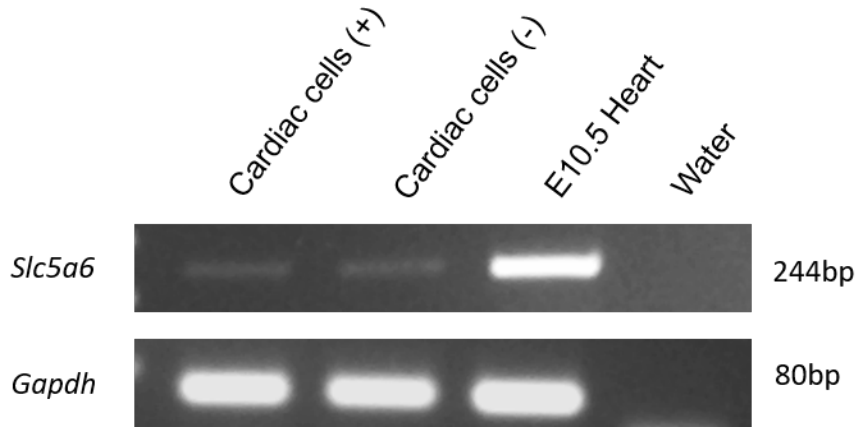

Figure 3.5. *Slc5a6* is expressed throughout the heart at E10.5.
Slc5a6 was faintly detected in E10.5 cardiac cells (+) (cardiomyocyte population) and (-) (non-cardiomyocyte population) compared to strong expression observed in E10.5 whole heart cDNA. *Gapdh* was used as a housekeeping gene.

As *Slc5a6* was detected in the whole heart at E10.5, it was important to establish if expression persisted through cardiac development, and if the expression altered depending on metabolic requirements of the heart.

3.3.2 Slc5a6 is expressed throughout murine cardiac development

Following the confirmation that *Slc5a6* is expressed in the early developing murine heart at E10.5, and to establish any changes in the requirement of *Slc5a6* during maturation of the heart, a cDNA developmental series from E13.5 to adulthood was used. qRT-PCR was performed to quantitatively determine if *Slc5a6* expression alters at any stage of development, which may help to infer its function within the heart using the developmental stages described. Ct values and primer efficiency for each gene of interest investigated are summarised in Table 3.1. All data was normalised to *Gapdh* and relative to E13.5. The Ct values for *Gapdh* for each biological group were E13.5 = 15.72±0.098, E17.5 = 16.11±0.123, P0 = 16.18±0.211, P6 = 15.38±0.100 and adult = 17.44±0.206 (n = 3 with 27 technical replicates). Slc5a6 expression was found to significantly decrease during the cardiomyocyte proliferation and cardiac chamber growth stage, from E13.5 compared to E17.5 (p<0.0001) and P0 (p<0.0001). Expression levels are also significantly decreased at P6 (p<0.0001) and in adulthood (p<0.0001); however, there is a slight increase in *Slc5a6* expression after the first week of life which persists into adulthood (Figure 3.6).

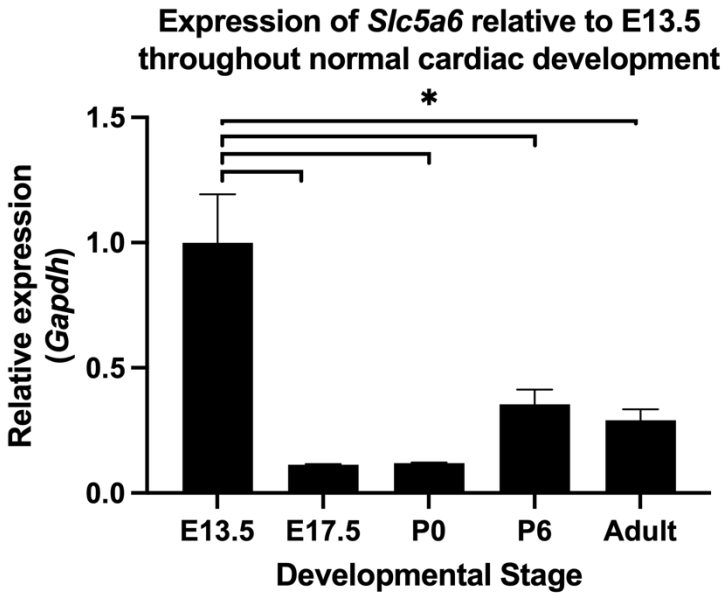

Figure 3.6. *Slc5a6* is expressed throughout murine embryonic and postnatal cardiac development.

qRT-PCR was performed on wild type whole heart cDNA collected at various developmental ages during embryogenesis through to adulthood. The data shows *Slc5a6* expression decreases from E13.5 to E17.5 and remains significantly decreased throughout postnatal life. However, over the first postnatal week of life *Slc5a6* expression appears to increase, maintaining the level of expression into adulthood. Data was analysed using comparative Ct ($2^{-\Delta\Delta ct}$) normalised to *Gapdh* expression, relative to E13.5 data. One-Way ANOVA with multiple comparisons and Bonferroni correction was performed, * = <0.05, *n* = 3 hearts.

3.4 Energy metabolism during murine cardiac development

As *Slc5a6* transports substrates essential for energy metabolism, including glycolysis and oxidative phosphorylation (OXPHOS) pathways, the expression pattern of genes involved in mitochondrial biogenesis and energy metabolism pathways were investigated during development.

3.4.1 Expression of genes involved in energy metabolism during development

To map the expression of genes related to these pathways, qRT-PCR was performed on the murine cardiac developmental series as described above. This included genes involved in mitochondrial biogenesis (Figure 3.7), mitochondrial regulation (Figure 3.8), OXPHOS (Figure 3.9), as well as genes involved in glycolysis, β-oxidation and fatty acid synthesis and transport (Figure 3.10). It is known that during early embryogenesis, embryonic stem cells rely on ATP sourced from glycolysis rather than OXPHOS (Folmes *et al.*, 2011). As embryonic stem cells differentiate, the mitochondrial copy number increases prompting mitochondrial biogenesis (Facucho-Oliveira and St. John,

2009). This provides support for the metabolic switch from anaerobic (glycolytic) energy production to aerobic metabolism (OXPHOS) following birth.

Mitochondrial biogenesis and dynamics play an essential role in mitochondrial function and their ability to adapt to the changing metabolic environment. The expression of *Mfn1,* a mitofusin protein which mediates mitochondrial fusion; the joining of two mitochondria to form one entity, at the outer mitochondrial membrane (OMM). *Mfn1* expression is shown to remain relatively constant throughout embryogenesis through to P0; however, following birth a significant increase is seen in *Mfn1* expression postnatally at P6 compared to E13.5 ($p<0.0001$), E17.5 ($p<0.0001$) and P0 ($p<0.0001$). *Mfn1* expression continues to significantly increase as shown in the adult heart compared to all developmental stages ($p<0.0001$) (Figure 3.7.A). This correlates with findings by Papanicolaou *et al.* (2012) who showed an increase in *Mfn1* and *Mfn2* expression during postnatal cardiac growth and maturation allowing mitochondria to develop elongated morphologies to create dynamic networks throughout the heart. *Tfam* is a mitochondrial transcription factor involved in the maintenance of mitochondrial DNA (mtDNA) and regulation of glycolytic pathway (Araujo *et al.*, 2018). In this analysis, expression of *Tfam* (blue), similar to *Mfn1*, remains constant during embryogenesis and following birth levels significantly increase in the first week of postnatal life at P6 compared to embryogenesis ($p<0.0001$) during which a shift in metabolic pathways occurs (Figure 3.7.B). Expression of *Tfam* then significantly decreases to the same levels observed during embryogenesis ($p<0.0001$), once heart development is complete. It was also determined that the expression pattern of *Ulk1*, a gene known to be essential for the formation of the autophagosome in the autophagy pathway (Zachari and Ganley, 2017). Very low levels of expression of *Ulk1* (green) were observed during embryogenesis, with data showing a trend towards increased expression at P6 followed by a reduction in adulthood; however, no significant difference was observed between each developmental stage (Figure 3.7.C). This data suggests that the regulation of mtDNA copy number occurs at a proportional rate to autophagy during early postnatal cardiac development.

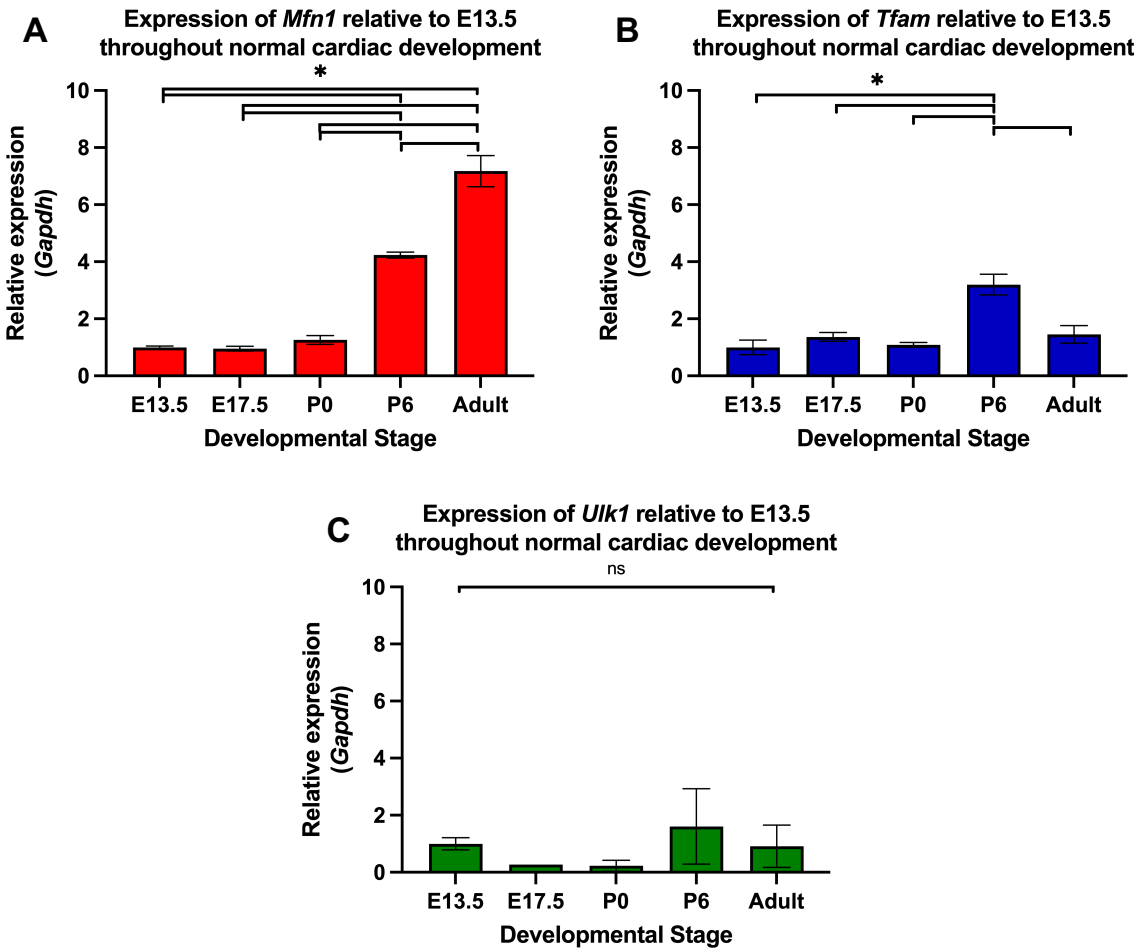

Figure 3.7. Mitochondrial biogenesis gene expression increases following birth. qRT-PCR data of wild type whole heart cDNA collected at various developmental ages. A) *Mfn1* expression is relatively low during embryogenesis through to birth (E13.5-P0); however, expression significantly increases postnatally at P6 and again in adulthood. B) *Tfam* expression remains consistent during embryogenesis to birth, with a significant increase at P6 which then significantly decreases to embryonic levels in adulthood. C) *Ulk1* expressions levels are remain low during embryogenesis and following birth, with no significant changes observed in this dataset. Data was analysed using comparative Ct ($2^{-\Delta\Delta ct}$) normalised to *Gapdh* expression, relative to E13.5 data. One-Way ANOVA with multiple comparisons and Bonferroni correction was performed, ns no significance, * = <0.05, *n* = 3 hearts.

In addition to investigating mitochondrial biogenesis, determination of the expression of key regulatory genes was carried out including *Klf4* (Figure 3.8.A), *Pparα* (Figure 3.8.B) and *Ppargc1α* (Figure 3.8.C). *Klf4* is a transcription factor which has been linked to the regulation of mitochondrial biogenesis and homeostasis by forming a complex with other regulatory genes including *Ppargc1α* shown by Liao *et al.* (2015). Here it is shown that *Klf4* (red) is expressed during embryogenesis and the early formation of the heart from E13.5 to P0 (Figure 3.8.A). As expected, *Klf4* expression increases to a similar level seen in mitochondrial biogenesis markers following birth at P6 compared to E13.5 (*p*=0.0014), E17.5 (*p*=0.0009) and P0 (*p*=0.0009), and remains significantly

increased into adulthood in comparison to E13.5 (p=0.0057), E17.5 (p=0.0035) and P0 (p=0.0037) expression levels. A similar expression pattern is also noted for *Ppargc1α* (green), the master regulator of mitochondrial biogenesis, with a significant increase in expression from E13.5 to E17.5 (p=0.0399) with another significant increase in expression observed postnatally at P6 and in adulthood compared to E13.5, E17.5 and P0 (p<0.0001) (Figure 3.8.C). However, these results contradict findings by Lehman *et al.* (2000), who report very high levels of *Ppargc1α* at birth P0 and in adulthood. However, they also note the same high levels of expression of *Pparα,* a key regulator of FA synthesis and known interactor of *Ppargc1α,* whereas a significant increase in *Pparα* expression was observed in adulthood when compared to E13.5 (p=0.0095) (Figure 3.8.B). This may be due to differences in experimental investigation as Lehman *et al.* (2000) detected expression using Northern blot rather than qRT-PCR as described here.

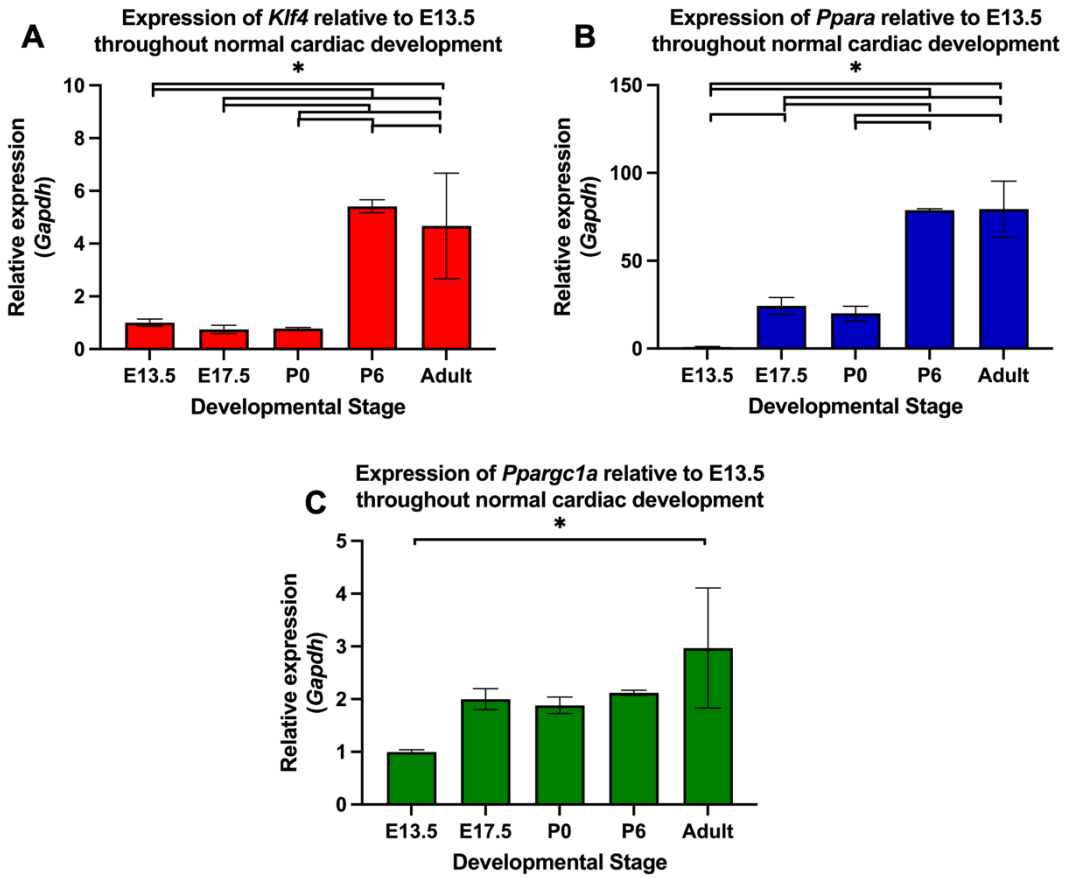

Figure 3.8. Increased expression of mitochondrial regulatory genes following birth.
qRT-PCR data of mitochondrial regulatory genes throughout a cardiac developmental series. A) *Klf4* has a low expression profile during embryogenesis and immediately following birth. Postnatally, expression of *Klf4* significantly increases. B) Expression of *Ppara* is significantly upregulated to similar levels at E17.5 and P0; however, has a second significant increase in expression postnatally at P6 and adult. C) *Ppargc1a* expression is significantly increased in adulthood compared to E13.5, with a plateau in expression from late embryogenesis to early postnatal stages. Data was analysed using comparative Ct ($2^{-\Delta\Delta ct}$) normalised to *Gapdh* expression, relative to E13.5 data. One-Way ANOVA with multiple comparisons and Bonferroni correction was performed, * = <0.05, *n* = 3 hearts.

One of the largest ATP yielding processes to occur within the mitochondria is OXPHOS. This process comprises an electron transport chain made up of four complexes with an ATP synthase at the terminus of the pathway. This chapter has investigated the expression of mitochondrial encoded (mt) complexes *Nd1* (complex I), *Cytb* (complex III), *Co2* (complex IV) and *Atp6* (ATP synthase), which are known to form super complexes, as an indication of OXPHOS capacity throughout normal cardiac development and maturation (Figure 3.9). *mtND1* encodes complex I of the ETC, known as the NADH:ubiquitone oxidoreductase. This complex oxidises NADH

from the TCA cycle, the initial step in generating proton motive force throughout the ETC to ultimately produce ATP (Sharma *et al.*, 2009). This data shows that as the heart develops during embryogenesis and early postnatal life *mtND1* expression builds until maturation is complete in adulthood where there is a significant increase compared to E13.5 (p=0.0003), E17.5 (*p*=0.0011), P0 (*p*=0.0031) and P6 (*p*=0.0017) (Figure 3.9.A). This expression profile is also observed for complex III*,* where *mt-Cytb* expression is significantly increased in adulthood compared to early postnatal stages P0 (*p*=0.0051), as well as embryogenic stages E17.5 (*p*=0.0076) and E13.5 (*p*=0.0035) (Figure 3.9.B). Complex IV is one of the most important complexes within the ETC as it transfers electrons to the terminal electron acceptor (oxygen) to generate H_2O, whilst contributing protons to the PMF for ATP production at complex V (ATP synthase). Here a significant increase is observed in *mtCo2* expression in adulthood compared to E13.5 (*p*=0.0008), E17.5 (*p*=0.0101), P0 (*p*=0.0378) and P6 (*p*=0.0292) once cardiomyocyte maturation and the metabolic switch to OXPHOS has completed (Figure 3.9.C). Finally, investigation into the terminal complex V of OXPHOS pathway, ATP synthase, revealed 5-fold increase in gene expression in adulthood compared to all early developmental stages; E13.5 (*p*=0.0002), E17.5 (*p*=0.0002), P0 (*p*=0.0004), P6 (*p*=0.0013) (Figure 3.9.D). As expected, this building gene expression profile of OXPHOS complexes is indicative of the metabolic switch from glycolytic energy production during embryogenesis and birth, to OXPHOS dependent energy production over the first week of life which becomes established in adulthood.

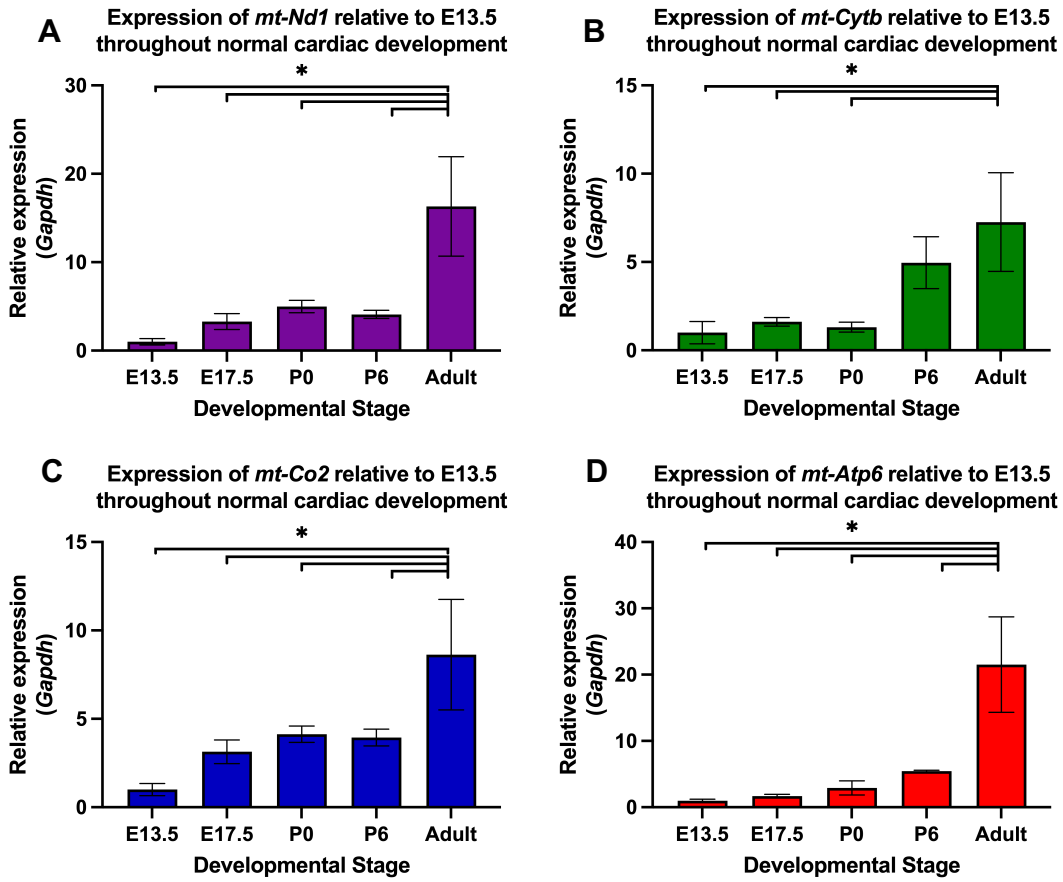

Figure 3.9. OXPHOS gene expression increases into adulthood.
A developmental series was used to determine gene expression during embryogenesis through to adulthood. A) The expression of *mtNd1* is shown to significantly increase in adulthood compared to early postnatal and embryogenic stages. B) *mtCytb* expression show a trend towards an increase following birth which becomes significant into adulthood. C) *mtCo2* expression trends towards increased expression during late embryogenesis, which is sustained following birth into early postnatal life, however, significantly increases into adulthood. D) Expression of the final complex V, *mtAtp6,* shows the same trend towards increased expression during development before a significant increase in expression in adulthood. Data was analysed using comparative Ct ($2^{-\Delta\Delta ct}$) normalised to *Gapdh* expression, relative to E13.5 data. One-Way ANOVA with multiple comparisons and Bonferroni correction was performed, * = <0.05, *n* = 3 hearts.

Once the fetus is born the environment changes from hypoxic to normoxic, with increased atmospheric oxygen prompting a change from glycolysis to FA β-oxidation as a source of energy via OXHOS. Here the expression of genes involved in fatty acid uptake (*Lpl*), transport (*Cpt2*) and β-oxidation (*Acadvl*), as well as the glycolytic master regulator (*Hif1a*) is investigated (Figure 3.10). The resulting data correlates with this pathway and shows following birth *Acadvl* expression significantly increases at P6 compared to developmental stage E13.5 (p=0.0021), E17.5 (p=0.0038) and P0 (p=0.0010) (Figure 3.10.A). Although a trend is observed towards decreased expression in adulthood compared to P6, the expression level in adulthood is

significantly increased compared to E13.5 (p=0.0412). *Lpl* encodes the lipoprotein lipase protein which acts to hydrolyse circulating triglycerides and plays an important role in receptor-mediated FA uptake (Weinstock *et al.*, 1995; Goulbourne *et al.*, 2014). Within this dataset, *Lpl* expression is low during embryogenesis, as the heart utilises glucose for energy metabolism, however, following birth there is a trend towards increased expression which peaks in adulthood with significant upregulation compared to E13.5 (p=0.0008), E17.5 (p=0.001) and P0 (p=0.003) (Figure 3.10.B). In addition to FA uptake, the expression of genes involved in mediating FA transport into mitochondria was determined, including *Cpt2* which encodes carnitine palmitoyl transferase 2 located on the IMM and with *Cpt1* forms the CPT complex for transport of FAs from the cytosol into the mitochondrial matrix. It was hypothesised that as the dependency of FA as a source of energy metabolism increases, genes involved in FA transport would increase to mediate β-oxidation. The data correlates with this hypothesis and shows that *Cpt2* expression significantly increases postnatally at P6 compared to E13.5 (p=0.0009), E17.5 (p=0.0016) and P0 (p=0.0044) (Figure 3.10.C). Expression remains significantly increased in adulthood in comparison to E13.5 (p=0.001), E17.5 (p=0.0019) and P0 (p=0.005) levels. As an overall increase in β-oxidation gene expression was observed following birth, a decrease in *Hif1a* was predicted (Figure 3.10.D). In fact, the data shows expression of *Hif1a* is low during embryogenesis at E13.5 and significantly decreases further at E17.5 (p<0.0001) and P0 (p<0.0001) when glycolysis is reported to be the main source of energy metabolism within the proliferative stage of heart development (Lopaschuk *et al.*, 1991; Lopaschuk and Jaswal, 2010). At P6 a significant increase was observed in *Hif1a* expression compared to E17.5 (p<0.0001) and P0 (p<0.0001) when glycolysis was expected to be decreased following the completion of the metabolic switch. In adulthood, *Hif1a* expression is significantly downregulated compared to E13.5 (p<0.0001) and P6 (p=0.0003). This *Hif1a* data contradicts many studies which investigate energy metabolism during embryogenic and postnatal cardiomyocyte maturation; however, these studies also determine gene expression of many genes involved in each process and therefore, future work should aim to repeat *Hif1a* gene expression and look at expression of alternative indicators of glycolysis such as *Ldha* and *Glut1*.

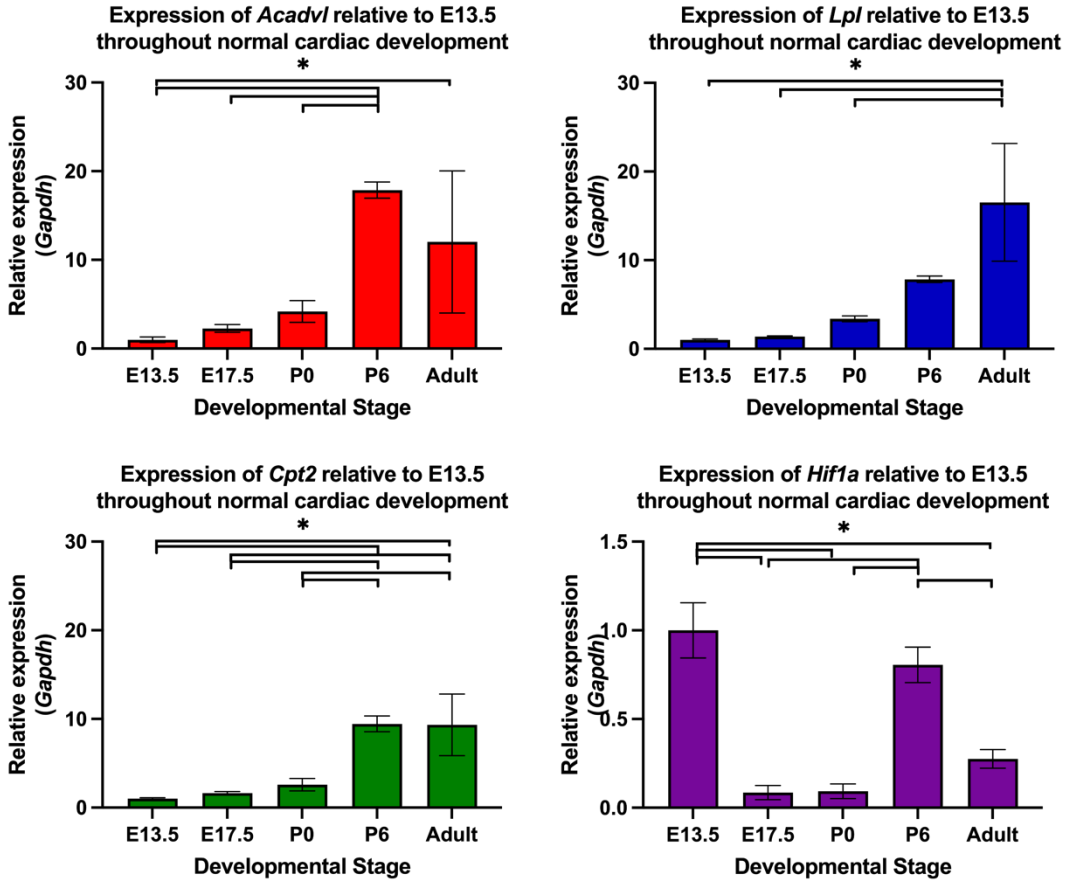

Figure 3.10. Genes involved in B-oxidation increase postnatally whereas glycolysis marker decreases in adulthood.
qRT-PCR performed on whole heart cDNA collected at developmental stages during embryogenesis through to adulthood. A) β-oxidation marker *Acadvl* expression is significantly upregulated at postnatal ages compared to expression during embryogenesis. B) Expression of FA uptake marker *Lpl* has an incremental trend towards significantly increased expression in adulthood as reliance on glucose as an energy source shifts towards FA. C) FA transport also significantly increases postnatally at P6 and in adulthood compared to expression during embryogenesis. D) The regulator of glycolysis *Hif1a* shows low expression throughout development with a significant decrease in expression at E17.5 and P0. Expression then significantly increases postnatally at P6 followed by a significant decrease in adulthood. Data was analysed using comparative Ct ($2^{-\Delta\Delta ct}$) normalised to *Gapdh* expression, relative to E13.5 data. One-Way ANOVA with multiple comparisons and Bonferroni correction was performed, * = <0.05, *n* = 3 hearts.

Here, it has been determined that *Slc5a6* is expressed throughout murine cardiac development both embryonically and during postnatal development, however, expression is low compared to gene expression for key genes in mitochondrial biogenesis, regulation and OXPHOS relative to expression levels at E13.5. This suggests *Slc5a6* may not be a pre-requisite for any changes to energy metabolism within the developing heart.

Table 3.1. Summary of Ct values and primer efficiencies for each gene of interest investigated by qRT-PCR.
For each gene of interest, the Ct values are shown (mean±SEM) for each developmental stage. The primer efficiencies (%) are shown below each gene of interest.

Stage	*Gapdh* (97%)	*Mfn1* (100%)	*mtAtp6* (100%)	*mtCytb* (94%)	*mtCo2* (100%)	*Acadvl* (98%)	*Lpl* (97%)	*Gapdh* (97%)	*Klf4* (97%)	*Ppara* (86%)	*Pparg c1a* (99%)	*mtNd1* (94%)	*Cpt2* (100%)	*Tfam* (96%)	*Gapdh* (97%)	*Hif1a* (98%)	*Slc5a6* (91%)	*Ulk1* (100%)
E13.5	15.536 ±0.105	23.181 ±0.135	15.193 ±0.233	28.853 ±0.570	16.770 ±0.343	22.584 ±0.278	21.190 ±0.156	15.821 ±0.184	26.660 ±0.281	31.414 ±0.324	24.463 ±0.212	15.442 ±0.432	24.474 ±0.261	25.071 ±0.210	15.817 ±0.209	20.748 ±0.226	24.942 ±0.245	24.487 ±0.051
E17.5	16.366 ±0.180	24.079 ±0.138	15.257 ±0.279	28.817 ±0.268	15.920 ±0.331	22.205 ±0.224	21.557 ±0.173	16.088 ±0.281	27.365 ±0.434	27.085 ±0.223	23.735 ±0.269	13.971 ±0.053	24.023 ±0.304	24.863 ±0.353	15.869 ±0.087	24.426 ±0.444	28.127 ±0.105	26.408 ±0.089
P0	16.274 ±0.426	23.593 ±0.364	14.421 ±0.479	29.0369 ±0.323	15.413 ±0.479	21.252 0.192	20.170 ±0.488	16.215 ±0.452	27.411 ±0.412	27.493 ±0.282	23.947 ±0.485	13.473 ±0.352	23.532 ±0.299	25.312 ±0.505	16.049 ±0.370	24.481 ±0.674	28.226 ±0.347	26.318 ±0.794
P6	15.319 ±0.335	20.880 ±0.214	12.506 ±0.172	26.187 ±0.092	14.527 ±0.192	18.166 0.158	17.996 ±0.203	15.586 ±0.147	23.981 ±0.118	24.866 ±0.154	23.143 ±0.162	13.124 ±0.105	20.997 ±0.196	23.133 ±0.197	15.225 ±0.163	20.463 ±0.157	25.843 ±0.110	22.705 ±0.202
Adult	17.169 ±0.572	21.972 ±0.513	12.425 ±0.297	27.520 ±0.905	15.313 ±0.885	20.914 ±1.290	18.864 ±0.927	17.712 ±0.297	26.402 ±0.597	27.001 ±0.328	24.850 ±0.114	13.317 ±0.304	23.199 ±0.045	26.415 ±0.199	17.446 ±0.137	24.244 ±0.269	28.348 ±0.096	25.869 ±0.204

3.5 Discussion

Mutations in *SLC5A6* (SMVT) were identified as a potential cause of cardiomyopathy in the siblings described in 1.3;however, there is very little known about the expression of *Slc5a6* in the heart. Prasad *et al.* (1998) first reported *Slc5a6* expression in rat across many tissues by Northern blot, showing faint expression in the heart. This was repeated by Wang *et al.* (1999a) investigating *SLC5A6* expression in human tissues, and a similar level of expression in the heart was observed. To date, only one group have shown Slc5a6 to be expressed within the mouse heart; however, the study focused on expression levels during the circadian cycle in 12-16wk old mice (He *et al.*, 2016b). Therefore, this chapter aimed to determine the expression pattern of *Slc5a6* during murine cardiac development and to confirm *SLC5A6* expression throughout human heart development, to enable investigation into *SLC5A6* as a novel cause of cardiomyopathy.

Preliminary data shown in this chapter showed some evidence of SLC5A6 expression at CS13-14, CS17/19 and CS23 in cardiac development by IHC as well as RT-PCR. *SLC5A6* expression was identified during cardiac looping at CS13 and following septation at CS17 by RT-PCR. Interestingly, *SLC5A6* was not found in adult fibroblasts; however, was strongly expressed in adult myoblasts contrary to findings by Wang *et al.* (1999a) who showed a faint expression of *SLC5A6* in human skeletal muscle by Northern blot analysis. Following this, this study planned to investigate the protein expression of SLC5A6 in human developmental stages by IHC. However, due to the limited supply of human developmental tissue a thorough investigation of SLC5A6 at every stage of human cardiac development was not possible and therefore only three stages were studied, CS14, CS19 and CS23 (n = 1). Previous studies have shown that *Slc5a6* is strongly expressed within the brain and gut (Chatterjee *et al.*, 1999; Wang *et al.*, 1999a; Uchida *et al.*, 2015) and therefore sections of these tissues were included as positive controls. SLC5A6 staining was apparent in both brain and gut across all developmental stages examined. However, within the heart sections SLC5A6 staining was found to be inconsistent across the developmental stages with very little staining observed at CS14 and CS23. At CS19, SLC5A6 antibody staining shows some localised expression at the epicardium. *SLC5A6* expression was also shown in cDNA from whole hearts at CS17. From this initial data, it is possible to

suggest that there may be a requirement for biotin, PA and LA transport within the cardiomyocytes at CS17. As the images from the IF data showed an inconsistent pattern of SLC5A6 expression, future studies should aim to increase the number of human developmental sections used for SLC5A6 IF. Alternatively, *in situ* hybridisation techniques could be adopted, such as RNAscope, to identify RNA transcripts within cardiac sections which could then be quantified (Wang *et al.*, 2012). Future work could also involve investigation into the expression of conduction markers such as connexins, to determine if the expression of SLC5A6 co-localises with conductive cells within the heart.

Investigation into *Slc5a6* expression within murine development relied solely upon expression at the RNA level. This was due to the non-specific staining of available Slc5a6 antibodies on mouse tissue.

In this chapter, it has been shown that *Slc5a6* is strongly expressed in E10.5 whole heart RNA, however, FACS cardiac cells showed faint expression in cardiomyocyte and non-cardiomyocyte cell populations. This may be due to cell death during the protocol or the contribution of multiple cell lineages within the whole heart. A transcriptome study performed by Litviňuková *et al.* (2020) investigated the cellular composition of the human adult heart, and found differing levels of cellular composition between the atria and ventricles. The atria contain a lower percentage of cardiomyocytes (~30%) compared to 50% in the ventricles; however, the atria have a higher percentage of fibroblasts (24%) compared to ~15% in the ventricles. They also found 17-21% were mural cells (pericytes and smooth muscle cells), 7-12% were endothelial cells and 5-10% were immune cell contribution. Therefore, the lower *Slc5a6* expression detected in isolated cardiomyocyte and non-cardiomyocyte populations could be decreased compared to the multiple cell contribution of the whole heart. This suggests Slc5a6 may also be expressed in other cell lineages such as smooth muscle cells or endothelial cells. Further work should be performed to comprehensively determine *Slc5a6* expression throughout the major cell types which contribute to the cardiac structure and function. To extend this analysis, qRT-PCR was performed using whole heart cDNA from a developmental series from control mice to determine if the level of *Slc5a6* changes throughout normal cardiac development. For all qRT-PCR primer sets, DART-PCR was used to determine the efficiency of primers used, which were >86%. Using the *Slc5a6* pairs (91%) the relative levels of *Slc5a6*

expression throughout murine cardiac development was investigated from E13.5 to adulthood. This revealed that *Slc5a6* levels decreased as the myocardium becomes more compact during embryogenesis and at birth. This contradicted the hypothesis, that as cardiomyocytes proliferated and mitochondrial biogenesis increased, *Slc5a6* would be expressed to enable vitamin transport across the plasma membrane of cardiomyocytes to contribute to energy production. Interestingly a metabolic profiling study performed by Patel *et al.* (2017) also showed low levels of *Slc5a6* expressed in adult mice relative to *Gapdh*. They performed qRT-PCR in livers rather than hearts, however, again it is expected that the expression of Slc5a6 should be high in the liver as it stores vitamins and other sources of energy metabolism from the circulation and therefore the vitamin transport should be needed for transport into hepatocytes. This expression profile of *Slc5a6* within the liver is also observed in data published by Ghosal *et al.* (2012). As there are no other studies looking into the expression of *Slc5a6* within the mouse heart during development it is possible *Slc5a6* is not required during cardiomyocyte proliferation and therefore expression remains low. Once born, *Slc5a6* expression showed a trend towards increasing to similar levels observed at E13.5, suggesting environmental changes occurring at birth affect *Slc5a6* expression levels within the heart. One of the major changes to affect offspring at birth, is the increase in haemodynamic load prompting a switch from glycolytic ATP production to β-oxidation via OXPHOS.

As *Slc5a6* is responsible for the transport of essential substrates required for energy metabolism and homeostasis, this chapter also looked at determining the expression of energy metabolism markers and mitochondrial biogenesis throughout normal murine cardiac development to help determine *Slc5a6* in relation to the metabolic switch.

During early development, the number of mitochondria are low, immature and do not provide much oxidative capacity (Morita Y, 2020). However, during the cardiomyocyte proliferative stage, mitochondrial number increases to one third of the cardiomyocyte cell volume along with maturation, giving rise to an increase in oxidative capacity. From this, it was expected expression of *Hif1a*, which regulates the activation of genes involved in glycolysis, should be high during the early stages of embryogenesis as the bulk of ATP produced is generated by glycolysis (Dengler *et al.*, 2014; Cerychova and Pavlinkova, 2018; Morita Y, 2020). However, low levels of expression were observed,

with a significant decrease at E17.5 and P0. Alternatively, *Gapdh* data could be used to indicate the glycolytic state of the control hearts. The Ct values shown in Table 3.1 seem to indicate *Gapdh* expression decreases postnatally into adulthood, which correlates with a decrease in glycolytic dependency as the switch to OXPHOS occurs. Additionally, Breckenridge *et al.* (2013) have shown that another transcription factor controls the metabolic switch from glycolysis to OXPHOS, *Hand1,* which is regulated by the expression of *Hif1a.* Therefore, to further investigate the metabolic switch in murine cardiac development *Hand1* expression could also be investigated to compliment the changes observed in *Gapdh* expression.

Throughout the later stages as embryos near birth, levels of lactate and FA oxidation increase as shown in Figure 1.2, therefore it is hypothesised that genes involved in aerobic respiration should increase based on energy demand and mitochondrial maturity, causing a switch in the energy production pathway towards OXPHOS (de Carvalho *et al.*, 2017; Morita Y, 2020). This investigation into the normal expression of OXPHOS complexes revealed a similar expression profile of complex I (*mtNd1*), complex III (*mtCytb*) and complex IV (*mtCo2*) where expression increases postnatally with significantly increased expression in adulthood. This follows the expected pattern described, whereby mitochondrial biogenesis increases as the myocardium thickens due to cardiomyocyte proliferation, in preparation for an increase in haemodynamic load, switching energy production from glycolysis to oxidative phosphorylation following birth (Facucho-Oliveira and St. John, 2009; Morita Y, 2020). Further evidence to support this increase in mitochondrial biogenesis is provided within this chapter as biogenesis and proliferation markers *Mfn1* and *Tfam* are upregulated during postnatal maturation. Studies from Lopaschuk *et al.* (1991) and de Carvalho *et al.* (2017) investigated cardiac metabolism at P1 compared to P7 in rabbits and rats, respectively. They showed immediately following birth glycolysis is still the main ATP production pathway, although ATP production by OXPHOS is apparent. At P7 they both show OXPHOS takes over as major contributor by glucose, lactate or palmitate (FA) as the initial substrate, with low levels of glycolysis present. From the experiments in this chapter, it is noted that the expression of *Hif1a* is low throughout early development; however, expression slowly increases and peaks at postnatally before decreasing in adulthood. Mitochondrial gene expression is reduced at birth, but gradually increases in the first week of life and in adulthood which is consistent with

results from Lopaschuk *et al.* (1991) and de Carvalho *et al.* (2017). A possible criticism of this dataset includes the use of *Gapdh* as the housekeeping gene. *Gapdh* encodes the glyceraldehyde-3-phosphat dehydrogenase, one of the key enzymes involved in the initial step of the glycolysis pathway (Tarze *et al.*, 2007). Therefore, future studies should be performed to determine the appropriate housekeeping gene/s for each research question asked of the dataset. Online resources including geNorm and Normfinder could be used as the algorithms determine the best reference genes to use based on the stability of gene expression (St-Pierre *et al.*, 2017).

3.6 Conclusion

To conclude, *Slc5a6* does appear to be expressed within the murine heart whilst studies to determine SLC5A6 expression within human cardiac development have proved difficult. From this, the study then focused on investigating the effect of altering *Slc5a6* expression within mice.

Chapter 4 Characterisation of a novel *Slc5a6*^{R252W} mouse model

4.1 Introduction

4.1.1 Identification of SLC5A6 mutations in siblings with DCM

As previously described in 1.3, two siblings with DCM underwent WES analysis, where a homozygous missense mutation (A/A) in *SLC5A6* (p.R253W) was identified as the potential cause of the disease. Sanger sequencing was performed on DNA collected from immediate family members, to confirm the mutation segregated with disease within the family. Figure 4.1 shows the unaffected consanguineous parents are heterozygous carriers of the mutation (G/A) as well as the unaffected sibling. The homozygous mutation (A/A) is present in both affected siblings.

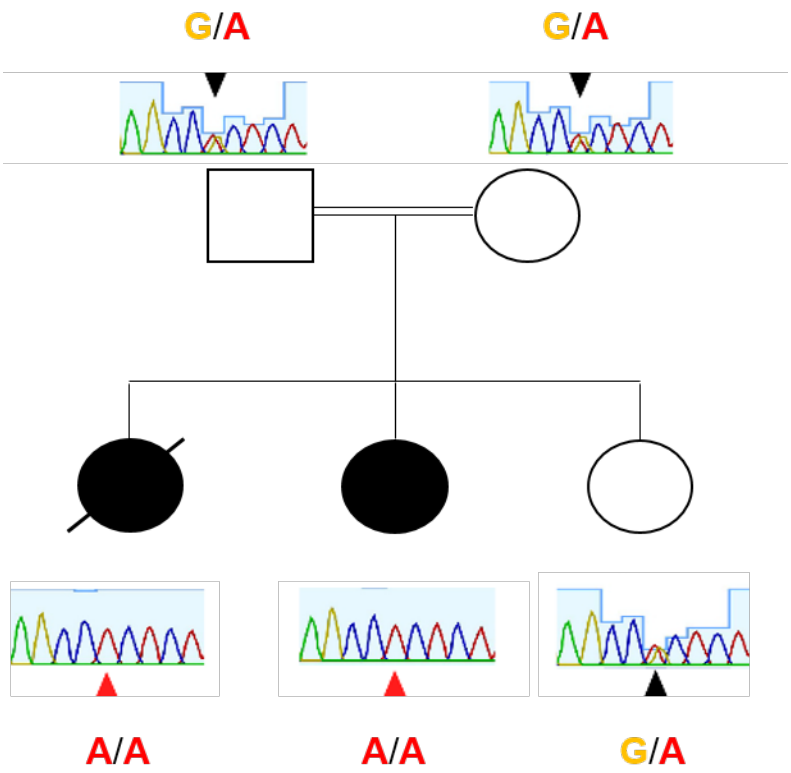

Figure 4.1. Family pedigree and Sanger sequencing results for *SLC5A6* (p.R253W).
Modified from Figure 1.9. Unaffected consanguineous parents and unaffected sibling (white) were heterozygous for the SLC5A6 (p.R253W) mutation (G/A) indicated by black arrowheads. The homozygous mutation (A/A), indicated by red arrowheads, was confirmed in both affected siblings (black).

The eldest affected sibling died at 2 years of age due to undiagnosed DCM. The second affected child suffered multiple poor cardiac output events before undergoing heart transplantation at 7 years of age. Sections of the diseased heart were collected and sent to a clinical pathology laboratory for histological and ultrastructural analysis (1.3.1). Staining of the heart showed sarcomeric disarray and wasting, a high degree of interstitial fibrosis as well as marked regions of increased mitochondrial proliferation, all indicators of cardiomyopathy.

As the patient underwent heart transplantation, no further investigation into the effect of the *SLC5A6* (p.R253W) mutation on the heart could be performed. One way in which human mutations can be studied for causality is by replicating them in the mouse utilising CRISPR-Cas9 technology.

4.1.2 CRISPR-Cas9

Previously, gene editing technology relied on homologous recombination within embryonic stem cells injected into pseudo pregnant females to induce a gene knockin or knockout allele. However, genome editing technologies have advanced to allow the introduction of single point mutations into the target genome. The discovery of CRISPR-Cas9 was a research effort made by many scientists across the world, described by Deltcheva *et al.* (2011). The first successful use of CRISPR-Cas9 in mammalian cells was achieved by Cong *et al.* (2013) and Mali *et al.* (2013). From this, the technology has been widely utilised ranging from the introduction of targeted genomic alterations to the modulation of gene expression. The generation of transgenic mammals was revolutionised by the successful use of CRISPR-Cas9 in mice by Mashiko *et al.* (2013). The gene editing technology utilises an RNA-guided system from the bacterial adaptive immune response to introduce changes within the host genome. The system requires the introduction of *Cas9* enzyme and guide RNAs which bind to the target site and guide the *Cas9* enzyme to the target region (Figure 4.2). Once bound, the nuclease domain of *Cas9* cleaves the double-stranded DNA (dsDNA) located at the 5' end of the protospacer adjacent motif (PAM) to create a double-strand break (DSB) within the target gene (Sander and Joung, 2014; Rodríguez-Rodríguez *et al.*, 2019). From this, DSBs are repaired by DNA mechanisms, including non-homologous end-joining and homologous-directed repair, which allow for insertions or deletions to be incorporated into the host genome.

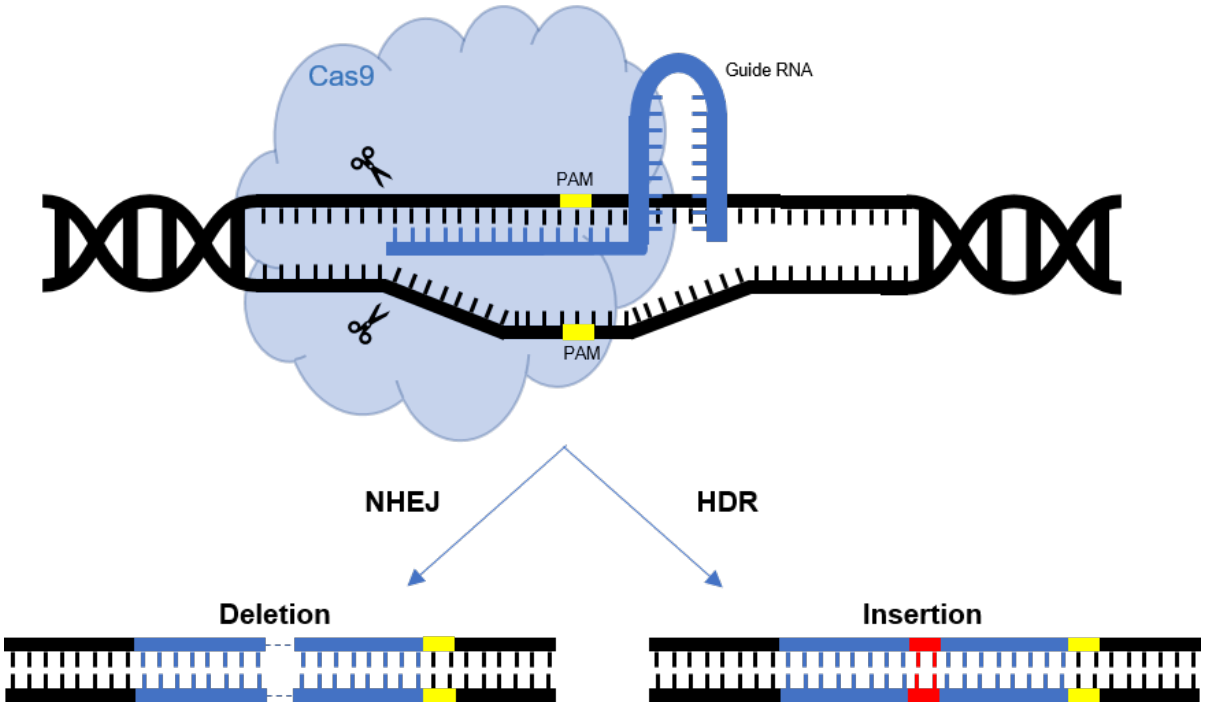

Figure 4.2. CRISPR-Cas9 genome editing system.
To allow genome editing, Cas9 and guide RNAs are introduced to genomic DNA. Guide RNA binds to the target site within the genome and directs Cas9 enzyme to cleave the dsDNA at the PAM site to create a DSB. Once created, the DSB can be repaired using NHEJ to induce a targeted deletion, or HDR to insert new DNA template into the genome. Homologous directed repair HDR, non-homologous end-joining NHEJ, protospacer adjacent motif PAM.

In this chapter, CRISPR-Cas9 technology will be utilised to insert the patient mutation (p.R253W) into the mouse at the equivalent amino acid (p.R252) to generate a *Slc5a6*^{R252W} mouse line as described in 2.1.2.

4.1.3 Aims of the chapter

The main aim of this chapter is to characterise the effects of the homozygous mutation on the development and phenotype of the adult mouse, with particular focus on cardiac function and morphology. ECG will be utilised to assess cardiac function *in vivo*, followed by histological staining to investigate any pathological changes within the heart.

It is hypothesised that by introducing the patient's homozygous *SLC5A6* (p.R253W) mutation into the mouse, the patient cardiac phenotype will be recapitulated, enabling studies into potential therapeutic interventions

4.2 Genomic analysis of mutations in *SLC5A6*

As described in 1.3.2, a mutation in SLC5A6 was identified as a potential novel cause of disease in siblings with DCM. To assess the impact of the amino acid substitution of R253W *in silico* prediction tools were used to determine if the mutation was tolerated, i.e. is not predicted to affect protein function or deleterious (damaging), thought to be disease causing. In addition to R253W, previously reported mutations in *SLC5A6* were also investigated (Table 2.1). All *in silico* tools used predicted the R253W mutation to be disease causing, deleterious, damaging or probably damaging by MutationTaster, SIFT, FATHMM and PolyPhen respectively. The mutation also scored 27.8 by CADD software indicating the mutation is predicted to be damaging. Analysis of the reported patient mutations showed that those described by Subramanian *et al.* (2017); Byrne *et al.* (2019) were predicted to be deleterious by SIFT, disease causing by MutationTaster, and the missense mutations were predicted damaging by FATHMM. Additional mutations in *SLC5A6* have been reported in patients with a spectrum of clinical features (Table 2.1), including developmental delay, bone abnormalities and feeding difficulties. The wide spectrum of clinical features may be due to the location of mutations throughout the transporter (Figure 4.3). Amongst the patients described, only one patient presented with right HF but died due to gastrointestinal complications. Her sibling did not have right HF but showed non-specific ST and T wave changes by ECG, however no cardiac follow up is described after treatment (Byrne *et al.*, 2019).

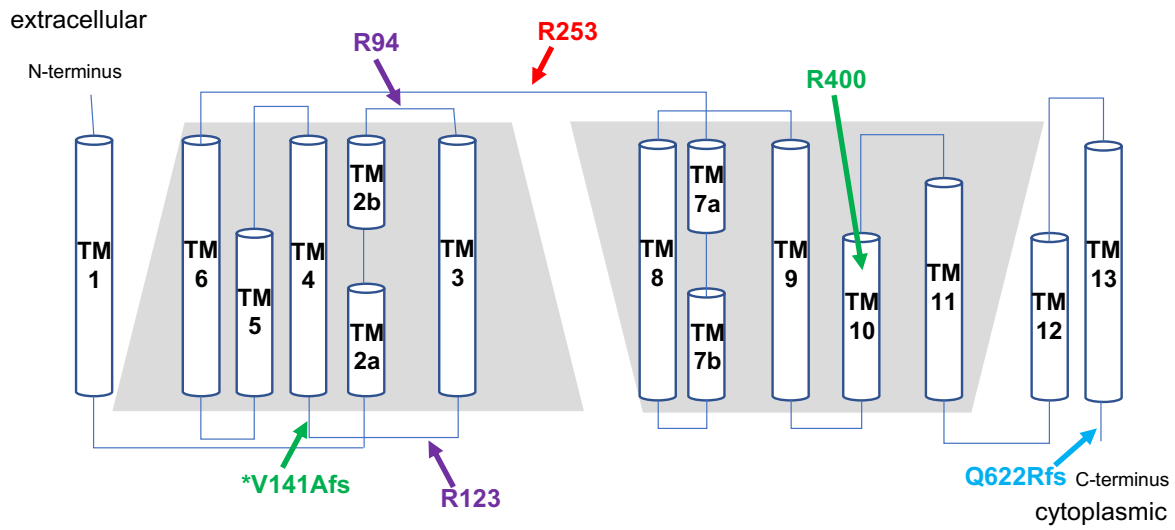

Figure 4.3. Location of reported SLC5A6 mutations within transporter.
Schematic modified from figure 1.10. DCM patient homozygous mutation location noted (red), in addition to compound heterozygous mutations reported by Subramanian *et al.* (2017) (purple), Byrne *et al.* (2019) (green) and Schwantje *et al.* (2019) (blue and *). * = mutation also present in additional patient. R = arginine, V = valine, Q = glutamine.

Table 4.1. Summary of mutations reported in *SLC5A6*.
Genomic mutations outlined for the DCM siblings reported in this project, in addition to previously reported mutations found in *SLC5A6.* Results of the *in silico* prediction tools (SIFT, PolyPhen, MutationTaster, FATHMM and CADD) of the mutations' effect on protein structure and function. CADD scores the effect of the mutation at a pathogenicity threshold of 20, therefore a score >20 predicts the mutation to be damaging, and <0.05 is predicted tolerable. The frequency of the mutation within a control population (141,456 samples) from the GnomAD database is noted. *mutation is also found/reported in a second patient.

Patient	Mutation	Genomic location	Ref	Alt	Type	Consequence	SIFT	PolyPhen	MutationTaster	FATHMM	CADD	Freq. in GnomAD
DCM siblings	R253W	Chr 2:27427777	G	A	Missense	Non Synonymous	Deleterious	Probably damaging	Disease causing	Damaging	27.8	<0.0001
Subramanian *et al.*, 2017	R94X	Chr2:27207371	C	T	Nonsense	Stop gain	N/A	N/A	N/A	N/A	36	Novel
	R123L	Chr2:27207283	G	T	Missense	Non Synonymous	Deleterious	Probably damaging	Disease causing	Damaging	24.8	<0.0001
Byrne *et al.*, 2019	*V141Afs34	Chr2:2742978_ 27429784	ACA	A	Deletion	Frameshift	Deleterious	Benign	Disease causing	N/A	27.9	0.0001
	R400T	Chr2:27426108	C	G	Missense	Non Synonymous	Deleterious	Benign	Disease causing	Damaging	22.6	<0.0001
Schwantje *et al.* 2019 *	Q622Rfs51	Chr2:27423346_ 27423347	CAG	C	Deletion	Frameshift	Tolerated	Benign	Polymorphism	N/A	12.33	<0.0001

Table 4.2. Summary of patient phenotypes with mutations in SLC5A6.

Details of the mutations reported in patients with phenotypic features noted in addition to details reported of treatment given in each case. AR = autosomal recessive, F = female, IM = intramuscular, IV = intravenous, M = male.

	Mutation	Inheritance	Patient	Sex	Age at onset	Phenotype	Treatment
DCM siblings	R253W	AR Homozygous	I	F	-	Died at 2 years of DCM	-
			II	F	9 months	DCM, feeding difficulties, pneumonia, left-side paralysis, seizures, developmental delay.	LVAD, heart transplant
Subramanian *et al.*, 2017	R94X / R123L	AR Compound heterozygous	I	M	Birth	Failure to thrive, feeding difficulties, microcephaly, cerebral palsy, developmental delay, osteoporosis and immunodeficiency	Biotin 10-30mg/d (oral), pantothenic acid 250-500mg/d (oral) and α-lipoic acid 150-300mg/d (oral)
Byrne *et al.*, 2019	V141Afs34 / R400T	AR Compound heterozygous	I	F	14 months	Microcephaly, hyperreflexia, feeding difficulties, asthma, right heart failure. Died at 2 years from acute gastrointestinal haemorrhage.	-
			II	M	12 months	Seizures, cerebral atrophy, feeding difficulties, immunodeficiency, asthma, non-specific ST and T wave changes.	Biotin 10mg/w (IM), Dexpanthenol 250mg/w (IM) and α-lipoic acid 300mg/w (IV)
Schwantje *et al.* 2019	V141Afs34 / Q622Rfs51	AR Compound heterozygous	I	F	10 months	Feeding difficulties, developmental delay, gastroenteritis, metabolic acidosis, respiratory insufficiency, ventricular fibrillation,	Biotin 20mg/d (oral), pantothenic acid 250mg/d (oral)

Protein homology between human and mouse was assessed by *in silico* tool, EMBOSS Needle (EMBL-EBI). The software aligns the two sequences and identifies any alterations or gaps in protein sequence between the two species (Figure 4.4). From this analysis we can observe three gaps in the mouse protein sequence (red) when aligned to human (blue). The software also indicated that there was 88.4% sequence homology between species, with the amino acid residue R253 conserved in mouse at position R252 (orange box).

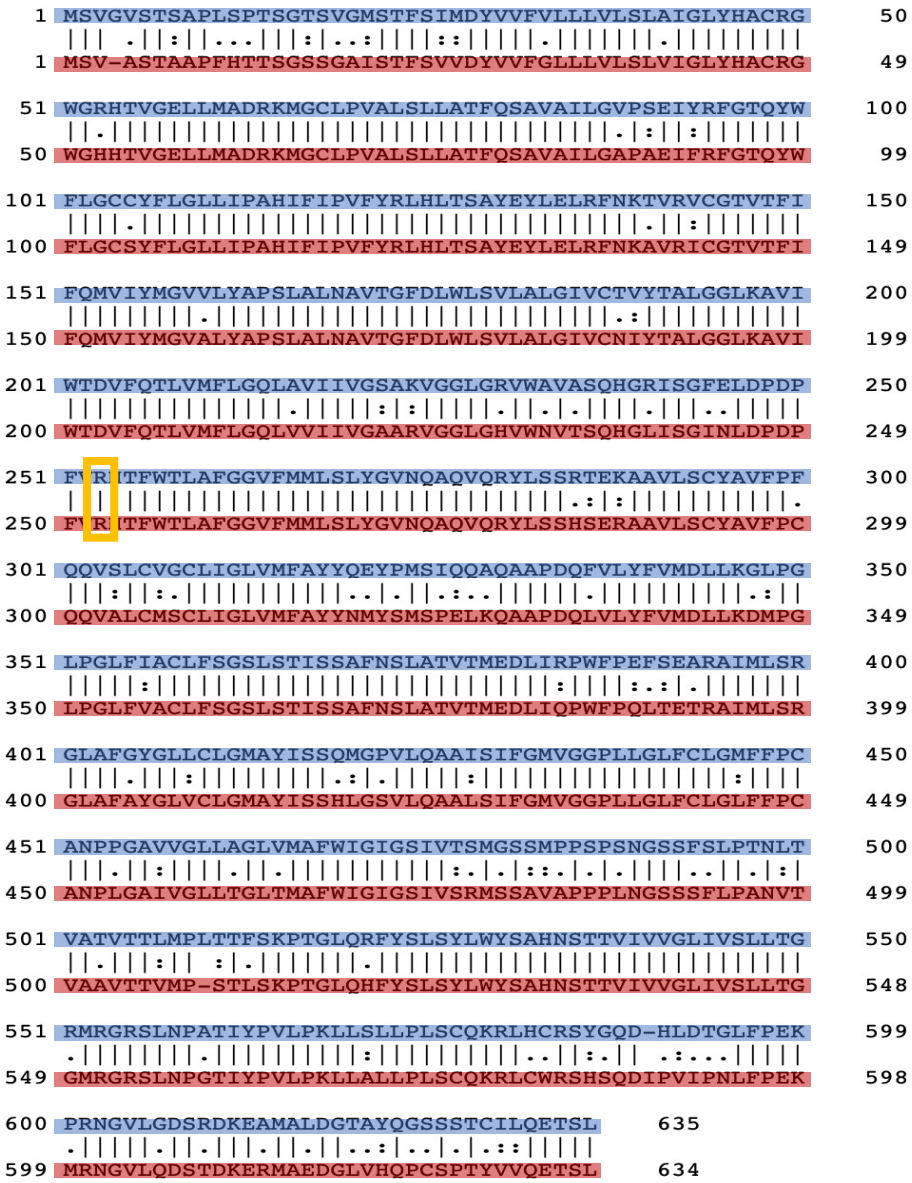

Figure 4.4. Protein homology of human SLC5A6 aligned to mouse Slc5a6. Protein sequence alignment of 635 amino acids in human SLC5A6 (blue) to 634 amino acids of mouse Slc5a6 (red) using EMBOSS Needle tool (Needleman and Wunsch, 1970). R253(human)-R252(mouse) conservation indicated by orange box. | = amino acid is conserved between species, **.** = conservation of groups of amino acids with weakly similar properties between species, **:** = conservation of groups of strongly similar amino acids between species.

As the amino acid residue was shown to be conserved between species, CRISPR-Cas9 technology was adopted to introduce the patient mutation (R253W) into mouse (R252W) for phenotypic analysis.

4.3 Phenotypic analysis of *Slc5a6^{R252W}* mouse model

4.3.1 Generation and validation of Slc5a6^{R252W} mouse model

Slc5a6^{R252W} mice were generated as described in 2.1.2, shown in Figure 4.5**.**A. In addition to altering the mutation site, PAM sites are changed from TGG to TCG and CCT to CGT (Figure 2.1). This alteration is beneficial for the genotyping of *Slc5a6^{R252W}* mice, as the first PAM site is also a restriction site, recognised by *BamHI.* This enables the wild type allele (Slc5a6$^{+/+}$) to be cleaved by the restriction enzyme into two products (97bp and 244bp) once amplified and digested (Figure 4.5B). By introducing a mutation into this restriction site on the *Slc5a6^{R252W}* allele, it is unable to undergo cleavage when exposed to *BamHI* therefore yielding a single uncut PCR product (341bp) shown in Figure 4.5B. Sanger sequencing of both the altered PAM sites and targeted mutation site confirmed no unwanted or unintended alterations of the mutated PAM sequence or the targeted mutation site, and therefore unintended changes to the amino acid sequence are not predicted to occur (Figure 4.5C). Following this *Slc5a6$^{+/R252W}$* mice were crossed to generate *Slc5a6$^{R252W/R252W}$* mice for analysis.

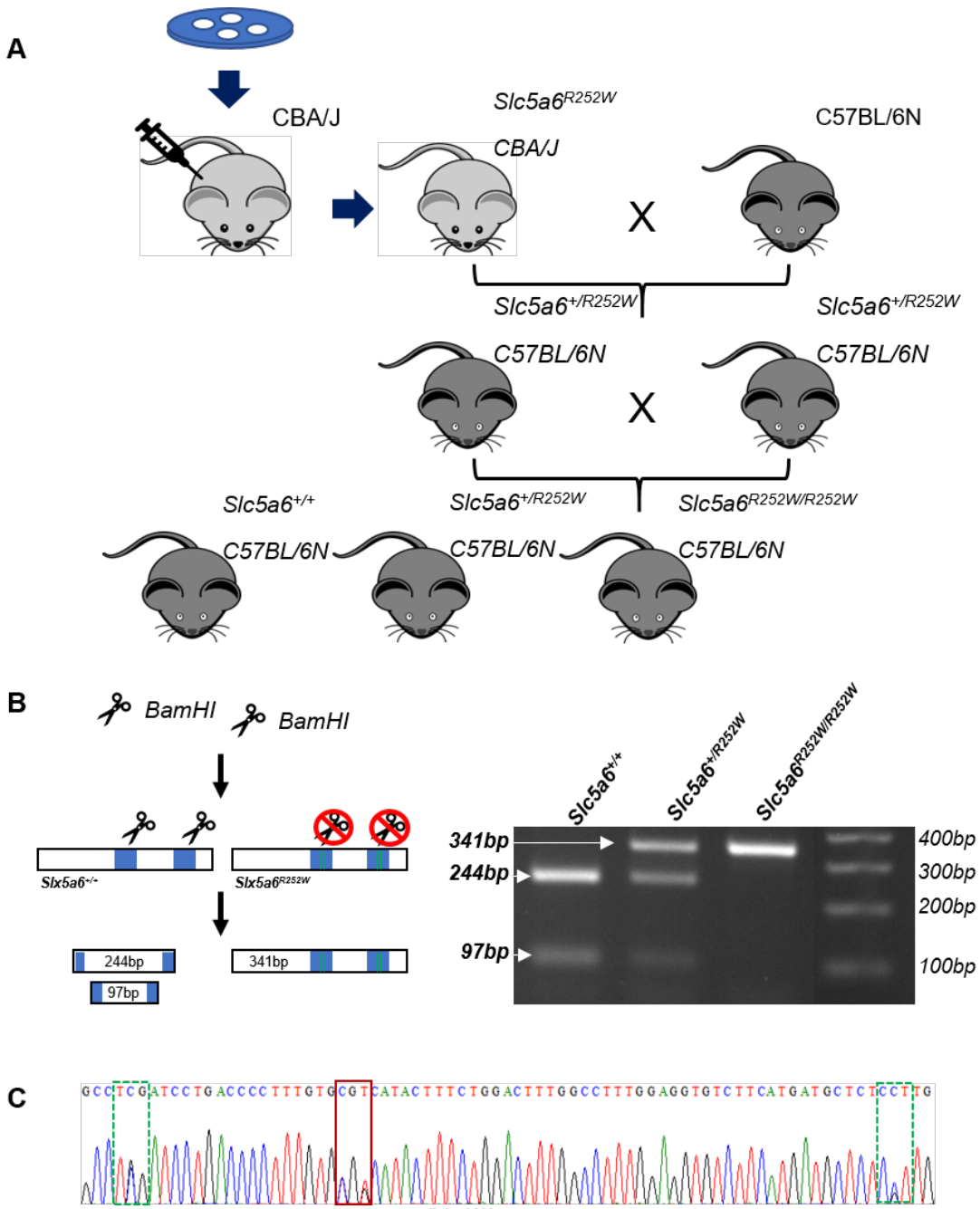

Figure 4.5. Generation of *Slc5a6*^{R252W} mice and validation of the R252W mutation in resultant offspring.

A) Taken from Figure 2.2. The construct was injected into CBA/J dams by Dr Colin Miles. The offspring were crossed with C57BL/6N mice to generate *Slc5a6*$^{+/R252W}$ mice which were then used to generate three genotypes including *Slc5a6*$^{R252W/R252W}$ for analysis. BamHI acts upon the first PAM site cleaving the sequence allowing the wild type allele to be identified by standard PCR followed by a restriction enzyme digest, whereas the mutated *Slc5a6*^{R252W} allele will be uncut and result in a single uncut product. B) shows the two BamHI cut PCR products from *Slc5a6*$^{+/+}$(244bp and 97bp), and uncut *Slc5a6*$^{R252W/R252W}$ (341bp). *Slc5a6*$^{+/R252W}$ mice have both cut and uncut alleles resulting in three bands (97bp, 244bp and 341bp). C) A chromatograph from the Sanger sequencing of the targeted region from a *Slc5a6*$^{+/R252W}$ mouse. The PAM site mutations are present (green), and the amino acid sequence change is confirmed (red) on one allele with the wild type bases also present.

4.3.2 Slc5a6$^{R252W/R252W}$ mice survive embryogenesis

Heterozygous F1 *Slc5a6$^{+/R252W}$* mice were crossed to generate *Slc5a6$^{R252W/R252W}$* mice for analysis as previously described. Mice were genotyped at postnatal day 21 (P21) to confirm survival up to weaning. Chi-squared test was used to determine whether the observed number of *Slc5a6$^{R252W/R252W}$* followed the expected Mendelian ratio. The expected Mendelian ratio of *Slc5a6$^{R252W/R252W}$* mice is observed at weaning (Table 4.3). This suggests the homozygous mutation does not affect mouse development or survival postnatally.

Table 4.3 Mendelian ratio of *Slc5a6$^{R252W/R252W}$* at P21.
Total number of *Slc5a6^{R252W}* mice genotyped at P21. Chi-squared test was used to determine statistical significance.

Age	Total number	*Slc5a6$^{R252W/R252W}$* expected	*Slc5a6$^{R252W/R252W}$* observed	p value
P21	106	26.5	27	0.985949

4.3.3 Sudden death of Slc5a6$^{R252W/R252W}$ mice occurs in early adulthood

As *Slc5a6$^{R252W/R252W}$* mice survived gestation through to genotyping at P21, mice were weaned to investigate cardiac function during adulthood. However, post weaning, sudden death (SD) occurred in 3/6 *Slc5a6$^{R252W/R252W}$* mice between 5.5-6.5 weeks, within two separate litters, with the SD mutants appearing smaller than littermates (Table 4.4). Littermate controls (*Slc5a6$^{+/+}$* and *Slc5a6$^{+/R252W}$*) were unaffected and subsequently culled alongside the remaining three homozygous mutant mice. The hearts were dissected from the three dead mice and the culled littermates to determine if the cause of sudden death in *Slc5a6$^{R252W/R252W}$* mice was of a cardiac origin.

Table 4.4. Sudden death of *Slc5a6^{R252W}* mice.
A total of 12 mice from two litters are listed. All pups survived to weaning; however, three of the 6 *Slc5a6$^{R252W/R252W}$* mutants died between 5-7 weeks.

Genotype	Total number of mice collected	Total number of mice found dead
Slc5a6$^{+/+}$	2	0
Slc5a6$^{+/R252W}$	4	0
Slc5a6$^{R252W/R252W}$	6	3

The dissected hearts were imaged before processing for histological staining (Figure 4.6). The gross morphology of *Slc5a6$^{R252W/R252W}$* (SD) hearts showed no evidence of a myocardial infarct (MI) or scarring of the epicardium (Figure 4.6D). However,

enlargement of the ventricle and atria is visible but on further investigation, is suggestive of blood pooling, which may be secondary to the cause of death as indicated by H&E staining (Figure 4.6H).

As no obvious cardiac defects were observed externally, hearts were paraffin embedded and sectioned to enable further investigation by H&E. The four chambered views of *Slc5a6*$^{+/+}$ (Figure 4.6E), *Slc5a6*$^{+/R252W}$ (Figure 4.6F), *Slc5a6*$^{R252W/R252W}$(Figure 4.6G) hearts are shown, as well as *Slc5a6*$^{R252W/R252W}$ SD (Figure 4.6H). Here no obvious structural abnormalities within the *Slc5a6*$^{R252W/R252W}$ SD heart were observed, such as ventricular wall defects, compared to *Slc5a6*$^{R252W/R252W}$ mice which were culled at the same age. The myocardium of the left and right ventricles across all genotypes appears healthy and compact, lacking any clinical signs of pathological remodelling.

Further histological staining was carried out to look at myocardial fibrosis. Often when the myocardium undergoes volume or pressure overload, it triggers the deposition of extracellular matrix proteins which destabilise the architecture causing functional defects. To view fibrosis within these sections, Masson's Trichrome staining was performed (Figure 4.6I-L) and, using brightfield microscopy, collagen fibres can be visualised (blue). The degree of myocardial fibrosis appears comparable between *Slc5a6*$^{R252W/R252W}$ SD (Figure 4.6L) and *Slc5a6*$^{R252W/R252W}$ (Figure 4.6K) hearts as well as littermate controls; *Slc5a6*$^{+/+}$(Figure 4.6.I) and *Slc5a6*$^{+/R252W}$ (Figure 4.6.J).

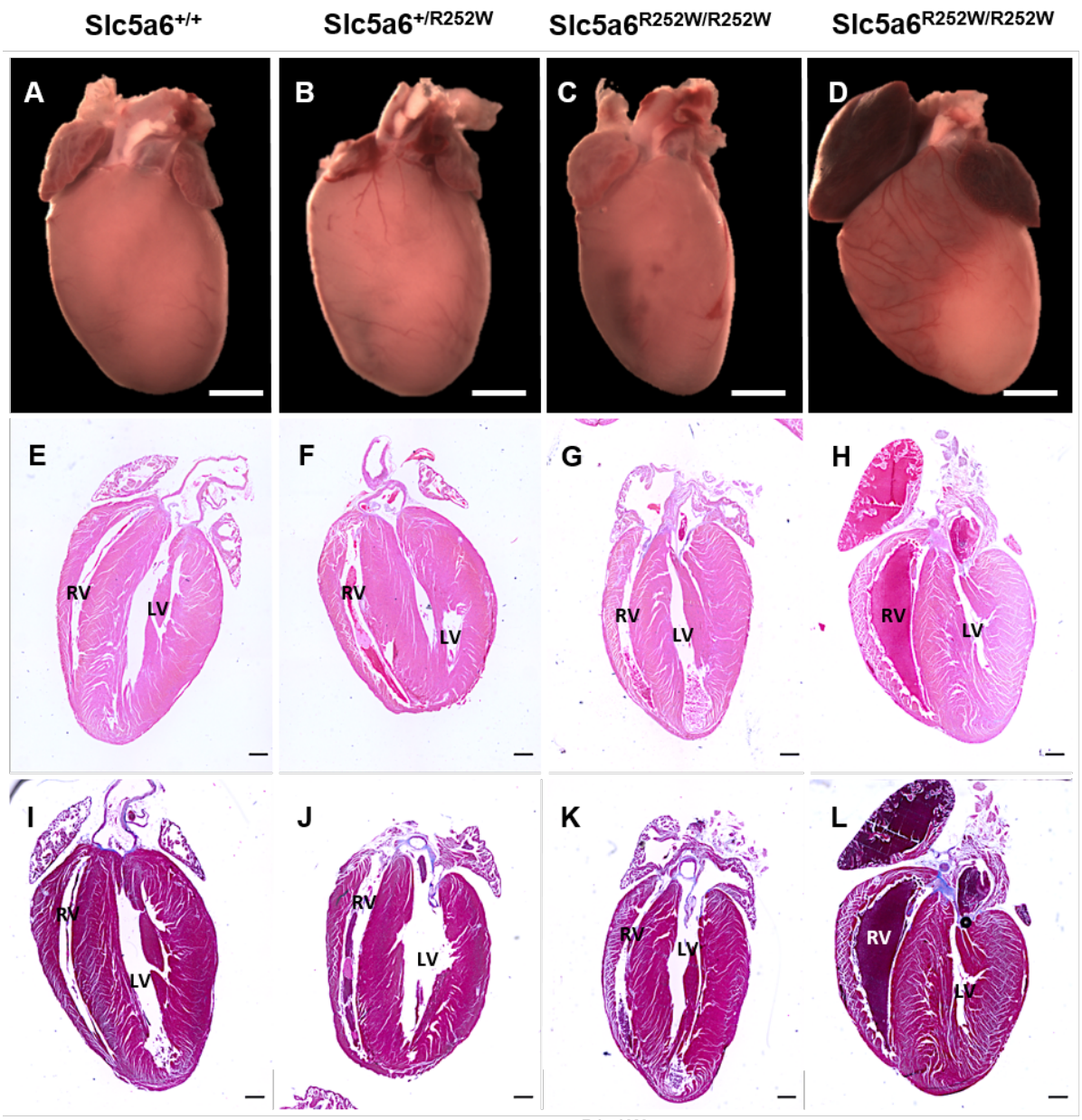

Figure 4.6. Histological analysis of *Slc5a6*^{R252W} SD hearts.
The hearts were dissected from the whole *Slc5a6*^{R252W} litter and imaged using a light microscope at 0.63x magnification and a representative image of each genotype is shown (A-D). H&E staining was performed on each heart (E-H) and shows no structural changes between *Slc5a6*$^{R252W/R252W}$ SD mice (H), culled *Slc5a6*$^{R252W/R252W}$ mice (G) and littermate controls; *Slc5a6*$^{+/+}$ (E) and *Slc5a6*$^{+/R252W}$ (F); however, blood pooling is apparent in the RA and RV of *Slc5a6*$^{R252W/R252W}$ SD mice. Masson's Trichrome staining was performed on each genotype to investigate fibrosis (blue) within the heart (I-L). No obvious increase in myocardial fibrosis apparent in *Slc5a6*$^{R252W/R252W}$ SD (L) compared to *Slc5a6*$^{R252W/R252W}$ mice which were culled (K) as well as *Slc5a6*$^{+/+}$ (I) and *Slc5a6*$^{+/R252W}$ (J). n= 2 *Slc5a6*$^{+/+}$, 4 *Slc5a6*$^{+/R252W}$, 3 *Slc5a6*$^{R252W/R252W}$ and 3 *Slc5a6*$^{R252W/R252W}$ SD. Right atria RA, right ventricle RV, left atria LA, left ventricle LV. Scale bars A-D = 2mm, E-L = 500µm.

4.3.4 *Slc5a6$^{R252W/R252W}$ mice fail to thrive post-weaning*

Following the investigation into sudden death within this line, any resultant *Slc5a6$^{R252W/R252W}$* mice were to be monitored for signs of ill health; starry coat, lack of responsiveness or mobility, as well as body weight monitoring three times a week. To prevent any suffering to future *Slc5a6$^{R252W/R252W}$* mice, mice were culled at 5 weeks of age (P35).

As the Slc5a6$^{R252W/R252W}$ SD mice appeared to be physically smaller, body weight was monitored from weaning at P21, to collection at P35 (Figure 4.7). From the longitudinal averaged data (Figure 4.7A), *Slc5a6$^{+/+}$* and *Slc5a6$^{+/R252W}$* mice gain weight at a similar rate throughout the monitoring period, with no significant difference observed between the two genotypes. *Slc5a6$^{R252W/R252W}$* mice consistently weighed less than *Slc5a6$^{+/+}$* and *Slc5a6$^{+/R252W}$* littermates from P21. Between P30 and P35 there is a statistically significant difference (p=<0.0001) between littermates and *Slc5a6$^{R252W/R252W}$* mice. *Slc5a6$^{R252W/R252W}$* mice gained weight incrementally until P28, after which body weight levelled and began to drop at P35. *Slc5a6$^{R252W/R252W}$* mice are shown to gain significantly less body weight compared to *Slc5a6$^{+/+}$* (p=0.0006) and *Slc5a6$^{+/R252W}$* (p=0.001) littermates (Figure 4.7B). Water-soaked diet was supplied to all litters as it was possible that the failure to thrive may be due to an inability to feed independently following weaning or dehydration.

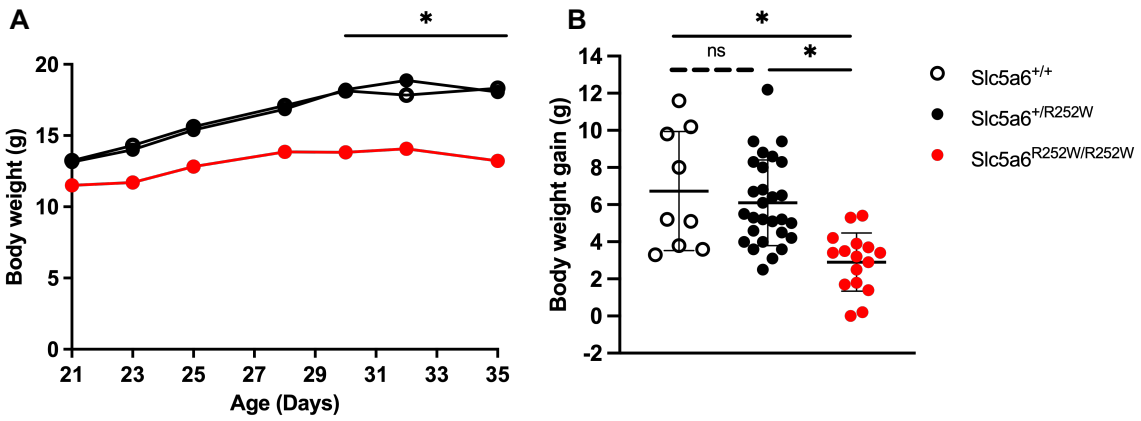

Figure 4.7. Body weight monitoring of *Slc5a6^{R252W}* mice post weaning.
(A) Average body weight of Slc5a6+/+ (white), Slc5a6+/R252W (black) and Slc5a6$^{R252W/R252W}$ (red) mice from weaning at P21 to collection at P35. (B) Individual data showing body weight gain of each mouse monitored. One way ANOVA with multiple comparisons and Bonferroni correction was applied to each dataset, * = <0.05, n = 9 Slc5a6+/+, 28 Slc5a6+/R252W, 16 Slc5a6$^{R252W/R252W}$.

4.3.5 Normal cardiac function is observed in Slc5a6$^{R252W/R252W}$ mice

As observed, the morphology of the hearts from *Slc5a6*$^{R252W/R252W}$ mutants was normal but to assess if cardiac function within the *Slc5a6*^{R252W} line was altered, ECGs were performed (see section 2.9) at 5 weeks prior to culling (Figure 4.8). Averaged ECG traces are shown for *Slc5a6*$^{+/+}$ (Figure 4.8A), *Slc5a6*$^{+/R252W}$ (Figure 4.8B) and *Slc5a6*$^{R252W/R252W}$ (Figure 4.8C). There are no gross observational differences between each genotype, apart from the lengthening of QT in *Slc5a6*$^{R252W/R252W}$ trace in Figure 4.8C. However, when quantified a one-way ANOVA statistical test shows there is no significant difference between genotypes (Figure 4.8G). Similarly, there are no differences observed in heart rate (Figure 4.8D), PR interval (Figure 4.8E), QRS interval (Figure 4.8F), nor at the recovery stage of the conduction cycle; ST height (Figure 4.8H) and T amplitude (Figure 4.8I).

Our investigation into the effect of the R252W mutation on the normal cardiac function of mice at P35 indicated no significant changes suggesting heart function may not be affected by the presence of the R252W mutation in this model.

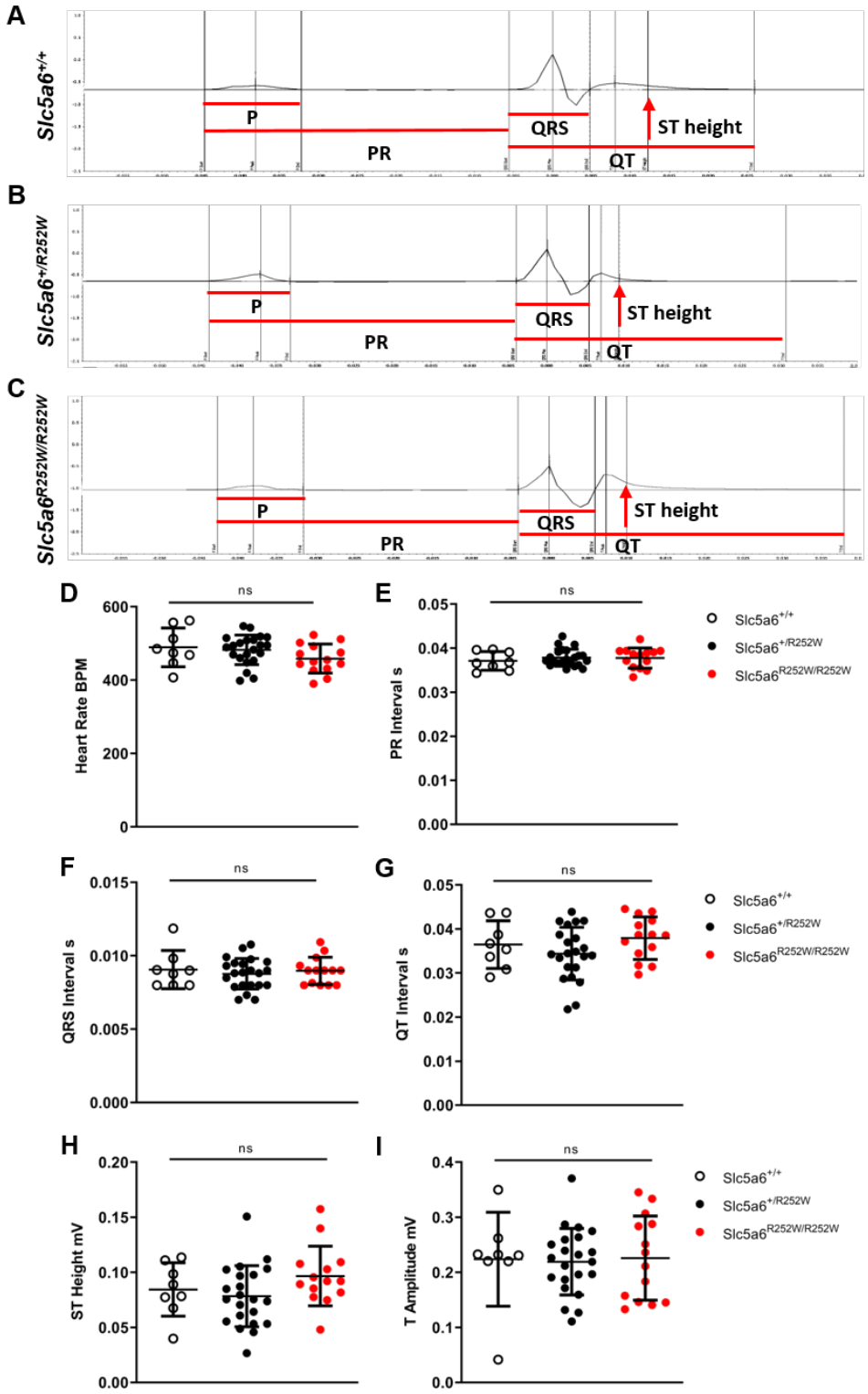

Figure 4.8. ECG traces and quantification of parameters for *Slc5a6*^{R252W} mice at 5 weeks.

(A-C) ECG traces representing the conduction cycle (averaged over a 60 second period) of *Slc5a6*$^{+/+}$ (A), *Slc5a6*$^{+/R252W}$ (B), *Slc5a6*$^{R252W/R252W}$ (C) mice at 5 weeks. ECG parameters are indicated on each trace. (D-I) Quantification of ECG parameters; heart rate (D), PR interval (E), QRS interval (F), QT interval (G), ST height (H), T amplitude (I). One-way ANOVA with multiple comparisons and Bonferroni correction was applied to each dataset; n= 8 *Slc5a6*$^{+/+}$; 22 *Slc5a6*$^{+/R252W}$; 14 *Slc5a6*$^{R252W/R252W}$.

4.3.6 Skeletal analysis of Slc5a6^{R252W} mice

Previous studies into the intestinal specific *Slc5a6* knockout mouse showed gross bone abnormalities, including a significant decrease in bone length compared to littermate controls (Ghosal *et al.*, 2012). They also reported sudden death of knockout mice at a similar age as described in 4.3.3. To determine if similar bone abnormalities were present in *Slc5a6*$^{R252W/R252W}$ mice, which may account for their smaller size, X-ray was performed at 5 weeks prior to culling following ECG recording (Figure 4.9). From the X-ray images, bone measurements were taken from each mouse to determine skull length (D), intercanthal distance (E), femur length (F), tibia length (G) as well as body length (H). As the *n* was low, statistical testing could not be performed; however, from the data shown, there are no observable differences in cranial bone measurements (D-E) or long bone measurements (F-G). Body length measurements (H) suggest *Slc5a6*$^{R252W/R252W}$ mice may have a shorter body at ~65 mm compared to *Slc5a6*$^{+/+}$ and *Slc5a6*$^{+/R252W}$ mice with a body length of ~72 mm however, statistical testing could not be applied to the dataset.

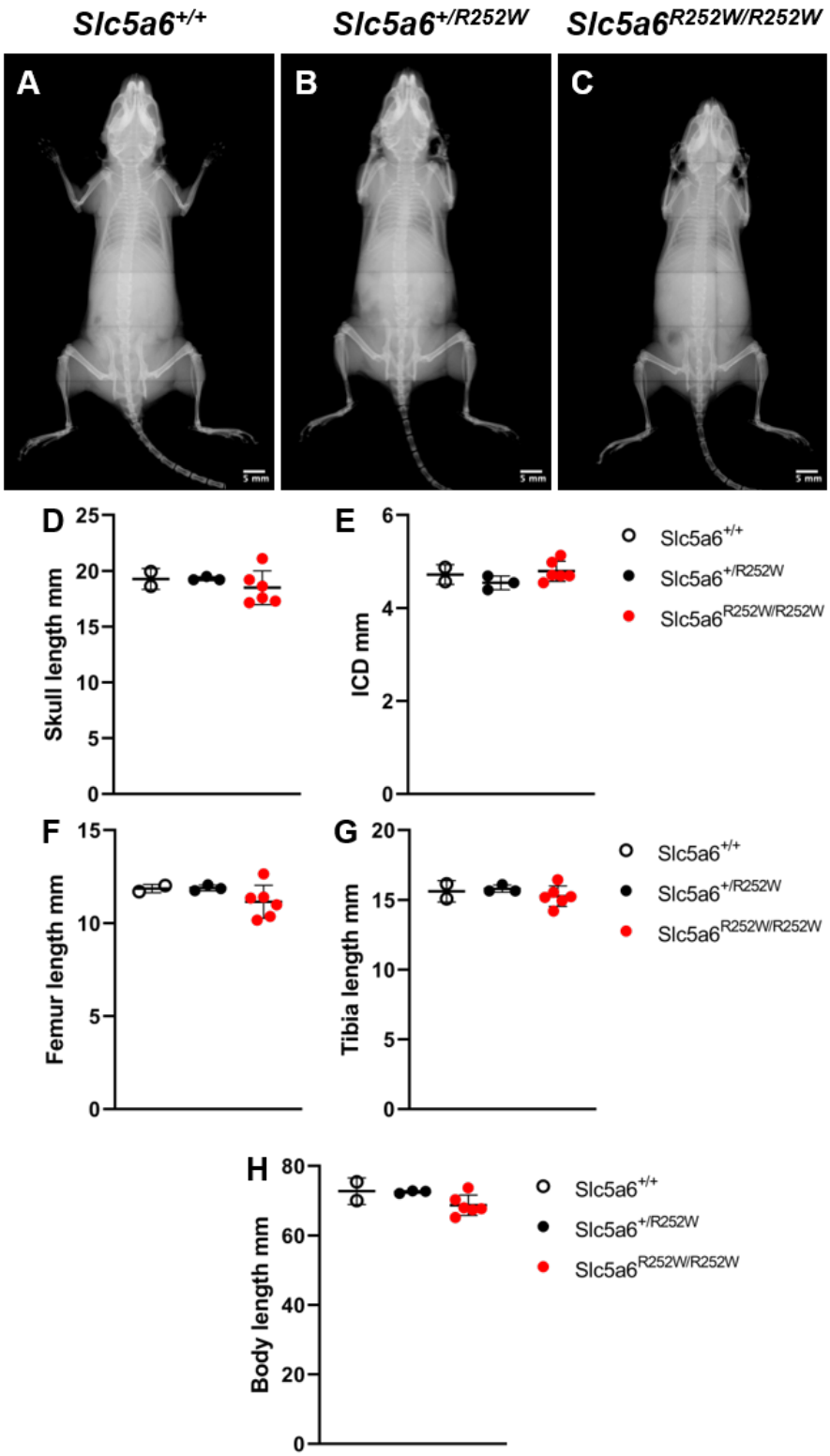

Figure 4.9. No bone abnormalities were present in *Slc5a6^{R252W}* mice at 5 weeks. (A-C) representative X-Ray images of each genotype at 5 weeks. (D-H) Bone measurements taken from X-Ray images, showing no observable difference between genotypes. n=2 *Slc5a6$^{+/+}$;* 3 *Slc5a6$^{+/R252W}$*; 6 *Slc5a6$^{R252W/R252W}$*.

4.3.7 No cardiac abnormalities observed in Slc5a6$^{R252W/R252W}$ during early adulthood

Following functional and skeletal analysis of *Slc5a6*^{R252W} mice at 5 weeks, hearts were collected, imaged, and weighed before processing for histological analysis. Whole heart images of *Slc5a6*$^{+/+}$ (Figure 4.10A), *Slc5a6*$^{+/R252W}$ (Figure 4.10B) and *Slc5a6*$^{R252W/R252W}$ (Figure 4.10C) mice are shown. The gross morphology of the hearts collected appear visually comparable between each genotype with no apparent scarring or ventricular enlargement apparent externally in *Slc5a6*$^{R252W/R252W}$ hearts (Figure 4.10C) compared to littermate controls, *Slc5a6*$^{+/+}$ (Figure 4.10A) and *Slc5a6*$^{+/R252W}$ (Figure 4.10B). Heart weight was calculated and used to determine any changes in gross cardiac mass (mg) between each genotype. This data was normalised to tibia length (mm^3) as well as body weight (g) (Figure 4.10). Although *Slc5a6*$^{R252W/R252W}$ mice weigh significantly less than littermate controls (Figure 4.7) at the point of collection, the data indicates that heart weight to body weight ratio is comparable across all genotypes (Figure 4.10D). To remove any bias due to body composition, suggested by the appearance and body weight of *Slc5a6*$^{R252W/R252W}$ mice, heart weight was divided by tibia length (mm^3) to index heart weight to the "normal" size of the mouse as described by Hagdorn *et al.* (2019). The ratio of heart weight to tibia length shows no significant difference is observed between *Slc5a6*$^{R252W/R252W}$ and littermate controls (Figure 4.10A). This data suggests there is no detrimental effect of the mutation, in either the heterozygous or homozygous state, on the overall mass of the heart. Although the initial cardiac functional and gross structural findings do not suggest *Slc5a6*$^{R252W/R252W}$ mice have any heart defects, a thorough histological analysis was performed to confirm this conclusion.

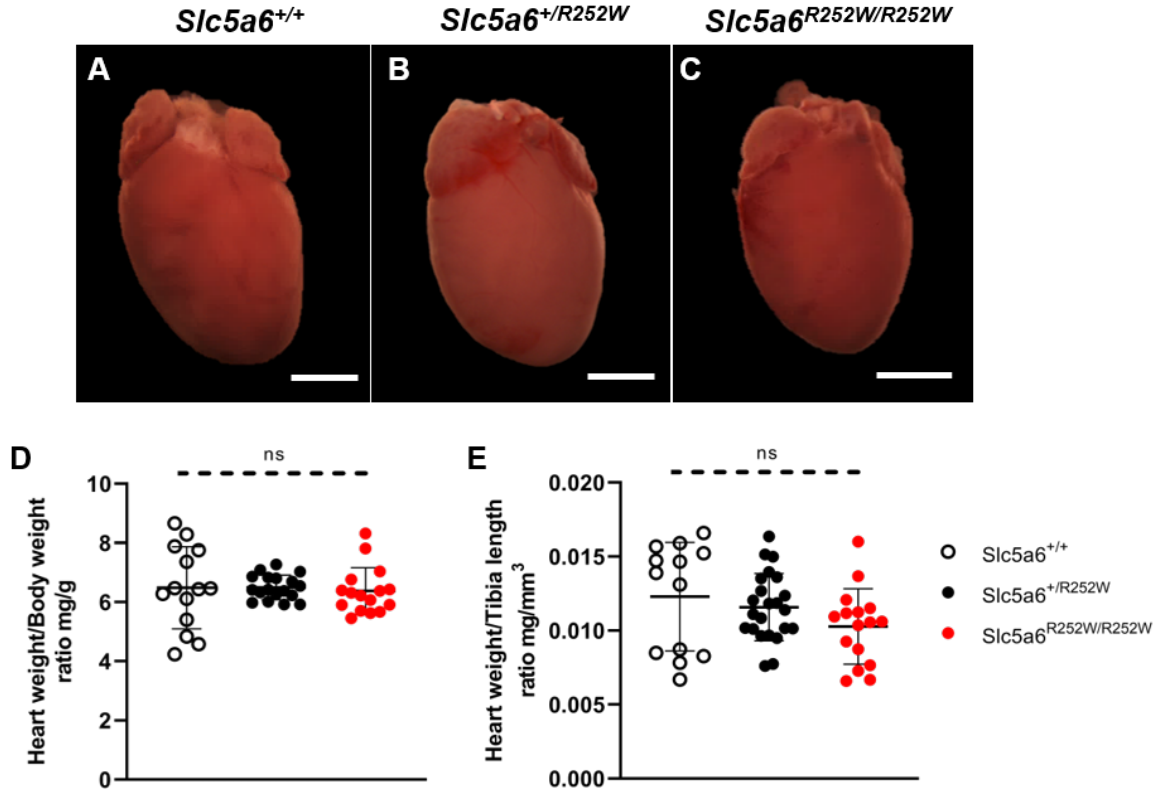

Figure 4.10. Whole heart images and heart weight ratios collected from *Slc5a6^{R252W}* mice at 5 weeks.
(A-C) whole heart images acquired following dissection at 5 weeks of *Slc5a6$^{+/+}$* (A), *Slc5a6$^{+/R252W}$* (B) and *Slc5a6$^{R252W/R252W}$* (C) mice. (D) heart weight (mg) was normalised to tibia length (mm^3) shown for each genotype. (B) heart weight was also normalised to body weight (g) for each genotype. One way ANOVA with multiple comparisons and Bonferroni correction was applied to each dataset. n = 13 *Slc5a6$^{+/+}$*, 23 *Slc5a6$^{+/R252W}$*, 16 *Slc5a6$^{R252W/R252W}$*. Scale bars A-C = 2mm.

Hearts were coronally sectioned to obtain four-chamber view sections for analysis. Sections were stained with H&E (2.6.1) to observe any structural abnormalities and, Masson's Trichrome (2.6.2) to identify any areas of fibrosis (blue) throughout the heart. Sections were imaged using a brightfield microscope. Sections stained with H&E indicate *Slc5a6$^{R252W/R252W}$* hearts (Figure 4.11C) appear visually comparable to *Slc5a6$^{+/+}$* (Figure 4.11A) and *Slc5a6$^{+/R252W}$* (Figure 4.11B) hearts collected at 5 weeks. No ventricular chamber dilation is apparent, nor any signs of ventricular wall thinning.

From staining with Masson's Trichrome, there are no signs to indicate pathological fibrosis remodelling in *Slc5a6*$^{R252W/R252W}$ hearts (Figure 4.11F). Blue staining (collagen fibres) is observed at the valves across all genotypes, including some physiological fibrosis throughout the myocardium in *Slc5a6*$^{+/+}$ (Figure 4.11D), *Slc5a6*$^{+/R252W}$ (Figure 4.11F) and *Slc5a6*$^{R252W/R252W}$ hearts (Figure 4.11F).

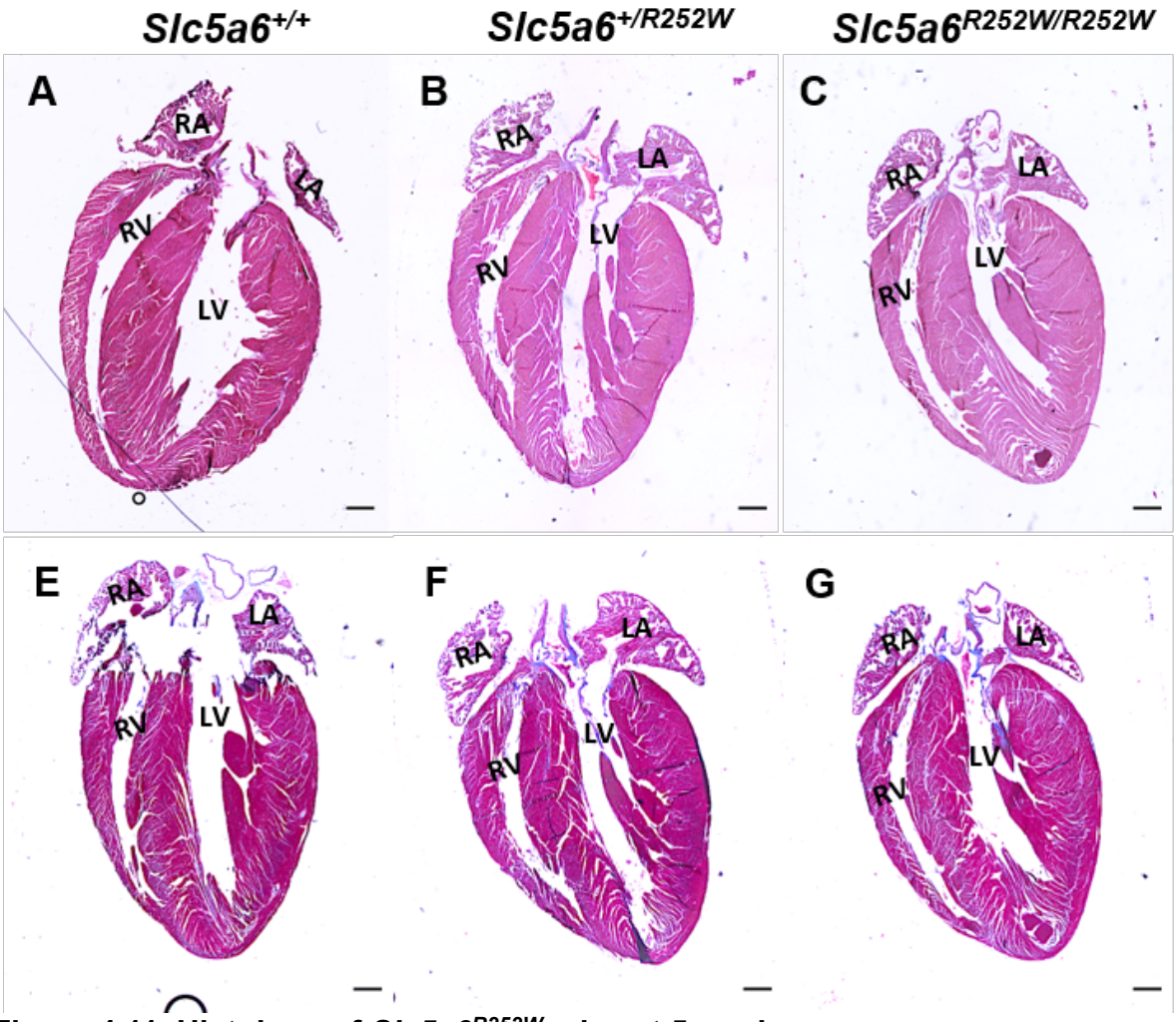

Figure 4.11. Histology of *Slc5a6*^{R252W} mice at 5 weeks.
Representative images of H&E staining for *Slc5a6*$^{+/+}$ (A), *Slc5a6*$^{+/R252W}$(B) and *Slc5a6*$^{R252W/R252W}$ (C) hearts. Masson's Trichrome staining to identify areas of fibrosis, are shown for *Slc5a6*$^{+/+}$ (E), *Slc5a6*$^{+/R252W}$(F) and *Slc5a6*$^{R252W/R252W}$ (G) hearts. Right atria RA, right ventricle RV, left atria LA, left ventricle LV. Scale bar = 500µm.

To conclude, the F1 generation of *Slc5a6*$^{R252W/R252W}$ mice do not survive beyond 5.5 weeks, with no apparent difference in gross cardiac mass, structure or function compared to littermate controls when investigated at 5 weeks. However, we do note a decrease in body weight gain in *Slc5a6*$^{R252W/R252W}$ mice, but skeletal analysis showed no changes in bone or overall body length.

4.4 Backcross of *Slc5a6*^{R252W} mice onto C57BL/6 genetic background

As the *Slc5a6*^{R252W} mice were generated on a mixed background of both CBA/J and C57BL/6, *Slc5a6*$^{+/R252W}$ mice were backcrossed using wild type C57BL/6 mice (Figure 4.12). This was to negate any strain-specific modifiers of the mixed background influencing the phenotype of the CRISPR-Cas9 generated *Slc5a6*^{R252W} mice. F1 *Slc5a6*$^{+/R252W}$ mice were crossed with wild type C57BL/6 mice to produce F2 *Slc5a6*$^{+/R252W}$ mice with 75% C57BL/6 background. These mice were backcrossed again, twice, until F4 *Slc5a6*$^{+/R252W}$ mice were generated with 93.75% C57BL/6 genetic background. From this cross, the resultant F4 *Slc5a6*$^{+/R252W}$ mice were crossed together to generate F4 *Slc5a6*$^{R252W/R252W}$ mice for analysis.

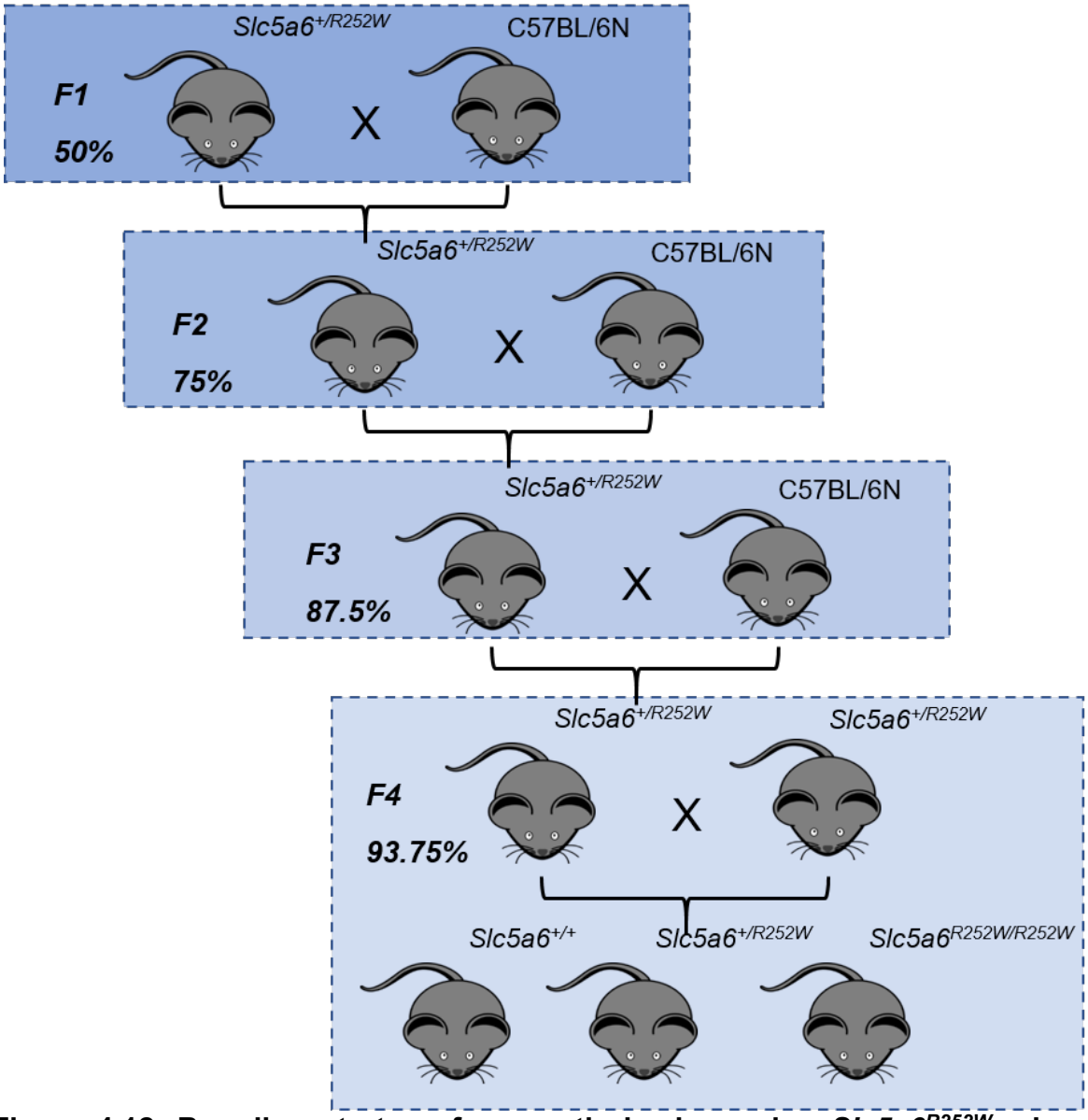

Figure 4.12. Breeding strategy for genetic backcrossing *Slc5a6*^{R252W} mice to C57BL/6 strain.

F1 *Slc5a6*$^{+/R252W}$ male mice were crossed with C57BL/6 females to generate F2 *Slc5a6*$^{+/R252W}$ mice (75% C57BL/6). The resultant F2 *Slc5a6*$^{+/R252W}$ mice were further backcrossed another two generations; F3 *Slc5a6*$^{+/R252W}$ (87.5% C57BL/6), until F4 *Slc5a6*$^{+/R252W}$ mice were generated with 93.75% C57BL/6 genetic background. These mice were then inter-crossed to generate F4 *Slc5a6*$^{R252W/R252W}$ mice for analysis.

Once the F4 *Slc5a6*^{R252W} generation was produced, DNA was collected from *Slc5a6*$^{+/R252W}$ mice and Sanger sequencing was performed to confirm the presence of the targeted p.*R252W* mutation. Sanger sequencing confirmed successful transmission of the R252W mutation in both an F1 *Slc5a6*$^{+/R252W}$ mouse (Figure 4.13A) and F4 *Slc5a6*$^{+/R252W}$ mouse (Figure 4.13B). Both chromatographs show the presence of the altered allele with changes to the PAM sites from C>G in the first site and G>C in the second (green). The targeted amino acid sequence change from CGT>TGG (red) is also confirmed in both chromatographs, showing the mutation has been maintained throughout the backcross generations. F4 *Slc5a6*$^{+/R252W}$ were inter-crossed to generate *Slc5a6*$^{R252W/R252W}$ mice for analysis.

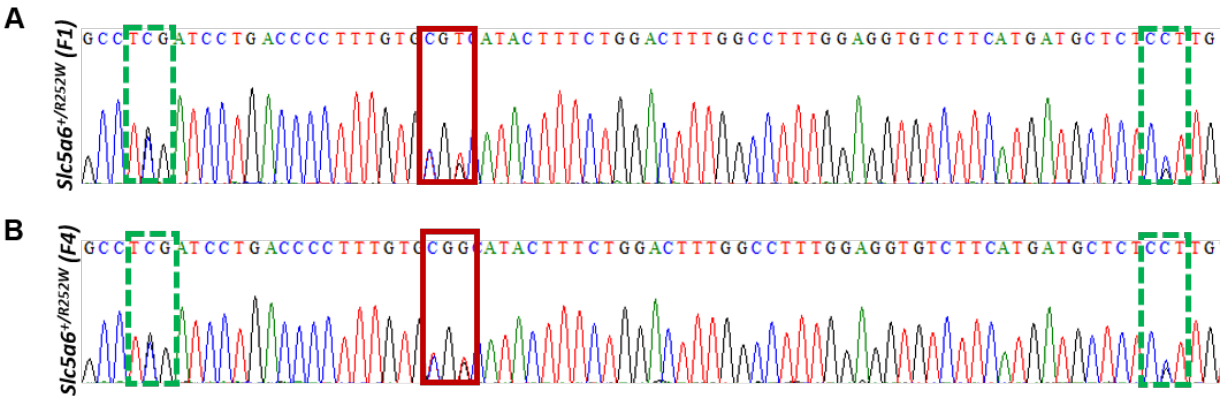

Figure 4.13. Sanger sequencing chromatographs of the *Slc5a6*^{R252W} mutation in F1 and F4 *Slc5a6*$^{+/R252W}$ mice.
(A) chromatograph from the Sanger sequencing of the targeted region from a *Slc5a6*$^{+/R252W}$ (F1) mouse. (B) chromatograph of the targeted region from a *Slc5a6*$^{+/R252W}$ (F4) mouse. In both generations the PAM site mutations (C>G, G>C) are present (dashed green boxes), and the amino acid sequence change (CGT>TGG) is confirmed (red box) on one allele, with the wild type bases present also.

4.4.1 F4 Slc5a6$^{R252W/R252W}$ *mice survive embryogenesis without any cardiac abnormalities*

Following the generation of the F4 *Slc5a6*^{R252W} line and confirmation of the transmission of the targeted mutation, F4 *Slc5a6*$^{+/R252W}$ heterozygous mice were crossed together. From this, embryos were collected for analysis at E15.5, and the expected mendelian ratio of *Slc5a6*$^{R252W/R252W}$ embryos was observed (Table 4.5).

Table 4.5. Mendelian ratios for F4 *Slc5a6*^{R252W} mice during embryogenesis.
Total number of F4 *Slc5a6*^{R252W} mice genotyped at E15.5. Chi-squared test was used to determine statistical significance.

Age	Total number	*Slc5a6*$^{R252W/R252W}$ expected	*Slc5a6*$^{R252W/R252W}$ observed	p value
E15.5	24	6	5	0.779

Gross embryonic and cardiac morphology at E15.5 indicate no external abnormalities at the point of collection in *Slc5a6*$^{R252W/R252W}$ embryos (Figure 4.14C) compared to littermate controls, *Slc5a6*$^{+/+}$ (Figure 4.14A) and *Slc5a6*$^{+/R252W}$ (Figure 4.14B). Histological staining of two *Slc5a6*$^{R252W/R252W}$ embryos by H&E showed no cardiac malformations, such as VSDs, present in *Slc5a6*$^{R252W/R252W}$ (Figure 4.14F) compared to *Slc5a6*$^{+/+}$ (Figure 4.14D) or *Slc5a6*$^{+/R252W}$ (Figure 4.14E). The remaining, *Slc5a6*$^{R252W/R252W}$ embryos were collected for RNA and therefore could not be used for histological analysis. However, increased numbers of *Slc5a6*$^{R252W/R252W}$ embryos should be collected and further investigated to identify any changes in cardiac morphology in *Slc5a6*$^{R252W/R252W}$ hearts at E15.5. From the data collected, it is suggested that the *Slc5a6*$^{R252W/R252W}$ mutant embryos are developing normally at this stage of development.

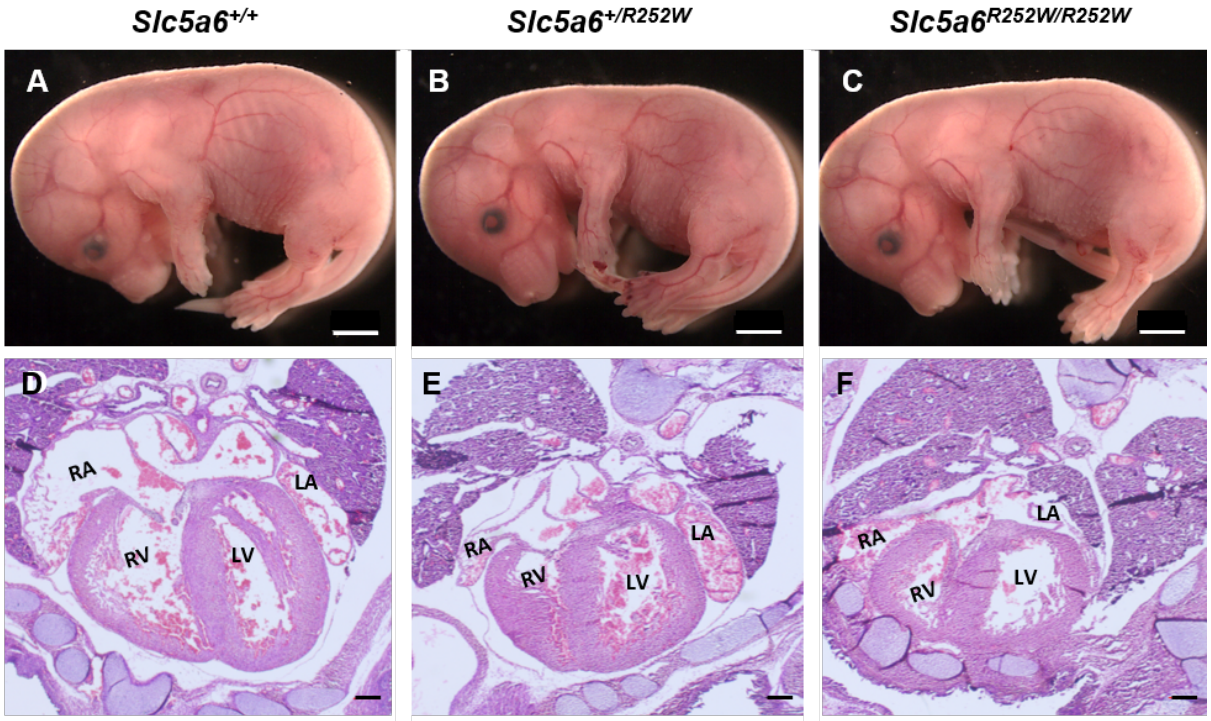

Figure 4.14. Whole embryo and histological staining of *Slc5a6*^{R252W} (F4) mice at E15.5.
Representative whole embryo images of F4 *Slc5a6*$^{+/+,}$(A), *Slc5a6*$^{+/R252W}$ (B) and *Slc5a6*$^{R252W/R252W}$ (C) mice at E15.5. H&E images taken at 2.5x magnification of *Slc5a6*$^{+/+,}$ (D), *Slc5a6*$^{+/R252W}$ (E) and *Slc5a6*$^{R252W/R252W}$ (F) mice. n = 2 *Slc5a6*$^{+/+,}$ 4 *Slc5a6*$^{+/R252W}$, 2 *Slc5a6*$^{R252W/R252W}$. Right atria RA, right ventricle RV, left atria RA, left ventricle LV. Scale D-F = 200µm.

4.4.2 Postnatal death occurs in Slc5a6$^{R252W/R252W}$ *(F4) mice*

Due to the survival of F4 *Slc5a6*$^{R252W/R252W}$ embryos at E15.5, it was decided to allow pups to be born and be genotyped at P21 as it was expected that the F4 generation would follow the F1 generation and survive to this point. However, at P21 no *Slc5a6*$^{R252W/R252W}$ mice were identified (Table 4.6) and therefore mice were then collected following birth, at P0 and at P7. Mendelian inheritance ratio was observed at P0; however, *Slc5a6*$^{R252W/R252W}$ mice were significantly underrepresented at P7 (Table 4.6). This suggests *Slc5a6*$^{R252W/R252W}$ mice are not able to survive during the first week of life which was unexpected. Tissue was collected at P0 to investigate the cause of early postnatal death in the F4 *Slc5a6*^{R252W} line.

Table 4.6. Observed and expected Mendelian ratios for *Slc5a6*$^{R252W/R252W}$ postnatal mice.
Total number of F4 *Slc5a6*^{R252W} mice genotyped postnatally. Chi-squared test was used to determine statistical significance.

Age	Total number	*Slc5a6*$^{R252W/R252W}$ expected	*Slc5a6*$^{R252W/R252W}$ observed	p value
P0	141	35.25	28	0.997
P7	45	11.25	1	0.000000623
P21	62	15.5	0	*

Hearts collected at P0 show no gross visual differences apparent between *Slc5a6*$^{+/+}$ (Figure 4.15A), *Slc5a6*$^{+/R252W}$ (Figure 4.15B) or *Slc5a6*$^{R252W/R252W}$ (Figure 4.15C) mice. Unfortunately, due to processing difficulties, histological analysis could not be performed.

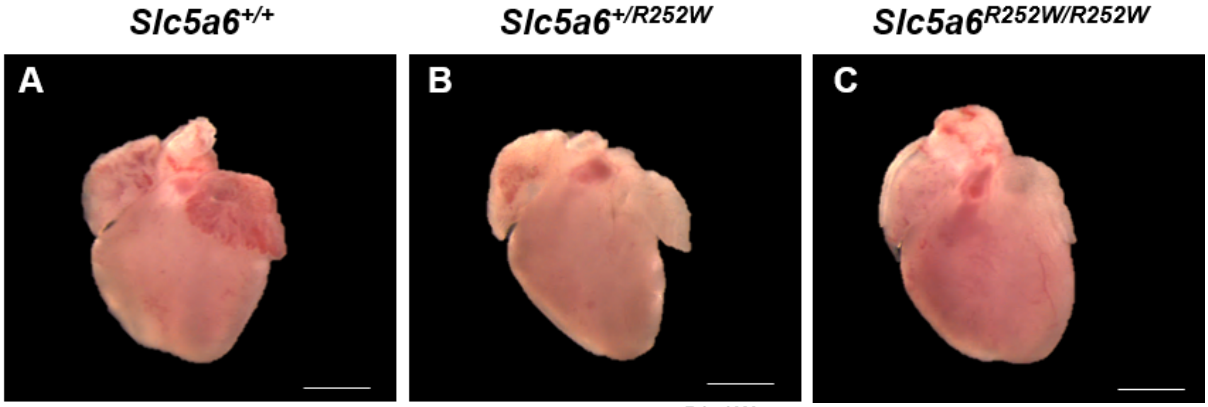

Figure 4.15. Whole heart images of F4 *Slc5a6*^{R252W} mice at P0.
Representative whole heart images of *Slc5a6*$^{+/+}$(A), *Slc5a6*$^{+/R252W}$ (B) and *Slc5a6*$^{R252W/R252W}$ (C). No obvious gross structural abnormalities are observed. n= *7 Slc5a6*$^{+/+}$*,* 17 *Slc5a6*$^{+/R252W}$*and* 6 *Slc5a6*$^{R252W/R252W}$. Scale bar = 1mm.

4.4.3 Ultrastructural analysis of F4 Slc5a6^{R252W} *mice at birth*

Following collection, a 2mm^3 section of the apex was taken from P0 hearts for transmission electron microscopy (TEM) to explore the ultrastructure of the heart to determine if the R252W mutation was impacting on cellular, sarcomeric or mitochondrial structure. Due to time constraints and breeding difficulties following the COVID-19 pandemic, only *Slc5a6*$^{+/R252W}$ (*n*=3) and *Slc5a6*$^{R252W/R252W}$ (*n*=1) were collected for TEM imaging. Representative images are shown in Figure 4.16.

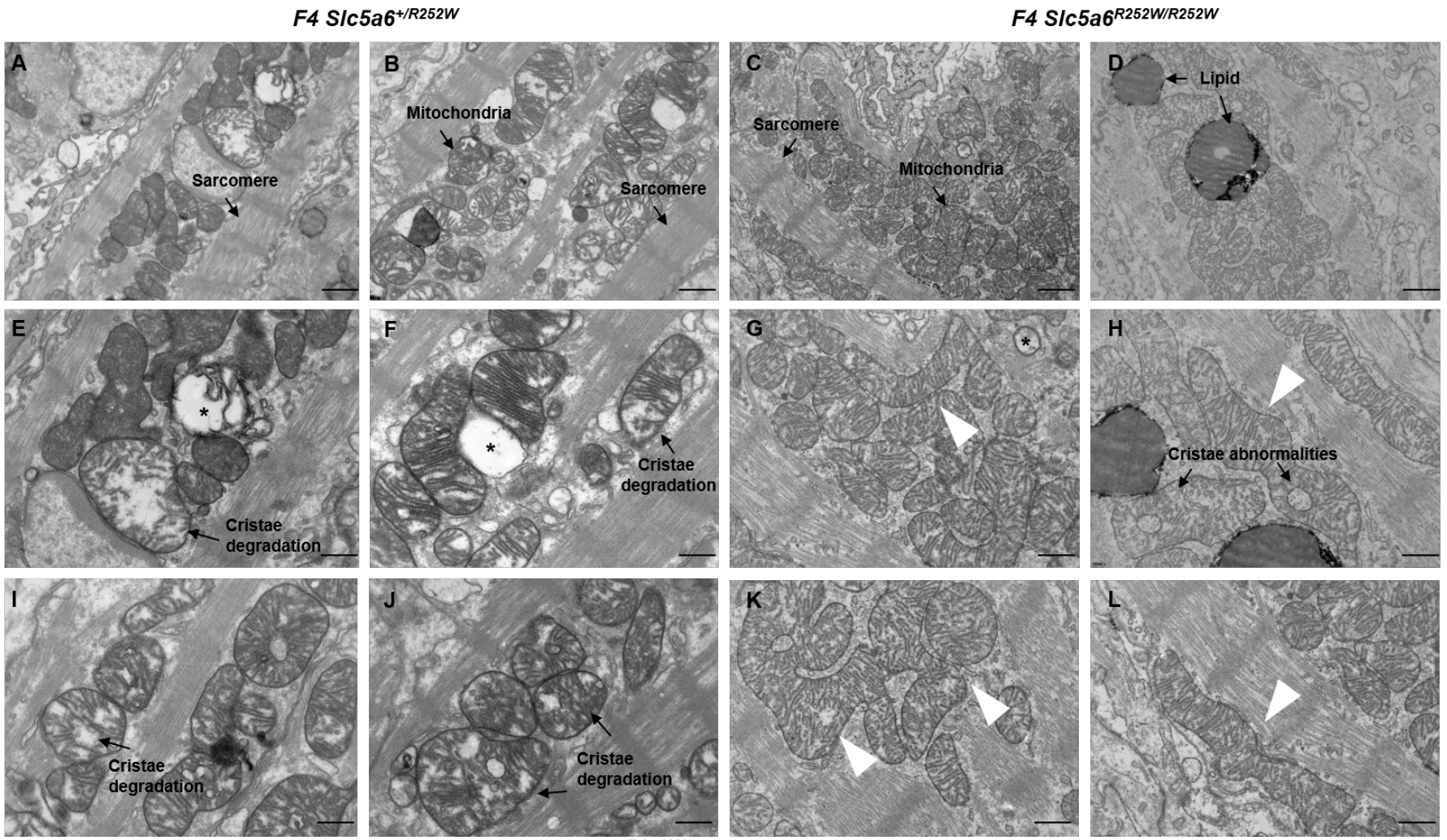

Figure 4.16. Representative TEM images of F4 *Slc5a6*^{R252W} hearts at P0.

TEM images taken at 8,000x for *Slc5a6*$^{+/R252W}$ (A,B) and *Slc5a6*$^{R252W/R252W}$ (C,D). Higher power images at 15,000x show abnormalities in *Slc5a6*$^{+/R252W}$ (E,F,I,J) and *Slc5a6*$^{R252W/R252W}$ mice (G,H,K,L). * Indicates total mitochondrial degradation, arrowheads (white) indicate mitochondria undergoing fusion. n= 3 *Slc5a6*$^{+/R252W}$, 1 *Slc5a6*$^{R252W/R252W}$. Scale bar A-D = 1μm, E-L = 500nm.

Sarcomeres appear well defined in both *Slc5a6*$^{+/R252W}$ (Figure 4.16A,B) and *Slc5a6*$^{R252W/R252W}$ (Figure 4.16C,D) cardiac sections at 8,000x, suggesting contractility of the myocardium may be unaffected by the presence of the mutation at P0. Mitochondria within all three *Slc5a6*$^{+/R252W}$ samples analysed show varying degrees of degradation. As indicated, complete cristae loss and mitochondrial degradation can be observed (Figure 4.16E,F) as well as mitochondria with less dense and partially degraded cristae (Figure 4.16I,J). Interestingly, cardiac sections from *Slc5a6*$^{R252W/R252W}$ mice show clustering of mitochondria (Figure 4.16C,D) which may indicate an increase in proliferation in response to stimuli, e.g. stress; however, further investigation is required to confirm this hypothesis. Higher power images of the *Slc5a6*$^{R252W/R252W}$ heart (Figure 4.16G,H,K,L), reveal mitochondria have more dense cristae compared to *Slc5a6*$^{+/R252W}$ sections; however, some cristae degradation is shown in Figure 4.16H. Indicated by white arrowheads, mitochondria undergoing mitochondrial fusion are observed (Figure 4.16G,H,K,L). This could suggest mitochondria within *Slc5a6*$^{R252W/R252W}$ mice are halted in fusion and unable to undergo mitochondrial fission. However, as the images are from TEM and represent a 2D cross-section, it is possible the mitochondria were arrested in fusion during collection and is not caused by the homozygous mutation. More *Slc5a6*$^{R252W/R252W}$ hearts are needed to confirm if mitochondrial fusion is affected. Additionally, cardiac samples from *Slc5a6*$^{+/+}$ mice should be included to compare ultrastructural changes observed in both *Slc5a6*$^{+/R252W}$ and *Slc5a6*$^{R252W/R252W}$ hearts. Therefore, at this stage it is not possible to draw any final conclusions from the TEM analysis

4.5 Discussion

The main aim of this chapter was to explore the effect of the patient's *SLC5A6* (p.R253W) mutation on the heart using a novel CRISPR-Cas9 generated mouse model. Initial *in silico* analysis of the patient mutation using prediction tools determined the amino acid substitution to be damaging and potentially disease causing, similar to previously reported mutations in *SLC5A6* (Subramanian et al., 2017; Byrne et al., 2019; Schwantje et al., 2019). Protein homology modelling of the human SLC5A6 protein vs mouse Slc5a6 revealed 88.4% sequence identity, with the amino acid residue R253 (human) conserved in mouse at position R252. Using CRISPR-Cas9 technology the R252 residue was altered to R252W, *Slc5a6*^{R252W}. This models the

patients as the mutation is present within every cell of the body, therefore it is possible that additional organs as well as the heart may be affected, as seen in the patient. As noted in 1.3.1, in addition to suffering poor cardiac output, our patient also showed signs of feeding difficulties, developmental delay and absent seizures, which suggest the R253W mutation may also influence cognitive development and intestinal absorption. The intestinal and brain phenotype is also described in two families with SLC5A6 mutations; however, no cardiac abnormalities were described (Subramanian *et al.*, 2017; Byrne *et al.*, 2019). Within our study however, only the heart was investigated in *Slc5a6*^{R252W} mice. Once generated, F1 *Slc5a6*^{R252W} mice survived embryogenesis and Mendelian inheritance ratio was observed at P21 (p= 0.986), allowing for cardiac function to be assessed in adulthood. However, sudden death of *Slc5a6*$^{R252W/R252W}$ mice occurred between 5.5-6.5 weeks (*n*=3). Histological staining of *Slc5a6*$^{R252W/R252W}$ (SD) revealed no gross cardiac defects, such as thinning of the myocardial walls or cardiac fibrosis. Due to post-mortem collection, blood pooling contributed to the ballooning of the right atria and ventricle, which impinged on the accuracy of the post-mortem analysis and therefore further litters were collected for thorough analysis. Collection of *Slc5a6*$^{R252W/R252W}$ hearts, which did not suffer sudden death, showed no obvious signs of pathological remodelling and were comparable to *Slc5a6*$^{+/+}$ and *Slc5a6*$^{+/R252W}$ hearts. Interestingly, weight monitoring of *Slc5a6*^{R252W} mice following weaning revealed *Slc5a6*$^{R252W/R252W}$ fail to gain weight compared to *Slc5a6*$^{+/+}$ and *Slc5a6*$^{+/R252W}$. A similar phenotype has been described by Ghosal *et al.* (2012), where they show mice with an intestinal specific KO of *Slc5a6* suddenly die due to acute peritonitis. *Slc5a6* is known to be expressed throughout the intestinal tract and is required for the vital absorption of biotin, PA and LA (Chatterjee *et al.*, 1999; Said, 2004; Said, 2011). As the focus of this project was to investigate the effect of the *R252W* mutation on the heart, exploration of other tissues was not performed and therefore cause of sudden death within the *Slc5a6*^{R252W} mouse line may have been due to intestinal abnormalities. The intestinal specific KO mice also show significant growth abnormalities (reduction in body weight) also observed in *Slc5a6*$^{R252W/R252W}$ mice. This phenotype is also reported in biotin deficient mouse models (Báez-Saldaña and Ortega, 2004; Pindolia *et al.*, 2011), contributing further evidence that death within the *Slc5a6*^{R252W} mouse line is may be due to impaired biotin absorption within the intestinal tract. Ghosal *et al.* (2012) also report significant

changes to the villi length throughout the intestinal tract. As villi length plays a major role in absorption of nutrients any decrease in length would result in a reduction in surface area to volume ratio, leading to a decrease in vitamin absorption (Pappenheimer and Michel, 2003). The premature death and weight phenotype in our *Slc5a6*$^{R252W/R252W}$ does draw some similarities with the intestinal specific *Slc5a6* KO model, and future work should look to further investigate the effect of the R252W mutation on the gastrointestinal tract to determine if abnormalities at the intestine are the cause of reduced body weight and premature death in F1 *Slc5a6*$^{R252W/R252W}$ mice. From the data presented in this chapter, it is suggested that *Slc5a6*$^{R252W/R252W}$ mice die before the development of a cardiac phenotype, as seen in the patient, possibly due to the homozygous *R252W* mutation causing nutritional deficiency by inefficient transport of biotin, PA and LA across the intestinal membrane. It is suggested that the lack of severe nutritional deficiency was not observed in our SLC5A6 patient due to clinical interventions described in 1.3.1, which included the insertion of a nasogastric tube to aid with feeding difficulties and the administration of TPN which contains essential nutrients including biotin, PA and LA, which was not provided to the *Slc5a6*$^{R252W/R252W}$ mice within this study.

Genetic background plays an important role in transgenic mouse models including CRISPR-Cas9 generated lines. The *Slc5a6*^{R252W} line was generated on a mixed genetic background potentially resulting in the presence of strain-specific modifiers not related to the targeted gene of interest, which may affect the severity of the disease phenotype (Rodriguez-Gil *et al.*, 2020). Similarly, off-target mutations have been widely reported when utilising CRISPR-Cas9 technology (Birling *et al.*, 2017). Off target mutations often occur at a higher frequency than the intended mutation, potentially leading to genome instability affecting the functionality of non-targeted genes which may also influence the phenotype of the mouse model (Zhang *et al.*, 2015). One way in which to reduce the occurrence of off-target mutations is to optimise the design of the guide RNA used. This can be achieved using various bioinformatic tools to improve CRISPR-Cas9 genome editing as reviewed by Rodríguez-Rodríguez *et al.* (2019). To rule out any effects of off-target mutations or conflicting strain-specific modifiers on the previously generated *Slc5a6*^{R252W} mouse line, genetic backcrossing was performed for 4 generations to achieve 93.75% C57BL/6 genetic background F4 *Slc5a6*^{R252W} mice.

From embryos collected at E15.5, F4 *Slc5a6*$^{R252W/R252W}$ mice were represented and followed the expected Mendelian inheritance, with no cardiac phenotype observed by histological staining (*n*=2). Subsequent litters were genotyped at P21, where it was apparent F4 *Slc5a6*$^{R252W/R252W}$ mice were not present at weaning, suggesting death was occurring postnatally. Collections at P0 (*n*=28) and P7 (*n*=1), narrowed the time frame to a loss of F4 *Slc5a6*$^{R252W/R252W}$ mice within the first week of life. Unfortunately, due to processing difficulties histological analysis could not be performed; however, the gross morphology of F4 *Slc5a6*$^{R252W/R252W}$ P0 hearts did appear comparable to *Slc5a6*$^{+/+}$ and *Slc5a6*$^{+/R252W}$ hearts upon collection.

Slc5a6 is responsible for the transport of essential nutrients required for energy metabolism and homeostasis. One of the largest physiological and metabolic changes to occur following birth is the shift in the reliance on glycolysis as the main process for producing energy to oxidative phosphorylation (Folmes *et al.*, 2011; de Carvalho *et al.*, 2017). To investigate whether the postnatal lethality in F4 *Slc5a6*$^{R252W/R252W}$ mice is due to energy metabolism defects, sections of P0 hearts were submitted for TEM imaging to look at the ultrastructure of the heart for indicators of mitochondrial dysfunction. Due to time constraints and breeding difficulties following the COVID-19 pandemic, only F4 *Slc5a6*$^{+/R252W}$ (*n*=3) and *Slc5a6*$^{R252W/R252W}$ (F4) (*n*=1) mice were investigated. Mitochondrial morphology is vitally linked to their overall functional capacity (Cogliati *et al.*, 2013), therefore mitochondrial structure within P0 hearts was investigated. Abnormalities affecting the cristae of mitochondria are linked to mitochondrial dysfunction contributing to the pathophysiology of disease phenotypes including mitochondrial disease and cardiomyopathies (Chung and Kang, 2015; Vincent *et al.*, 2016). Mitochondrial abnormalities were observed, including degradation of the cristae; site of the TCA cycle and OXPHOS, as well as the presence of fused mitochondria across both genotypes. Mitochondrial fusion and fission play an important role in regulating mitochondrial number and maintaining the mitochondrial genome, and help mitochondria adapt in response to changes in energy metabolism and mitochondrial damage (Chen *et al.*, 2005; Westermann, 2010). Defects in mitochondrial fission have been reported to cause elongated mitochondria due to an inability of fused mitochondria to disassociate, this includes the K38A mutation in *Dlp1,* a dynamin related protein*,* which resulted in elongated mitochondria which was shown to be caused by a GTPase binding defect (Yoon *et al.*, 2001). Interestingly, there are

a number of studies that have investigated the effect of downregulating mitochondrial GTPases which have been reviewed by Dai and Jiang (2019). Here they summarise the effect of knockout lines *in vitro* and *in vivo* and show if GTPases are overexpressed this results in enhanced OXPHOS whereas reduction in expression results in decreased OXPHOS and destabilisation of ETC complexes. As we observe a suspected defect in mitochondrial dynamics, future work should look to investigate the expression of mitochondrial fission and fusion proteins, *Dlp1/Drp1, Fis1* as well as *Mfn1/2/Opa1*, respectively. In F4 *Slc5a6*$^{R252W/R252W}$ mice, a potential issue in the mitochondrial fusion/fission pathway may have been identified; however, with only one heart included in the investigation it is difficult to discern whether this could be associated with the mutation or an artefact; by chance mitochondria were undergoing normal fusion/fission and were arrested mid-phase during processing. To confirm these changes, more *Slc5a6*$^{R252W/R252W}$ mice must be included in the analysis as well as *Slc5a6*$^{+/+}$ to draw accurate conclusions from the data. In addition, serial block face scanning electron microscopy (SBF-SEM) could be performed to achieve a more representative view of the 3D mitochondrial network throughout the cardiac section across the three genotypes. In addition, TEM images also show some evidence of mitochondrial disarray, potentially indicating some level of mitochondrial stress. A study by de Carvalho *et al.* (2017) into the energy metabolism requirements of early postnatal cardiomyocytes highlighted that oxygen consumption does not correlate with the expression of genes involved in energy metabolism as you would expect and therefore, gene expression may not be a good indicative tool to assess energy metabolism capacity within postnatal cardiomyocytes. Therefore, utilising methods such as Seahorse oxygen consumption assays would provide a more accurate determination of the efficiency of respiration within the postnatal F4 *Slc5a6*$^{R252W/R252W}$ hearts. Seahorse is a plate based technique which measures glycolytic flux and oxygen consumption rate of cells allowing determination of extracellular flux *in vitro* (Plitzko and Loesgen, 2018). A study by Readnower *et al.* (2012) has standardised the procedure for isolated cardiomyocytes and therefore this protocol could be utilised to investigate the bioenergetic profile of *Slc5a6*^{R252W} mice. Alternatively, Sakamuri *et al.* (2018) described a detailed protocol for the isolation of cardiac mitochondria for determining the respiratory rate of isolated mitochondria.

4.6 Conclusion

The data presented in this chapter suggests a defect in Slc5a6 results in *Slc5a6*$^{R252W/R252W}$ failing to thrive postnatally. Due to its essential role in vitamin transport, it is hypothesised that the R252W mutation reduces the efficiency of Slc5a6 to transport biotin, PA and LA which would have a negative impact on energy metabolism within the cell. However, further work is required to fully characterise the mitochondrial phenotype in F4 *Slc5a6*$^{R252W/R252W}$ and investigate the effect of the R252W mutation on energy metabolism. Overall, the CRISPR-Cas9 generated *Slc5a6*^{R252W} mouse model did not prove to be a suitable transgenic line to investigate the effect of the patient mutation on the heart. As the model did not recapitulate the cardiac phenotype observed in the patient, cre/loxP technology will be used to investigate the effect of global knockout of *Slc5a6* as well as targeted removal within the heart.

Chapter 5 Investigating the effect of a global conditional knockout of *Slc5a6* on the heart

5.1 Introduction

In addition to characterising the CRISPR-Cas9 generated *Slc5a6*$^{R252W/R252W}$ mouse line, a global conditional knockout mouse line was generated concurrently, to investigate the novel effect of dysfunctional protein, Slc5a6. To do this, the genome editing Cre-loxP technology was utilised, in which a targeted region within a gene is flanked by loxP sites. These sites are recognised and cleaved by *Cre* recombinase to remove the targeted site, generating a knockout mouse model. In this chapter, we will be utilising a promoter driven *Cre* recombinase, *Sox2Cre*, to drive *Cre* mediated recombination within *Slc5a6* in all epiblast-derived cells from E6.5 as described in 2.3.3 (Hayashi *et al.*, 2002).

5.1.1 Generation of the Slc5a6^{Sox2cre} *mouse model*

Slc5a6^{Sox2Cre} mice were generated as described in 2.1.3. Briefly, the *Slc5a6*$^{Tm1a/Tm1a}$ was found to be embryonic lethal, and therefore, tissue specific *Slc5a6* knockout mice were generated using a flippase (*Flp*) mouse which cleaves the FRT sites, removing the *lacZ-neomycin* cassette, resulting in the generation of the *Slc5a6*^{Tm1c} allele, referred to as *Slc5a6*^{F} from this point forward. (Figure 5.1). This allele was then crossed with a *Sox2Cre* recombinase mouse line which removes exons 7-10 during gastrulation.

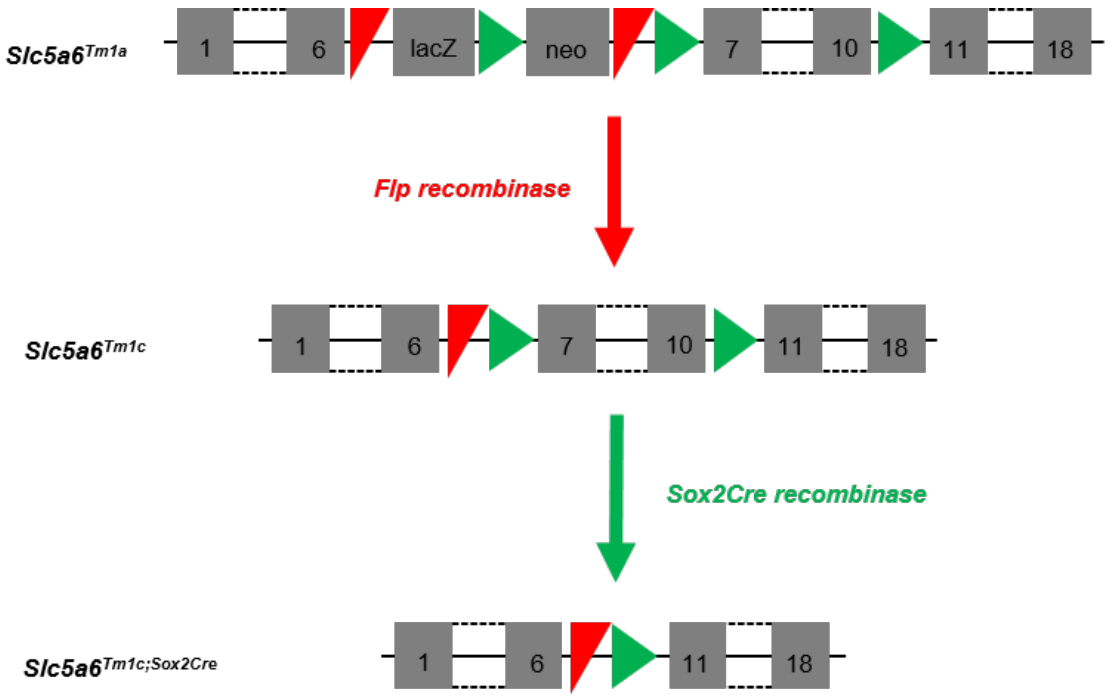

Figure 5.1. Generation of the global conditional *Slc5a6* knockout allele.
Modified from **Figure 2.3**. *Slc5a6*^{Tm1a} allele contains lacZ-neomycin cassette flanked by FRT sites (red) between exons 6-7 of *Slc5a6*. When crossed with a Flp recombinase mouse line, the FRT sites are cleaved to remove the lacZ-neomycin cassette generating the *Slc5a6*^{Tm1c} allele. LoxP sites (green) were also inserted to flank exons 7-10. When crossed with a *Cre* recombinase mouse line, Cre acts upon the loxP sites to remove exons 7-10, generating the *Slc5a6*$^{Tm1c;Sox2Cre}$ mouse line.

The targeted deletion results in splicing of exon 6-11, resulting in the introduction of a premature stop codon at exon 12 which allows a tissue specific *Slc5a6* knockout mouse to be generated when crossed with the appropriate promoter driven *Cre* recombinase mouse line (Figure 5.2).

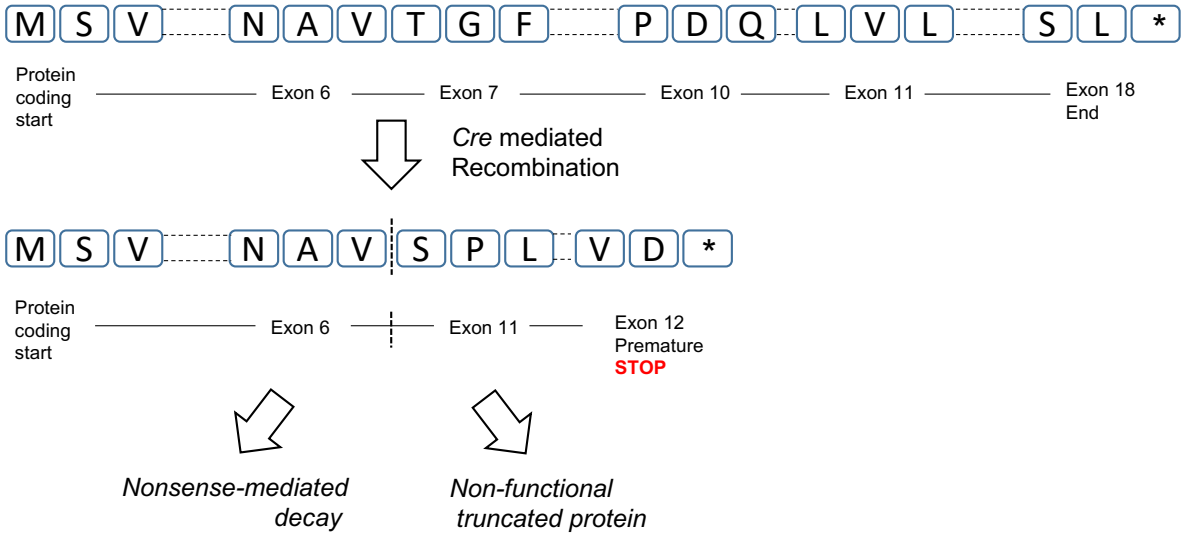

Figure 5.2. Effect of targeted deletion of *Slc5a6* critical region on protein coding sequence.
Simplified amino acid protein coding sequence is shown for Slc5a6, in addition to labels for relevant exon. Following removal of exon 7-10 by Cre recombinase, exon 6 becomes spliced to exon 11 causing a frameshift and the introduction of a premature stop codon within exon 12. At the protein level, the amino acid sequence reads NAV (exon 6) to SPL (exon 11), shifting the amino acid sequence causing the generation of a premature stop following VD in exon 12. This may result in nonsense-mediated decay of the mRNA sequence or generation of a truncated Slc5a6 protein. A = alanine, D = aspartate, F = phenylalanine, G = glycine, L = leucine, M = methionine, N = asparagine, P = proline, Q = glutamine, S = serine, T = threonine, V = valine, * = stop codon.

Global conditional *Slc5a6* knockout mouse line using *Sox2Cre* were obtained using the breeding strategy depicted in Figure 5.3. The use of Sox2Cre promoter driven *Cre* recombinase, allows for the targeted removal of exon 7-10 in all cells following gastrulation. Therefore, the early cardiac precursors which form from the mesoderm layer following gastrulation will contain the *Slc5a6* knockout allele in addition to cells formed within the developing ectoderm and endoderm which undergo further differentiation into specific tissue and organ types (Ivanovitch *et al.*, 2017). The generation of this global conditional *Slc5a6* mouse model involved breeding male *Sox2Cre* mice with female homozygous $Slc5a6^{F/F}$ mice. Resultant male heterozygous ($Slc5a6^{+/F;Sox2Cre}$) mice were then used to generate $Slc5a6^{F/F;Sox2Cre}$ mice, by further breeding with $Slc5a6^{F/F}$ females, for phenotypic analysis.

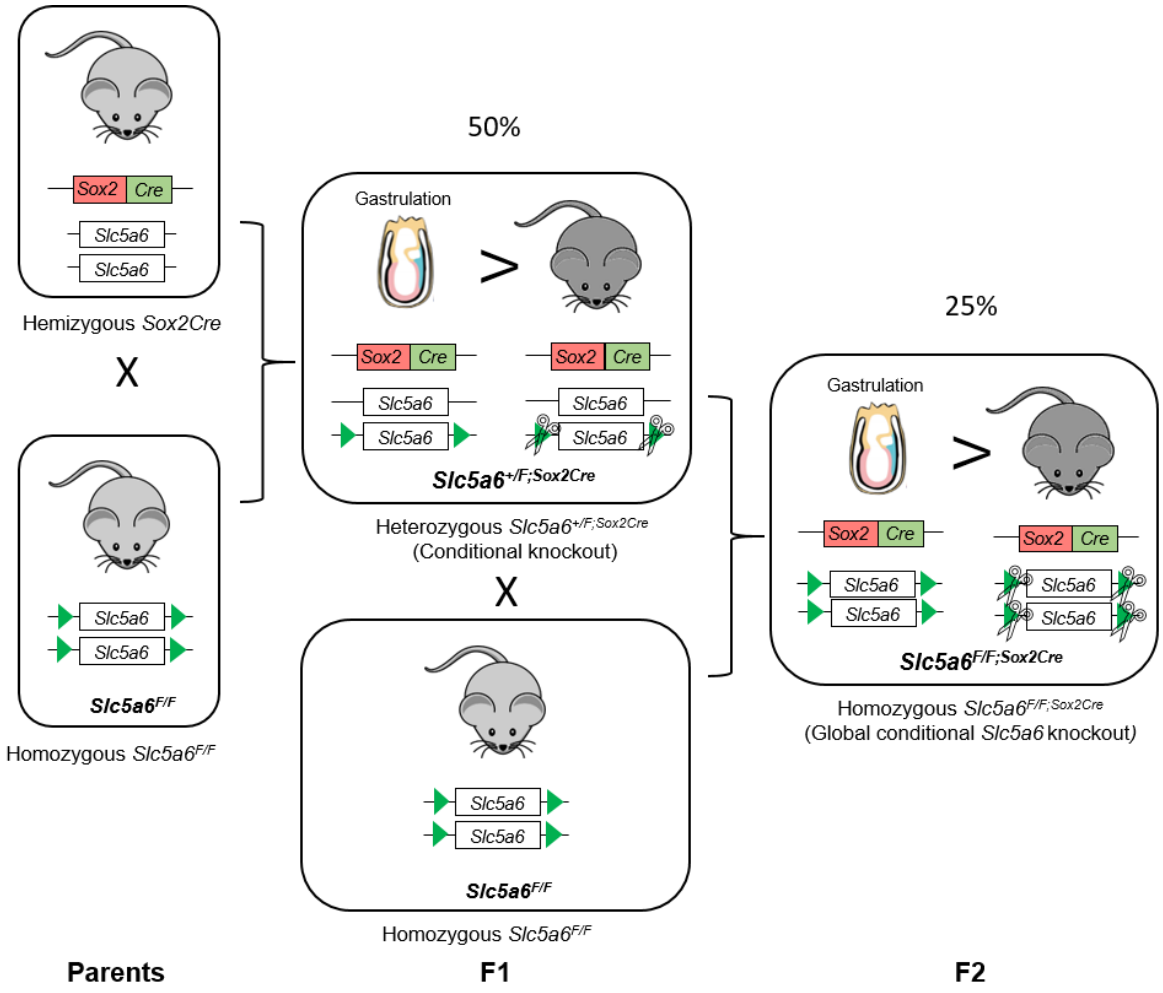

Figure 5.3. Breeding strategy for generating global conditional Slc5a6 knockout mice (*Slc5a6*$^{F/F;Sox2Cre}$).
Initially, a *Sox2Cre* male was bred with a homozygous *Slc5a6*$^{F/F}$ female. From this cross, heterozygous *Slc5a6*$^{+/F;Sox2Cre}$ male mice were further bred with *Slc5a6*$^{F/F}$ females to generate global conditional *Slc5a6* knockout mice (*Slc5a6*$^{F/F;Sox2Cre}$).

5.1.2 Aims of the chapter

Due to the postnatal death of CRISPR-Cas9 generated *Slc5a6*$^{R252W/R252W}$ mice prior to the development of a cardiac phenotype, we wanted to generate a mouse model which recapitulated the patient phenotype utilising *Cre-loxP* technology. As reduced functionality of *Slc5a6* was predicted to occur due to the R252W mutation, it was hypothesised that the global deletion of *Slc5a6* would recapitulate the development of cardiomyopathy.

Our main aim for this chapter is to investigate the effect of globally removing *Slc5a6* on the heart during development through to early adulthood. Cardiac morphology will be assessed by histological staining and cardiomyocyte ultrastructure will be investigated by transmission electron microscopy (TEM).

5.2 Phenotypic analysis of *Slc5a6*^{Sox2cre} mouse model

5.2.1 Slc5a6$^{F/F;Sox2Cre}$ *mice survive embryonic development*

As previously described, *Slc5a6*$^{F/F}$ female mice were crossed with *Slc5a6*$^{+/F;Sox2Cre}$ males to generate mutant *Slc5a6*$^{F/F;Sox2Cre}$ mice for phenotypic analysis. Embryos were collected and genotyped at three time points throughout development from E10.5 to E17.5. Chi-squared analysis showed the expected mendelian ratio was observed (Table 5.1), suggesting *Slc5a6*$^{F/F;Sox2Cre}$ embryos survive embryogenesis.

Table 5.1. Mendelian inheritance ratio of Slc5a6$^{F/F;Sox2Cre}$ mice during development. Chi-squared test was used to determine statistical significance.

Age	Total number	*Slc5a6*$^{F/F;Sox2Cre}$ expected	*Slc5a6*$^{F/F;Sox2Cre}$ observed	*p* value
E10.5	9	2.25	2	
E15.5	10	2.5	3	0.7477 ns
E17.5	27	6.75	5	

To investigate the effect of the global removal of *Slc5a6* within the heart, cardiac morphology was assessed during developmental stages E15.5 and E17.5.

5.2.2 No cardiac abnormalities are observed in Slc5a6$^{F/F;Sox2Cre}$ *during development*

At collection all embryos were imaged and investigated for any external gross abnormalities such as neural tube defects or the presence of oedema. From this, no gross embryonic defects were identified in *Slc5a6*$^{+/+}$ (Figure 5.4.A), *Slc5a6*$^{+/F;Sox2Cre}$ (Figure 5.4.B) or *Slc5a6*$^{F/F;Sox2Cre}$ (Figure 5.4.C) embryos at E15.5. Similarly, in embryos collected at E17.5 no gross abnormalities were identified in either *Slc5a6*$^{+/+}$ (Figure 5.4.D), *Slc5a6*$^{+/F;Sox2Cre}$ (Figure 5.4.E) or *Slc5a6*$^{F/F;Sox2Cre}$ (Figure 5.4.F) embryos.

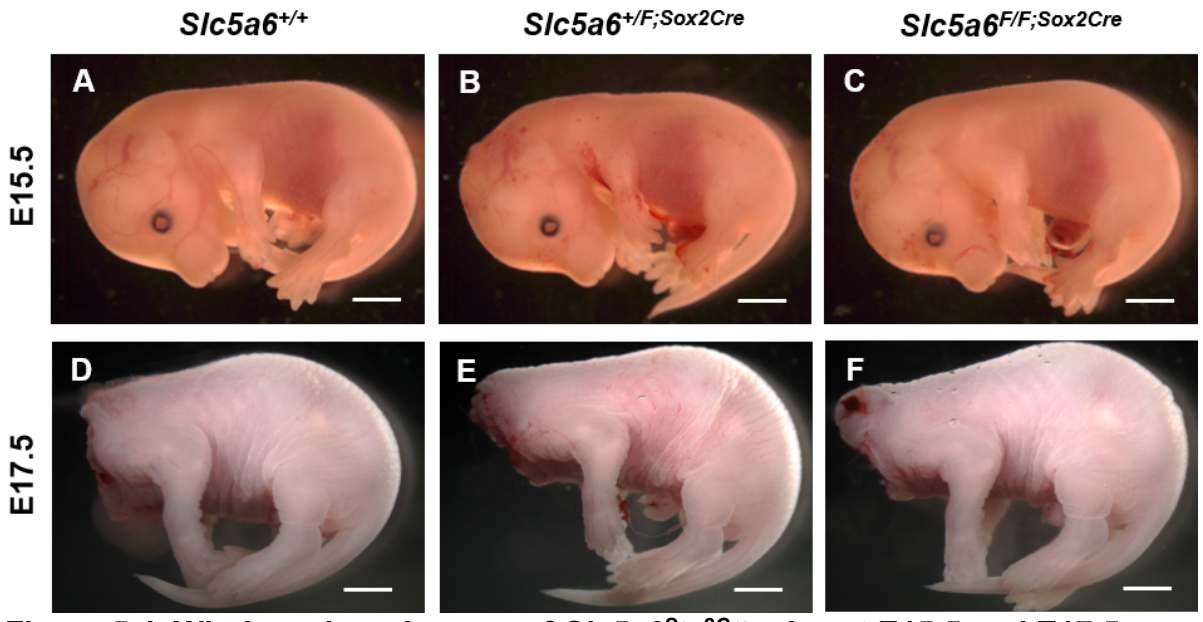

Figure 5.4. Whole embryo images of *Slc5a6*^{Sox2Cre} mice at E15.5 and E17.5. Images acquired at 0.63x magnification show no external abnormalities in *Slc5a6*$^{+/+}$ (A,D), *Slc5a6*$^{+/F;Sox2Cre}$ (B,E) or *Slc5a6*$^{F/F;Sox2Cre}$ (E,F) embryos at E15.5 and E17.5 respectively. E15.5 n = 3 *Slc5a6*$^{+/+}$, 4 *Slc5a6*$^{+/F;Sox2Cre}$ and 3 *Slc5a6*$^{F/F;Sox2Cre}$ E17.5 n = 14 *Slc5a6*$^{+/+}$, 8 *Slc5a6*$^{+/F;Sox2Cre}$ and 5 *Slc5a6*$^{F/F;Sox2Cre}$. Scale bar = 2mm.

Following collection, embryos were paraffin embedded and transversely sectioned to achieve a four-chamber view of the heart. Cardiac sections were then stained with H&E to assess the structure of the heart. No obvious cardiac abnormalities, such as ventricle septal defects (VSD) were apparent at E15.5 in *Slc5a6*$^{F/F;Sox2Cre}$ (Figure 5.5.C) embryos compared to control *Slc5a6*$^{+/+}$ (Figure 5.5.A) and *Slc5a6*$^{+/F;}$Sox2Cre (Figure 5.5.B) cardiac sections. Heart size was determined by calculating the cardiothoracic ratio for 3 cardiac sections per heart and compared between each genotype (Figure 5.5.D). This analysis measures the width of the heart relative to the thoracic chamber size. Here, we find no significant difference between *Slc5a6*$^{+/+}$ (white), *Slc5a6*$^{+/F;Sox2Cre}$ (black) and *Slc5a6*$^{F/F;Sox2Cre}$ (red) embryos at E15.5. In addition, the thickness of the left ventricle (LV) and right ventricle (RV) wall was measured in three sections per heart and compared between genotypes (Figure 5.5.D). This revealed that each genotype had a similar mean LV thickness ~0.08μm and average ~0.07μm in the RV.

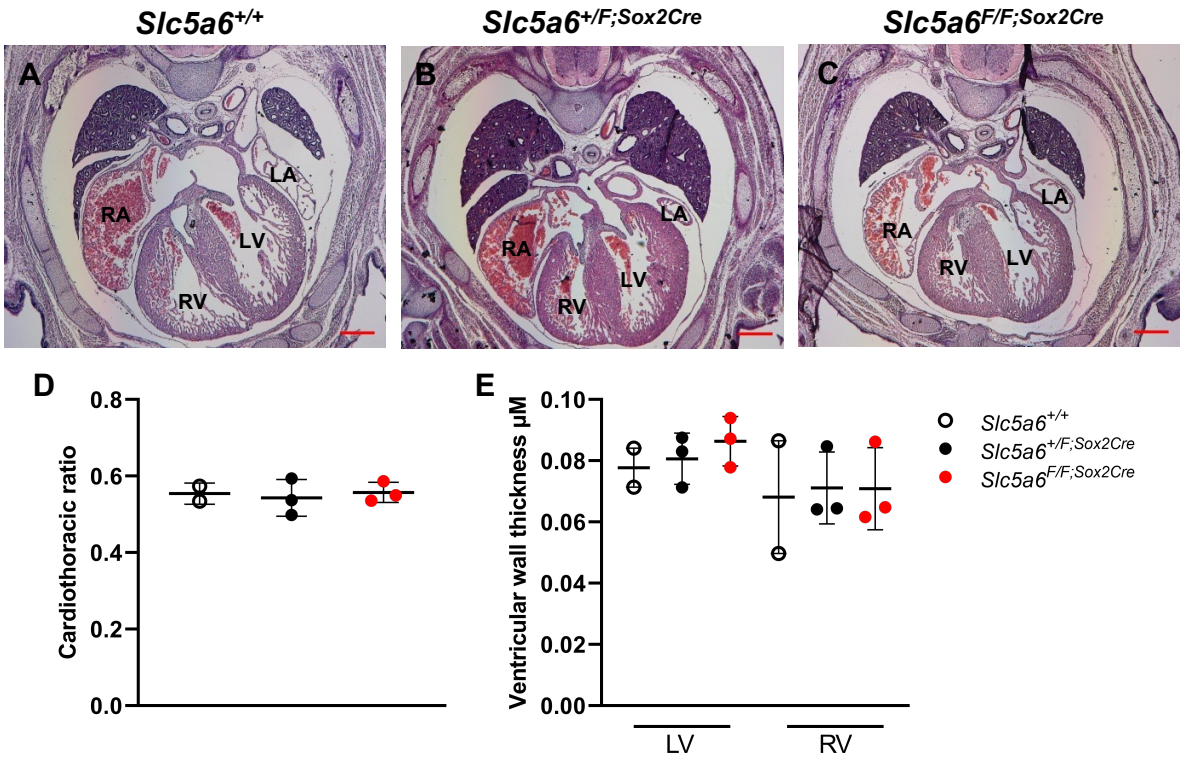

Figure 5.5. Histological staining and analysis of *Slc5a6*^{Sox2Cre} embryos at E15.5. Representative images of H&E staining of the heart are shown for *Slc5a6*$^{+/+}$ (A), *Slc5a6*$^{+/F;Sox2Cre}$ (B) and *Slc5a6*$^{F/F;Sox2Cre}$ (C) embryos. D) The cardiothoracic ratio was determined for *Slc5a6*$^{+/+}$ (white), *Slc5a6*$^{+/F;Sox2Cre}$ (black) and *Slc5a6*$^{F/F;Sox2Cre}$ (red) embryos. E) Ventricular wall thickness was measured in both the LV and RV for *Slc5a6*$^{+/+}$ (white), *Slc5a6*$^{+/F;Sox2Cre}$ (black) and *Slc5a6*$^{F/F;Sox2Cre}$ (red) embryos. n = 2 *Slc5a6*$^{+/+}$, 3 *Slc5a6*$^{+/F;Sox2Cre}$ and 3 *Slc5a6*$^{F/F;Sox2Cre}$. Data shown as mean±SD except where *n* =2 then shown as mean±SEM. A-C Scale bar A-C = 500µm. Left atria LA, left ventricle LV, right atria RA, right ventricle RV.

Investigation into the effect of the global loss of *Slc5a6* on the heart continued in embryos collected at E17.5 (Figure 5.6). Similar to embryos at E15.5, hearts at E17.5 show no obvious gross abnormalities in *Slc5a6*$^{+/+}$ (Figure 5.6.A), *Slc5a6*$^{+/F;Sox2Cre}$ (Figure 5.6.B), *Slc5a6*$^{F/F;Sox2Cre}$ (Figure 5.6.C). Ventricular wall thickness measurements show no significant difference between *Slc5a6*$^{F/F;Sox2Cre}$ (red) and *Slc5a6*$^{+/+}$ (white), *Slc5a6*$^{+/F;Sox2Cre}$ (black) embryos in both the left and right ventricle (p>0.9999 for all comparisons in LV and RV) (Figure 5.6.E). The cardiothoracic ratio was determined and we find no significant difference between *Slc5a6*$^{F/F;Sox2Cre}$ and *Slc5a6*$^{+/+}$ (p>0.9999) as well as *Slc5a6*$^{+/F;Sox2Cre}$ (p>0.9999) embryos (Figure 5.6.D).

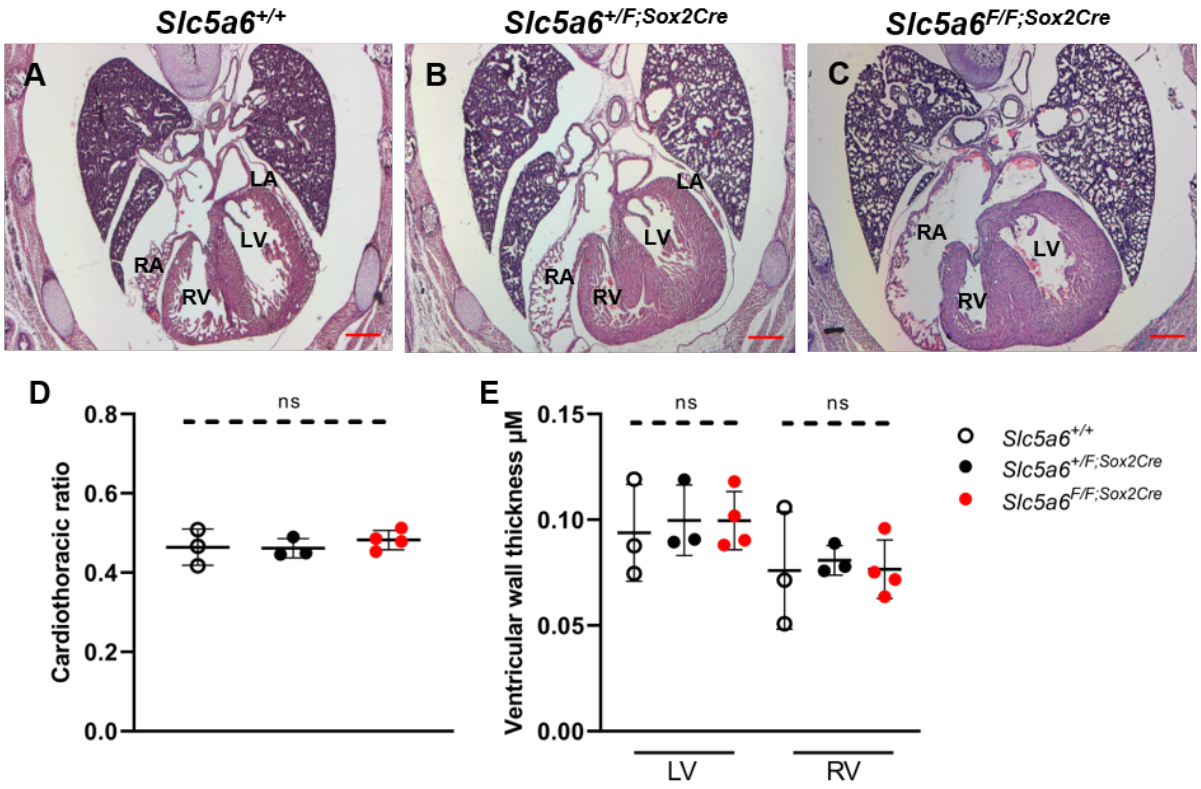

Figure 5.6. Histological staining and analysis of *Slc5a6*^{Sox2Cre} embryos at E17.5. Representative H&E images of *Slc5a6*$^{+/+}$ (A), *Slc5a6*$^{+/F;Sox2Cre}$ (B) and *Slc5a6*$^{F/F;Sox2Cre}$ (C) cardiac sections. D) Cardiothoracic ratio shown for *Slc5a6*$^{+/+}$ (white), *Slc5a6*$^{+/F;Sox2Cre}$ (black) and *Slc5a6*$^{F/F;Sox2Cre}$ (red) embryos. E) Ventricular wall thickness in both the LV and RV for *Slc5a6*$^{+/+}$ (white), *Slc5a6*$^{+/F;Sox2Cre}$ (black) and *Slc5a6*$^{F/F;Sox2Cre}$ (red) embryos. n = 3 *Slc5a6*$^{+/+}$, 3 *Slc5a6*$^{+/F;Sox2Cre}$ and 4 *Slc5a6*$^{F/F;Sox2Cre}$. One-way ANOVA with multiple comparisons and Bonferroni correction, ns= no signifcance. Scale bar A-C = 500µm. Left atria LA, left ventricle LV, right atria RA, right ventricle RV.

Histological staining and analysis of embryos during development suggest the global conditional loss of *Slc5a6* does not affect the formation of the heart or development of the ventricular wall. Following this analysis, embryos were then allowed to litter for postnatal analysis.

5.2.3 Perinatal death occurs in Slc5a6$^{F/F;Sox2Cre}$*mice*

Following developmental analysis, *Slc5a6*^{Sox2Cre} mice were allowed to litter and genotyped at weaning, postnatal day (P) 21, which revealed *Slc5a6*$^{F/F;Sox2Cre}$ mice were not present at weaning. This prompted collections at birth to ensure *Slc5a6*$^{F/F;Sox2Cre}$ pups survived the birthing process and throughout the first week of life (Table *5.2*). Genotypic analysis revealed from a total of 78 pups collected at P0, ~19

Slc5a6$^{F/F;Sox2Cre}$ pups were expected; however, only 12 pups were observed alive. This shows that *Slc5a6*$^{F/F;Sox2Cre}$ pups were slightly underrepresented at birth (p=0.267). At collection all pups had noticeable milk spots suggesting the pups were able to feed and were not abandoned by the dam. However, it is possible that pups were born dead and were eaten by the dam prior to collection. Further collections beyond P0 showed only three *Slc5a6*$^{F/F;Sox2Cre}$ pups survived past the first day of birth; one at P2 and two pups found dead at P4. This suggests that *Slc5a6*$^{F/F;Sox2Cre}$ pups are failing to thrive in the first week of life (*p*=0.009).

Table 5.2. Mendelian inheritance ratio of expected and observed Slc5a6$^{F/F;Sox2Cre}$ postnatal mice.
Number of Slc5a6$^{F/F;Sox2Cre}$ pups found dead are listed. Chi-squared test was used to determine statistical significance.

Age	Total number	*Slc5a6*$^{F/F;Sox2Cre}$ expected	*Slc5a6*$^{F/F;Sox2Cre}$ observed	*Slc5a6*$^{F/F;Sox2Cre}$ dead	*p* value
P0	77	19.25	12	-	0.267 ns
P2	11	2.75	1	-	
P4	11	2.75	2	2	0.009 *
P9	8	2	0	-	
P21	33	8.25	0	-	

The aim of this chapter was to investigate the effect of the global loss of *Slc5a6* on the heart. At collection, the dissected hearts were imaged and investigated for any gross structural abnormalities (Figure *5.7*). This revealed no obvious gross cardiac structural abnormalities in *Slc5a6*$^{+/+}$ (Figure *5.7*.A), *Slc5a6*$^{+/F;Sox2Cre}$ (Figure *5.7*.B) or *Slc5a6*$^{F/F;Sox2Cre}$ (Figure *5.7*.C) pups.

Figure 5.7. Whole heart images of *Slc5a6*^{Sox2Cre} hearts collected at P0.
Representative images of the heart at P0 for *Slc5a6*$^{+/+}$ (A), *Slc5a6*$^{+/F;Sox2Cre}$ (B) and *Slc5a6*$^{F/F;Sox2Cre}$ (C) pups. n= 34 *Slc5a6*$^{+/+}$, 15 *Slc5a6*$^{+/F;Sox2Cre}$, 12 *Slc5a6*$^{F/F;Sox2Cre}$. Scale bar = 1mm.

To assess the effect of global loss of *Slc5a6* on the structure of the heart at P0, at collection a 2mm piece of the heart was taken for ultrastructural analysis by TEM and the remainder of each heart was paraffin wax embedded for histological staining. However, due to processing difficulties, P0 hearts could not be sectioned due to tissue crumbling. Due to the Covid-19 pandemic, further *Slc5a6*$^{F/F;Sox2Cre}$ mice could not be collected for analysis. Although the structure of the heart could not be assessed histologically, the ultrastructure of the heart could still be investigated by TEM.

5.2.4 Ultrastructural defects present in the hearts of Slc5a6$^{F/F;Sox2Cre}$*mice*

As previously described, a 2mm piece of the heart of each genotype was collected for TEM imaging; 4 *Slc5a6*$^{+/+}$, 3 *Slc5a6*$^{+/F;Sox2Cre}$ and 4 *Slc5a6*$^{F/F;Sox2Cre}$. The tissue was processed by the electron microscopy research service (EMRS), Newcastle University. Once processed, TEM images were acquired at 3,000x, 8,000x and 15,000x magnifications to assess the ultrastructural integrity of the cardiomyocytes within the heart (Figure *5.8*). Low power TEM images at 3,000x show *Slc5a6*$^{+/+}$ (Figure *5.8*.A) and *Slc5a6*$^{+/F;Sox2Cre}$ (Figure *5.8*.B) cardiomyocytes have intact sarcomeres with mitochondria evenly distributed between myofibrils. This is also observed in some areas of *Slc5a6*$^{F/F;Sox2Cre}$ hearts shown in Figure *5.8*.D; however, more frequently mitochondria appeared severely degraded and disorganised highlighted in Figure *5.8*.C. Higher power images show *Slc5a6*$^{+/+}$ (Figure *5.8*.E,I) and *Slc5a6*$^{+/F;Sox2Cre}$ (Figure *5.8*.F,J) mitochondria have well defined cristae with some minor degradation (red asterisk); however, this appears more widespread within *Slc5a6*$^{F/F;Sox2Cre}$ hearts

where mitochondrial cristae are almost absent (Figure *5.8*.G). Mitochondrial cristae are essential for energy production and therefore the absence of these structures suggest energy metabolism is severely compromised within *Slc5a6*$^{F/F;Sox2Cre}$ hearts. In addition to the absence of mitochondrial cristae, *Slc5a6*$^{F/F;Sox2Cre}$ cardiomyocytes also appear to have more prevalent degradation by mitochondrial herniation as indicated by red arrowheads (Figure *5.8*.G,K-L), compared to *Slc5a6*$^{+/+}$ (Figure *5.8*.E) and *Slc5a6*$^{+/F;Sox2Cre}$ (Figure *5.8*.F) hearts. Mitochondrial herniation can occur in response to stress, which causes the mitochondrial matrix to swell and the cristae to unfold. This results in the rupturing of the outer membrane, often observed in the late stages of apoptosis (Mannella, 2020). Another interesting observation made in a *Slc5a6*$^{F/F;Sox2Cre}$ heart was the presence of giant mitochondrion (Figure *5.8*.H). This giant mitochondrion appears to consist of several mitochondria fused together with marked cristae degradation suggesting impaired metabolic function.

In addition to visually identifying ultrastructural defects, changes to mitochondrial shape can be quantified for comparison between genotypes.

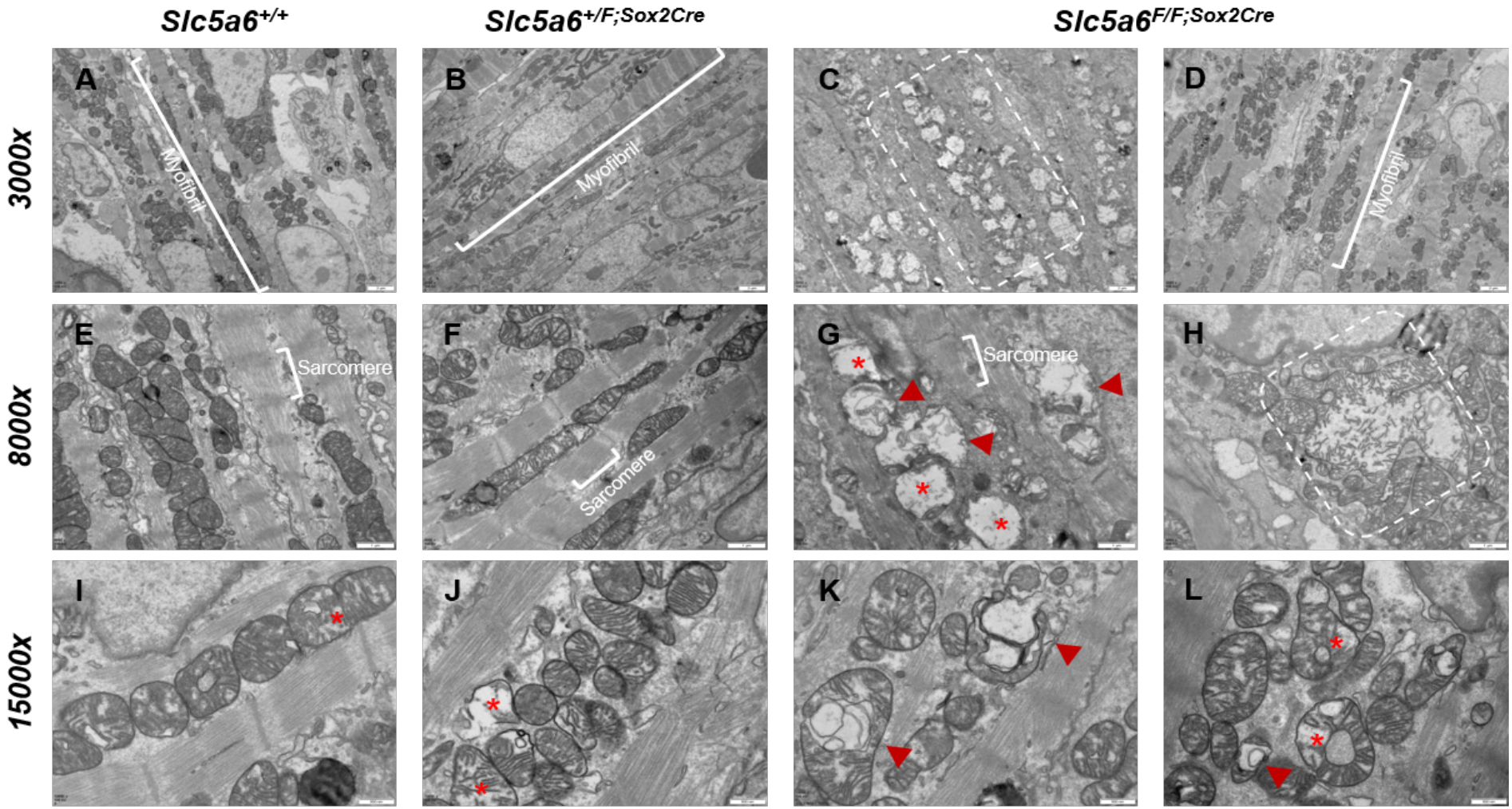

Figure 5.8. Transmission electron microscopy images of *Slc5a6*^{Sox2Cre} mice at P0.
Representative micrographs of *Slc5a6*$^{+/+}$ (A,E,I), *Slc5a6*$^{+/F;Sox2Cre}$ (B,F,J) and *Slc5a6*$^{F/F;Sox2Cre}$ (C-D,G-H,K-L) at 3,000x, 8,000x and 15,000x magnification. Sarcomeres appear intact with mitochondria even distributed between myofibrils as shown in *Slc5a6*$^{+/+}$ (A) and *Slc5a6*$^{+/F;Sox2Cre}$ (B). In *Slc5a6*$^{F/F;Sox2Cre}$ hearts, some cardiomyocytes have a similar morphology to littermate controls (D), whereas some appear to have widespread mitochondrial disorganisation and degradation highlighted by white dashed box (C). Mitochondrial cristae breakdown (red asterisk) and mitochondrial degradation (red arrowhead) is noted in each genotype, however, is more prevalent in *Slc5a6*$^{F/F;Sox2Cre}$ hearts (G,K-L). Giant mitochondria was also identified (white dashed box) in a *Slc5a6*$^{F/F;Sox2Cre}$ heart (H). n = 4 *Slc5a6*$^{+/+}$, 3 *Slc5a6*$^{+/F;Sox2Cre}$ and 4 *Slc5a6*$^{F/F;Sox2Cre}$.

Mitochondria were manually traced to determine shape descriptors including area and perimeter (μm) which are used to calculate form factor, an indicator of branching and complexity of the mitochondria. Aspect ratio was calculated using the minor and major axis of the mitochondria to indicate length-width ratio. Circularity is a measure of mitochondrial sphericity and Feret's diameter (μm) which represents the largest distance between two points within any mitochondrion. Table *5.3* shows the median and mean (± standard deviation) for each parameter of *Slc5a6*$^{+/+}$, *Slc5a6*$^{+/F;Sox2Cre}$ and *Slc5a6*$^{F/F;Sox2Cre}$ mitochondria. To determine if the datasets follow the normal Gaussian distribution, the level of skewness was determined. Skewness is defined as a measure of asymmetry in the distribution of data where '0' is equal to a normally distributed dataset, '>0' indicates a larger proportion of smaller values are found than expected and, '<0' shows a bigger proportion of large values than expected. From this analysis, data is shown to be skewed >1 for all parameters, except circularity (~-1.1), in *Slc5a6*$^{+/+}$, *Slc5a6*$^{+/F;Sox2Cre}$ and *Slc5a6*$^{F/F;Sox2Cre}$ mitochondria resulting in the need for non-parametric Kruskal-Wallis statistical test with multiple comparisons and Dunn's correction to be performed on each dataset. Data for each mitochondrion was placed into one of 10 bins of equal sizes to visualise the frequency distribution of each morphological parameter (Figure *5.9*).

Table 5.3. Shape descriptors for mitochondria in P0 *Slc5a6*^{Sox2Cre} hearts.
Skewness was calculated for each parameter as a measure of asymmetry in distribution of data where '0' is equal to a normally distributed population. n = 4 *Slc5a6*$^{+/+}$, 3 *Slc5a6*$^{+/F;Sox2Cre}$, 4 *Slc5a6*$^{F/F;Sox2Cre}$ hearts, mitochondrial n = 361 *Slc5a6*$^{+/+}$, 356 *Slc5a6*$^{+/F;Sox2Cre}$, 362 *Slc5a6*$^{F/F;Sox2Cre}$.

Shape descriptor	*Slc5a6*$^{+/+}$			*Slc5a6*$^{+/F;Sox2Cre}$			*Slc5a6*$^{F/F;Sox2Cre}$		
	Median	Mean ± SD	Skewness	Median	Mean ± SD	Skewness	Median	Mean ± SD	Skewness
Aspect ratio	1.489	1.755±0.713	1.711	1.617	2.018±1.142	2.897	1.517	1.799±0.798	2.088
Form factor	1.155	1.279±0.325	2.434	1.182	1.362±0.467	3.198	1.143	1.323±0.416	2.566
Area µm	0.601	0.705±0.428	1.577	0.548	0.704±0.734	5.768	0.713	0.946±0.924	5.856
Perimeter µm	2.985	3.272±1.270	1.428	2.851	3.252±1.540	1.627	3.270	3.743±1.900	2.572
Circularity (0-1)	0.866	0.817±0.147	-1.159	0.846	0.788±0.169	-1.119	0.875	0.805±0.165	-1.194
Feret's diameter µm	1.103	1.250±0.539	1.421	1.106	1.277±0.645	1.414	1.254	1.420±0.722	1.696

In addition to plotting the frequency distribution, median values (±95% confidence interval) were plotted for each parameter with the non-parametric statistical significance noted on each graph (Figure *5.9*). This analysis revealed no significant difference was observed between *Slc5a6*$^{+/+}$ (white), *Slc5a6*$^{+/F;Sox2Cre}$ (black) and *Slc5a6*$^{F/F;Sox2Cre}$ (red) mitochondrial complexity indicated by form factor (Figure *5.9*D) or circularity (Figure *5.9*L). We do observe a significant increase in the length-width ratio (aspect ratio) in the mitochondria of *Slc5a6*$^{+/F;Sox2Cre}$ hearts compared to *Slc5a6*$^{+/+}$ (p=0.0102) and *Slc5a6*$^{F/F;Sox2Cre}$ (p=0.0361) mitochondria (Figure *5.9*B). Feret's diameter; largest distance between two mitochondrial axis, was significantly increased in *Slc5a6*$^{F/F;Sox2Cre}$ compared to *Slc5a6*$^{+/+}$ (p=0.0126) and *Slc5a6*$^{+/F;Sox2Cre}$ (p=0.0048) (Figure *5.9*F), suggesting mitochondria are larger in *Slc5a6*$^{F/F;Sox2Cre}$ hearts compared to littermate controls. This is also shown by a significant increase in mitochondrial area (Figure *5.9*H) and perimeter (Figure *5.9*J) in *Slc5a6*$^{F/F;Sox2Cre}$ hearts compared to *Slc5a6*$^{+/+}$ (area p=0.0039, perimeter p=0.0081) and *Slc5a6*$^{+/F;Sox2Cre}$ (area p<0.0001, perimeter p<0.0001). However, for the remaining parameters there was no significant difference observed between *Slc5a6*$^{+/F;Sox2Cre}$ and *Slc5a6*$^{+/+}$ mitochondria, with all p values >0.999.

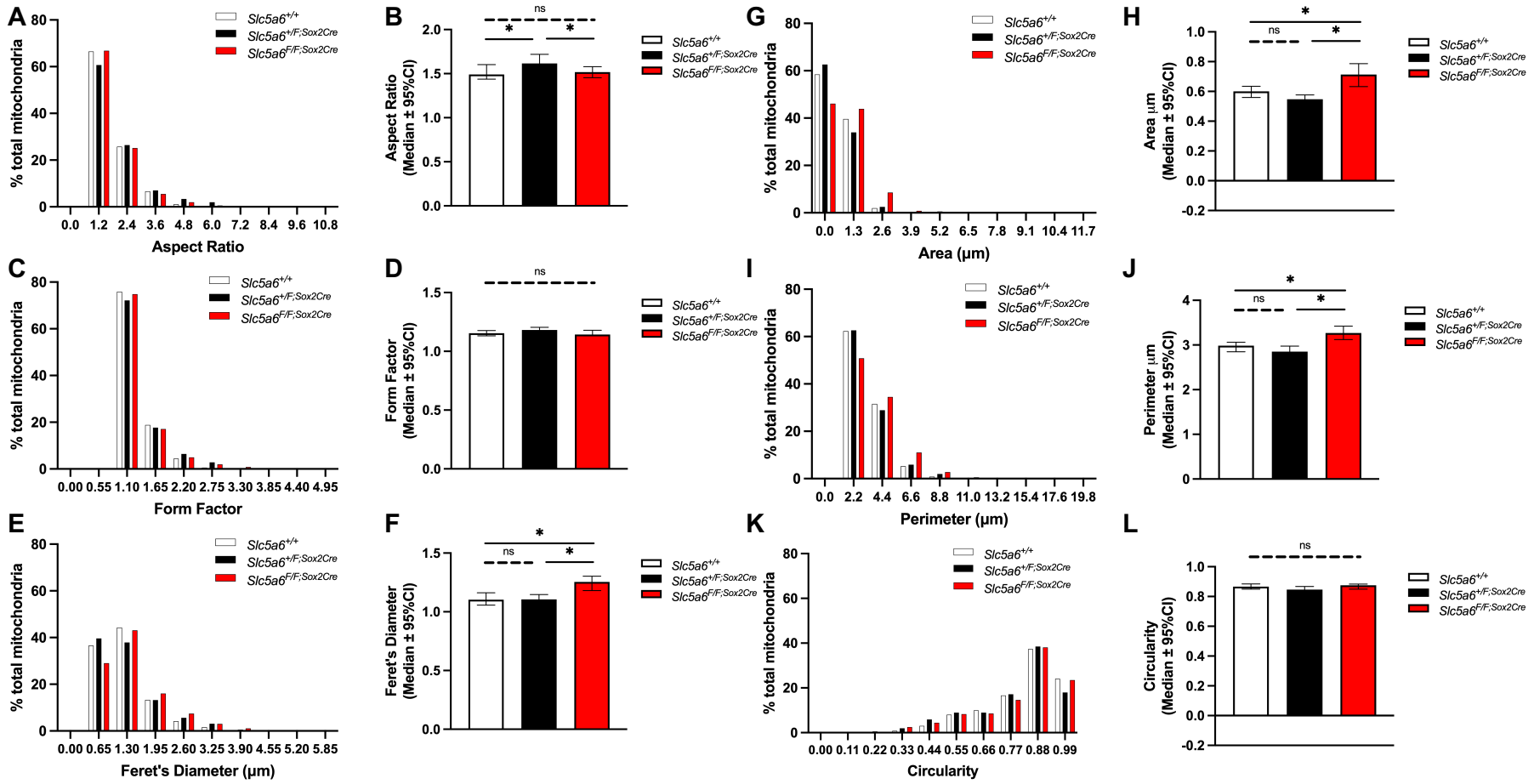

Figure 5.9. Quantification of mitochondrial shape descriptors of *Slc5a6*^{Sox2Cre} mice at P0.
Mitochondria were manually traced in micrographs taken at 8000x to quantify morphological changes for *Slc5a6*$^{+/+}$ (white), *Slc5a6*$^{+/F;Sox2Cre}$ (black) and *Slc5a6*$^{F/F;Sox2Cre}$ (red) mitochondria. Frequency distribution graphs were generated for each parameter (A,C,E,G,I,K). The median of data collected *is shown* (B,D,F,H,J,L). Non-parametric Kruskal-Wallis statistical test with Dunn's multiple comparisons; ns = not significant, * = p<0.05. n = 4 *Slc5a6*$^{+/+}$, 3 *Slc5a6*$^{+/F;Sox2Cre}$, 4 *Slc5a6*$^{F/F;Sox2Cre}$, mitochondria n = 361 *Slc5a6*$^{+/+}$, 356 *Slc5a6*$^{+/F;Sox2Cre}$, 362 *Slc5a6*$^{F/F;Sox2Cre}$

Together, the TEM images showing severe mitochondrial degradation in addition to the significant increase in mitochondrial size, suggest mitochondrial stress within *Slc5a6*$^{F/F;Sox2Cre}$ hearts compared to littermate controls. Reduced mitochondrial structure and function in *Slc5a6*$^{F/F;Sox2Cre}$ hearts may explain why *Slc5a6*$^{F/F;Sox2Cre}$ pups are underrepresented following birth within the first week of life as energy metabolism switches from predominantly cytosolic glycolysis *in utero,* to aerobic respiration by oxidative phosphorylation (OXPHOS) within the mitochondria. Further work to characterise the metabolic switch and mitochondrial function in *Slc5a6*$^{F/F;Sox2Cre}$ mice was to be performed; however, due to the Covid-19 pandemic further investigation was not possible.

5.3 Discussion

The main aim for this chapter was to investigate the effect of globally removing *Slc5a6* on the heart during development through to early adulthood. In this chapter it was shown that *Slc5a6*$^{F/F;Sox2Cre}$ mice survive embryogenesis and are present throughout development at the expected Mendelian ratio. Collection at both E15.5 and E17.5 showed no gross embryonic abnormalities such as variation in embryo size or presence of oedema in *Slc5a6*$^{F/F;Sox2Cre}$ embryos compared to littermate controls. Histological staining of cardiac sections revealed comparable cardiac structural development between each genotype without any gross cardiac abnormalities present at either E15.5 and E17.5. The cardiothoracic ratio and ventricle wall thickness was also comparable between *Slc5a6*$^{+/+}$, *Slc5a6*$^{+/F;Sox2Cre}$ and *Slc5a6*$^{F/F;Sox2Cre}$ embryos suggesting loss of *Slc5a6* does not affect the development and maturation of the heart. Interestingly, it was shown that *Slc5a6*$^{F/F;Sox2Cre}$ mice were significantly underrepresented following birth (P0) and absent from litters at weaning (p=0.006). Further collections throughout the first week of life revealed only one *Slc5a6*$^{F/F;Sox2Cre}$ pup alive after P0, which was collected at P2 with an additional two dead *Slc5a6*$^{F/F;Sox2Cre}$ pups collected at P4. This suggests the global loss of *Slc5a6* is affecting survival following birth. Due to processing difficulties, the collected P0 hearts could not be investigated histologically; however, ultrastructural analysis was performed by TEM. Imaging revealed all the *Slc5a6*$^{F/F;Sox2Cre}$ hearts had severely degraded mitochondrial cristae as well as herniation of the mitochondrial contents, which may have a detrimental effect on energy production within the heart. Quantification of mitochondrial morphology showed mitochondria were significantly larger in *Slc5a6*$^{F/F;Sox2Cre}$ hearts compared to littermate controls, suggesting

dysregulation of mitochondrial morphogenesis possibly caused by mitochondrial stress. However, further investigation into mitochondrial biogenesis, dynamics and function is needed to fully characterise the effect of the global loss of *Slc5a6* on cardiac mitochondria, and how this affects postnatal survival.

Slc5a6$^{F/F;Sox2Cre}$ embryos survived embryogenesis without any cardiac abnormalities observed. As shown in Chapter 3, *Slc5a6* is expressed at low levels during cardiac development and following birth, therefore the global conditional removal of *Slc5a6* was not expected to affect embryonic or fetal survival. However, *Slc5a6*$^{F/F;Sox2Cre}$ mice were shown to be underrepresented at birth and did not survive past the first two days of life. Interestingly, perinatal death also occurred in *Slc5a6*$^{R252W/R252W}$ F4 mice as described in Chapter 4, with only one mutant pup found alive at P7, which suggests *Slc5a6* is required for postnatal survival. There are many components and conditions which need to be met for the embryo to survive following birth. Turgeon and Meloche (2009) describe that over the first 24 hours following birth, three physiological processes are required for survival; respiratory function, energy metabolism and homeostasis, and the ability of the newborn pup to suckle. The most vital to immediate survival of the newborn pup is the ability to take its first breath, without which the mice remain cyanotic and die within minutes (Matzuk *et al.*, 1995; Turgeon and Meloche, 2009). As *Slc5a6*$^{F/F;Sox2Cre}$ pups collected at P0 were alive hours following birth and did not display signs of cyanosis, it is possible to hypothesise that *Slc5a6*$^{F/F;Sox2Cre}$ mice were able to breathe independently and perinatal loss was not due to respiratory insufficiency. Successful respiration following birth triggers a cascade of changes throughout the newborn body, most notable is the effect on the heart and circulatory system (Tan and Lewandowski, 2020). Following birth, the heart is subjected to an increase in haemodynamic load as oxygen content increases. This increase in workload for the heart and increased availability of oxygen prompts the change in metabolic pathways from anaerobic glycolysis to aerobic respiration via FAO (Lopaschuk *et al.*, 1991; Ritterhoff and Tian, 2017; Talman *et al.*, 2018). A key transcription factor heavily involved in the embryonic survival whilst under the hypoxic conditions *in utero* is Hif1a *(Eltzschig and Carmeliet, 2011)*. This is a master regulator of over 40 genes that encode proteins which act to increase the transportation and utilisation of oxygen during hypoxic conditions (Eckle *et al.*, 2013). A study by Iyer *et al.* (1998) showed *Hif1a*$^{-/-}$ mice die during mid-gestation (E10.5) with severe

cardiovascular defects such as myocardial disorganisation and signs of cardiac stress including myocardial hyperplasia as well as non-cardiac features (enlargement of hindbrain and neural tube prolapse). Whereas *Hif1a+/-* embryos survive and develop normally compared to Hif1a+/+ embryos but demonstrate a more severe response to hypoxia including a significant decrease in weight gain and development of pulmonary hypertension (Yu *et al.*, 1999). Additionally, transcriptional control of genes involved in the glycolytic pathway was demonstrated to be mediated by *Hif1a* expression during hypoxic conditions (Iyer *et al.*, 1998). Together these studies have shown *Hif1a* is directly involved in the development of essential physiological systems required for survival during embryogenesis and postnally. As *Slc5a6* transports essential substrates vital for the contribution of intermediates for energy metabolism, it is possible that the global removal of *Slc5a6* within newborn pups is severely affecting this process, which is essential for postnatal survival. Further investigation into the role of *Hif1a* and genes involved in the metabolic switch in *Slc5a6*$^{F/F;Sox2Cre}$ late embryonic and postnatal hearts may help to unpick the underlying cause of perinatal death occurring within this mouse model.

Investigation into the ultrastructure of *Slc5a6*$^{F/F;Sox2Cre}$ hearts collected at P0 showed severe mitochondrial degradation, suggesting loss of *Slc5a6* is having a detrimental effect on mitochondrial structure and causing dysfunction. Mitochondrial dysfunction can occur in response to electron transport defects, insufficient mitochondrial number to cope with energy demand or a reduction in substrate availability required for energy metabolism (Nicolson, 2014). However, when dysfunctional mitochondria are present, three processes can be activated to mitigate any detrimental effects on overall cell function. Mitochondrial fusion of dysfunctional mitochondria allows for the pooling of unaffected components of the mitochondria to maintain overall mitochondrial function (Scott and Youle, 2010). Mitochondria fission, whereby daughter mitochondria are produced to increase mitochondrial number within the cell, and mitophagy, which allows for the complete degradation of dysfunctional mitochondria (Twig and Shirihai, 2011; Nicolson, 2014). TEM images acquired in *Slc5a6*$^{F/F;Sox2Cre}$ found an enlarged mitochondria with partially intact mitochondrial cristae. This may be a mitochondrion which has undergone mitochondrial fusion in order to preserve cristae structure and maintain overall function. Additionally, mitochondria within *Slc5a6*$^{F/F;Sox2Cre}$ hearts also show severe degradation without the presence of autophagosomes suggesting

mitophagy is not the cause of degradation within the cardiac mitochondria. This leads us to hypothesise that the mitochondrial degradation may be due to apoptosis and the activation of BAK-BAX pathway. Mitochondrial apoptosis is mediated by two proteins, BAK and BAX, which when activated, the two proteins act to permeabilise the outer mitochondrial membrane (OMM) causing herniation of mitochondrial contents and cytochrome c release which then triggers activation of apoptotic caspases (McArthur *et al.*, 2018). To confirm mitochondrial degradation in *Slc5a6*$^{F/F;Sox2Cre}$ postnatal hearts is caused by apoptosis, cleaved-caspase staining should be performed.

Additionally, if mitochondria suffer metabolic insult this can trigger mitochondrial fragmentation due to reduced fusion and increased fission causing unbalanced mitochondrial dynamics. Fragmentation is a stress response which can also be induced by a reduction in mitochondrial membrane potential, oxidative stress or reduction in ATP (Twig and Shirihai, 2011). This may contribute to the hypothesis that *Slc5a6*$^{F/F;Sox2Cre}$ newborn mice are dying of mitochondrial dysfunction due to metabolic insufficiency as a result of substrate deficiency. However, future work should investigate mitochondrial morphology and function in other tissues in addition to the heart.

As previously described, *Slc5a6* is responsible for the transport of essential substrates required for metabolism; biotin, PA and LA, throughout the body including the intestine, heart, and brain (Ghosal and Said, 2011; Vadlapudi *et al.*, 2012; Uchida *et al.*, 2015). Therefore, removing *Slc5a6* within epiblast derived cells may inhibit transport of each substrate causing a global substrate deficiency. Biotin deficiency is well known to affect energy metabolism by reducing the generation of important intermediates for the TCA cycle which may be lethal to the newborn (Pacheco-Alvarez *et al.*, 2005; Atamna *et al.*, 2007). A study by Mock *et al.* (1988) revealed that changes in the fatty acid composition including TCA intermediates due to biotin deficiency in rats are detected at early as 4 weeks after biotin deficiency was induced. In addition to direct biotin deficiency, a group of recessive disorders of biotin metabolism termed ‘inborn errors of biotin metabolism’ can occur due to impaired biotin availability by deficiency of enzymes such as holocarboxylase synthetase (HCS); which facilitates biotinylation of biotin-dependent carboxylases, and biotinidase (BTD); the enzyme responsible for cleaving biotin from food and proteins, which ultimately result in multiple carboxylase deficiency (MCD) (Sweetman *et al.*, 1982; Dupuis *et al.*, 1999; Pacheco-Alvarez *et al.*, 2002). The onset of symptoms for MCD patients ranges from 1.5 hours after birth up to 2 years of age,

with HCS deficiency presenting the most severe clinical phenotype (Dupuis *et al.*, 1999; Pacheco-Alvarez *et al.*, 2002). Both deficiencies if left untreated lead to coma followed by death. Although *Slc5a6* does not directly interact with HCS or BTD, the reduction in the transport of biotin into cells of *Slc5a6*$^{F/F;Sox2Cre}$ mice by loss of *Slc5a6* may mimic MCD, resulting in a similar pathogenesis leading to perinatal death. However, further investigation into enzyme expression and activity levels should be performed to assess biotin status within *Slc5a6*$^{F/F;Sox2Cre}$ mice before and after birth.

5.4 Conclusion

In conclusion, the global conditional loss of *Slc5a6* does not affect embryonic survival or cardiac development. However, following birth *Slc5a6*$^{F/F;Sox2Cre}$ mice fail to survive postnatally. Without cardiac histology it is difficult to accurately determine the effect of the global loss of *Slc5a6* on the postnatal heart. Although, severe mitochondrial abnormalities were identified in *Slc5a6*$^{F/F;Sox2Cre}$ cardiomyocytes at P0 suggesting the loss of *Slc5a6* is detrimental to mitochondrial structure and potential function. Future work should focus on the assessment of cardiac structure by histological staining and characterising the mechanism behind mitochondrial degradation in *Slc5a6*$^{F/F;Sox2Cre}$ postnatal mice.

Chapter 6 Characterisation of a cardiomyocyte-specific *Slc5a6* knockout mouse model

6.1 Introduction

As shown in Chapter 5, the global removal of *Slc5a6* results in perinatal death, without any apparent cardiovascular involvement during embryogenesis. However, *Slc5a6*$^{F/F;Sox2Cre}$ pups died, therefore long term analysis of the heart was impeded. As both affected sibling patients developed severe DCM, a model to investigate the heart was required to further the understanding of how SLC5A6 may be involved in the patient phenotype. A cardiomyocyte specific *Slc5a6* knockout mouse model was generated using Cre-loxP technology to remove *Slc5a6,* specifically within cardiomyocytes, using a well-established cardiac troponin driven *Cre* recombinase (*TnTCre*) line (Jiao *et al.*, 2003) to assess possible links between dysfunctional *Slc5a6* protein and the heart.

6.1.1 Dilated cardiomyopathy

DCM is characterised by an increase in LV volume, mass and systolic dysfunction, and has a global incidence of ~1:2,700 (Sweet *et al.*, 2015). Within the heart, the LV becomes dilated, and the ventricle wall becomes stressed. This results in pathological remodelling of the myocardium, leading to a reduction in systolic function and, often the development of cardiac arrhythmias, which are detected by functional assessments (Jefferies and Towbin, 2010; McNally and Mestroni, 2017; Schultheiss *et al.*, 2019b). The presence of arrhythmias is indicative that the cardiac conduction system plays a pathological role in DCM. Clinical diagnosis of DCM can be confirmed with the presence of systolic dysfunction with reduced ejection fraction or fractional shortening, which are used as measures of muscle contractility using CMR and echocardiography, respectively (Fatkin *et al.*, 2017; Mathew *et al.*, 2017; McKenna William *et al.*, 2017; McNally and Mestroni, 2017). Although not always present, the right ventricle can also be affected by reduced functionality.

Approximately 50% of DCM cases are caused by infection or inflammation caused by autoimmune diseases (McKenna William *et al.*, 2017). The remaining cases have an unknown cause, although ~30% are thought to be caused by genetic mutations within the sarcomere (Mathew *et al.*, 2017) (Figure 6.1).

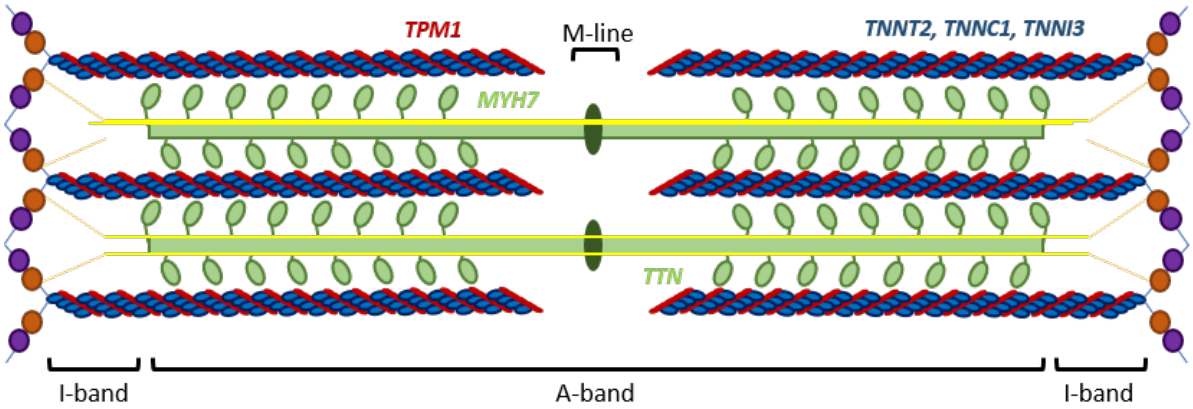

Figure 6.1. Schematic diagram of the sarcomere with DCM associated genes. Modified from Figure 1.4.B. Sarcomeric structure consisting of thin myosin (green) and thick actin (blue) myofilaments. Genes associated with DCM are noted on the schematic.

DCM can also be secondary to underlying molecular or cellular dysfunction, which cause multi-systemic disorders such as ion channel and mitochondrial diseases (McKenna William *et al.*, 2017). In mitochondrial diseases, specifically mitochondrial encephalopathies, are characterised by dysfunction of oxidative phosphorylation during energy metabolism. In the majority of mitochondrial diseases the development of cardiomyopathy is not uncommon due to the effects on energy metabolism and the high energy demand within the heart (Oldfors and Tulinius, 2003).

6.1.2 Energy metabolism

As previously described, Slc5a6 is essential for the transport of biotin, PA and LA, key nutrients required for energy metabolism and homeostasis for all cells, including high energy dependent organs such as the heart. All living cells require energy to function, and in adult mammals this occurs through cellular respiration. In short, glucose, in addition to carbohydrates, proteins and fats, is metabolised into acetyl coenzyme A, which enters the tricarboxylic acid cycle (TCA) and is oxidised via oxidative phosphorylation to generate ATP, carbon dioxide (CO_2) and water (Huskisson *et al.*, 2007; Hroudová and Fišar, 2013; Hill, 2014) (Figure 6.2).

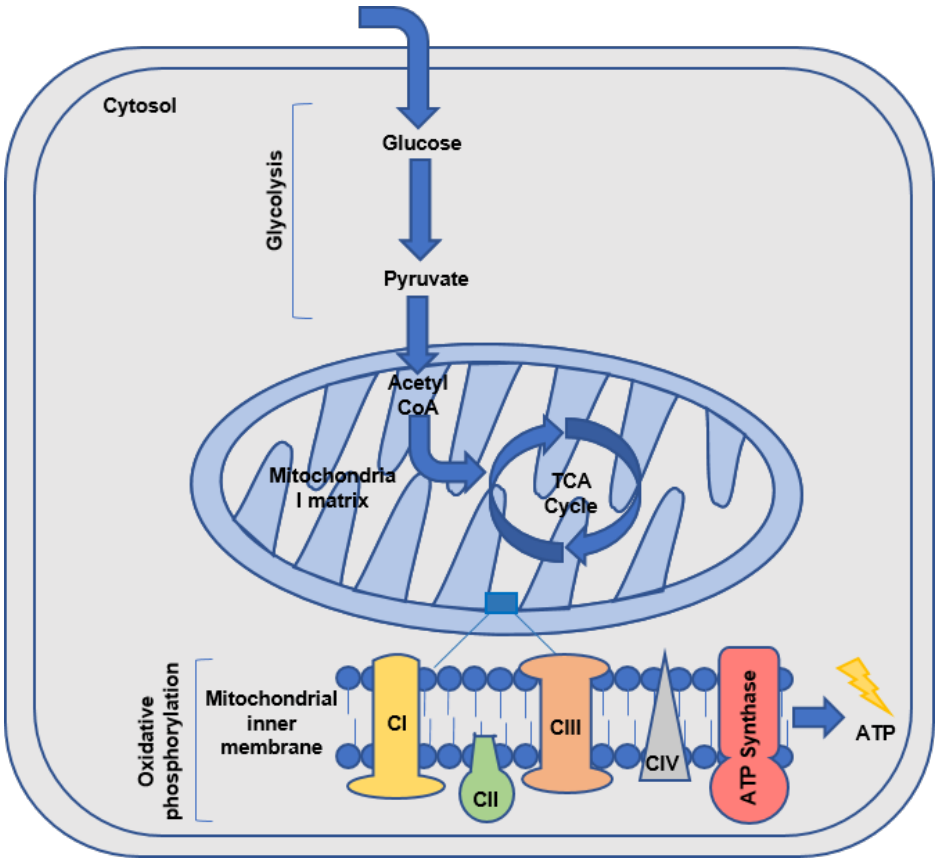

Figure 6.2. Simplified overview of aerobic energy metabolism pathway.
Glucose is transported into the cell by glucose transporters on the plasma membrane. Once in the cell, glucose is converted to pyruvate through glycolysis within the cytosol. Pyruvate is converted to acetyl CoA within mitochondria, which contributes to the TCA cycle to generate intermediates which are utilised by complexes 1-4 (CI-CIV) + ATP synthase in oxidative phosphorylation to produce ATP (energy).

Energy production is triggered in response to energy demand and therefore the yield of ATP varies between cell types. The heart has one of the highest metabolic demands in the human body and therefore any defects in this pathway often has detrimental effects on the heart which could lead to heart disease resulting in cardiac failure (Nathania *et al.*, 2017; Hassanpour *et al.*, 2018).

Efficient cardiac function heavily relies upon a constant energy supply, to provide the body with oxygen and essential nutrients (Lopaschuk and Kelly, 2008). To maintain this high energy supply, cardiac processes have adapted to utilise any available substrate for ATP synthesis. When operating under normal conditions, the heart uses two-thirds of its ATP supply for contraction with the remaining third is used for normal functioning of ion pumps (Hassanpour *et al.*, 2018). The majority of ATP generated within the heart stems from fatty acid β-oxidation (~60-90%), the remaining 10-40% is generated from pyruvate using lactate taken from blood (Kolwicz *et al.*, 2013; Ritterhoff and Tian, 2017).

6.1.3 Generation of *Slc5a6*^{TnTCre} mouse line

To investigate the loss of *Slc5a6* within the heart, the conditional *Slc5a6*^{Tm1c} allele, referred to as *Slc5a6*^{F} from this point forward was used (Figure 6.3). To target the early cardiomyocytes, the *Slc5a6*^{F} transgenic mice were crossed with *TnTCre* mouse line (Jiao *et al.*, 2006), allowing deletion of *Slc5a6* from E7.5 within cardiomyocytes.

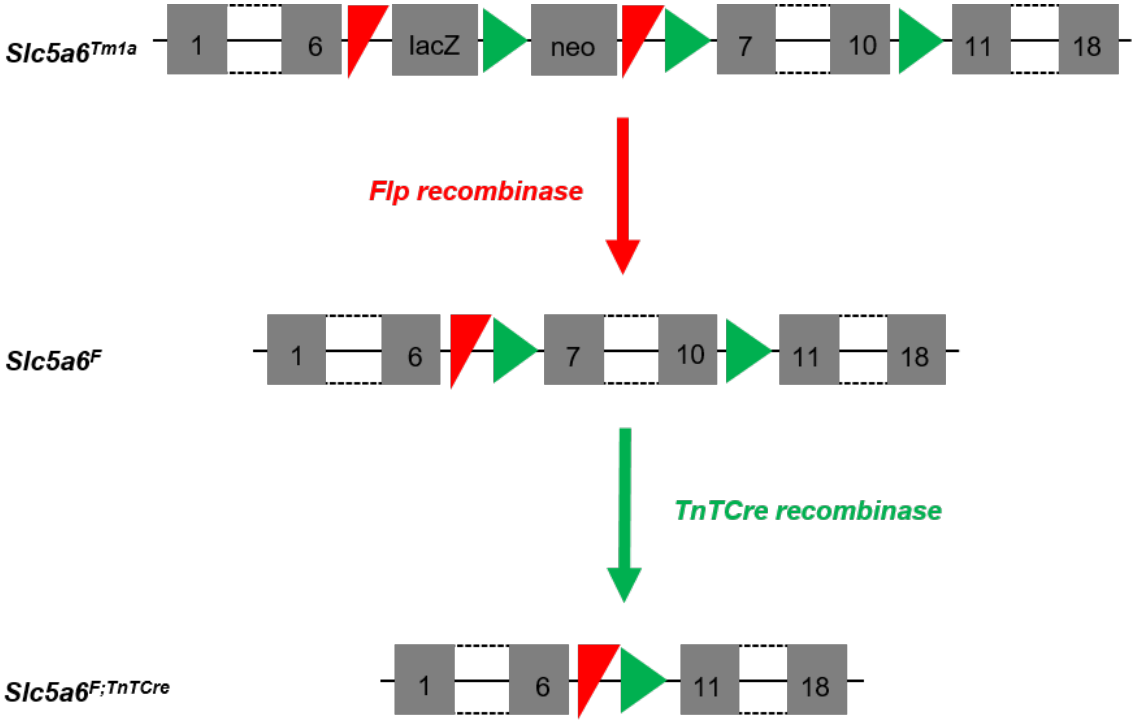

Figure 6.3. Schematic diagram for the generation of *Slc5a6* transgenic alleles for promoter specific knockout models.
Modified from **Figure 2.3**.The *Slc5a6*^{Tm1a} allele produced by MRC Harwell. The *Slc5a6*^{Tm1a} allele contains a *lacZ-neomycin* cassette flanked by FRT sites (red) which enable the generation of the conditional *Slc5a6*^{F} allele when crossed with a *Flp* recombinase mouse line, removing the lacZ-neomycin cassette. The *Slc5a6*^{F} allele can then be crossed with a *TnTCre* recombinase mouse line to remove the targeted region (exons 7-10) flanked by *loxP* sites (green) specifically within cardiomyocytes.

Using this, a cardiomyocyte-specific knockout was generated by crossing a heterozygous male (*Slc5a6*$^{+/F;TnTCre}$) with a homozygous female (*Slc5a6*$^{F/F}$), producing cardiomyocyte specific *Slc5a6* knockout (*Slc5a6*$^{F/F;TnTCre}$) mice (Figure 6.4). The mice generated from this cross were then used for analysis of the mutant phenotype.

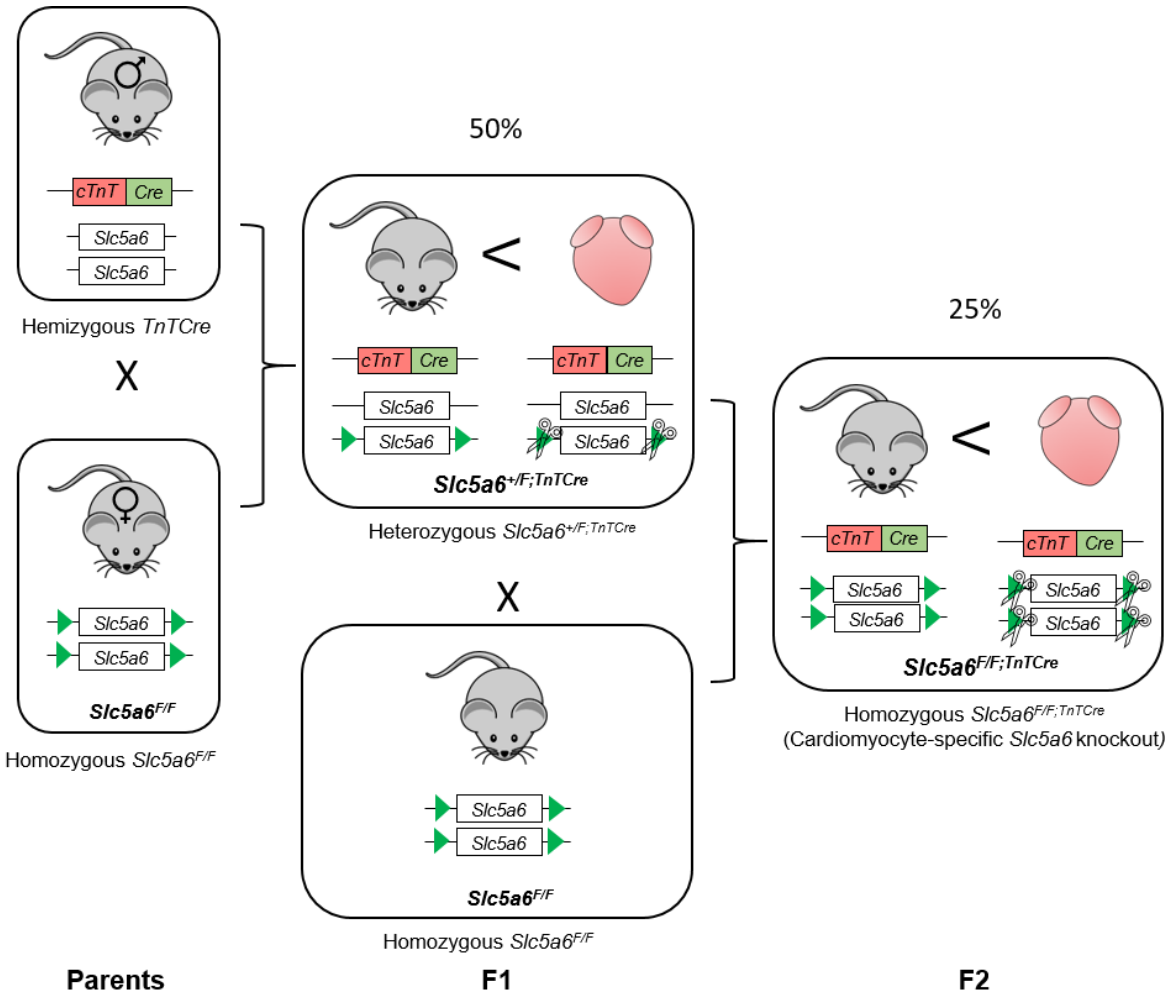

Figure 6.4. Breeding strategy for generation of cardiomyocyte specific *Slc5a6* conditional knockout mice (*Slc5a6*$^{F/F;TnTCre}$) for analysis.
Modified from Figure 5.3**.** A hemizygous *TnTCre* male was crossed with a homozygous *Slc5a6*$^{F/F}$ female. Of the offspring produced, ~50% are heterozygous for the *Slc5a6*$^{+/F}$ allele and express *Cre* recombinase specifically within cardiomyocytes (*Slc5a6*$^{+/F;TnTCre}$). Heterozygous males were crossed with a homozygous *Slc5a6*$^{F/F}$. From this cross ~25% of offspring are homozygous for the *Slc5a6*^{F} allele and express *Cre* recombinase within the cardiomyocytes only (*Slc5a6*$^{F/F;TnTCre}$), generating cardiomyocyte specific *Slc5a6* knockout mice which are used for analysis.

To confirm the specific deletion of *Slc5a6* within the heart, RT-PCR was performed using whole heart tissue collected at E15.5, a limb was included as a tissue specific control (Saumil Shah). Figure 6.5 shows the targeted region, exons 7-10 are removed specifically within the heart (96bp) but not in the limb (590bp) in *Slc5a6*$^{F/F;TnTCre}$ mice. The deletion results in a premature stop codon leading to protein truncation or mRNA degradation due to non-sense mediated decay as described in 5.1.2.

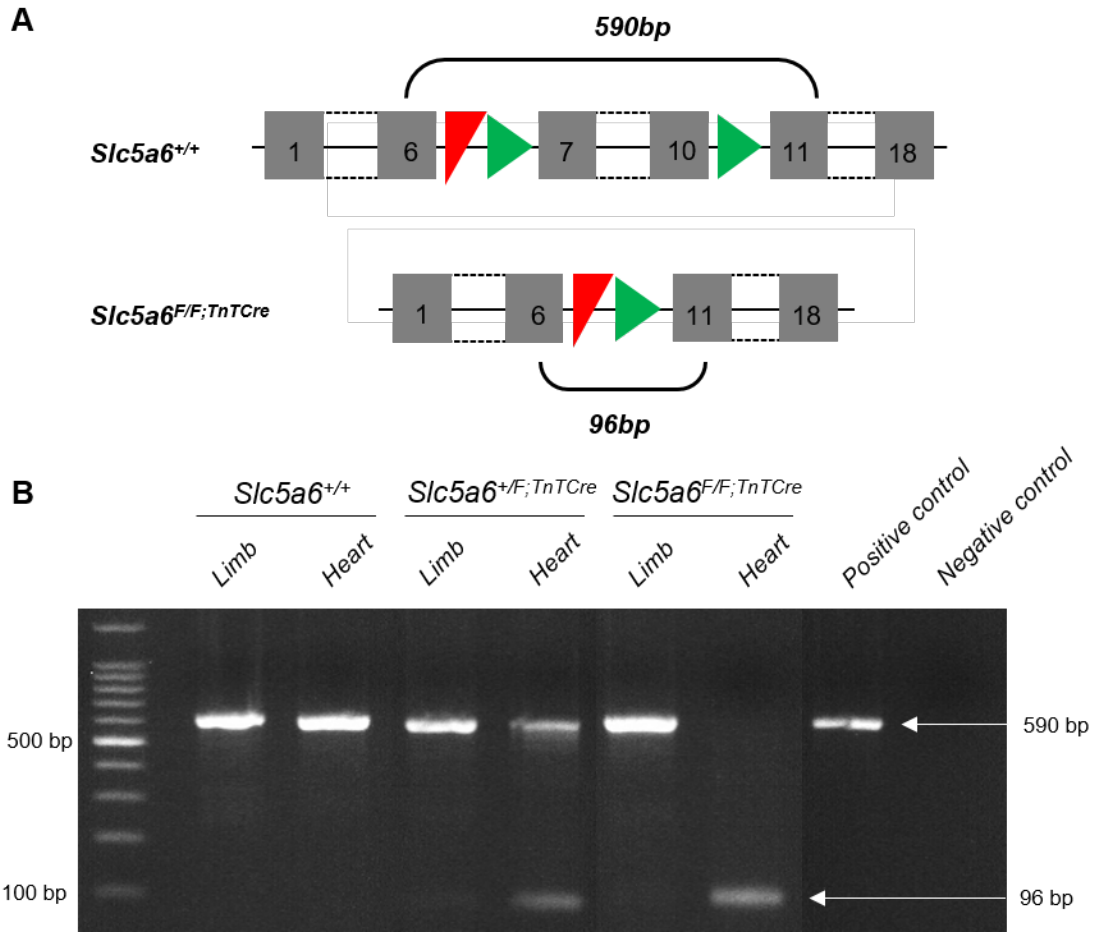

Figure 6.5. RT-PCR of targeted region using cDNA from embryos from a *Slc5a6*^{TnTCre} litter.
Hearts and limbs were collected at E15.5. A) Primers designed to target the deleted region of *Slc5a6*^{Tm1c} allele were used on cDNA synthesised from E15.5 hearts and limbs for each genotype. If the targeted region was deleted a 96bp PCR product would be present, without the deletion the region would result in a 590bp product. B) The wild type (*Slc5a6*$^{+/+}$) mice contain the full 590bp region in both the heart and limb. Homozygous (*Slc5a6*$^{F/F;TnTCre}$) mice show the targeted region is deleted resulting in a smaller PCR product (96bp) within the heart but contains the intact region within the limb. The heterozygous (*Slc5a6*$^{+/F;TnTCre}$) mice show one copy of the deleted region 96bp and one copy of the intact 590bp region within the heart and only the intact region within the limb. Image provided by Saumil Shah.

Preliminary studies were performed using H&E on E15.5 embryos to identify any cardiac abnormalities (Figure 6.6). No embryonic phenotypic differences, such as ventricular septal defects (VSD) or ventricular dilation were observed between *Slc5a6*$^{+/+}$ and *Slc5a6*$^{F/F;TnTCre}$ hearts.

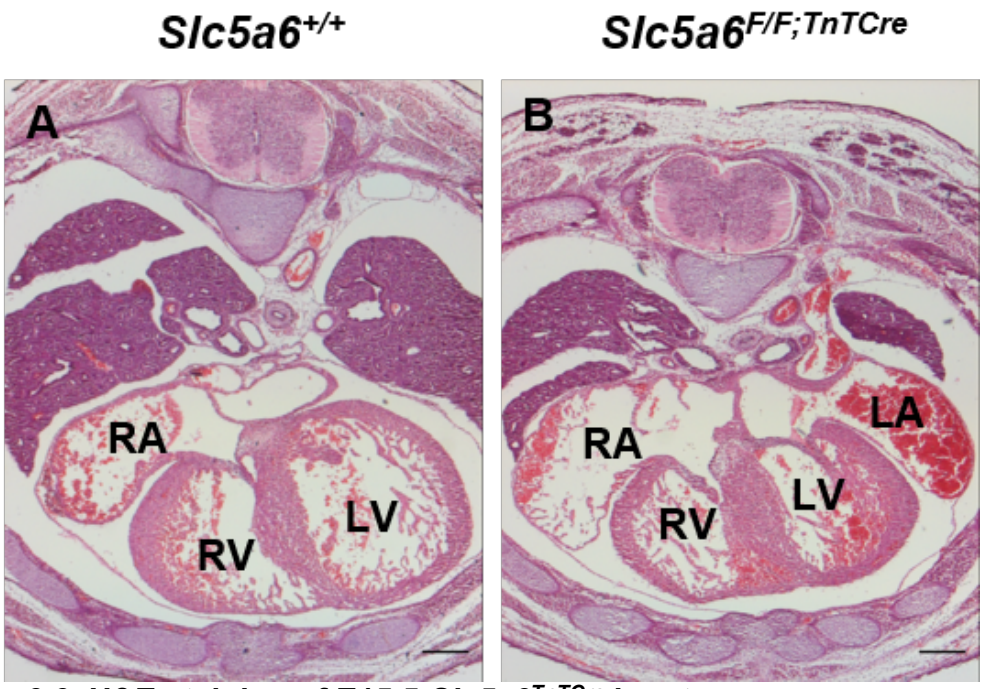

Figure 6.6. H&E staining of E15.5 *Slc5a6*^{TnTCre} hearts.
Representative H&E images of *Slc5a6*$^{+/+}$ (A) and *Slc5a6*$^{F/F;TnTCre}$ (B) hearts collected at E15.5. No visible changes are observed in the structure of the heart between *Slc5a6*$^{F/F;TnTCre}$ and *Slc5a6*$^{+/+}$ *mice*. Left atria LA, left ventricle LV, right atria LA, right ventricle RV. n= 3 Slc5a6$^{+/+}$ and 1 Slc5a6$^{F/F;TnTCre}$. Scale bar = 500μm. Images provided by Saumil Shah.

Preliminary data confirmed the removal of the critical region (exon 7-10) of *Slc5a6* within the heart during embryogenesis. Initial analysis revealed no embryonic lethality with no cardiac phenotype observed at E15.5. Further investigation into the effect of removing *Slc5a6* within the heart will be carried out using functional and histological analysis.

6.1.4 Aims of the chapter

It is hypothesised that by removing *Slc5a6* within the heart will lead to the development of cardiomyopathy within *Slc5a6*$^{F/F;TnTCre}$ mice, possibly due to the disruption of energy metabolism within cardiomyocytes.

The aim was to establish the cardiac phenotype of the mouse model using ECG and CMR imaging to assess cardiac function and histology to determine any changes to cardiac structure. Mitochondrial structure was investigated to evaluate the effect of the loss of *Slc5a6* on energy metabolism within cardiomyocytes.

6.2 Phenotypic analysis of *Slc5a6TnTCre* mouse line

6.2.1 Confirmation of Slc5a6 deletion within cardiomyocytes

Previous work confirmed exon 6 was spliced to exon 11 of *Slc5a6* within *Slc5a6*$^{F/F;TnTCre}$ hearts by RT-PCR. However, it was not known if the transcript would undergo non-sense mediated decay or be translated into a truncated protein. Therefore, western blotting was performed on E15.5 samples of the head, heart and limb of *Slc5a6*$^{+/+}$ and *Slc5a6*$^{F/F;TnTCre}$ embryos to determine if Slc5a6 was translated. From this, it was shown that Slc5a6 (69kDa) was detected in the head (n=2) and limb (n=1) of both *Slc5a6*$^{+/+}$ and *Slc5a6*$^{F/F;TnTCre}$ embryos. However, within the heart Slc5a6 was only detected in *Slc5a6*$^{+/+}$ samples (n=2) and was reduced in *Slc5a6*$^{F/F;TnTCre}$ cardiac protein. There is a very faint band present in *Slc5a6*$^{F/F;TnTCre}$ which may account for the non-cardiomyocyte population of cells which will not have Slc5a6 deleted. Together with the data from the RT-PCR confirms the targeted removal of exon7-10 results in the introduction of a premature stop codon leading to non-sense mediated decay and therefore deletion of Slc5a6 specifically within cardiomyocytes.

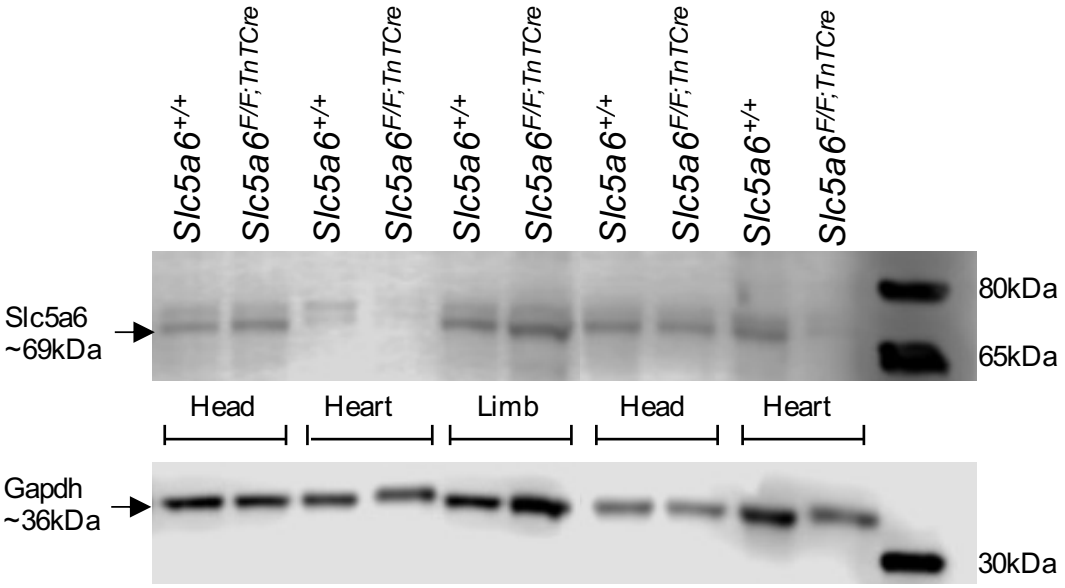

Figure 6.7. Slc5a6 is deleted in *Slc5a6*$^{F/F;TnTCre}$ hearts.
Western blot to detect Slc5a6 (69kDa) in *Slc5a6*$^{+/+}$ and *Slc5a6*$^{F/F;TnTCre}$ samples of the head (n= 2), heart (n=2) and limb (n=1). Slc5a6 is detected in the head and limb of both *Slc5a6*$^{+/+}$ and *Slc5a6*$^{F/F;TnTCre}$; however, it is not detected in the heart of *Slc5a6*$^{F/F;TnTCre}$ mice. Gapdh (36kDa) was detected as a housekeeping protein in all samples.

6.2.2 Sudden death of Slc5a6$^{F/F;TnTCre}$ mice in early adulthood

The survival of *Slc5a6$^{F/F;TnTCre}$* mice during embryogenesis and postnatally was determined. All pups were clipped and genotyped at 3 weeks of age, prior to weaning. *Slc5a6$^{F/F;TnTCre}$* mice were present at weaning and Mendelian inheritance was observed (Table 6.1).

Table 6.1. Mendelian inheritance ratio of *Slc5a6$^{F/F;TnTCre}$* mice at weaning P21 (3 weeks).
Chi-squared test was used to determine statistical significance.

Age	Total number	*Slc5a6$^{F/F;TnTCre}$* expected	*Slc5a6$^{F/F;TnTCre}$* observed	*p* value
P21	56	14	20	0.81768452

As the study began, there was the sudden death of *Slc5a6$^{F/F;TnTCre}$* mice (n=3) within 1 cage at 26 weeks of age. Hearts from the sudden death (SD) mice were collected, paraffin embedded, sectioned and stained with H&E. An age-matched *Slc5a6$^{+/+}$* heart was also collected for comparison (Figure 6.8). Whole heart images show SD *Slc5a6$^{F/F;TnTCre}$* hearts (Figure 6.8B) were visually enlarged compared to *Slc5a6$^{+/+}$* mice (Figure 6.8A). However, as the hearts were collected post-mortem this could be due to blood pooling. H&E staining of the SD *Slc5a6$^{F/F;TnTCre}$* hearts revealed chamber enlargement of both atria and ventricles, with blood present in the chambers, as well as thinning of the myocardial walls (Figure 6.8D), compared to *Slc5a6$^{+/+}$* (Figure 6.8C). Higher powered images of the LV show *Slc5a6$^{+/+}$* hearts (Figure 6.8E) have a compact myocardium with a small degree of spacing between cardiomyocytes; however, this interstitial space between the cardiomyocytes is more widespread in SD *Slc5a6$^{F/F;TnTCre}$* hearts (Figure 6.8F). Picro-Sirius red staining revealed the interstitial space to be collagen deposits between cardiomyocytes in SD *Slc5a6$^{F/F;TnTCre}$* (Figure 6.8H) mice, compared to *Slc5a6$^{+/+}$* (Figure 6.8G).

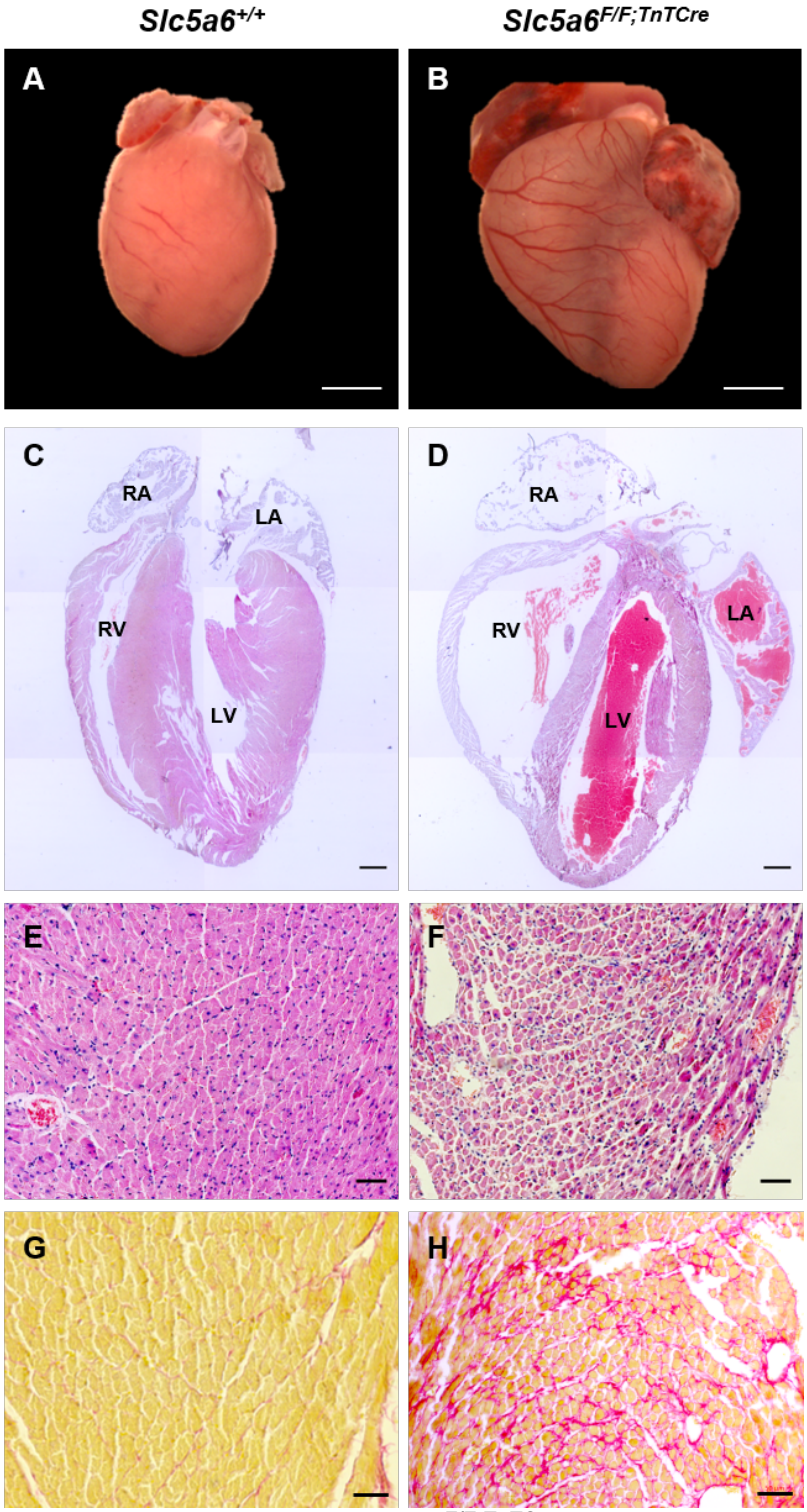

Figure 6.8. Histological staining of *Slc5a6*$^{F/F;TnTCre}$ sudden death mice at 26 weeks.

Slc5a6$^{F/F;TnTCre}$ hearts (B) were imaged post-mortem, with a *Slc5a6*$^{+/+}$ heart (A) also collected and imaged for comparison. *Slc5a6*$^{F/F;TnTCre}$ hearts were visibly enlarged compared to *Slc5a6*$^{+/+}$ heart at the same age. H&E staining showed ventricular and atrial enlargement present in *Slc5a6*$^{F/F;TnTCre}$ hearts (D) compared to *Slc5a6*$^{+/+}$ (C). The LV showed an increase in interstitial space between cardiomyocytes in *Slc5a6*$^{F/F;TnTCre}$ myocardium (E) compared to *Slc5a6*$^{+/+}$ (E). Confirmed to be interstitial fibrosis by Picro-Sirius red staining of *Slc5a6*$^{+/+}$ (G) and *Slc5a6*$^{F/F;TnTCre}$ (H) hearts. *n* = 1 *Slc5a6*$^{+/+}$ and 3 *Slc5a6*$^{F/F;TnTCre}$. Scale bars A-B = 2mm, C-D = 1000μm, E-F = 50μm.

Changes in the cardiac morphology of the sudden death *Slc5a6*$^{F/F;TnTCre}$ mice may be due to cardiomyopathy; however, due to collection of the hearts post-mortem, interpretation of findings cannot be relied upon.

6.2.3 Weight monitoring of Slc5a6$^{F/F;TnTCre}$

Due to the sudden death of the 3 *Slc5a6*$^{F/F;TnTCre}$ mice at 26 weeks, and to prevent further potential suffering within this mouse line, all future offspring were monitored for signs of ill health, in addition to weekly weight recordings, and culled at 20 weeks. From the longitudinal weight data collected, *Slc5a6*$^{+/F;TnTCre}$ and *Slc5a6*$^{F/F;TnTCre}$ mice weighed significantly less than *Slc5a6*$^{+/+}$ mice ($p < 0.0001$) throughout early adulthood (Figure 6.9A). However, at collection, body weight gain was determined for each genotype, from 4-14 weeks and 4-20 weeks (Figure 6.9B) and no significant difference was observed between *Slc5a6*$^{+/+}$, *Slc5a6*$^{+/F;TnTCre}$ or *Slc5a6*$^{F/F;TnTCre}$ mice at either time point, suggesting all genotypes gain weight at a proportionate rate over time.

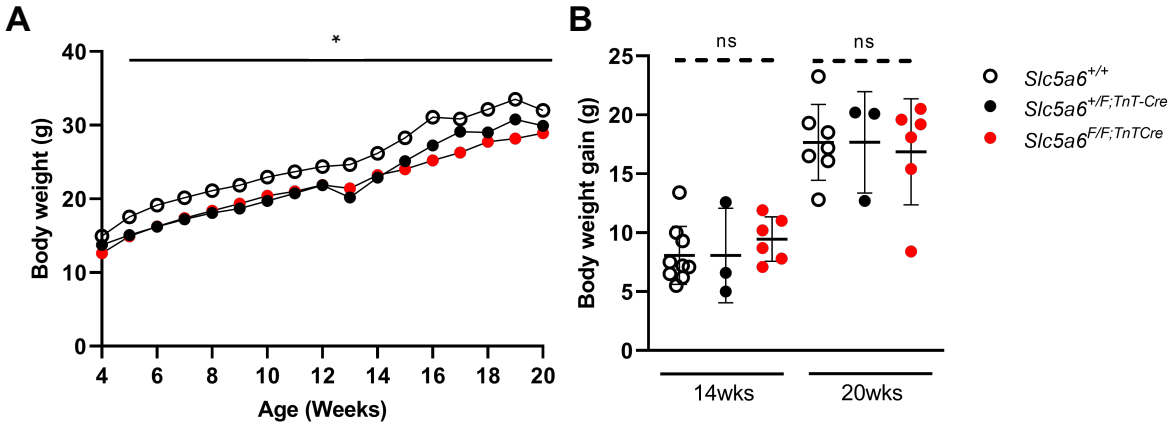

Figure 6.9. Weight monitoring of *Slc5a6*^{TnTCre} mice.
A) Average weekly body weight data presented for *Slc5a6*$^{+/+}$(white), *Slc5a6*$^{+/F;TnTCre}$ (red) and *Slc5a6*$^{F/F;TnTCre}$ (red) from weaning to collection at 20 weeks. No significant difference was observed between *Slc5a6*$^{+/F;TnTCre}$ and *Slc5a6*$^{F/F;TnTCre}$ weights; however, *Slc5a6*$^{+/+}$ weighed significantly more than *Slc5a6*$^{+/F;TnTCre}$ ($p<0.0001$) and *Slc5a6*$^{F/F;TnTCre}$ ($p<0.0001$). B) Body weight gain determined for each mouse at age of collection (14 and 20 weeks). 14 weeks: n= 9 *Slc5a6*$^{+/+}$, 3 *Slc5a6*$^{+/F;TnTCre}$ and 6 *Slc5a6*$^{F/F;TnTCre}$ mice, 20 weeks n= 7 *Slc5a6*$^{+/+}$, 3 *Slc5a6*$^{+/F;TnTCre}$ and 6 *Slc5a6*$^{F/F;TnTCre}$. One-way ANOVA with multiple comparisons and Bonferroni correction was applied to each dataset. * $p<0.05$.

6.2.4 Cardiac conduction abnormalities present in Slc5a6$^{F/F;TnTCre}$ mice

The cardiac conduction system consists of the sinoatrial node (SAN) referred to as the pacemaker of the heart, the atrioventricular node (AVN), the bundle of His and the left and right bundle branches. The cardiac conduction cycle can be broken down into 3 main processes. 1) Atrial contraction and depolarisation, where electrical impulses travel from the SAN through conductive cells (P wave) and held at the AVN while blood moves from the atria into the ventricle (PR interval). 2) Ventricular contraction, the impulse is passed down through the bundle of His to the left and right bundle branches triggering the ventricles to contract, pumping blood throughout the body (QRS complex). 3) Ventricular depolarisation, following contraction the ventricles repolarise ready for a new cycle to begin (QT interval, ST height and T wave amplitude). To assess cardiac conduction *in vivo,* a three-lead ECG was performed at four timepoints throughout early adulthood; 5, 8, 14 and 18 weeks. Representative traces are shown for each genotype at 8 weeks in Figure 6.10. The ECG traces of *Slc5a6*$^{+/+}$ (Figure 6.10A) and *Slc5a6*$^{+/F;TnTCre}$ (Figure 6.10B) are visually comparable, whereas the ECG trace for *Slc5a6*$^{F/F;TnTCre}$ mice (Figure 6.10C) shows lengthening of the PR interval, QRS interval abnormalities as well as ST height and T wave depression. Although visual changes are apparent, each parameter was quantified for all genotypes at 5, 8 and 14 weeks.

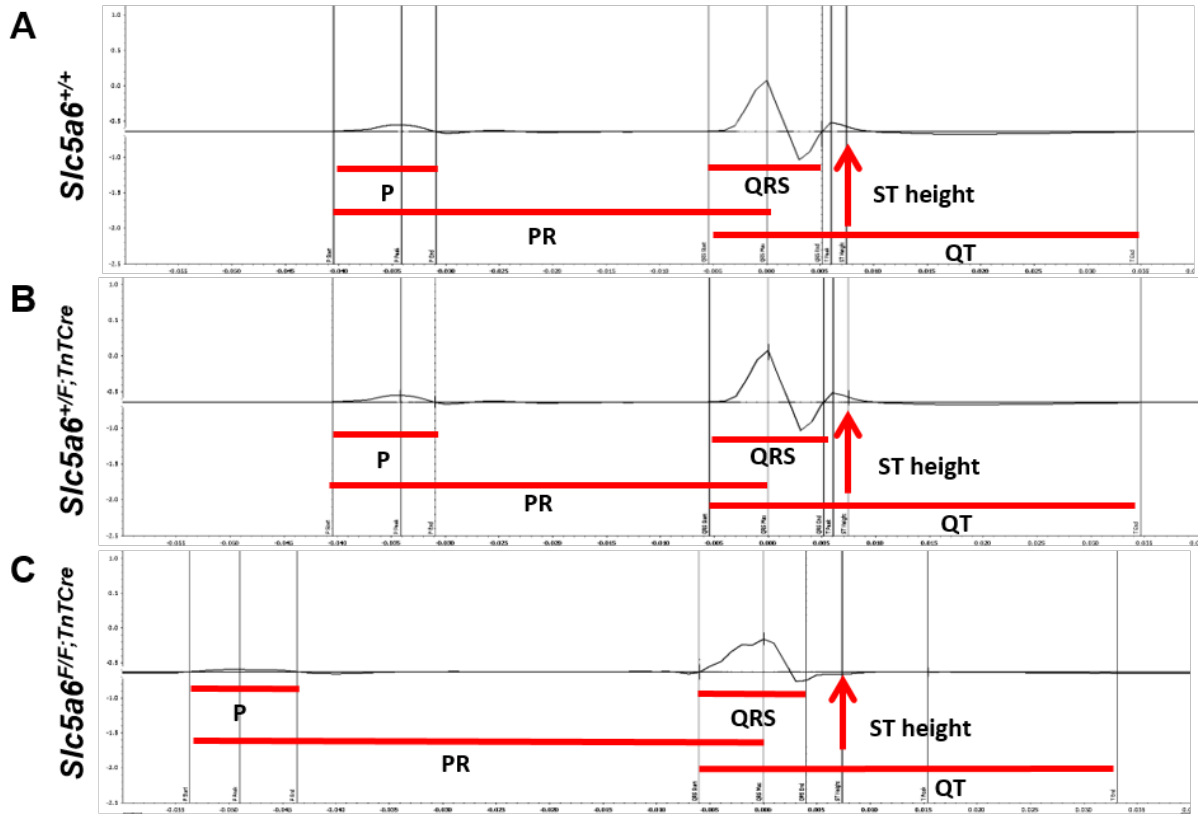

Figure 6.10. Representative ECG traces of *Slc5a6*^{TnTCre} mice at 8 weeks.
ECG was performed on mice at 5, 8, 14 and 18 weeks. Data was averaged over 60 seconds, for three minute recordings. Representative images of traces are shown from 60-120 second period for *Slc5a6TnTCre* mice at 8 weeks, to show ECG parameters (red); P wave, PR interval, QRS interval, QT interval and ST height are shown on *Slc5a6*$^{+/+}$ (A), *Slc5a6*$^{+/F;TnTCre}$ (B) and *Slc5a6*$^{F/F;TnTCre}$ (C) traces. 8 weeks n= 7 *Slc5a6*$^{+/+}$, 7 *Slc5a6*$^{+/F;TnTCre}$, 7 *Slc5a6*$^{F/F;TnTCre}$.

At 5 weeks, *Slc5a6*^{TnTCre} mice were anaesthetised for 5 minutes to record ECG for three minutes. ECG data collected between 60-120 seconds was used for analysis to minimise any movement/breathing artefacts from probe placement (Figure 6.11). There are no apparent changes in heart rate (HR) (Figure 6.11A), PR interval (Figure 6.11B), QRS (Figure 6.11C) or QT interval (Figure 6.11D) between each genotype. Although not significant, 2 *Slc5a6*$^{F/F;TnTCre}$ mice show an inverted ST segment (Figure 6.11E). T wave amplitude is significantly decreased in *Slc5a6*$^{F/F;TnTCre}$ mice compared to *Slc5a6*$^{+/+}$ (p=0.0038) and *Slc5a6*$^{+/F;TnTCre}$ (p=0.0006). This suggests there are some early conduction alterations to the terminal end of the cycle, where the ventricles repolarise following contraction. To assess the progression of these changes, ECGs were performed on *Slc5a6*^{TnTCre} mice at 8 weeks.

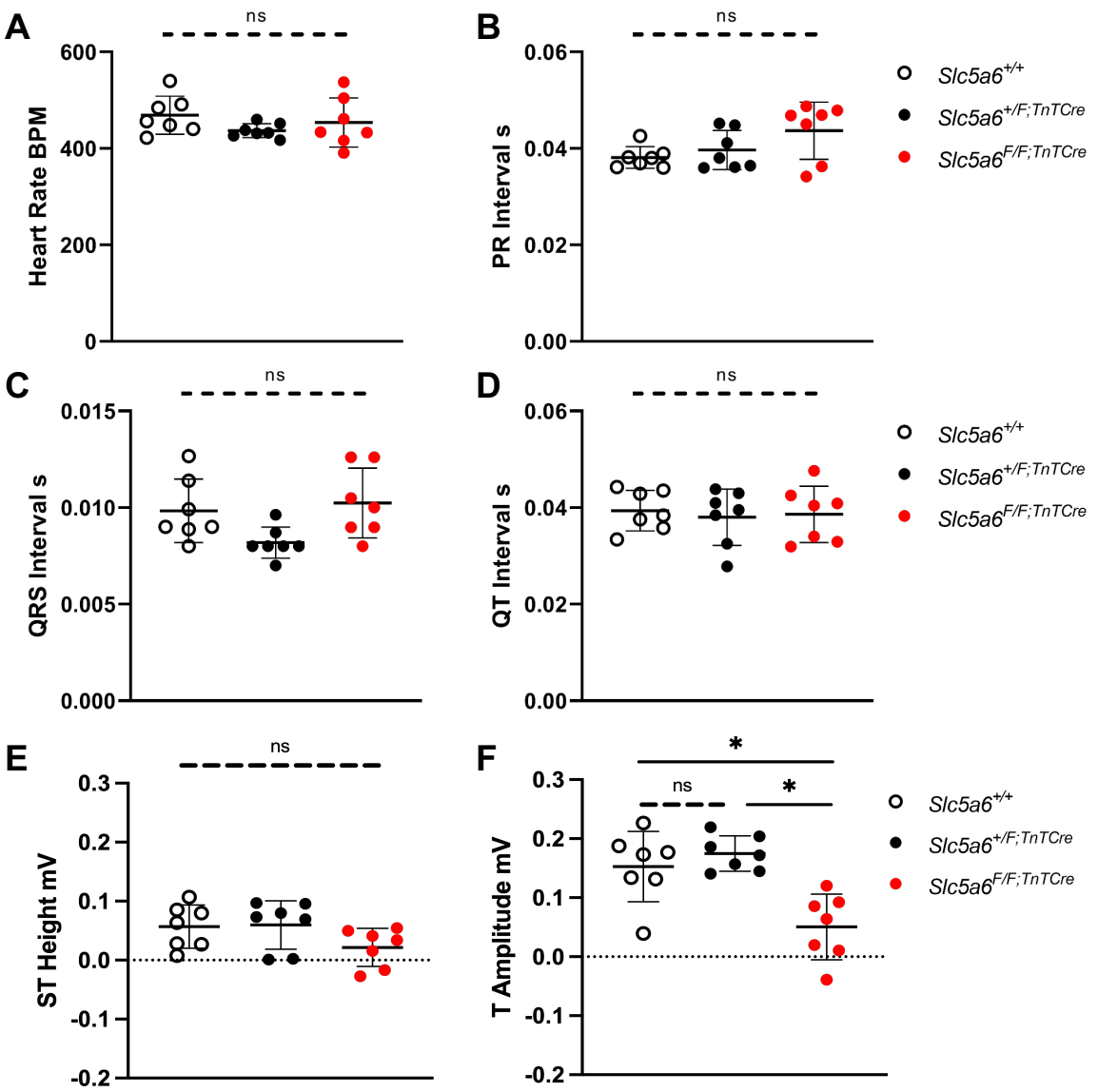

Figure 6.11. Quantification of ECG parameters for *Slc5a6*^{TnTCre} mice at 5 weeks. Parameters were quantified automatically using LabChart software. Where the software did not detect parameters accurately, this was adjusted manually. No alterations were observed between *Slc5a6*$^{+/+}$ (white), *Slc5a6*$^{+/F;TnTCre}$ (black) or *Slc5a6*$^{F/F;TnTCre}$ mice (red) in heart rate (HR) (A), PR interval (B), QRS interval (C), QT interval (D) or ST height (E). At 5 weeks, *Slc5a6*$^{F/F;TnTCre}$ mice show a significant decrease in T wave amplitude (F) compared with *Slc5a6*$^{+/+}$ and *Slc5a6*$^{+/F;TnTCre}$ mice. One-way ANOVA with multiple comparisons and Bonferroni correction was applied to each dataset; n= 7 *Slc5a6*$^{+/+}$, 7 *Slc5a6*$^{+/F;TnTCre}$ and 7 *Slc5a6*$^{F/F;TnTCre}$ mice. * = p<0.05.

Data from ECG recordings at 8 weeks show significant changes across the conduction cycle (Figure 6.12). The PR interval is significantly lengthened in *Slc5a6*$^{F/F;TnTCre}$ mice compared to both *Slc5a6*$^{+/+}$ (p<0.0001) and *Slc5a6*$^{+/F;TnTCre}$ (p=0.0016) mice (Figure 6.12B). Lengthening of the PR interval suggests the electrical impulse from the SAN, is held at the AVN longer than it should resulting in atrioventricular block. *Slc5a6*$^{F/F;TnTCre}$ mice also show a significant widening of the QRS interval at 8 weeks, compared to *Slc5a6*$^{+/+}$ (p=0.0039) and *Slc5a6*$^{+/F;TnTCre}$ (p=0.0029) mice (Figure 6.12C). QRS interval signals the contraction of the ventricles to pump blood from the ventricular chamber throughout the body. Widening of this complex is indicative of myocardial fibrosis, suggestive of stiffness throughout the myocardial wall. The changes to the PR and QRS intervals contribute to the lengthening of the cardiac contraction, highlighted by the significant decrease in the HR in *Slc5a6*$^{F/F;TnTCre}$ mice compared to *Slc5a6*$^{+/+}$ (p<0.0001);however, a decrease is also observed in *Slc5a6*$^{+/F;TnTCre}$ (p=0.0061) mice. The significant decrease in HR observed in *Slc5a6*$^{+/F;TnTCre}$ may be due to the variation observed across mice included in the analysis (Figure 6.12A). No changes were observed in the QT interval (Figure 6.12D), which shows that the duration of ventricular repolarisation is not affected. Interestingly, the downward trend in ST height observed at 5 weeks has progressed to a significant depression (below 0.0) in *Slc5a6*$^{F/F;TnTCre}$ mice compared with *Slc5a6*$^{+/+}$ (p<0.0001) and *Slc5a6*$^{+/F;TnTCre}$ (p<0.0001) mice at 8 weeks (Figure 6.12E). This together with a significant inversion in T wave amplitude in *Slc5a6*$^{F/F;TnTCre}$ mice compared to *Slc5a6*$^{+/+}$ (p<0.0001) and *Slc5a6*$^{F/F;TnTCre}$ (p<0.0001) mice (Figure 6.12F) is suggestive of LV strain pattern, a key marker of LV hypertrophy. To follow the progression of the phenotype, ECGs were taken at 14 weeks.

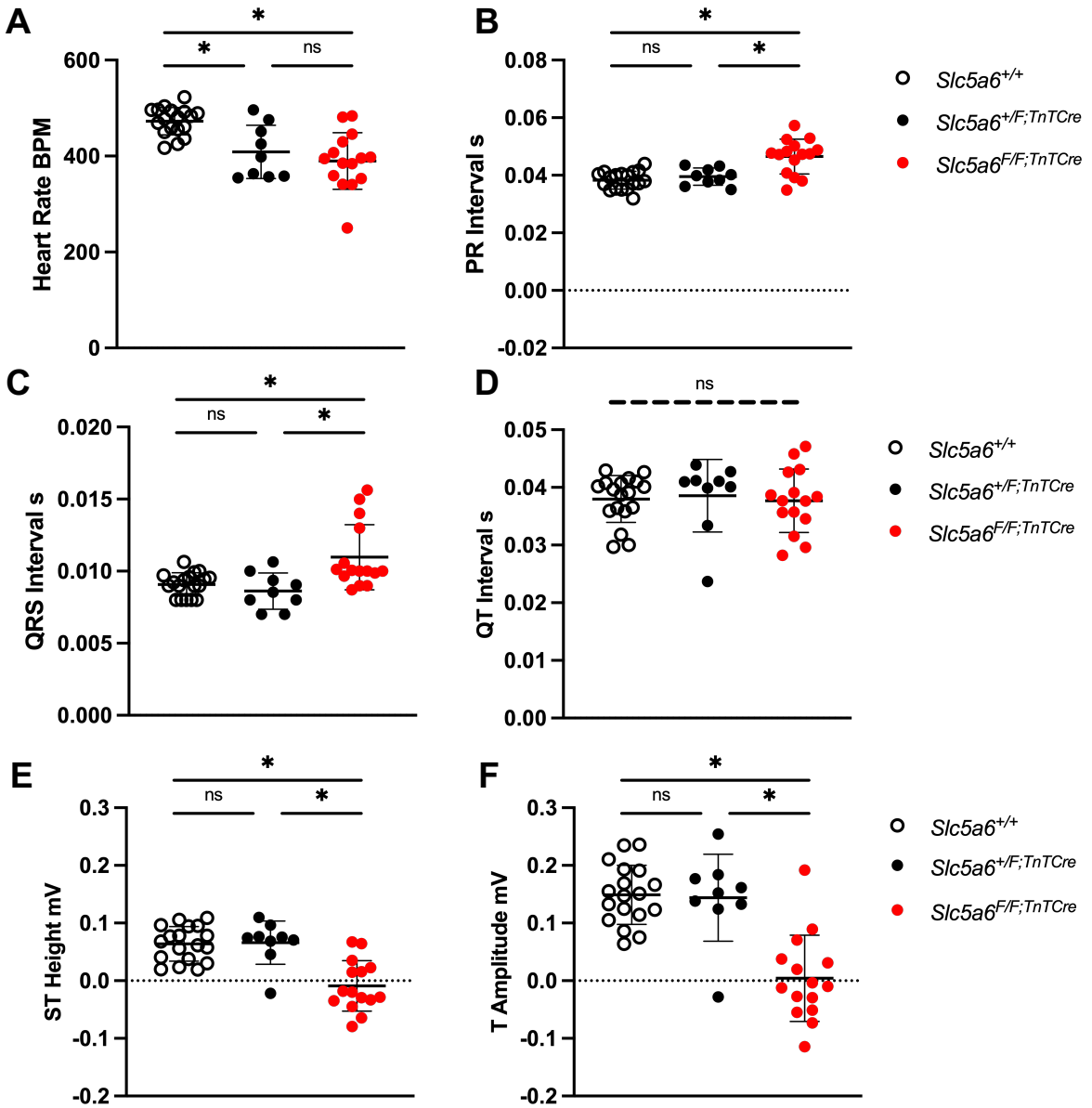

Figure 6.12. Quantification of ECG parameters for *Slc5a6*^{TnTCre} mice at 8 weeks. ECG recordings were analysed to quantify HR (A), PR interval (B), QRS interval (C), QT interval (D) or ST height (E), T amplitude (F) across three genotypes; *Slc5a6*$^{+/+}$ (white), *Slc5a6*$^{+/F;TnTCre}$ (black) and *Slc5a6*$^{F/F;TnTCre}$ mice (red). *Slc5a6*$^{F/F;TnTCre}$ mice show a significant decrease in HR, ST height and T wave amplitude compared to *Slc5a6*$^{+/+}$, *Slc5a6*$^{+/F;TnTCre}$ mice. A significant lengthening of PR interval and widening of the QRS interval is observed in *Slc5a6*$^{F/F;TnTCre}$ mice. One-way ANOVA with multiple comparisons and Bonferroni correction was applied to each dataset.; n= 18 *Slc5a6*$^{+/+}$, 9 *Slc5a6*$^{+/F;TnTCre}$ and 15 *Slc5a6*$^{F/F;TnTCre}$ mice. * = p<0.05.

Similar alterations observed in *Slc5a6*$^{F/F;TnTCre}$ at 8 weeks are apparent at 14 weeks (Figure 6.13). Heart rate is significantly decreased in *Slc5a6*$^{F/F;TnTCre}$ mice compared to *Slc5a6*$^{+/+}$ mice (p=0.0457) (Figure 6.13A). The PR interval is significantly decreased in *Slc5a6*$^{F/F;TnTCre}$ mice compared to *Slc5a6*$^{+/+}$ mice (p=0.0260). Additionally, a significantly widened QRS interval is observed compared to *Slc5a6*$^{+/F;TnTCre}$ (p=0.0065) and *Slc5a6*$^{+/+}$ (p=0.0159) mice. The length of ventricular repolarisation remains unaffected in *Slc5a6*$^{F/F;TnTCre}$ mice at 14 weeks shown in the QT interval (Figure 6.13D). As observed at 8 weeks, *Slc5a6*$^{F/F;TnTCre}$ mice continue to show LV strain pattern with ST height depression (Figure 6.13E) in comparison to *Slc5a6*$^{+/F;TnTCre}$ (p=0.0013) and *Slc5a6*$^{+/+}$ (p<0.0001), and T wave inversion (Figure 6.13F) not observed in *Slc5a6*$^{+/+}$ (p=0.0002) or *Slc5a6*$^{+/F;TnTCre}$ (p=0.0078) mice.

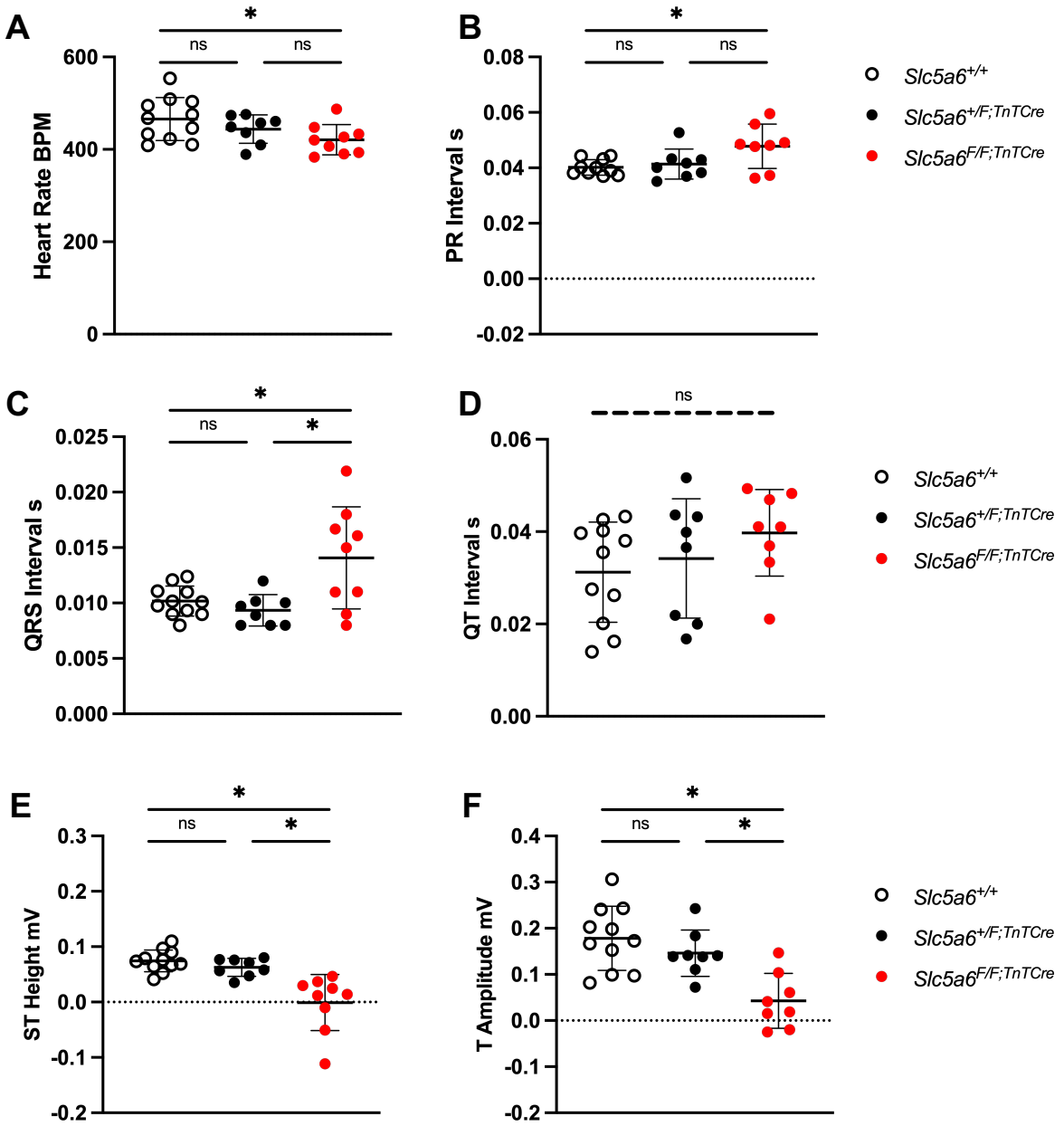

Figure 6.13. Quantification of ECG parameters for *Slc5a6*^{TnTCre} mice at 14 weeks. ECG recordings were analysed across three genotypes; *Slc5a6*$^{+/+}$ (white), *Slc5a6*$^{+/F;TnTCre}$ (black) and *Slc5a6*$^{F/F;TnTCre}$ mice (red). At 14 weeks, *Slc5a6*$^{F/F;TnTCre}$ mice show similar characteristics observed at 8 weeks; significant decrease in HR (A), ST height (E) and T wave amplitude (F), as well as a significant lengthening of PR interval (B) and wide QRS interval (C) compared to *Slc5a6*$^{+/+}$ and *Slc5a6*$^{+/F;TnTCre}$ mice. One-way ANOVA with multiple comparisons and Bonferroni correction was applied to each dataset. n= 11 *Slc5a6*$^{+/+}$, 8 *Slc5a6*$^{+/F;TnTCre}$ and 9 *Slc5a6*$^{F/F;TnTCre}$ mice. * = p<0.05.

To investigate the cardiac abnormalities further, 4 *Slc5a6*$^{F/F;TnTCre}$ mice underwent CMR imaging at 14 weeks. As there were no significant difference between *Slc5a6*$^{+/+}$ and *Slc5a6*$^{+/F;TnTCre}$ mice by ECG, and to reduce significant imaging costs, only *Slc5a6*$^{+/+}$ (*n*=3) were examined for comparison by CMR imaging as shown in 6.2.4.

The remaining *Slc5a6*$^{F/F;TnTCre}$ mice continued to be monitored by ECG at 18 weeks (Figure 6.14). However, following ECG recordings, it was found that cardiac conduction was heavily reduced in *Slc5a6*$^{F/F;TnTCre}$ mice at 18 weeks (Figure 6.14C), and hence quantification of ECG parameters could not be accurately determined. Traces from *Slc5a6*$^{+/+}$ (Figure 6.14A) and *Slc5a6*$^{+/F;TnTCre}$ (Figure 6.14B) mice appear “normal”; accurate determination of P wave, PR, QRS and QT interval could be performed by the analysis software. However, from the averaged ECG traces of *Slc5a6*$^{F/F;TnTCre}$ mice (Figure 6.14C) a number of issues arose including, mis-identification of the P wave with potentially two P waves observed, which hindered the quantification of the PR interval as two possible PR intervals could be analysed (software determined = red, manual determination = blue). The QRS complex lacked any identifiable Q wave, initiating the start of ventricular depolarisation, or terminal S wave marking the completion of ventricular contraction and the beginning of ventricular repolarisation. Without these markers, accurate quantification of the width of QRS cannot be determined, suggesting *Slc5a6*$^{F/F;TnTCre}$ mice have substantially reduced conductivity, which may cause the heart to fail.

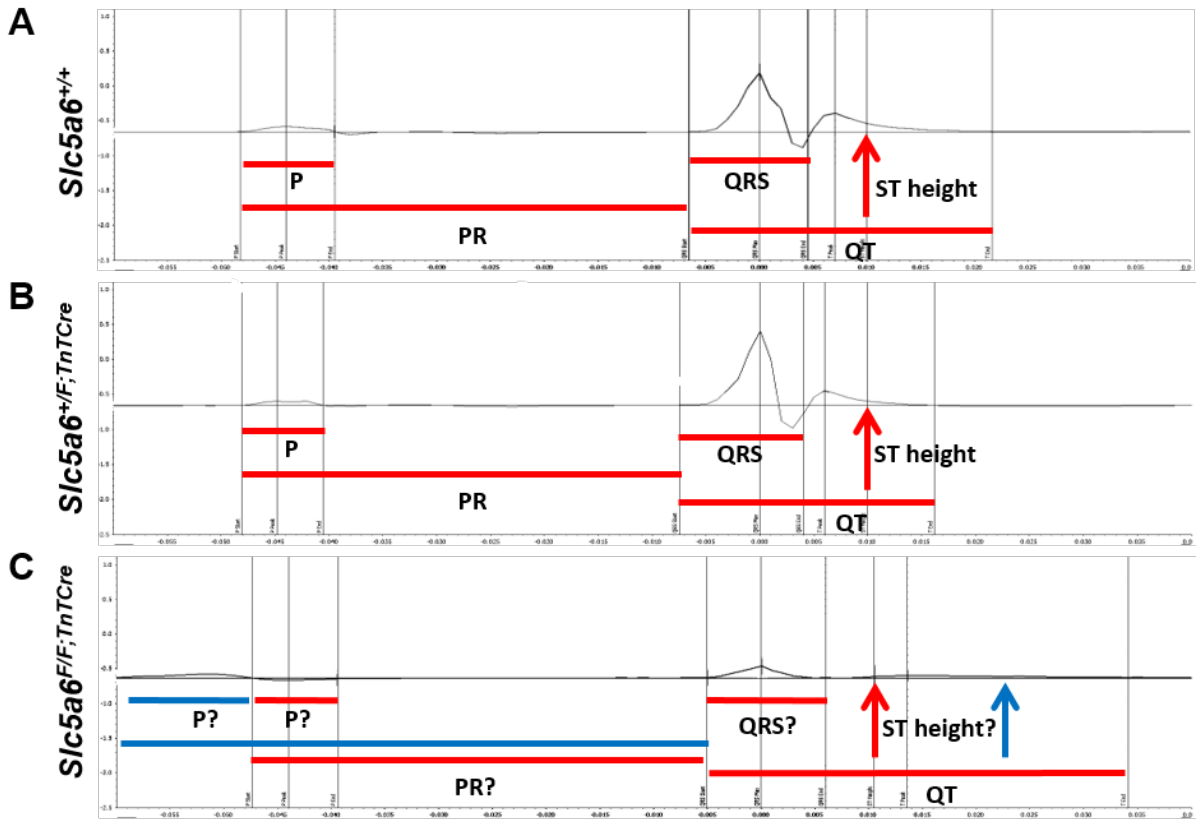

Figure 6.14. Representative ECG traces of *Slc5a6*^{TnTCre} mice at 18 weeks. Representative images of averaged ECG traces are shown from 60-120 second period for *Slc5a6TnTCre* mice at 18 weeks. ECG parameters are highlighted (red); P wave, PR interval, QRS interval, QT interval and ST height on each representative trace *Slc5a6*$^{+/+}$ (A), *Slc5a6*$^{+/F;TnTCre}$ (B) and *Slc5a6*$^{F/F;TnTCre}$ (C). 18 weeks: n= 7 *Slc5a6*$^{+/+}$, 5 *Slc5a6*$^{+/F;TnTCre}$ and 6 *Slc5a6*$^{F/F;TnTCre}$ mice.

It is important to note, at 18 weeks in the cage, the *Slc5a6*$^{F/F;TnTCre}$ mutant mice appeared phenotypically comparable to littermate controls, *Slc5a6*$^{+/+}$ and *Slc5a6*$^{+/F;TnTCre}$ mice. There were no clinical signs of ill health such as weight loss, lack of mobility or starry coats. Following the identification of the severity of the conduction defects, 4 *Slc5a6*$^{F/F;TnTCre}$ and 6 *Slc5a6*$^{+/+}$ mice underwent CMR imaging at 20 weeks, to further characterise the degree of cardiac dysfunction within this mouse line.

In summary, *Slc5a6*$^{F/F;TnTCre}$ mice development significant ECG abnormalities including prolonged PR interval indicating the presence of an atrioventricular block, widened QRS complex signifying myocardial fibrosis, and inversion of the ST and T wave amplitude suggestive of LV strain within the heart at 14 weeks. At 18 weeks ECG abnormalities become so pronounced accurate determination of parameters could not be performed.

6.2.5 *Cardiac function is severely reduced in Slc5a6$^{F/F;TnTCre}$ mice*

Investigation into the cardiac function of *Slc5a6^{TnTCre}* mice was carried out by CMR imaging at two time points; 14 and 20 weeks. Mice were orientated to capture the heart in the short axis plane for analysis. From the CMR images acquired, a number of measurements can be made to investigate changes to the LV chamber. Figure 6.15 shows the quantification of LV thickness in end diastole and end systole, as well as the absolute change (Δ) in LV thickness in *Slc5a6$^{+/+}$* and *Slc5a6$^{F/F;TnTCre}$* mice. There are no significant changes observed in LV thickness between *Slc5a6$^{+/+}$* and *Slc5a6$^{F/F;TnTCre}$* mice in end diastole (Figure 6.15A) or end systole (Figure 6.15B) at both time points. However, the data shows a significant decrease in the LV thickness of *Slc5a6$^{F/F;TnTCre}$* mice in comparison to *Slc5a6$^{+/+}$* mice at 14 weeks (p=0.0105) and 20 weeks (p=0.0065), when investigating the absolute (Δ) change in LV thickness from end systole to end diastole (Figure 6.15C). This reveals that there is a reduction in the thickening of the LV wall during contraction and relaxation in *Slc5a6$^{F/F;TnTCre}$* mice. A possible explanation for LV stiffening is the presence of myocardial fibrosis as suggested by ECG data.

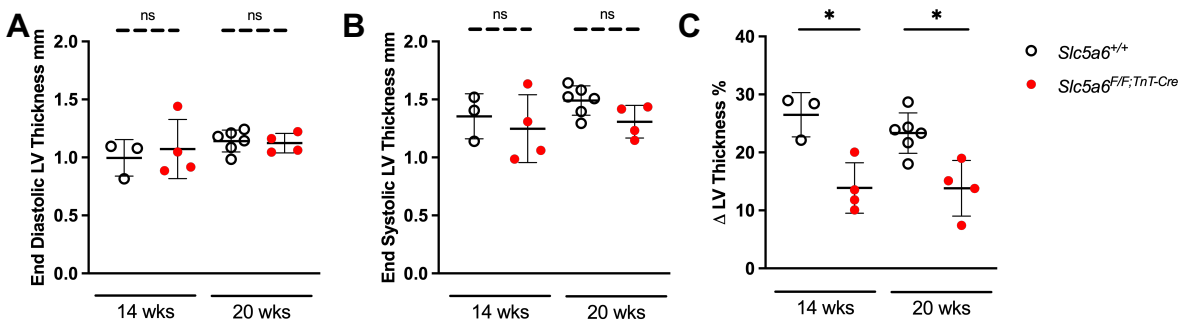

Figure 6.15. Quantification of LV thickness of *Slc5a6^{TnTCre}* mice at 14 and 20 weeks.

From CMR imaging, LV myocardial thickness was measured at end diastole and end systole and the Δ change in LV thickness was calculated at both timepoints. (A) No significant difference was observed between *Slc5a6$^{+/+}$* and *Slc5a6$^{F/F;TnTCre}$* LV thickness in diastole at 14 an 20 weeks. (B) Similarly, no difference in systolic LV thickness was observed between genotypes at both time points. (C) Δ change in LV thickness in end diastole compared to end systole shows a significant decrease in *Slc5a6$^{F/F;TnTCre}$* mice at 14 weeks (p = 0.0105) and 20 weeks (p = 0.0065). 14 weeks n = 3 *Slc5a6$^{+/+}$*, 4 *Slc5a6$^{F/F;TnTCre}$*. 20 weeks n= 6 *Slc5a6$^{+/+}$*, 4 *Slc5a6$^{F/F;TnTCre}$*. Students' unpaired two-tailed t-test was performed on each dataset. * = p<0.05.

In addition to measuring LV thickness, a number of volumetric parameters can be quantified to determine the efficiency of the heart *in vivo* (Figure 6.16). Using the same axial plane images, the mean mass of the heart can be calculated, in addition to the volume of blood pumped, per minute (cardiac output, CO) and per contraction (stroke volume, SV). SV can then be used to determine the contractility of the heart (ejection fraction, EF). Together these measurements provide an indication into the overall function of the heart. Although there is a significant decrease in the Δ change in LV thickness there is no significant difference observed in the mean mass of *Slc5a6*$^{F/F;TnTCre}$ mice compared to *Slc5a6*$^{+/+}$ at both time points investigated (Figure 6.16A).

In *Slc5a6*$^{F/F;TnTCre}$ mice at 14 weeks, there is an observable trend showing a decline in overall cardiac function compared to *Slc5a6*$^{+/+}$ mice. This is highlighted by changes in CO (Figure 6.16C) and EF (Figure 6.16D) with a significant decrease in SV (p=0.0226) (Figure 6.16B). The decline in cardiac function becomes significant at 20 weeks. A significant two-fold decrease is observed in SV (p=0.0146) (Figure 6.16B) and CO (p=0.007) (Figure 6.16C). Importantly, a significant decrease is seen in the EF of *Slc5a6*$^{F/F;TnTCre}$ mice averaging 28.8% (Figure 6.16D). Patients with an EF of less than 40% are diagnosed with heart failure (HF) with reduced EF (Riehle and Bauersachs, 2019), suggesting a reduction to 28.8% is indicative of systolic dysfunction and HF in *Slc5a6*$^{F/F;TnTCre}$ mice at 20 weeks.

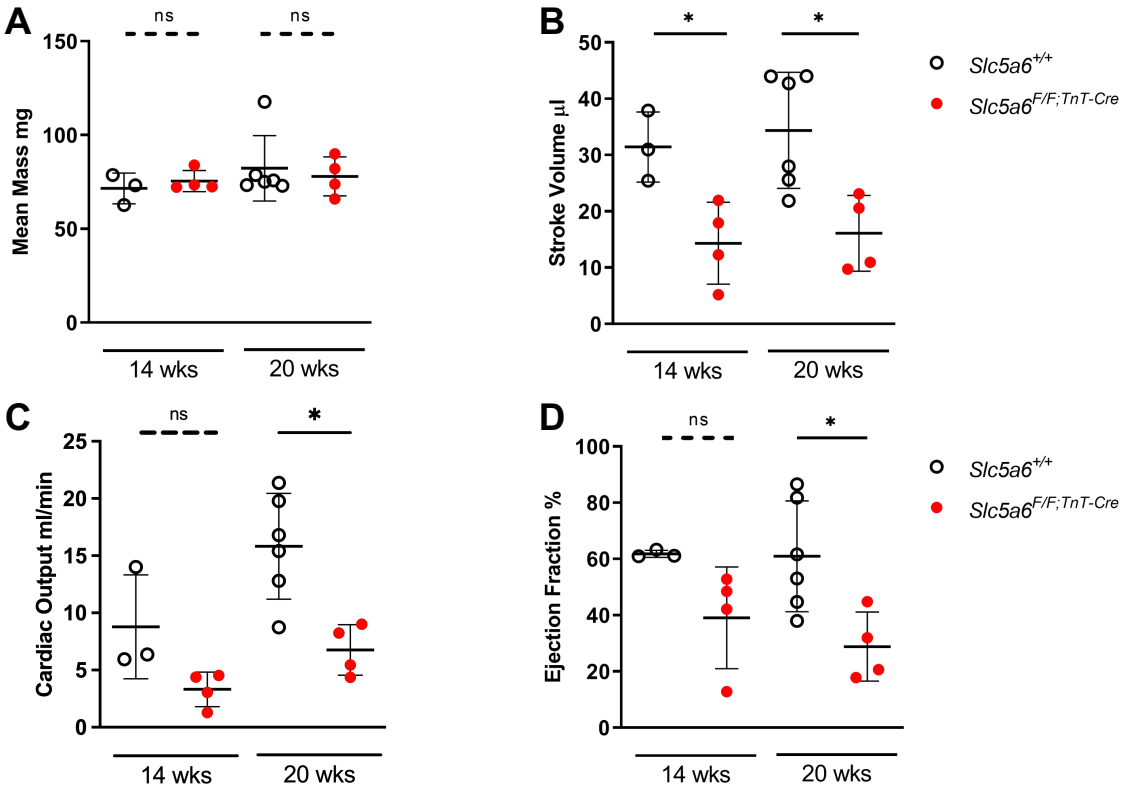

Figure 6.16. Volumetric analysis of LV chamber of *Slc5a6^{TnTCre}* mice at 14 and 20 weeks.
CMR imaging was performed on *Slc5a6^{TnTCre}* mice at 14 and 20 weeks. (A) Mean mass was comparable between *Slc5a6$^{+/+}$* and *Slc5a6$^{F/F;TnTCre}$* mice at 14 and 20 weeks. (B) Stroke volume is significantly reduced in *Slc5a6$^{F/F;TnTCre}$* mice compared to *Slc5a6$^{+/+}$* at both 14 (p=0.0226) and 20 weeks (p=0.0146). (C) At 14 weeks *Slc5a6$^{F/F;TnTCre}$* mice show a trend towards a decrease in cardiac output compared to *Slc5a6$^{+/+}$* mice. There is a significant decrease in cardiac output observed at 20 weeks (p=0.007). (D) A reduction in ejection fraction is observed in *Slc5a6$^{F/F;TnTCre}$* mice compared to *Slc5a6$^{+/+}$* mice at 14 weeks;however, the decrease is not significant. At 20 weeks *Slc5a6$^{F/F;TnTCre}$* mice show a significant two-fold decrease in ejection fraction (p=0.0207) compared to *Slc5a6$^{+/+}$* mice. Students' unpaired t-test was performed on each dataset. * = <0.05. 14 weeks n = 3 *Slc5a6$^{+/+}$*, 4 *Slc5a6$^{F/F;TnTCre}$*. 20 weeks n= 6 *Slc5a6$^{+/+}$*, 4 *Slc5a6$^{F/F;TnTCre}$*.

These results together with the ECG findings of atrioventricular block, myocardial fibrosis and left ventricular strain pattern strongly suggest that the loss of *Slc5a6* within the heart affects normal cardiac function. To further understand the changes in cardiac function on the structure of the heart in *Slc5a6$^{F/F;TnTCre}$* mice, histological staining was performed at both 14 and 20 weeks.

6.2.6 *Slc5a6$^{F/F;TnTCre}$ mice have an enlarged heart at 14 and 20 weeks*

As shown by functional data, *Slc5a6$^{F/F;TnTCre}$* mice display signs of cardiac dysfunction often associated with cardiomyopathy, namely a reduction in LV thickness, systolic dysfunction and signs of myocardial fibrosis. To confirm these changes, hearts were collected at 14 and 20 weeks, cryo-embedded and sectioned for histological analysis. All hearts were imaged and weighed at collection for comparison across genotypes at 14 (Figure 6.17) and 20 weeks (Figure 6.18).

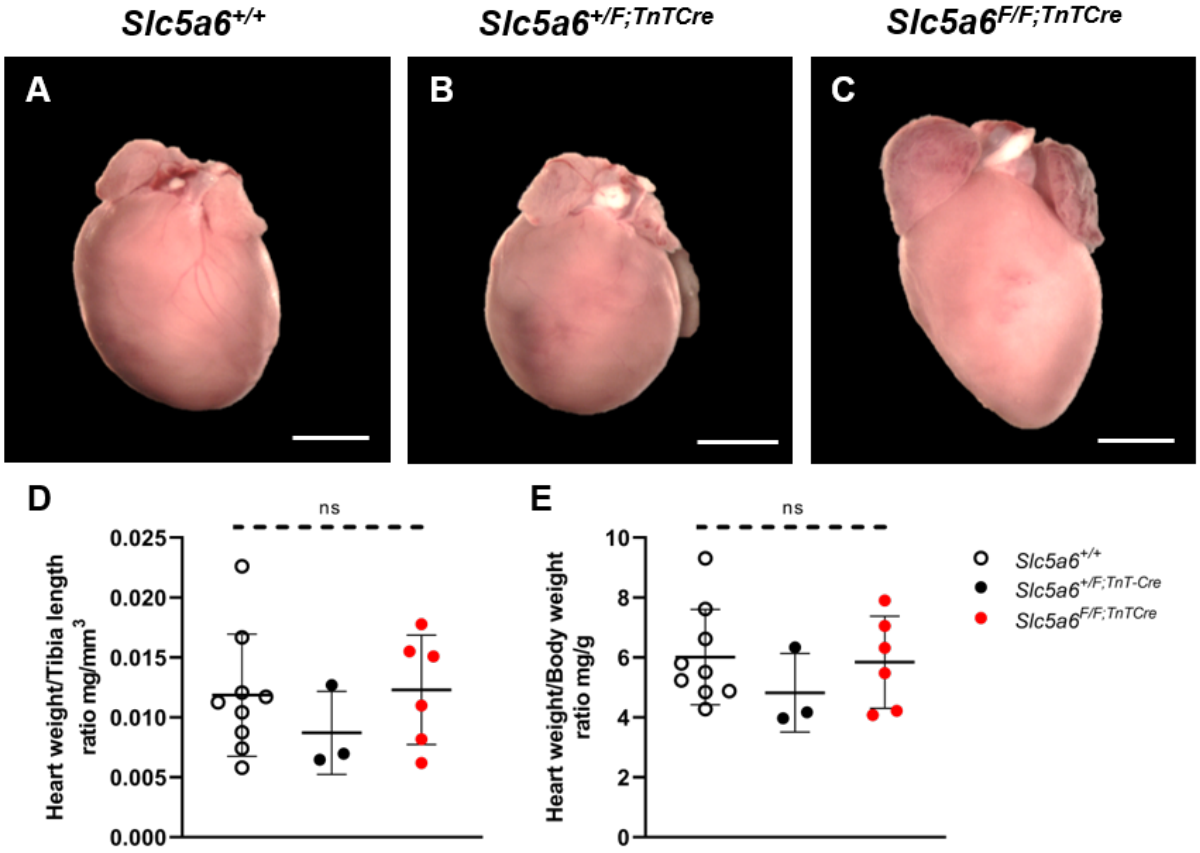

Figure 6.17. Whole heart images and heart weight ratios for *Slc5a6^{TnTCre}* mice at 14 weeks.
Whole heart images for *Slc5a6$^{+/+}$* (A), *Slc5a6$^{+/F;TnTCre}$* (B), *Slc5a6$^{F/F;TnTCre}$* (C) mice. Heart weight was normalised to tibia length (D) and body weight (E) for *Slc5a6$^{+/+}$* (white), *Slc5a6$^{+/F;TnTCre}$* (black) and *Slc5a6$^{F/F;TnTCre}$* (red) mice. No significant difference was found between each genotype for both datasets. One-way ANOVA with multiple comparisons and Bonferroni correction was applied to each dataset. n= 9 *Slc5a6$^{+/+}$*, 3 *Slc5a6$^{+/F;TnTCre}$* and 6 *Slc5a6$^{F/F;TnTCre}$* . Scale bars A-C = 2mm.

Hearts collected at 14 weeks show a visible enlargement of the atria and ventricles in *Slc5a6$^{F/F;TnTCre}$* (Figure 6.17C) mice compared to *Slc5a6$^{+/+}$* (Figure 6.17A), and *Slc5a6$^{+/F;TnTCre}$* (Figure 6.17B). This was also observed in the hearts collected from *Slc5a6$^{F/F;TnTCre}$* mice that suddenly died at 26 weeks. Heart weight was normalised to both tibia length (Figure 6.17D) and body weight (Figure 6.17E) at collection. Data

showed no significant difference between *Slc5a6*$^{+/+}$, *Slc5a6*$^{+/F;TnTCre}$ and *Slc5a6*$^{F/F;TnTCre}$ hearts at 14 weeks, despite a clear visible enlargement of *Slc5a6*$^{F/F;TnTCre}$ hearts.

Similarly, hearts collected at 20 weeks also show comparable heart weight ratios to tibia length (Figure 6.18D) and body weight (Figure 6.18E); however, due to a low *n of* *Slc5a6*$^{+/F;TnTCre}$ mice statistical testing could not be performed. Representative whole heart images taken after CMR imaging, on a digital camera are shown for *Slc5a6TnTCre* mice at 20 weeks (Figure 6.18). *Slc5a6*$^{F/F;TnTCre}$ hearts (Figure 6.18C) appear to have slightly larger atria and ventricles compared to *Slc5a6*$^{+/+}$ (Figure 6.18A) and *Slc5a6*$^{+/F;TnTCre}$ (Figure 6.18B).

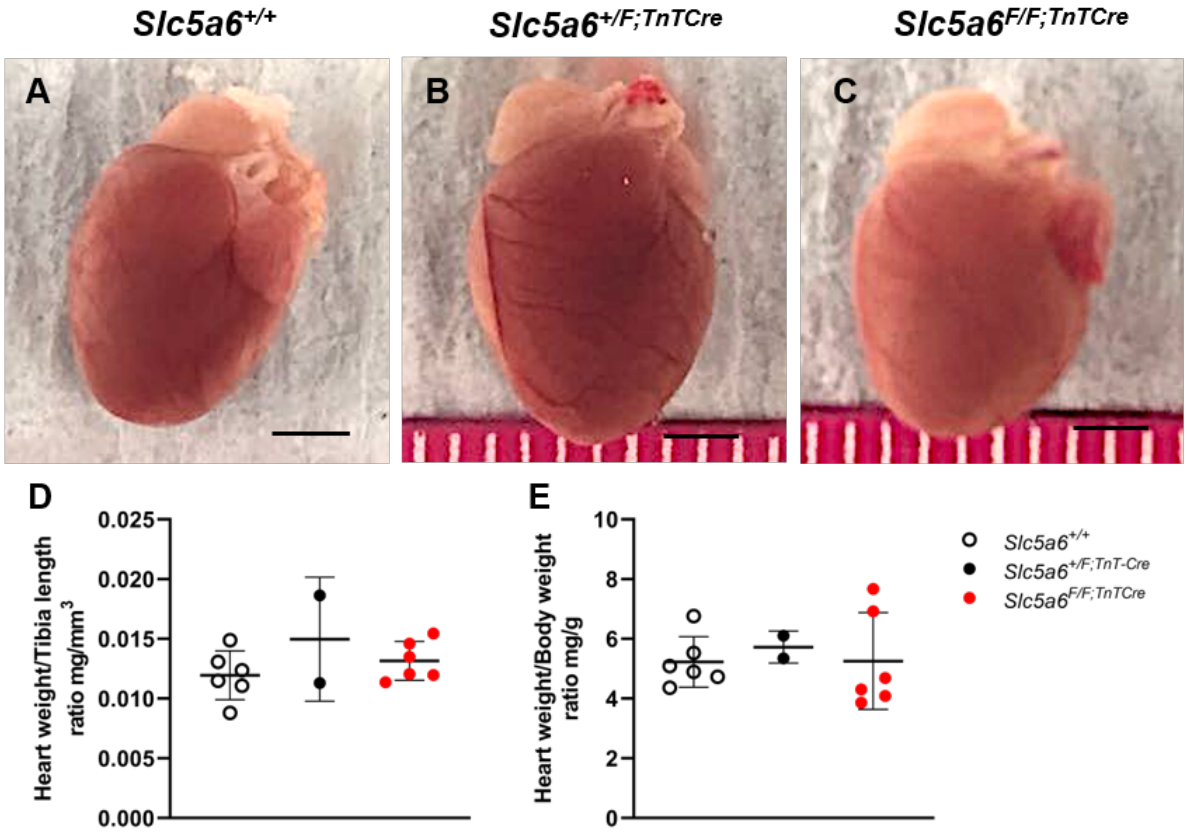

Figure 6.18. Whole heart images and heart weight ratios of *Slc5a6*^{TnTCre} mice at 20 weeks.
Digital images taken for *Slc5a6*$^{+/+}$ (A), *Slc5a6*$^{+/F;TnTCre}$ (B), *Slc5a6*$^{F/F;TnTCre}$ (C) mice at 20 weeks following CMR. Heart weight was normalised to tibia length (D) and body weight (E) for *Slc5a6*$^{+/+}$ (white), *Slc5a6*$^{+/F;TnTCre}$ (black) and *Slc5a6*$^{F/F;TnTCre}$ (red) mice. Statistical testing could not be performed as *n* was too low for *Slc5a6*$^{+/F;TnTCre}$ mice; however, the mean of each genotype appears comparable for both ratios. *n* = 6 *Slc5a6*$^{+/+}$, 2 *Slc5a6*$^{+/F;TnTCre}$ and 6 *Slc5a6*$^{F/F;TnTCre}$ mice. Scale bars A-C = 2mm (ruler included in images for scale).

One hypothesis for the comparable heart weight ratios at both ages, is that *Slc5a6*$^{F/F;TnTCre}$ hearts appear enlarged due to ventricular dilation and remodelling to compensate for reduced cardiac function and therefore the overall mass of *Slc5a6*$^{F/F;TnTCre}$ hearts are comparable to the unaffected *Slc5a6*$^{+/+}$ and *Slc5a6*$^{+/F;TnTCre}$ hearts. To investigate this, cryosections were examined by histological staining (Figure 6.19).

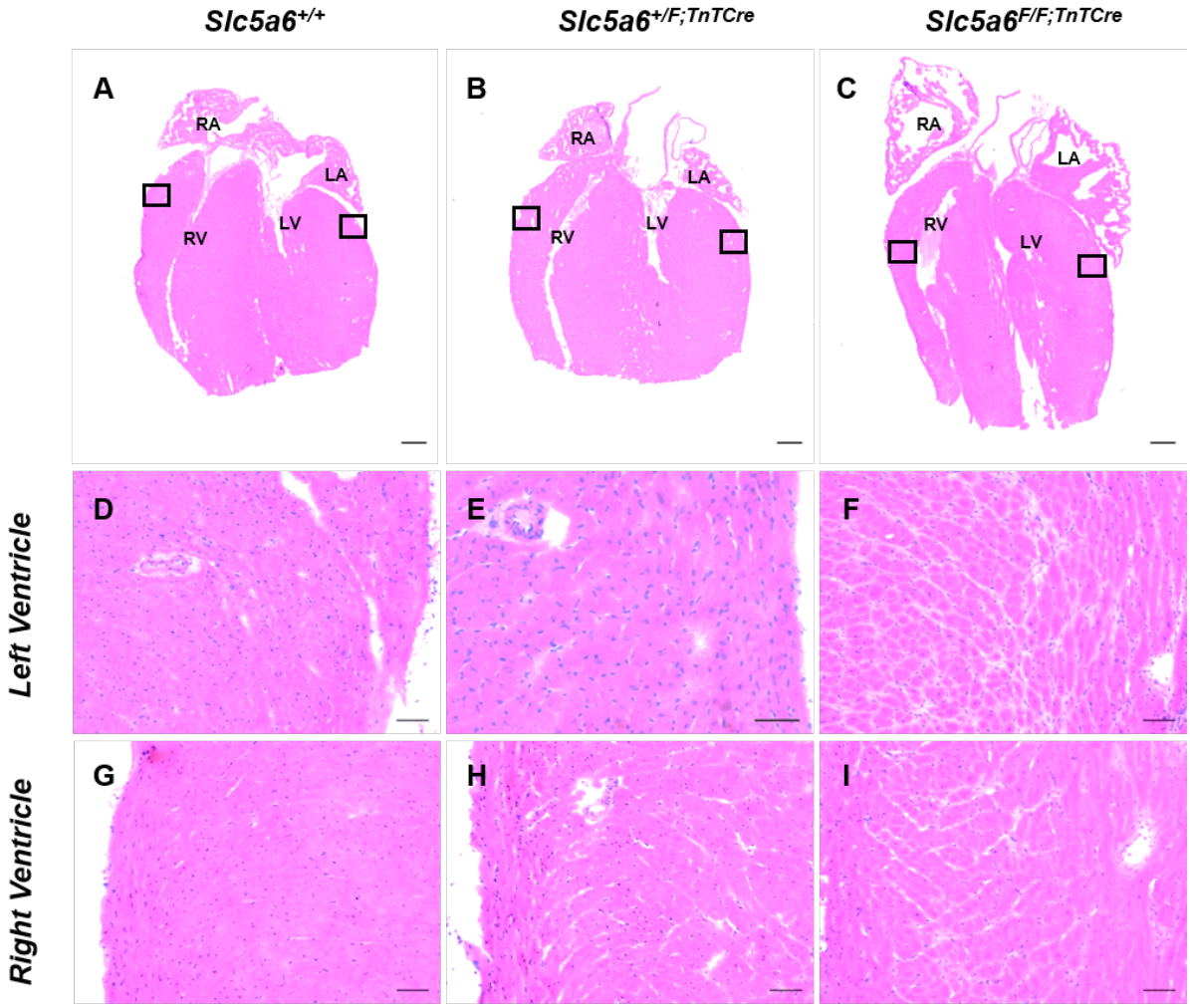

Figure 6.19. H&E staining of *Slc5a6*^{TnTCre} mice at 14 weeks.
Histological stain by H&E was performed on coronal sections of 14 week old hearts. Low magnification brightfield images were taken for *Slc5a6*$^{+/+}$ (A), *Slc5a6*$^{+/F;TnTCre}$ (B), *Slc5a6*$^{F/F;TnTCre}$ (C). Higher powered images were taken, of the LV and RV of *Slc5a6*$^{+/+}$ (D, G), *Slc5a6*$^{+/F;TnTCre}$ (E, H) and *Slc5a6*$^{F/F;TnTCre}$ (F, I), respectively. n = 5 *Slc5a6*$^{+/+}$, 3 *Slc5a6*$^{+/F;TnTCre}$ and 4 *Slc5a6*$^{F/F;TnTCre}$. Scale bars A-C = 500µm, D-I = 50µm. Left atria LA, left ventricle LV, right atria RA, right ventricle RV.

Staining by H&E revealed gross enlargement of the cardiac chambers in *Slc5a6*$^{F/F;TnTCre}$ hearts (Figure 6.19C) compared to *Slc5a6*$^{+/+}$ (Figure 6.19A) and *Slc5a6*$^{+/F;TnTCre}$ (Figure 6.19B) hearts at 14 weeks. Higher powered images of *Slc5a6*$^{+/+}$; LV (Figure 6.19D) and RV (Figure 6.19G), *Slc5a6*$^{+/F;TnTCre}$; LV (Figure 6.19E)

and RV (Figure 6.19H) show a compact myocardium with tightly packed cardiomyocytes at 14 weeks. In comparison, images taken in the LV of *Slc5a6*$^{F/F;TnTCre}$ hearts (Figure 6.19F) show a less compact myocardium due to a high level of interstitial space between cardiomyocytes. This is also observed to a lesser degree in the RV of *Slc5a6*$^{F/F;TnTCre}$ mice (Figure 6.19I).

Due to processing issues (freezing artefacts), histological staining could not be performed on hearts collected at 20 weeks.

6.2.7 Interstitial fibrosis is increased in Slc5a6$^{F/F;TnTCre}$ hearts

To investigate the cause of interstitial space between cardiomyocytes, Picro-Sirius red staining was performed on *Slc5a6*$^{+/+}$ (Figure 6.20A), *Slc5a6*$^{+/F;TnTCre}$ (Figure 6.20B) and *Slc5a6*$^{F/F;TnTCre}$ (Figure 6.20C) sections collected at 14 weeks. Picro-Sirius red is a commonly used histological method to visualise collagen fibres (red) within tissue sections. The stain also allows for quantification of the amount of collagen present in tissue sections.

Staining for fibrosis revealed comparable levels of collagen fibres in both *Slc5a6*$^{+/+}$; LV (Figure 6.20D), RV (Figure 6.20G) and *Slc5a6*$^{+/F;TnTCre}$; LV (Figure 6.20E), RV (Figure 6.20H). However, Picro-Sirius red stain in *Slc5a6*$^{F/F;TnTCre}$ hearts showed the interstitial space between cardiomyocytes observed by H&E is indeed fibrosis in the LV (Figure 6.20F) and RV (Figure 6.20I). The area of fibrosis was compared between each genotype for both the LV (Figure 6.20J) and RV (Figure 6.20K). Four images were acquired for 3 regions of interest throughout the LV and RV. The area of fibrosis was quantified for each image and averaged per section. This analysis was repeated on two further sections and averaged for each biological replicate. Analysis revealed a significant increase in the amount of fibrosis in the LV of *Slc5a6*$^{F/F;TnTCre}$ mice compared to *Slc5a6*$^{+/+}$ (p=0.001) and *Slc5a6*$^{+/F;TnTCre}$ (p=0.0009) mice. Fibrosis is also significantly increased in the RV of *Slc5a6*$^{F/F;TnTCre}$ mice compared to *Slc5a6*$^{+/+}$ (p<0.0001) and *Slc5a6*$^{+/F;TnTCre}$ (p<0.0001) mice.

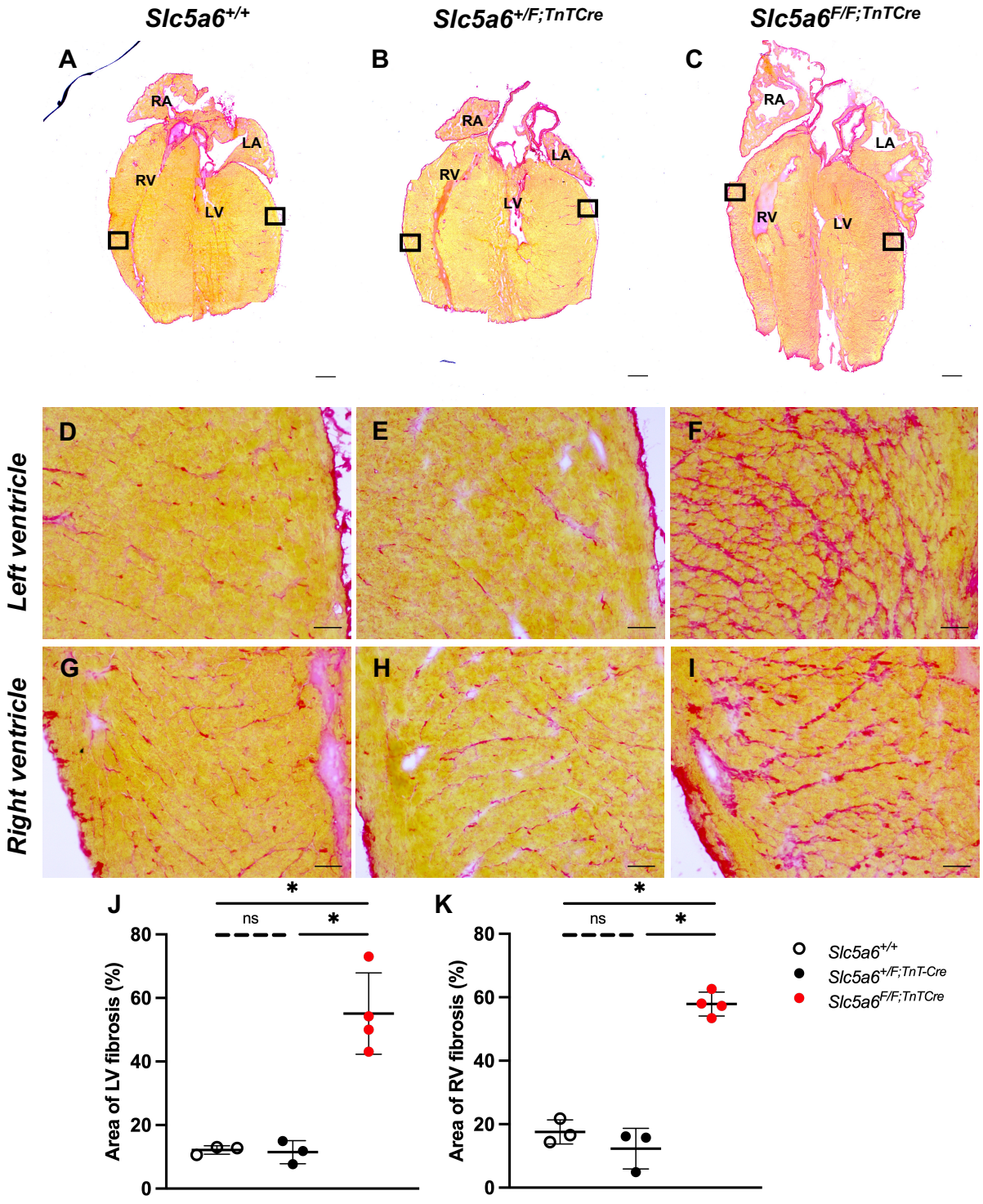

Figure 6.20. Picro-Sirius red staining of *Slc5a6*^{TnTCre} mice at 14 weeks.
Picro-Sirius red was performed on sections of *Slc5a6*$^{+/+}$ (A), *Slc5a6*$^{+/F;TnTCre}$ (B), *Slc5a6*$^{F/F;TnTCre}$ (C) hearts collected at 14 weeks. Higher powered images were taken, of the LV and RV of *Slc5a6*$^{+/+}$ (D, G), *Slc5a6*$^{+/F;TnTCre}$ (E, H) and *Slc5a6*$^{F/F;TnTCre}$ (F, I), respectively. One-way ANOVA with multiple comparisons and Bonferroni correction was applied to each dataset; n = 3 *Slc5a6*$^{+/+}$ (108 LV cardiomyocytes and RV cardiomyocytes), 3 *Slc5a6*$^{+/F;TnTCre}$ (108 LV cardiomyocytes and RV cardiomyocytes) and 4 *Slc5a6*$^{F/F;TnTCre}$ (144 LV cardiomyocytes and RV cardiomyocytes). * = p<0.05. Scale bars A-C = 500µm, D-I = 50 µm. Left atria LA, left ventricle LV, right atria RA, right ventricle RV.

The increase in fibrosis found in *Slc5a6*$^{F/F;TnTCre}$ hearts is suggestive of pathological remodelling within the myocardium due to the loss of *Slc5a6* within cardiomyocytes, as no significant difference in the amount of fibrosis between *Slc5a6*$^{+/+}$ and *Slc5a6*$^{+/F;TnTCre}$ in either the LV (p>0.9999) or RV (p=0.6264) at 14 weeks.

6.2.8 Cardiomyocyte hypertrophy present in Slc5a6$^{F/F;TnTCre}$ mice

One of the markers of cardiomyopathy commonly investigated is the presence of hypertrophic cardiomyocytes. This is an adaptive process, by which the heart undergoes mechanical stress and compensates to increase cardiac function by increasing cardiomyocyte size. To investigate the presence of cardiomyocyte hypertrophy, cardiac cryosections of 14 week old mice were stained with a fluorescently conjugated wheat germ agglutinin (WGA) antibody (Figure 6.21). This is a lectin that binds to N-acetyl-D-glucosamine found within the cell membrane of mammalian cells and allows for fluorescent labelling of cell membranes. Using image analysis software, the area of cardiomyocytes in the LV (Figure 6.21G) and RV (Figure 6.21H) was determined for comparison between genotypes.

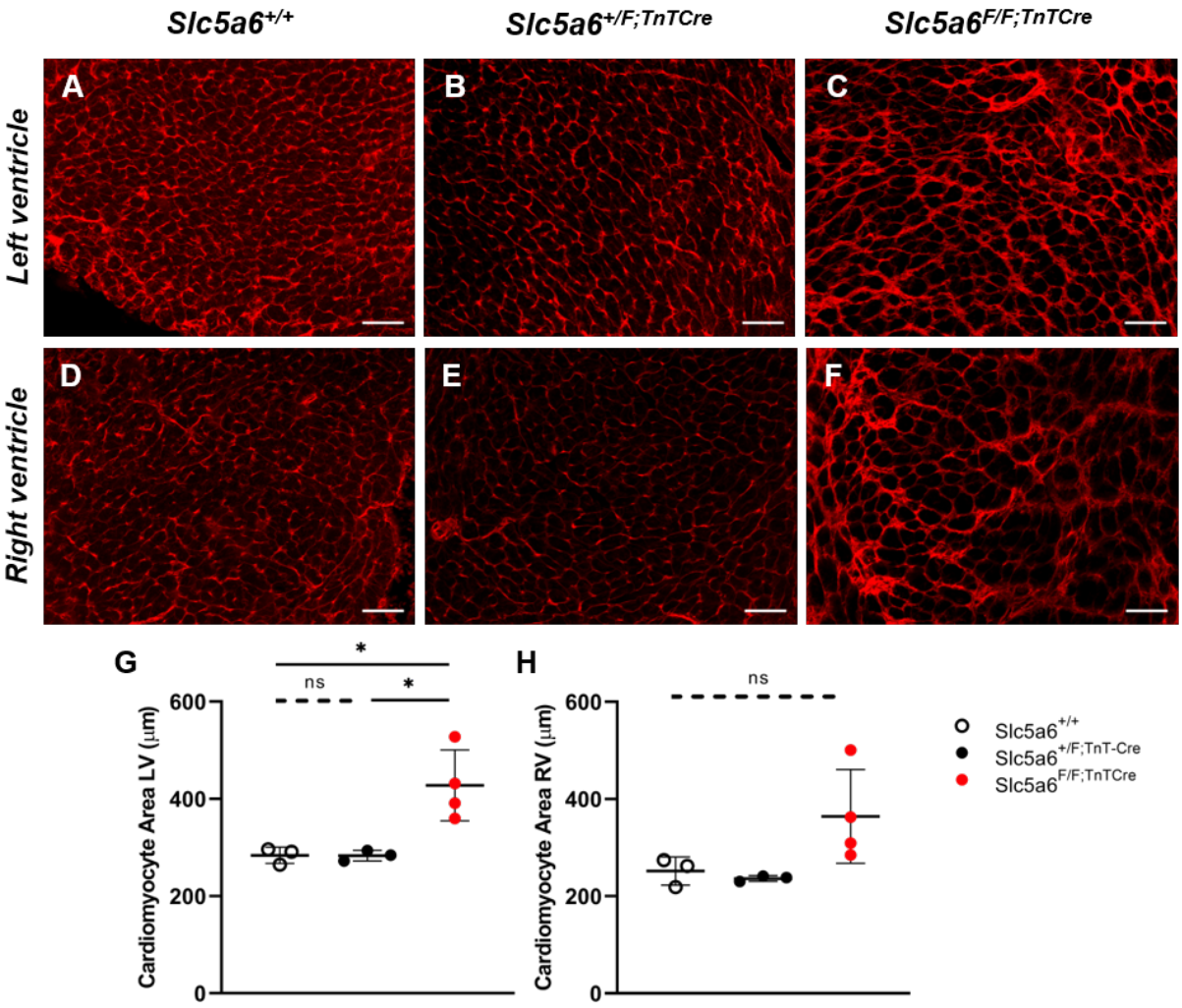

Figure 6.21. Cardiomyocyte area measurements for *Slc5a6*^{TnTCre} mice at 14 weeks.
WGA staining was performed on coronal sections of *Slc5a6*$^{+/+}$ (A, D), *Slc5a6*$^{+/F;TnTCre}$ (B, E), *Slc5a6*$^{F/F;TnTCre}$ (C, F) hearts collected at 14 weeks. Images taken of the LV (A-C) and RV (D-F) are shown for each genotype. From these images, the area of cardiomyocytes in both the LV (G) and RV (H) was measured for *Slc5a6*$^{+/+}$ (white), *Slc5a6*$^{+/F;TnTCre}$ (black) and *Slc5a6*$^{F/F;TnTCre}$ (red). One-way ANOVA with multiple comparisons and Bonferroni correction was applied to each dataset.; n = 3 *Slc5a6*$^{+/+}$ (2166 LV cardiomyocytes, 2159 RV cardiomyocytes), 3 *Slc5a6*$^{+/F;TnTCre}$ (2166 LV cardiomyocytes, 2159 RV cardiomyocytes) and 4 *Slc5a6*$^{F/F;TnTCre}$ (2886 LV cardiomyocytes, 2880 RV cardiomyocytes). * = p<0.05. Scale bars A-F = 50µm.

For each genotype, four images were acquired in three regions of each ventricle. This was performed in 3 sections of the same mouse, at least 10µm apart. Data was then averaged per mouse and used for analysis. The process was repeated for each mouse included in the analysis. Images acquired in the LV for *Slc5a6*$^{+/+}$ (Figure 6.21A) and *Slc5a6*$^{+/F;TnTCre}$ (Figure 6.21B) mice appear visibly comparable to one another. This similarity is also observed in the RV for *Slc5a6*$^{+/+}$ (Figure 6.21D) and *Slc5a6*$^{+/F;TnTCre}$ (Figure 6.21E) mice. Sections imaged from *Slc5a6*$^{F/F;TnTCre}$ mice show visibly enlarged

cardiomyocytes in both the LV (Figure 6.21C) and RV (Figure 6.21F); however, data shown in Figure 6.21H shows no significant difference observed in cardiomyocyte area of the RV between *Slc5a6*$^{F/F;TnTCre}$ mice and *Slc5a6*$^{+/+}$ (p=0.1744), *Slc5a6*$^{+/F;TnTCre}$ (p=0.1113). Whereas a significant increase in cardiomyocyte area is observed in the LV of *Slc5a6*$^{F/F;TnTCre}$ mice (Figure 6.21G) compared to *Slc5a6*$^{+/+}$ (p=0.00191) and *Slc5a6*$^{+/F;TnTCre}$ (p=0.0188). Although not a significant change in the cardiomyocyte area in the RV of *Slc5a6*$^{F/F;TnTCre}$ mice, there is certainly a trend towards larger cardiomyocytes found in *Slc5a6*$^{F/F;TnTCre}$ mice, compared to *Slc5a6*$^{+/+}$ and *Slc5a6*$^{+/F;TnTCre}$.

The presence of hypertrophic cardiomyocytes in *Slc5a6*$^{F/F;TnTCre}$ cardiac sections, in addition to increased myocardial fibrosis by Picro-Sirius red staining and signs of cardiac dysfunction suggest *Slc5a6* plays an important role within the heart. Loss of this transporter has a clear detrimental effect on normal cardiac function, causing the development of cardiomyopathy within *Slc5a6*$^{F/F;TnTCre}$ mice.

6.3 Ultrastructural abnormalities are present in *Slc5a6*$^{F/F;TnTCre}$ mice

Confirmation of cardiomyopathy within the *Slc5a6*$^{F/F;TnTCre}$ mice, triggered further study to underpin the mechanism causing disease of the myocardium within these mice. To do this, transmission electron microscopy (TEM) was performed following CMR. *Slc5a6*$^{+/+}$ *and Slc5a6*$^{F/F;TnTCre}$ hearts collected at 14 and 20 weeks, were dissected and a section of apex was sent to the electron microscopy research services (EMRS) at Newcastle University for heavy metal processing and sectioning for TEM. Figure 6.22 shows representative micrographs of *Slc5a6*$^{+/+}$ *and Slc5a6*$^{F/F;TnTCre}$ hearts at 14 weeks.

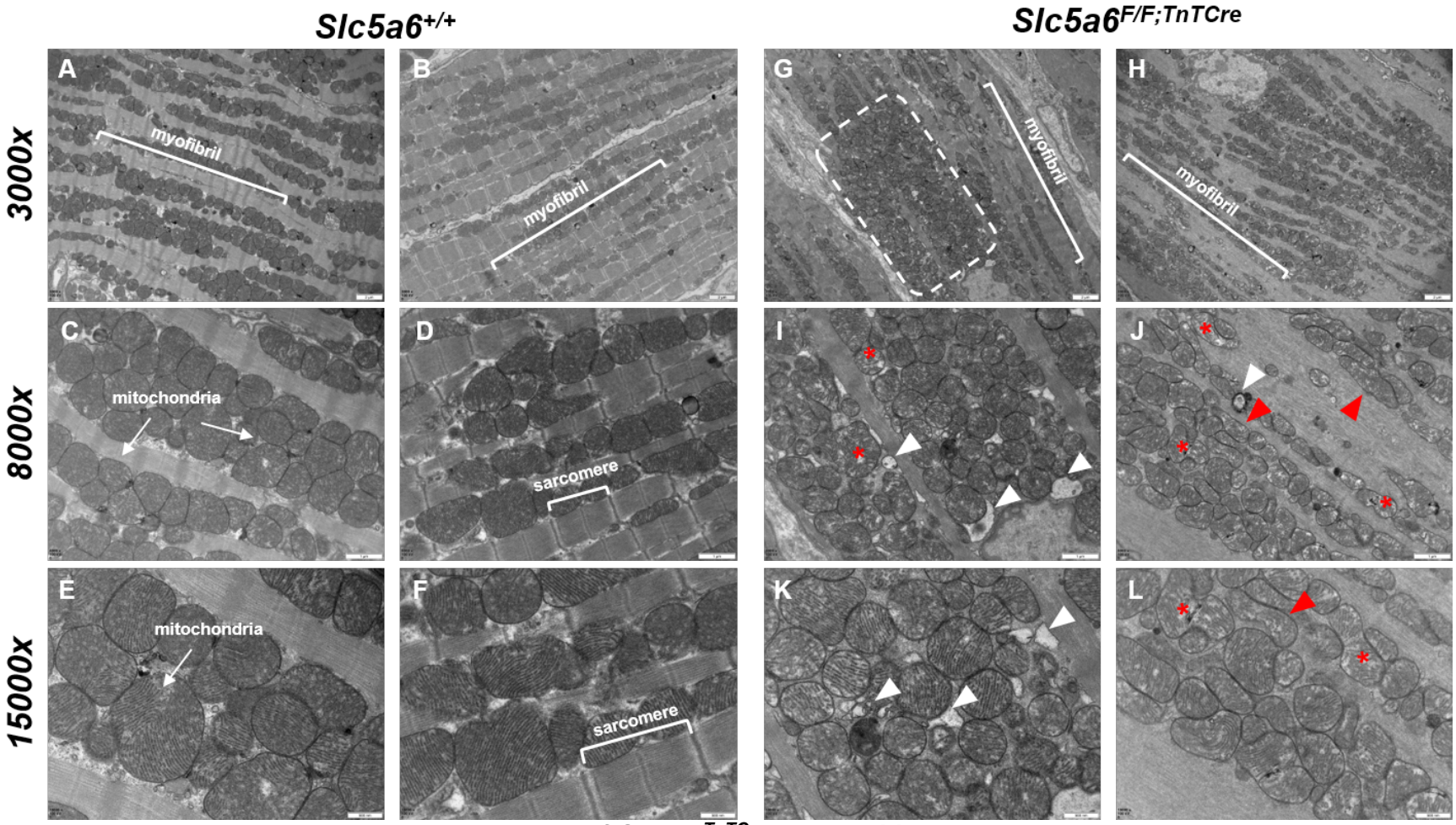

Figure 6.22. Transmission electron micrographs of *Slc5a6*^{TnTCre} mice at 14 weeks.
Representative micrographs are shown for *Slc5a6*$^{+/+}$ (A-F) and *Slc5a6*$^{F/F;TnTCre}$ (G-L) at 3000x, 8000x and 15000x magnifications. *Slc5a6*$^{+/+}$ show well defined sarcomeres with healthy rounded mitochondria; however, *Slc5a6*$^{F/F;TnTCre}$ sections reveal a lack of sarcomere definition between mitochondria, increased mitochondrial proliferation (dashed white boxes) and mitochondrial morphological abnormalities including mitochondrial degradation (white arrowheads), cristae degradation (red asterisk) and mitochondrial elongation (red arrowheads). *n* = 6 *Slc5a6*$^{+/+}$, 4 *Slc5a6*$^{F/F;TnTCre}$.

Micrographs taken at 3000x magnification from *Slc5a6*$^{+/+}$ hearts (Figure 6.22A,B) show uniformly, well-defined and highly organised sarcomeres with healthy round intermyofibrillar mitochondria evenly distributed throughout longitudinal sections. However, micrographs taken at the same magnification in *Slc5a6*$^{F/F;TnTCre}$ sections show a lack of sarcomeric definition and a pronounced increase in mitochondrial number (dashed white box) (Figure 6.22G and Figure 6.22H). Higher powered micrographs at 8000x magnification of *Slc5a6*$^{F/F;TnTCre}$ sections (Figure 6.22I,J) reveal a number of mitochondrial abnormalities including cristae degradation (red asterisk), mitochondrial degradation (white arrowhead) and elongation (red arrowhead). In comparison, *Slc5a6*$^{+/+}$ micrographs at 8000x show densely packed cristae within the mitochondria (Figure 6.22C) with intact, highly organised sarcomeres (Figure 6.22D). At 15000x, mitochondria found within *Slc5a6*$^{+/+}$ sections have a defined cristae structure with no signs of abnormalities (Figure 6.22E or Figure 6.22F). However, the mitochondria of *Slc5a6*$^{F/F;TnTCre}$ hearts appear smaller compared to *Slc5a6*$^{+/+}$ mitochondria, with noticeable mitochondrial degradation including mitochondrial remnants from degradation (Figure 6.22K) as well as whorled and degraded cristae (Figure 6.22L).

As described in 2.8.1, mitochondrial morphology was measured and analysed to quantify changes shown (Figure 6.22). At least 100 mitochondria were analysed per mouse in each genotype. For each parameter the level of skewness was determined as a measure of asymmetry in distribution of data where ‘0’ is equal to a normally distributed population set, ‘>0’ indicates a larger number of smaller values are found than expected and, ‘<0’ shows a bigger proportion of large values than expected. For *Slc5a6TnTCre* mice at 14 weeks (Table 6.2), data is shown to be skewed for all parameters in both *Slc5a6*$^{+/+}$ and *Slc5a6*$^{F/F;TnTCre}$ mitochondria resulting in the need for non-parametric Mann-Whitney test to be performed on each dataset. Data for each mitochondrion was placed into one of 15 bins of equal sizes to visualise the frequency distribution of each morphological parameter (Figure 6.23).

Table 6.2. Shape descriptors for mitochondria in *Slc5a6*^{TnTCre} hearts at 14 weeks. Skewness was calculated for each parameter as a measure of asymmetry in distribution of data where '0' is equal to a normally distributed population. *n* = 6 *Slc5a6*$^{+/+}$, 4 *Slc5a6*$^{F/F;TnTCre}$.

Shape descriptor	14 weeks					
	Slc5a6$^{+/+}$			*Slc5a6*$^{F/F;TnTCre}$		
	Median	Mean ± SD	Skewness	Median	Mean ± SD	Skewness
Aspect ratio	1.356	1.524±0.524	2.391	1.444	1.672±0.673	2.269
Form factor	1.104	1.183±0.202	2.522	1.13743	1.242±0.289	2.617
Area µm	0.781	0.843±0.418	1.122	0.579	0.645±0.350	1.756
Perimeter µm	3.341	3.349±0.975	0.838	2.897	3.093±1.070	1.691
Circularity (0-1)	0.906	0.864±0.112	-1.383	0.878	0.8355±0.136	-1.334
Feret's diameter µm	1.210	1.264±0.396	1.188	1.072	1.165±0.452	1.715

In addition to frequency distribution, median values were also plotted for each parameter with results of the non-parametric test shown on each graph (Figure 6.23). Mitochondria found in *Slc5a6*$^{F/F;TnTCre}$ hearts have a significant increase in aspect ratio (p<0.0001) compared to *Slc5a6*$^{+/+}$, suggesting mitochondria are long and narrow compared to mitochondria found in *Slc5a6*$^{+/+}$ hearts (Figure 6.23A,B). Similarly, the branching of mitochondria is significantly increased in *Slc5a6*$^{F/F;TnTCre}$ hearts compared to *Slc5a6*$^{+/+}$ (p<0.0001) shown by an increase in form factor (Figure 6.23C,D). Parameters which indicate mitochondrial size all show a decrease in mitochondrial size in Sc5a6$^{F/F;TnTCre}$ hearts; area (Figure 6.23E,F), perimeter (Figure 6.23G,H) and Feret's diameter (Figure 6.23K,L) are significantly decreased (p<0.0001) compared to *Slc5a6*$^{+/+}$. This together with the visible increase in the number of mitochondria found between sarcomeres in *Slc5a6*$^{F/F;TnTCre}$ hearts shown in Figure 6.22G, suggests an increase in mitochondrial proliferation. More morphological abnormalities are shown in *Slc5a6*$^{F/F;TnTCre}$ mitochondria by circularity ratio (Figure 6.23I,J), where 1 represents a perfect sphere. *Slc5a6*$^{F/F;TnTCre}$ mitochondria are significantly less circular compared to *Slc5a6*$^{+/+}$ mitochondria (p<0.0001).

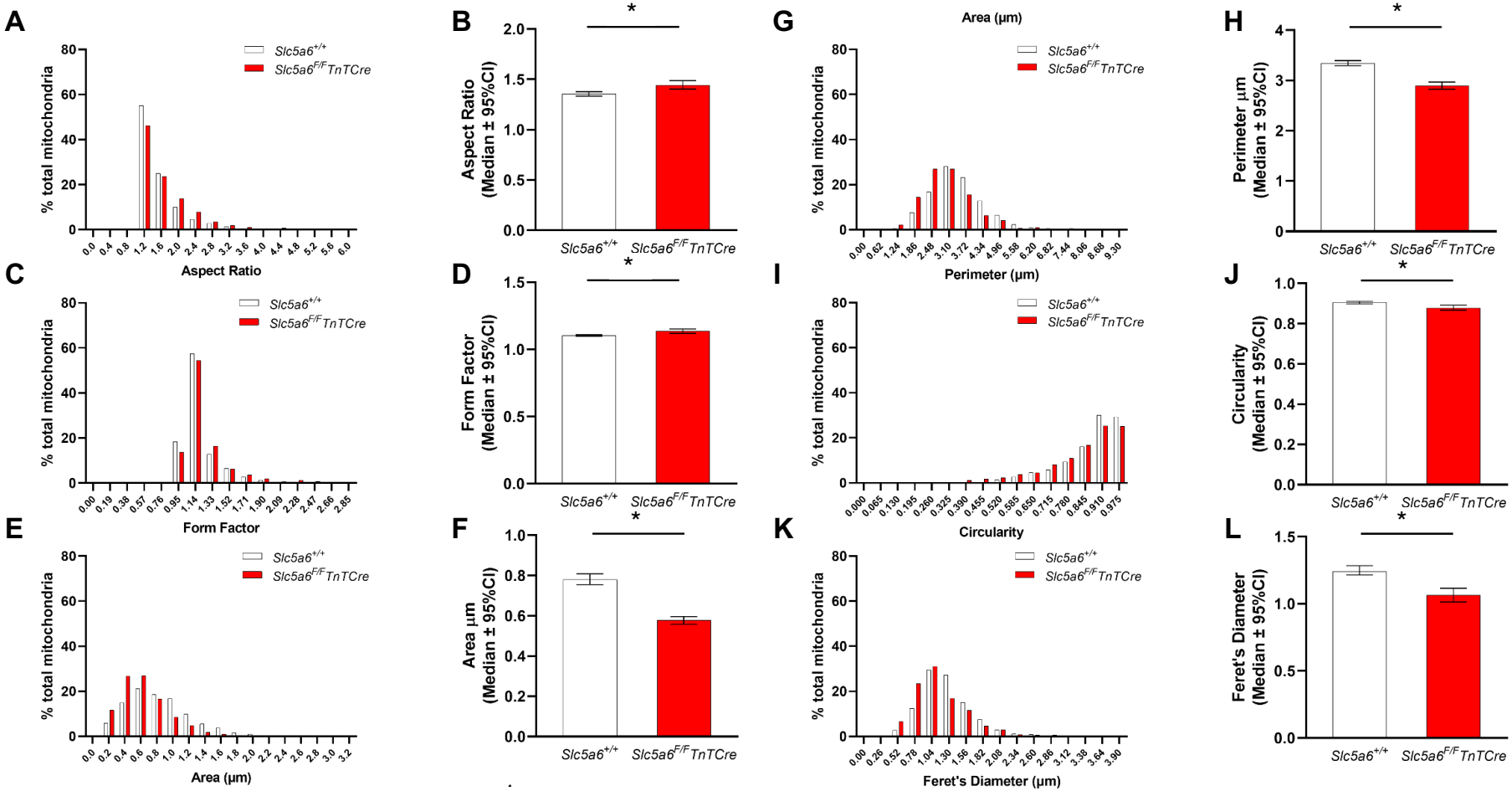

Figure 6.23. Quantification of shape descriptors of mitochondria from TEM images of *Slc5a6*^{TnTCre} mice at 14 weeks. Mitochondria were manually traced in micrographs taken at 8000x to quantify morphological changes for *Slc5a6*$^{+/+}$ (white) and *Slc5a6*$^{F/F;TnTCre}$ (red) mitochondria. Frequency distribution graphs were generated for each parameter (A,C,E,G,I,K). The median of data collected was plot (B,D,F,H,J,L). Mann Whitney statistical test was performed * = p <0.05. *n* = 6 *Slc5a6*$^{+/+}$, 4 *Slc5a6*$^{F/F;TnTCre}$ mice, mitochondria analysed *n* = 1343 *Slc5a6*$^{+/+}$, 884 *Slc5a6*$^{F/F;TnTCre}$.

TEM Micrographs taken of *Slc5a6*$^{F/F;TnTCre}$ and *Slc5a6*$^{+/+}$ heart sections at 20 weeks are shown (Figure 6.24). Similar to micrographs taken at 14 weeks, *Slc5a6*$^{+/+}$ display highly organised and well-structured sarcomeres with mitochondria evenly distributed between each longitudinal sarcomeric layer (Figure 6.24A-D). Comparatively, *Slc5a6*$^{F/F;TnTCre}$ show varying degrees of disruption to sarcomeres; lack of definition and organisation (Figure 6.24G-J). There are also noticeable mitochondrial abnormalities present in *Slc5a6*$^{F/F;TnTCre}$ such as gross interruption of the mitochondrial cristae (Figure 6.24I,K (red asterisk) indicating pathological mitochondrial changes which may result in an increase in mitophagy; the degradation of dysfunctional mitochondria. High power micrographs of *Slc5a6*$^{F/F;TnTCre}$ hearts reveal a number of mitochondria which have, or were in the process of being degraded highlighted in Figure 6.24J, as well as mitochondrial remnants found engulfed by double membraned autophagosomes (Figure 6.24L). This contributes further evidence of pathological defects in *Slc5a6*$^{F/F;TnTCre}$ mitochondria.

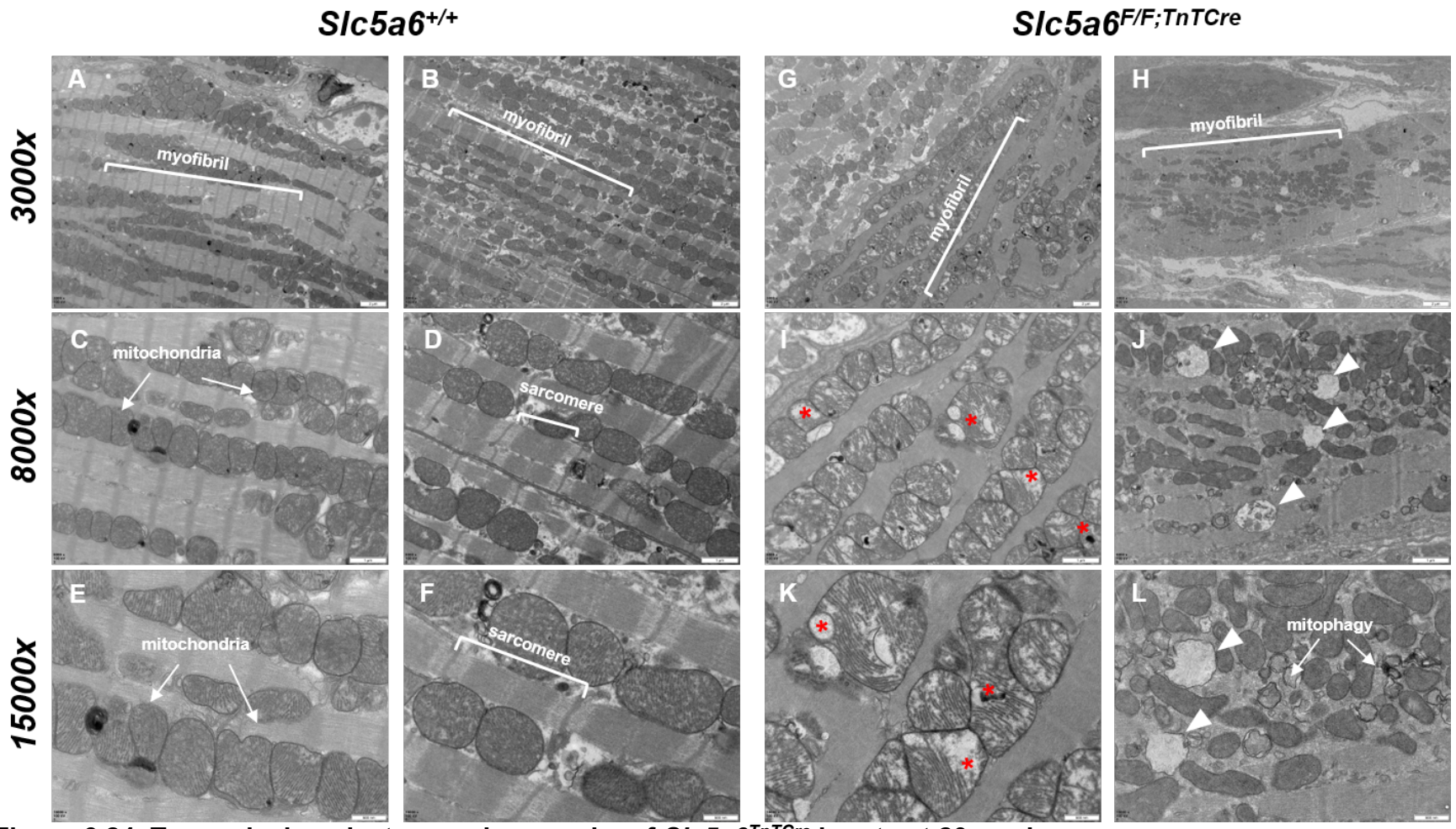

Figure 6.24. Transmission electrons micrographs of *Slc5a6*^{TnTCre} hearts at 20 weeks.
Representative micrographs are shown for *Slc5a6*$^{+/+}$ (A-F) and *Slc5a6*$^{F/F;TnTCre}$ (G-L) at 3000x, 8000x and 15000x magnification. Highly organised and well defined sarcomeres are shown in *Slc5a6*$^{+/+}$ hearts (A-F); however, sarcomeres found in *Slc5a6*$^{F/F;TnTCre}$ are less well defined and lack the fibre organisation (G-H). Mitochondrial abnormalities are observed in *Slc5a6*$^{F/F;TnTCre}$ micrographs, such as cristae breakdown shown by red asterisks (I,K) and degraded mitochondria (white arrowheads) (J,L) which is not seen in *Slc5a6*$^{+/+}$ sections (C-F). *n* = 3 *Slc5a6*$^{+/+}$, 3 *Slc5a6*$^{F/F;TnTCre}$.

Quantification of morphological shape descriptors was also performed on micrographs taken at 8000x for mice collected at 20 weeks. The level of skewness was determined for each parameter (Table 6.3). This revealed data for was skewed to a similar degree (within 0.5) in both *Slc5a6*$^{+/+}$ and *Slc5a6*$^{F/F;TnTCre}$ mitochondria for aspect ratio, form factor and circularity, also shown in frequency distribution graphs Figure 6.25.A,C,I, respectively. However, *Slc5a6*$^{F/F;TnTCre}$ mitochondrial data was skewed more than 0.5 compared to *Slc5a6*$^{+/+}$ data in mitochondrial area, perimeter and Feret's diameter, shown in frequency distribution graphs Figure 6.25.E,G,K. Median data was also plotted for each parameter and subject to Mann Whitney statistical testing. This revealed no difference in aspect ratio (Figure 6.25B), form factor (Figure 6.25D) or circularity (Figure 6.25J) between *Slc5a6*$^{+/+}$ and *Slc5a6*$^{F/F;TnTCre}$ mitochondria. However, we do find mitochondria in *Slc5a6*$^{F/F;TnTCre}$ to be smaller than *Slc5a6*$^{+/+}$ mitochondria shown by a significant decrease in area (Figure 6.25.F) (p<0.0001), perimeter (Figure 6.25.H) (p<0.0001) and Feret's diameter (Figure 6.25.L) (p<0.0001). This reflects findings of degraded and abnormal mitochondria shown (Figure 6.24).

Table 6.3. Shape descriptors for *Slc5a6*^{TnTCre} mice at 20 weeks.
Skewness was calculated for each parameter as a measure of asymmetry in distribution of data where '0' is equal to a normally distributed population. *n* = 3 *Slc5a6*$^{+/+}$, 3 *Slc5a6*$^{F/F;TnTCre}$.

Shape descriptor	20 weeks					
	Slc5a6$^{+/+}$			*Slc5a6*$^{F/F;TnTCre}$		
	Median	Mean ± SD	Skewness	Median	Mean ± SD	Skewness
Aspect ratio	1.353	1.524±0.524	2.391	1.392	1.672±0.673	2.269
Form factor	1.135	1.182±0.148	2.847	1.137	1.228±0.253	2.773
Area µm	0.823	0.899±0.441	1.492	0.560	0.750±0.584	2.404
Perimeter µm	3.448	3.556±0.900	0.999	2.893	3.190±1.182	1.498
Circularity (0-1)	0.740	0.717±0.155	-0.583	0.719	0.688±0.185	-0.563
Feret's diameter µm	1.244	1.298±0.356	1.140	1.066	1.183±0.466	1.731

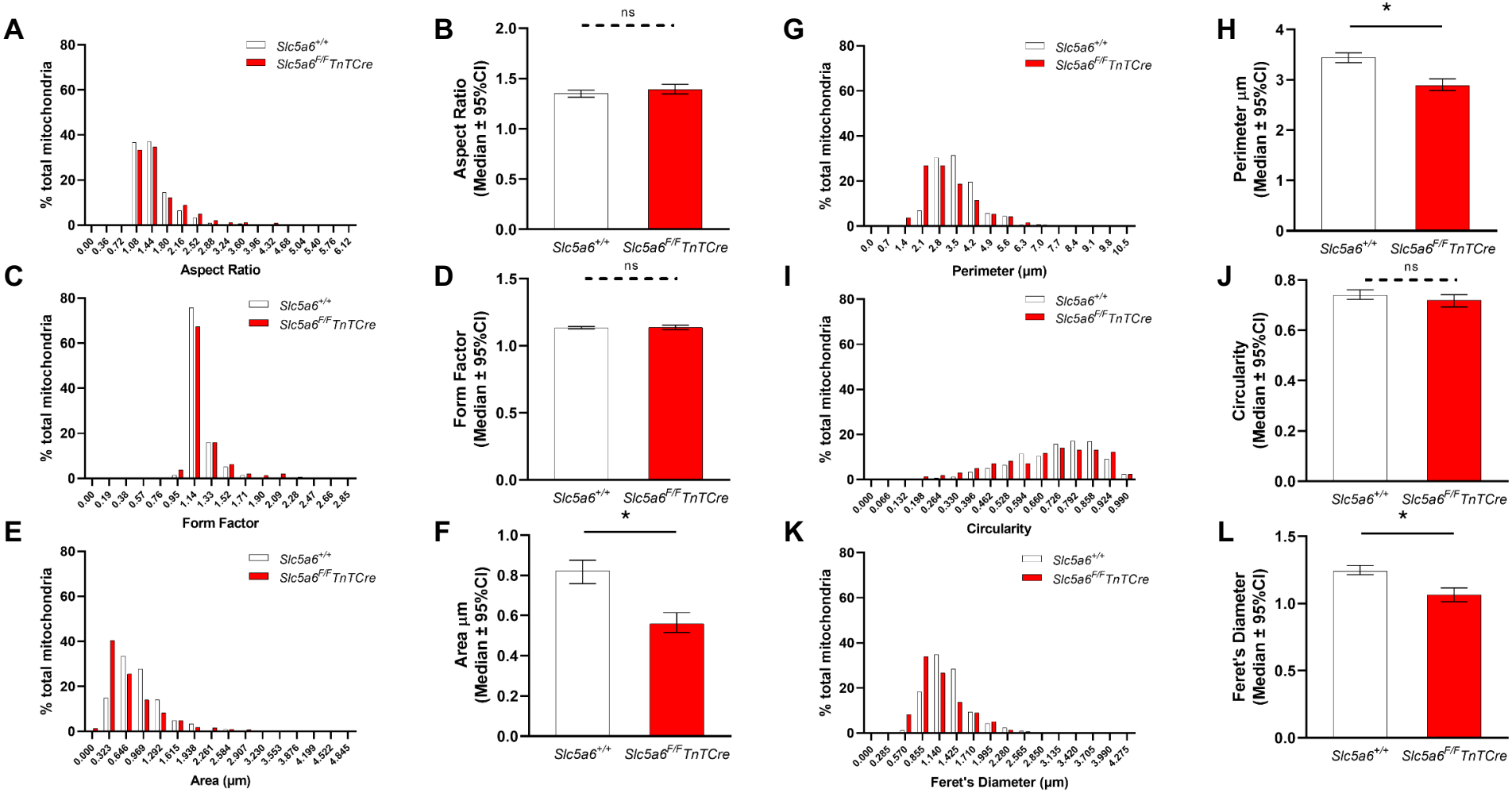

Figure 6.25. Quantification of shape descriptors for mitochondria in *Slc5a6*^{TnTCre} mice at 20 weeks.
Morphological parameters were quantified for *Slc5a6*$^{+/+}$ (white) and *Slc5a6*$^{F/F;TnTCre}$ (red) mitochondria. Frequency distribution graphs were generated for each parameter (A,C,E,G,I,K). The median of data collected was plot (B,D,F,H,J,L). Mann Whitney statistical test was performed * p= <0.05. *n* = 3 *Slc5a6*$^{+/+}$, 3 *Slc5a6*$^{F/F;TnTCre}$ mice, mitochondria analysed *n* = 450 *Slc5a6*$^{+/+}$, 450*Slc5a6*$^{F/F;TnTCre}$.

This data indicates *Slc5a6*$^{F/F;TnTCre}$ mitochondria are responding to stress triggering degradation by increasing mitochondrial proliferation at 14 weeks. At 20 weeks, mitochondria are abnormal and are undergoing mitophagy shown by the increased presence of autophagic events in sections of *Slc5a6*$^{F/F;TnTCre}$ hearts (Figure 6.24). Further investigations into the cause of stress within mitochondria was performed to determine the status of oxidative phosphorylation (OXPHOS) within *Slc5a6*^{TnTCre} hearts.

6.4 Mitochondrial complex abnormalities are apparent in *Slc5a6*$^{F/F;TnTCre}$ mice

To further investigate the mitochondrial abnormalities identified by TEM, a novel technique described by Rocha *et al.* (2015a) was used to quantify the presence of complex I (Ndufb8) and complex IV (Mtco2) of the electron transport chain, relative to the mitochondrial mass (Vdac1) within cardiomyocytes using quadruple immunofluorescence. This technique was optimised for use on mouse cardiac cryosections. Sections of each genotype; *Slc5a6*$^{+/+}$ (n=3) and *Slc5a6*$^{F/F;TnTCre}$ (n=3) were stained for complexes at 14 weeks (Figure 6.26). One four chambered section was stained with each antibody with another section used as a no primary control (NPC). Five areas of the LV were imaged at 20x magnification for analysis. Imaris was used to draw around ~20-30 cardiomyocytes per image (approx. 100-150 cells per heart). Intensity measurements were exported for each channel of the stained and NPC images. Data was subjected to background subtraction using NPC. Background subtracted values for complex I and complex IV were corrected according to mitochondrial mass. Z scores were determined for each complex relative to mitochondrial mass, and the expression profiles were plotted using GraphPad Prism 9 (Figure 6.26).

From this, we can see a negative shift in the number of cardiomyocytes expressing Complex IV in *Slc5a6*$^{F/F;TnTCre}$ mice (Figure 6.26B) compared to cardiomyocytes in *Slc5a6*$^{+/+}$ (Figure 6.26A) mice. When the data is quantified (Figure 6.26D), shows complex IV expression is significantly decreased in *Slc5a6*$^{F/F;TnTCre}$ mice compared to *Slc5a6*$^{+/+}$ (p<0.0001). We can also see a slight negative shift in the expression of complex I in *Slc5a6*$^{F/F;TnTCre}$ cardiomyocytes (Figure 6.26B) compared to *Slc5a6*$^{+/+}$ (Figure 6.26A), however when quantified, the median complex I expression is significantly increased (p=0.0117) compared to *Slc5a6*$^{+/+}$ (Figure 6.26C). This data

suggests loss of *Slc5a6* within the cardiomyocytes, is affecting the expression of complexes involved in the OXPHOS pathway.

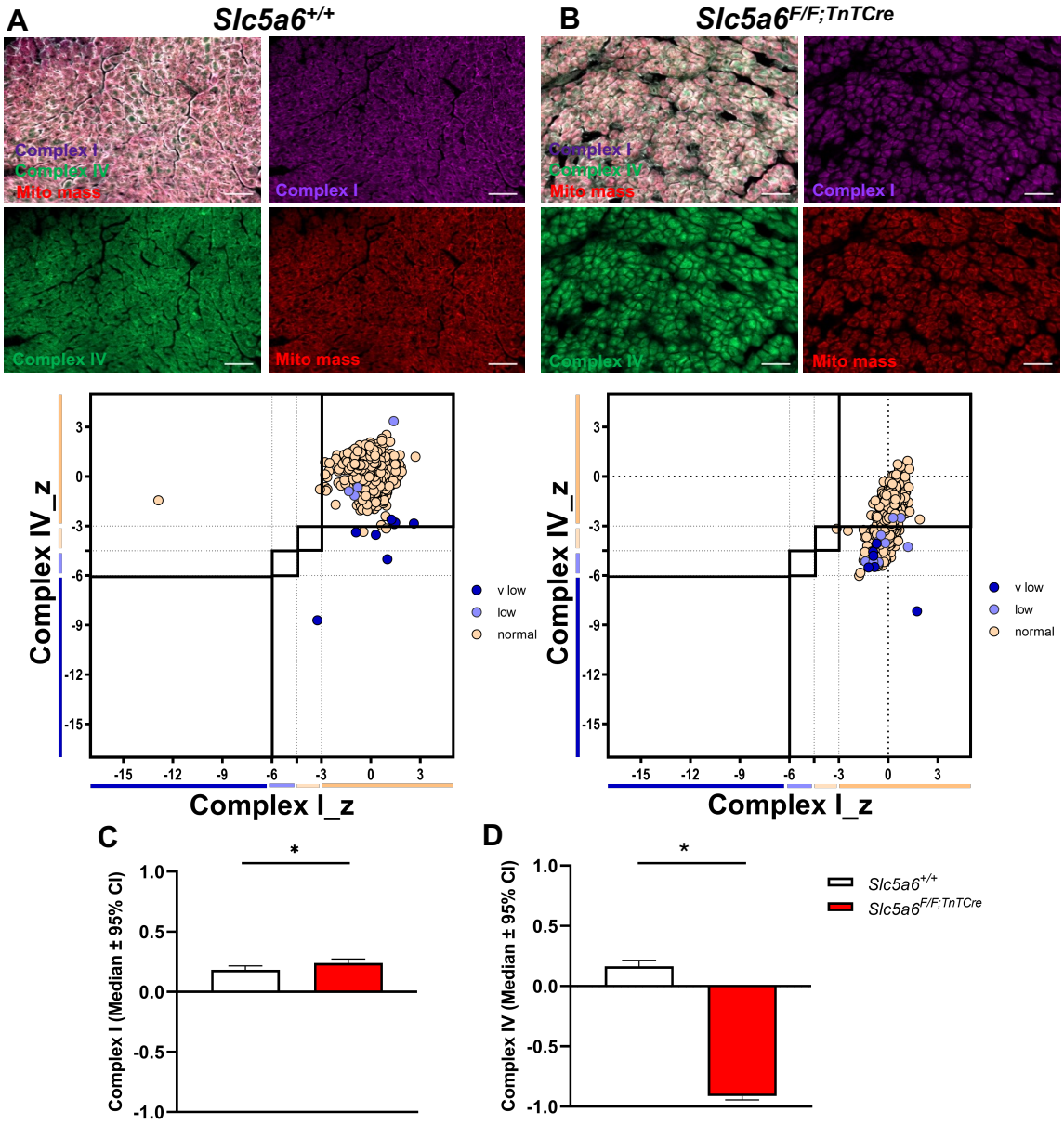

Figure 6.26. Quadruple IF images, expression profiles and quantification of complex I and IV in *Slc5a6*^{TnTCre} mice at 14 weeks.
Representative images of quadruple IF staining on *Slc5a6*$^{+/+}$ (A) and *Slc5a6*$^{F/F;TnTCre}$ (B), as well as the corresponding expression profiles for each genotype. Each cardiomyocyte is represented (circle), with their levels of mitochondrial mass represented; normal (yellow), low (light blue), v low (blue). Z scores (Mean±SD) for complex I (C) and complex IV (D) in *Slc5a6*$^{+/+}$ (white) and *Slc5a6*$^{F/F;TnTCre}$ (red) samples are shown. Mann Whitney statistical test was performed, * p<0.05. n = 3 *Slc5a6*$^{+/+}$ (cardiomyocytes = 652), 4 *Slc5a6*$^{F/F;TnTCre}$ (cardiomyocytes = 1147). Scale = 50µm.

Further work to characterise the effect of removing *Slc5a6* on OXPHOS and mitochondria could not be performed due to restrictions during the Covid-19 pandemic.

6.5 Discussion

This chapter aimed to investigate whether removal of *Slc5a6*, specifically within the heart, would result in the development of cardiomyopathy through assessment of cardiac function and morphology. Functional analysis revealed progressive conduction abnormalities as well as a marked reduction in LV systolic function in *Slc5a6*$^{F/F;TnTCre}$ mice. Histological analysis also showed morphological abnormalities within the heart including evidence of cardiac remodelling, together with functional data, suggest *Slc5a6*$^{F/F;TnTCre}$ mice develop cardiomyopathy. Further investigation into structural changes found within the heart revealed severe mitochondrial abnormalities and increased proliferation, suggesting removal of *Slc5a6* within cardiomyocytes is impacting mitochondrial biogenesis. *Slc5a6*$^{F/F;TnTCre}$ hearts were found to be deficient in complexes involved in OXPHOS within mitochondria, suggesting energy metabolism and homeostasis is affected in the heart. The presence of mitochondrial structural abnormalities as well as complex deficiencies within the heart suggests *Slc5a6* may play an essential role in facilitating energy metabolism and homeostasis within the heart, and its removal may result in energy metabolism defects which could lead to the development of cardiomyopathy in early adulthood (Figure 6.27).

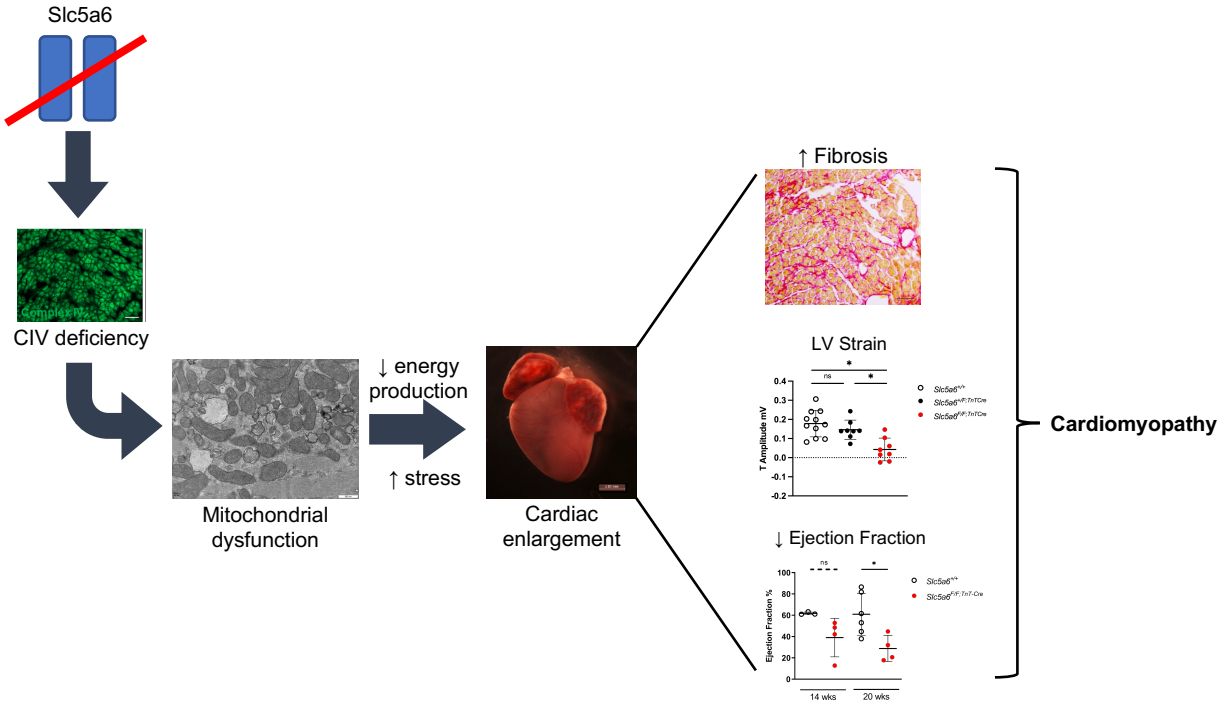

Figure 6.27. Summary of *Slc5a6*$^{F/F;TnTCre}$ phenotype.
Removal of Slc5a6 within the heart was shown to result in CIV deficiency of the ETC within the IMM which has been hypothesised to affect energy production via OXPHOS. Mitochondrial structure abnormalities were also observed, this combined with a possible reduction in energy production could induce stress leading to cardiac enlargement as a potential stress response. An increase in interstitial fibrosis, LV strain pattern by ECG and a reduction in ejection fraction were shown by CMR imaging; all reported markers of cardiomyopathy.

Initial analysis of the *Slc5a6*$^{F/F;TnTCre}$ allele by RT-PCR confirmed exon 6 was spliced to exon 11. It was then hypothesised that the mRNA may undergo nonsense mediated decay or be translated into a truncated protein. To confirm this western blot was used to investigate the presence of Slc5a6 protein in *Slc5a6*$^{F/F;TnTCre}$ and wild type heart lysates. Due to low *n* statistical analysis could not be performed however qualitatively there appeared to be a reduction in the amount of Slc5a6 detected in the *Slc5a6*$^{F/F;TnTCre}$ heart compared to the tissue control and biological control (*Slc5a6*$^{+/+}$). However, the peptide sequence for the antibody used binds to the terminal end of the protein, and as the *Slc5a6*$^{F/F;TnTCre}$ allele introduces a premature stop codon this antibody would not be suitable to detect a truncated Slc5a6 protein within the heart. Future studies should look to try any additional antibodies developed to detect Slc5a6 within mouse tissue.

Following this, the initial aim of this chapter was to identify if *Slc5a6*$^{F/F;TnTCre}$ mice developed cardiac dysfunction using ECG and cardiac MRI *in vivo*. Analysis of ECG traces taken throughout early adulthood revealed *Slc5a6*$^{F/F;TnTCre}$ mice develop conduction defects indicating LV strain pattern and myocardial fibrosis, confirmed by Picro-Sirius red staining. Additional functional changes were also identified by MRI including reduced EF, CO and SV indicative of diastolic and systolic dysfunction caused by myocardial stiffness. Similar functional characteristics are also identified in mouse models of DCM, such as the *TnnT2* knockin model of DCM by Du *et al.* (2007) who reported reduced EF, widening of the QRS and a decrease in ST segment. Similar changes to the QRS, ST segment are also reported in models of HCM (Polina Sysa-Shah *et al.*, 2015). In addition to genetic models of DCM, viral induced DCM mouse models such as Coxsackievirus B3 (CVB3) cause acute myocarditis which present with DCM phenotype with similar functional characteristics to *Slc5a6*$^{F/F;TnTCre}$ mice including reduced EF (~40%), increased fibrosis and ventricular enlargement (Lu *et al.*, 2019). In addition to similarities found with other mouse models of cardiomyopathy, the cardiac abnormalities present in *Slc5a6*$^{F/F;TnTCre}$ mice are also found in patients, and are often used as clinical indicators of HCM and DCM with HF in the presence of reduced SV (Edhouse *et al.*, 2002; Aleksova *et al.*, 2010; Francone, 2014; Lyon *et al.*, 2018; Schultheiss *et al.*, 2019b). Aoki *et al.* (2005) summarise the phenotype of dialysis (n=40) and non-dialysis (n=50) patients with DCM, with each group displaying EF <40%, fractional shortening <20% and pathological findings including interstitial fibrosis and hypertrophic cardiomyocytes. A recent review by Schultheiss *et al.* (2019a) also summarise common DCM features which include pathological collagen deposition and fibrosis, as well as cellular hypertrophy. Functional characteristics can be diverse but include ECG findings; T wave abnormalities, atrioventricular block and QRS changes, CMR features; ventricular dilation, reduced EF, presence of fibrosis. This provides further support that *Slc5a6*$^{F/F;TnTCre}$ mice may develop cardiomyopathy, characterised by the cardiac dysfunction observed in these mice.

In addition to characterising functional changes in *Slc5a6*$^{F/F;TnTCre}$ we also investigated cardiac morphology using histological and ultrastructural techniques. *Slc5a6*$^{F/F;TnTCre}$ mice were found to have enlarged hearts, with structural abnormalities apparent, indicating cardiac remodelling had occurred. This was characterised by visible reduction in cardiomyocyte compaction found to be caused by increased interstitial

fibrosis. Fibrosis is a characteristic feature of cardiomyopathy and often occurs after myocardial insult such as stress, caused by an increase in haemodynamic load, energy metabolism defects or increased oxidative stress (Brower and Janicki, 2001; Li *et al.*, 2014; Azevedo *et al.*, 2016). The initial increase of collagen fibres is an adaptive response to myocardial abnormalities, boosting growth of the myocardium to enhance contractile force (Weber, 1989). However, with prolonged myocardial injury remodelling becomes a pathological mechanism which reduces the contractility of the cardiomyocytes, resulting in a stiffening of the myocardium, reducing SV and EF until HF occurs (Weber, 1989; Li *et al.*, 2014; Schultheiss *et al.*, 2019b). In addition, myocardial stress also results in a hypertrophic response in cardiomyocytes. This an adaptive response from cardiomyocytes in order to preserve cardiac function and, depending on the trigger can be defined as concentric hypertrophy; caused by chamber pressure overload resulting in LV wall thickening, or eccentric hypertrophy; a result of volume overload characterised by chamber dilation, as seen in DCM (Grossman and Paulus, 2013; Li *et al.*, 2014). *Slc5a6*$^{F/F;TnTCre}$ mice show a clear increase in cardiomyocyte area indicating cardiomyocyte hypertrophy but with slight ventricular chamber dilation at 14 weeks, this was more pronounced in mice found dead at 26 weeks, suggesting *Slc5a6*$^{F/F;TnTCre}$ mice develop DCM features.

The project then focused on identifying the pathomechanism of cardiomyopathy within *Slc5a6*$^{F/F;TnTCre}$ mice. Mechanisms which commonly cause cardiac remodelling and dysfunction include, but are not limited to, energy metabolism defects, oxidative stress and inflammation (Azevedo *et al.*, 2016). As previously stated, *Slc5a6* encodes the sodium multivitamin transporter which is solely responsible for the transport of three essential micronutrients required for energy metabolism and homeostasis (de Carvalho and Quick, 2011; Ghosal and Said, 2011; Quick and Shi, 2015; Uchida *et al.*, 2015). As the effect of the targeted removal of exon 7-10 of *Slc5a6* on protein function has yet to be established, it is hypothesised that the potentially partial/non-functional Slc5a6 protein may inhibit/reduce the bioavailability of biotin, PA and LA within cardiomyocytes, compromising energy metabolism pathways, which rely on these substrates as cofactors, within the mitochondria (Figure 6.28). Further study is required to determine the functional status of Slc5a6 within this mouse model, such as site-directed mutagenesis to remove exons 7-10 *in vitro* and determine the vitamin uptake into cultured cells. This technique has been successfully utilised by Ghosal and Said (2011) to assess the effect of histidine modification in Slc5a6 on biotin uptake by the

transporter. Here they describe the importance of the two histidine residues investigated to ensure normal vitamin uptake via Slc5a6 by showing a significant decrease in the uptake of biotin in histidine mutated cells. They also demonstrate although the expression of *Slc5a6* is comparable in mutated vs wild type cells by RT-PCR, they do discover that there is a loss of Slc5a6 specifically at the cell membrane in mutated cells by performing a surface biotinylation assay, which they hypothesise is the cause of reduced biotin uptake. To summarise, in addition to confirming the effect of removing exon 70-10 in Slc5a6 on the protein structure, studies should also be performed to investigate vitamin uptake as well as cell membrane expression.

As mitochondrial morphology is fundamentally linked to their overall function, we therefore investigated the ultrastructure of cardiomyocytes within *Slc5a6*$^{F/F;TnTCre}$ hearts, with a particular focus on the assessment of intermyofibrillar mitochondrial morphology (Cogliati *et al.*, 2013; Vincent *et al.*, 2016). Analysis revealed severe abnormalities such as mitochondrial degradation, cristae breakdown and areas of increased mitochondrial proliferation marked by a reduction in mitochondrial size compared to controls. A number of studies inducing mitochondrial dysfunction in mice were found to result in the development of cardiomyopathy. Research by Graham *et al.* (1997) showed an increase in mitochondrial proliferation in addition to cardiomyocyte hypertrophy in their knockout model of *Ant1*, which is a solute carrier on the inner mitochondrial membrane (IMM) responsible for the exchange of ATP for ADP to the cytosol, ultimately providing energy to the cytosol (Neckelmann *et al.*, 1987). The mitochondrial and cardiac phenotype of *Ant1* knockout is similar to the findings in our model, which suggests similar mechanistic dysfunction may also be occurring in *Slc5a6*$^{F/F;TnTCre}$ mice. However, there is not a full overlap in mitochondrial findings in *Ant1* knockout mice, suggesting other factors may be involved in the development of mitochondrial dysfunction in *Slc5a6*$^{F/F;TnTCre}$ mice. Other knockout models targeting mitochondrial dynamics such as *Dmn1l* (Ashrafian *et al.*, 2010) and *Mfn2* (Chen and Dorn, 2013; Song *et al.*, 2015) described marked reductions in mitochondrial size, ATP production, oxygen consumption and increased reactive oxygen species (ROS) suggesting impaired mitochondrial respiration played a role in the development of DCM. The conservation of the inner mitochondrial membrane (IMM) is essential as it is where many of the complexes and enzymes involved in OXPHOS, the main energy production pathway within the heart, are located. Abnormalities affecting the cristae of mitochondria are linked to mitochondrial

dysfunction contributing to the pathophysiology of disease phenotypes including mitochondrial disease and cardiomyopathies (Chung and Kang, 2015; Vincent *et al.*, 2016). As severe abnormalities of cristae structure were identified within *Slc5a6*$^{F/F;TnTCre}$ hearts, investigation into the presence of OXPHOS complexes; I and IV, was performed in *Slc5a6*$^{F/F;TnTCre}$ hearts.

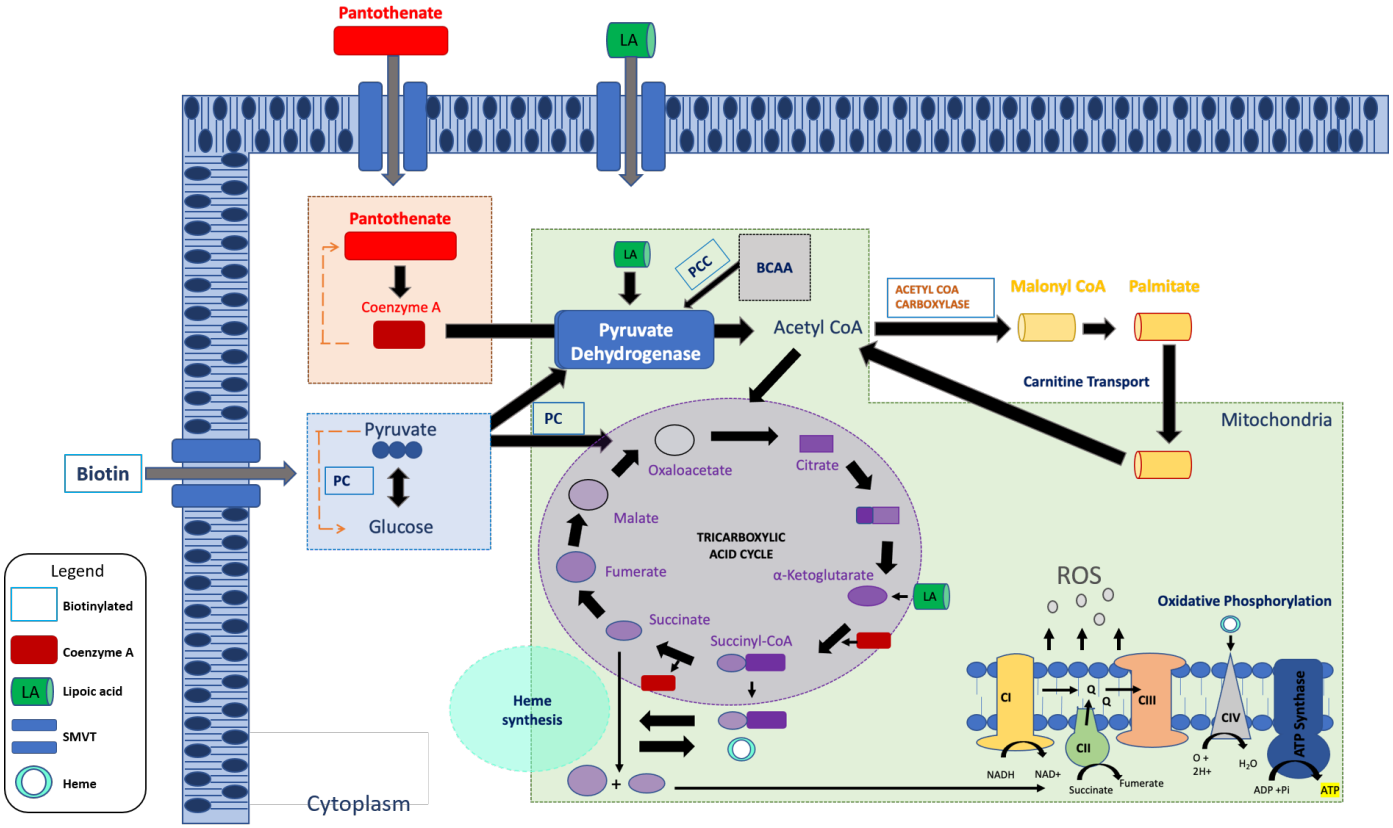

Figure 6.28. Schematic representation of biotin, PA and LA transport into the cell by sodium-dependent multivitamin transporter. Biotin (blue box) once transported, is used for the biotinylation of pyruvate carboxylase (PC); involved in conversion of pyruvate to i) glucose (gluconeogenesis) ii) oxaloacetate (TCA), acetyl CoA carboxylase; conversion of acetyl CoA to malonyl CoA, and propionyl-CoA carboxylase (PCC); conversion of branched chain amino acids (BCAA) to intermediates for acetyl CoA production. Pantothenate (red), once transported is converted to coenzyme A and used in the production of acetyl CoA by pyruvate dehydrogenase. Acetyl CoA is an important intermediate in the TCA cycle and in the formation of fatty acid palmitate. Lipoic acid (green), once transported is used in the pyruvate dehydrogenase complex for the generation of acetyl CoA and in α-ketoglutarate dehydrogenase complex for the generation of succinyl CoA, important for heme synthesis and generation of succinate, both of which are essential for oxidative phosphorylation (OXPHOS). OXPHOS uses these substrates to drive the electron transport chain generating ATP and a small amount of reactive oxygen species (ROS) as a by-product.

The main role of cardiac mitochondria is to provide vast amounts of ATP required for cardiac contraction by β-oxidation through OXPHOS. This process occurs within the IMM and consists of the five complexes previously described. In summary, the energy and intermediates produced from TCA cycle is used by Complex I, Complex III and Complex IV to pump protons across the IMM to the intermembranal space resulting in an electrochemical proton gradient, PMF (Chung and Kang, 2015). This is then utilised by Complex V (ATP synthase) to convert ADP to ATP (Hanna and Nelson, 1999; Berg JM, 2002b; Mailloux *et al.*, 2007). Mitochondrial ATP is then transported across the IMM by adenosine nucleotide translocator (Graham *et al.*, 1997). This exchange produces reactive oxidative species (ROS), which are known to impair cell function if respiratory chain dysfunction occurs (Hanna and Nelson, 1999; Zhou and Tian, 2018). Analysis from quadruple IF staining and quantification revealed a significant deficiency of complex IV in *Slc5a6*$^{F/F;TnTCre}$ hearts. This suggests respiratory chain dysfunction in *Slc5a6*$^{F/F;TnTCre}$ hearts and as a result may have increased toxic ROS production, contributing to the development of cardiomyopathy. However, further investigation into determining ROS levels in *Slc5a6*$^{F/F;TnTCre}$ hearts is required to confirm this hypothesis. Wüst *et al.* (2016) demonstrated rats with HF and cardiomyopathy had reduced CI and CIII in cardiomyocytes suggesting deficiency of these complexes contribute towards cardiac dysfunction. *Slc5a6*$^{F/F;TnTCre}$ mice show deficiency of CIV; however, CIII was not investigated. Characterisation of all mitochondrial complexes should be investigated to determine the comprehensive effect of Slc5a6 loss within the heart.

As previously described in section 1.4, biotin and PA are essential for energy metabolism and homeostasis, but biotin also plays a vital role in the regulation of gene expression. Both roles rely on the active form of biotin (biotinyl-AMP) which is transformed by holocarboxylase synthase (HCS). Once transformed, biotinyl-AMP can be used to biotinylate carboxylases for energy metabolism or is used to regulate gene expression by triggering the soluble guanylate cyclase-cGMP-dependent protein kinase (sGC-PKG) signal transduction pathway (Pacheco-Alvarez *et al.*, 2005). This pathway regulates genes involved in biotin homeostasis such as SMVT and HCS (Pacheco-Alvarez *et al.*, 2005; Vlasova *et al.*, 2005). Studies have shown that biotin transcriptional activity is not limited to biotin cycle regulation but suggest that biotin may regulate a wide range of genes throughout energy metabolism (Vlasova *et al.*, 2005). Interestingly, a study performed by Atamna *et al.* (2007) which investigated biotin deficiency on heme synthesis in human lung fibroblasts, found that levels of

mitochondrial complex IV were greatly reduced in biotin deficient cells, with normal levels of complex I and III compared to biotin sufficient cells. They also reported that prolonged deficiency decreased complex IV to almost undetectable levels. This potentially identifies why significantly decreased levels of complex IV were observed in *Slc5a6*$^{F/F;TnTCre}$ mice. Additionally, PA is a precursor to coenzyme A, a key component in acetyl CoA used in the TCA cycle to generate succinyl CoA. PA deficiencies are well known to result in anaemia caused by reduced heme synthesis (Schulman and Richert, 1957; Di Pierro and Granata, 2020). Heme, unlike biotin and PA, must be synthesised within the cell and cannot be recycled or supplied from external food sources (Atamna, 2004). Interestingly, complex IV is the only mitochondrial complex which contains a heme group, heme-α. In the assembly of complex IV, the initial step is the incorporation of heme-α into COX-I subunit followed by assembly of the remaining subunits (Atamna *et al.*, 2001; Atamna *et al.*, 2007). Therefore, it is possible a reduction in heme synthesis may be the cause of decreased complex IV levels in *Slc5a6*$^{F/F;TnTCre}$ mice.

CIV deficiencies in patients are known to cause multi-systemic disorders such as Leigh Syndrome (Tiranti *et al.*, 1999) where a more neurological phenotype is observed along with biochemical changes including lactic acidosis, noted in our patient with the *SLC5A6* mutation. This suggests there could be a phenotypic overlap between patients with CIV deficiency and the siblings with the *SLC5A6* mutation, as CIV deficiency has also been associated with the development of cardiomyopathy (Abdulhag *et al.*, 2015). Interestingly, in this study they show the beneficial effect of treating patient derived fibroblasts with vitamin C (ascorbate), which may be due to its ability to provide electrons to the ETC or its antioxidant properties. They propose vitamin supplementation as a therapeutic treatment for other patients with CIV deficiency.

In addition to the effect of potentially reducing/removing vitamin transport into the cell triggering a cascade of energy metabolism defects, consideration must also be given to the possible effect the removal of the transporter could have on Na^+ concentrations and therefore cardiac action potentials as well as cell integrity. As described in section 1.2.3, cardiac action potentials rely on the fine-tuned balance of the movement of ions in (influx) and out (efflux) of the cell to trigger and control contraction (depolarisation) and relaxation (repolarisation), including Na^+, Ca^{2+} and K^+ (Joukar, 2021). Therefore, if the transporter is responsible for contributing to the balance of Na^+ in the cell, it is possible that reduction in the concentration of Na^+ internally may have a detrimental

effect on the cardiac conduction of cardiomyocytes within *Slc5a6*$^{F/F;TnTCre}$ mice (Bers *et al.*, 2003). Interestingly, an increase in intracellular Na^+ has been shown in both human and animal models with HCM, as well as in HF models as shown by Despa *et al.* (2002) who reveal that at resting potential, Na^+ influx is doubled in animals with HF compared to controls which they suggest may be due to Na^+ transporter alteration or imbalance which may affect contractile function of cardiomyocytes as well as having a detrimental downstream effect on mitochondrial function (Gray *et al.*, 2001; Aksentijević and Shattock, 2021).

Further research into the exact mechanism causing cardiomyopathy in *Slc5a6*$^{F/F;TnTCre}$ mice is required. However, from the data shown in this chapter it is possible to propose a mechanism (Figure 6.29). It is hypothesised that removal of *Slc5a6* affects the sodium dependent transport of each substrate across the plasma membrane. This would result in decreased biotinylation of carboxylases, affecting gluconeogenesis, conversion of pyruvate to glucose via PC, as well as the conversion of pyruvate to oxaloacetate. Biotinylation of PCC would be affected and therefore a reduction in BCAA catabolism would occur. Additionally, ACC would be unable to convert acetyl CoA to malonyl CoA during FAS which would impact cardiac β-oxidation. If PA supply is reduced, CoA can be converted back to PA; however, this is a CoA concentration and availability dependent mechanism (Leonardi and Jackowski, 2007; Shi and Tu, 2015). Reduction of LA supply would severely affect the PDH complex causing reduction in the production of acetyl CoA and would affect the synthesis of succinate CoA. α-ketoglutarate is converted to succinyl CoA via α-ketoglutarate dehydrogenase. LA is an essential cofactor for these enzymes; however, it is recycled by the E3 subunit of the dehydrogenase complexes. This suggests *Slc5a6* transport of LA across the plasma may not be essential to its availability within the cell.

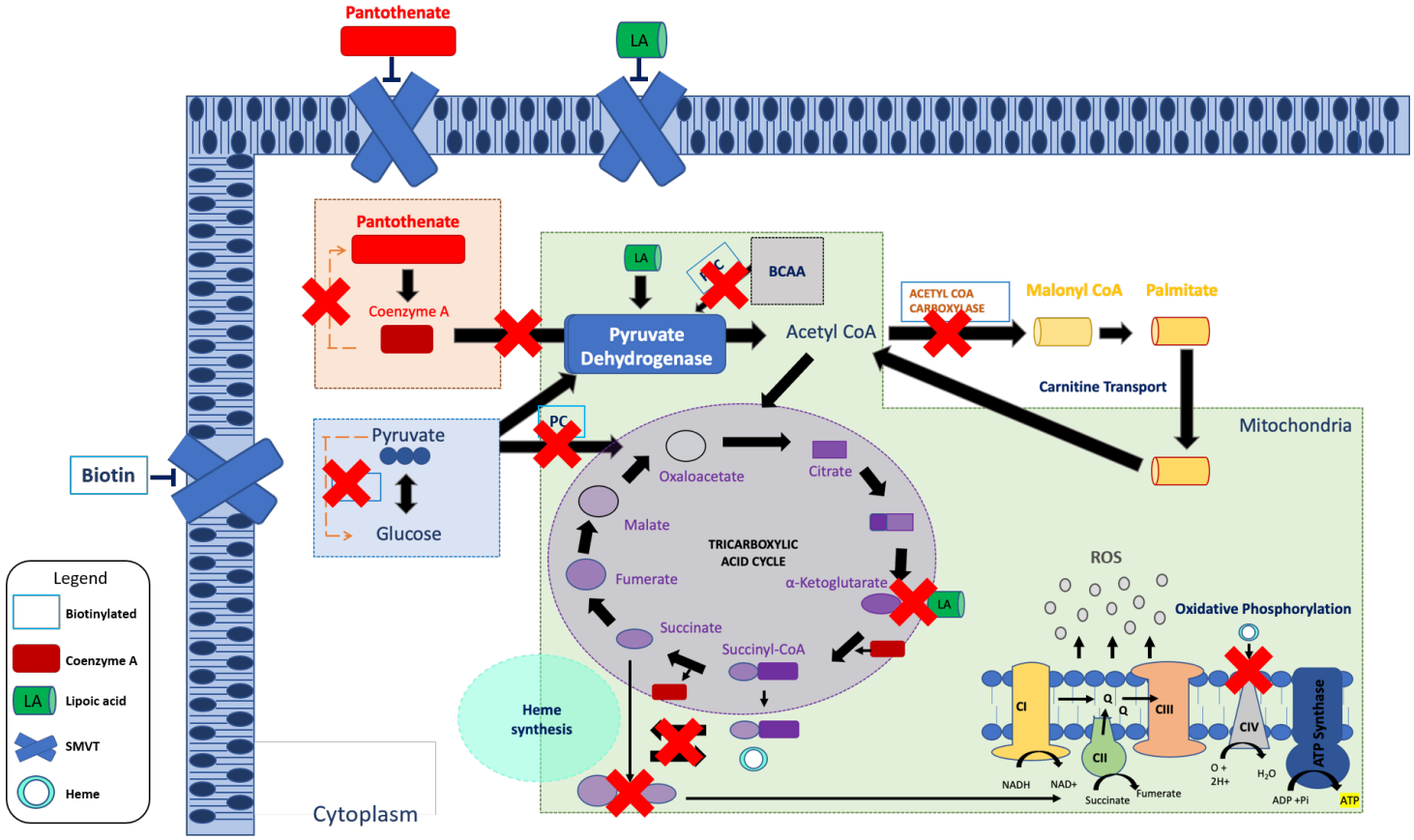

Figure 6.29. Hypothesised mechanism of disrupted vitamin transport by loss of Slc5a6.
Modified from Figure 6.28**.** The loss of Slc5a6 would severely reduce Biotin, pantothenic acid (pantothenate) and lipoic acid (LA) transport. Reduction in the bioavailability of these substrates would affect i) biotinylation of carboxylases involved in gluconeogenesis, oxaloacetate generation, BCAA conversion and fatty acid synthesis. ii) coenzyme A synthesis which is essential for the generation of acetyl CoA involved in fatty acid synthesis and the TCA cycle, as well as the formation of succinyl CoA. iii) The function of pyruvate dehydrogenase and α-ketoglutarate dehydrogenase complexes which require lipoic acid. Together these affected processes have a detrimental effect on the production of essential intermediates generated by the TCA cycle which are required for generation of NADH and succinate for OXPHOS and heme synthesis; essential for the assembly of CIV, without which oxygen will not be reduced to water causing an increase in ROS generation and a decrease in ATP production.

Together these changes would have an enormous effect on the availability of acetyl CoA for the TCA cycle and the production of intermediates for OXPHOS, therefore reducing ATP production. The reduction in ATP generation would cause cardiac conduction abnormalities leading to stress and prompting cardiac remodelling, ultimately resulting in cardiac dysfunction and failure. However, further investigation to confirm this hypothesis, using biochemical analysis, is required.

6.6 Conclusion

Overall, the data within this chapter has shown that deletion of *Slc5a6* within the heart has resulted in cardiac features which correlate with DCM, similar to the phenotype of the patient and therefore remains a strong candidate gene for disease within this family. Based on the hypothesis discussed above, investigation into the effect of vitamin supplementation on the development of cardiomyopathy within *Slc5a6*$^{F/F;TnTCre}$ mice will be explored in Chapter 7.

Chapter 7 Investigating the effect of vitamin supplementation on cardiac-specific *Slc5a6* knockout mice

7.1 Introduction

As shown in Chapter 6, loss of *Slc5a6* within cardiomyocytes resulted in the development of cardiomyopathic features. From this data, it was hypothesised that loss of *Slc5a6* may disrupt normal cellular metabolism pathways which require biotin, pantothenic acid (PA) and lipoic acid (LA) to function. It is well known that a small amount of substrate, ie. vitamins, can passively diffuse across the plasma membrane (Cooper, 2000b). With this in mind and in addition to the success of vitamin supplementation in four patients with mutations in *SLC5A6*, supplementation was considered as a possible therapeutic intervention for *Slc5a6*$^{F/F;TnTCre}$ mice (Subramanian *et al.*, 2017; Byrne *et al.*, 2019; Schwantje *et al.*, 2019). In this chapter the effect of oral vitamin supplementation on *Slc5a6*^{TnTCre} will be assessed to determine if oral supplementation will any effect on the pathological changes previously reported in *Slc5a6*$^{F/F;TnTCre}$ mice (chapter 6).

7.1.1 Sodium-dependent multivitamin transporter

As described in section 1.4, *Slc5a6* encodes SMVT, responsible for the transport of water-soluble vitamins; biotin, PA and LA in mammals (Prasad *et al.*, 1998; Said, 2011; Ghosal *et al.*, 2012; Quick and Shi, 2015). Water-soluble vitamins are essential for cellular growth, development, and function (Said, 2004; Said, 2011). Mammals cannot synthesise a number of vitamins and therefore rely upon the absorption of an external supply of nutrients via the intestinal tract (Quick and Shi, 2015). Vitamin absorption is facilitated by specialised carrier mediated transporters, such as SMVT (Said, 2004). However, passive diffusion across cell membranes also occurs when high volumes of extracellular vitamins are present (Zempleni *et al.*, 2009; Horváth and Vécsei, 2011). Following the characterisation of SMVT, studies to determine the stoichiometry of Na^+:substrate of the transporter gave conflicting reports. Experiments in brain microvessel endothelial cells, human colonic endothelial cells and rat kidney brush border membrane vesicles suggest a stoichiometric ratio of 1:1 (Na^+:biotin), indicating that electroneutral transport occurs (Baur *et al.*, 1990; Said *et al.*, 1998; Park and Sinko, 2005). Studies into biotin and PA uptake across human placental brush-border

membranes and intestinal Caco-2 cells, *X. laevis* oocytes and expression of rat SMVT in cos-7 cells show a coupling ratio of 2:1 (Na^+:vitamin) suggesting transport is electrogenic (Grassl, 1992; Prasad *et al.*, 1999; Prasad *et al.*, 2000). Discrepancies in the stoichiometric ratio may be due to tissue or inter-species differences (Vadlapudi *et al.*, 2012).

Often impairment of any substrate transport leads to vitamin deficiency, resulting in varied clinical phenotypes due to comprised mitochondrial function. Dependent on the vitamin deficiency, as shown in Table 7.1, this can result in development of growth abnormalities, development delay, seizures as well as dermatological disorders (Said, 2004). Vitamin deficiencies have also been reported to occur secondary to inflammatory bowel disorders, chronic alcoholism and long-term anticonvulsant therapy (Subramanian *et al.*, 2017). Normal brain function is reliant upon the supply of biotin and pantothenic acid through the blood brain barrier. Investigations into the mechanism of vitamin supply found SMVT was responsible for this transport and therefore a reduction in the efficiency of SMVT is associated with brain abnormalities (Uchida *et al.*, 2015).

Table 7.1. B vitamin deficiency associated conditions and genetic disorders. Adapted from Depeint *et al.* (2006); Berg *et al.* (2007).

B Vitamin	Coenzyme	Conditions	Disorders
Thiamine, B1	Thiamine pyrophosphate (TPP)	Neuropathy, cardiomyopathy	Leigh syndrome, Neurodegenerative disorders, maple syrup urine, cancer
Riboflavin, B2	Flavin adenine dinucleotide (FAD)	Neuropathy, anaemia, GI tract abnormalities	Glutaric aciduria
Niacin, B3	Nicotinamide adenine dinucleotide (NAD)	Pellagra, depression, insomnia, delusions	Hartnup disorder
Pantothenic acid, B5	Coenzyme A	Hypertension, hypoglycaemia, encephalopathy, anaemia	Neurodegenerative disorders
Biotin, B7	Biocytin	Fatigue, muscle pain, seizures, depression, congenital abnormalities, anaemia	Multiple carboxylase deficiency, propionic aciduria
Folic acid, B9	Tetrahydrofolate	Neural tube defects, anaemia	Hereditary folate malabsorption,

Biotin is required for normal cell growth and development, and acts as a cofactor for several carboxylases required for essential metabolic pathways (Waldrop *et al.*, 2012). Studies have identified that biotin plays a major role in regulating cell proliferation, gene expression and immune function (Rodriguez-Melendez and Zempleni, 2003; Wiedmann *et al.*, 2003). Biotin deficiency is known to result in a spectrum of clinical phenotypes including growth retardation, neurological disorders and developmental delay.

As described in section 4.2, compound heterozygous mutations in *SLC5A6* have been reported in one child who clinically presented with brain, bone, intestinal and immune dysfunction; however, cardiac involvement was not identified (Subramanian *et al.*, 2017). The patient was given biotin, PA and LA supplementation which clinically improved the neurological, growth and developmental disorders. Additionally, a second family was reported with compound heterozygous mutations in *SLC5A6* in two children. Both children displayed a severe neurodegenerative disorder, without cardiac involvement; however, the eldest child died of gastrointestinal abnormalities at 2.5 years of age (Byrne *et al.*, 2019). Upon identification of *SLC5A6* mutations, the remaining child was given biotin, PA and LA supplements and a marked clinical improvement in disease condition was reported. More recently, a case study published by Schwantje *et al.* (2019) described a child with mutations in *SLC5A6* who developed circulatory and respiratory insufficiency at 17 months of age, following the development of gastroenteritis. The patient also showed marked metabolic abnormalities, including metabolic acidosis and hypoglycemia. After the identification of the *SLC5A6* mutations, the patient was given biotin and PA supplements and showed clinical improvement in the disease phenotype. Interestingly, vitamin supplementation of biotin and PA was provided to an intestinal specific *Slc5a6* knockout mouse model and was reported to completely reverse the intestinal phenotype observed in knockout mice (Sabui *et al.*, 2018). These vitamin supplementation studies were the basis for our investigation into the effect of biotin and PA supplementation on the cardiac phenotype of $Slc5a6^{F/F;TnTCre}$ mice.

7.1.2 Vitamin supplementation strategy

Based on biotin and PA supplementation studies performed by Sabui *et al.* (2018), breeding pairs ($Slc5a6^{+/F;TnTCre}$ stud male and $Slc5a6^{F/F}$ dam) were provided with vitamin supplemented water, containing 1mM of biotin and PA, *ad libitum*. Furthermore, the pair were provided with vitamin supplemented food pellets,

containing the oral dose of biotin (2.5mg/kg/d) and PA (41.66mg/kg/d) given to a patient with *SLC5A6* mutations first reported by Subramanian *et al.* (2017) which reportedly improved the clinical phenotype. One soaked vitamin supplemented food pellet was provided per mouse, to maximise consumption, with additional non-soaked supplemented pellets supplied in the food hopper *ad libitum*. This strategy was continued throughout pregnancy and lactation and continued to be supplied to resultant offspring post-weaning until collection at 20 weeks (Figure 7.1). Due to the COVID-19 pandemic only one litter was able to be analysed, therefore the pilot data collected from this study will be presented in this chapter.

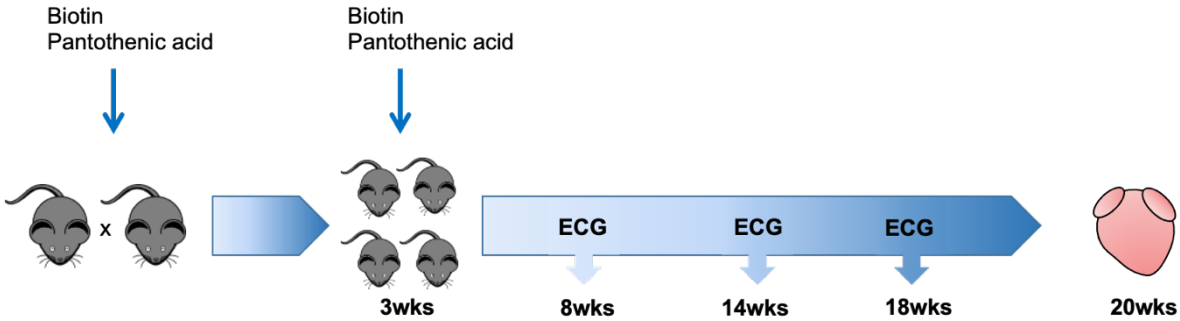

Figure 7.1. Timeline of vitamin supplementation and cardiac assessment. Breeding pairs were supplied with vitamin supplemented diet and drinking water throughout breeding, pregnancy and birth. Supplementation was continued while the pups developed and given to offspring once weaned. This was continued throughout adulthood until collection at 20 weeks.

7.1.3 Aims of the chapter

The main aim was to examine the effect of biotin and PA supplementation on the development of cardiomyopathy in *Slc5a6*$^{F/F;TnTCre}$ mice. It was hypothesised that the supplementation of biotin and PA would increase the bioavailability of the vitamins through passive diffusion, possibly leading to an improvement in disease development. As previously described, biotin and PA was provided to dams throughout pregnancy, lactation and given to weaned pups throughout early adulthood. Supplemented mice will then be assessed both functionally and histologically to examine the effect of vitamin supplementation on the disease phenotype.

7.2 Phenotypic analysis of vitamin supplemented *Slc5a6^{TnTCre}* mice

Due to COVID-19 restrictions, and breeding difficulties within the mouse colony, only one vitamin treated litter has been analysed. This litter included 2 *Slc5a6$^{+/+}$*, 1 *Slc5a6$^{+/F;TnTCre}$* and 2 *Slc5a6$^{F/F;TnTCre}$* mice.

Weight monitoring of this litter (Figure 7.2A) showed vitamin supplemented *Slc5a6$^{F/F;TnTCre}$* mice gain weight at a proportional rate to littermate controls, *Slc5a6$^{+/+}$* and *Slc5a6$^{+/F;TnTCre}$*. A comparison of body weight gain at 20 weeks (Figure 7.2B) showed a similar trend in weight gain between all three vitamin treated genotypes. Due to the low *n,* statistical testing could not be performed. Health monitoring of all vitamin supplemented mice did not show any signs of ill health, such as reduced reactivity or movement, or changes to coat condition.

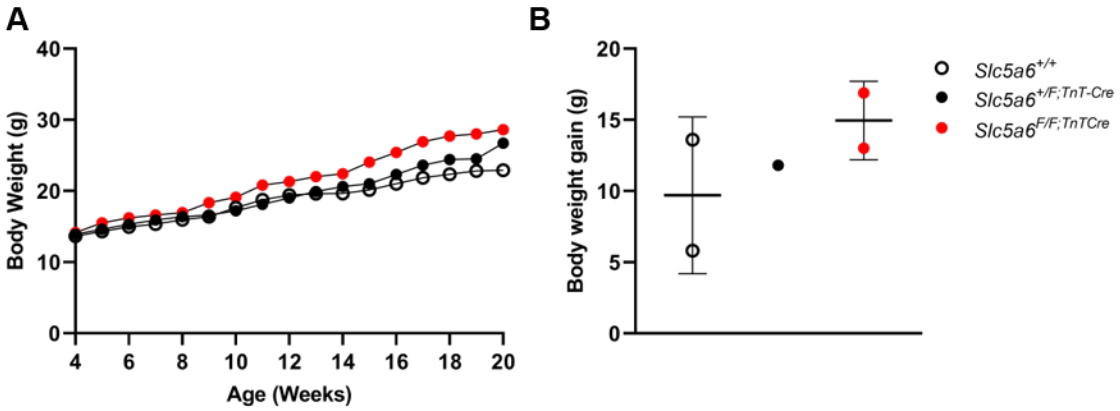

Figure 7.2. Weight monitoring of vitamin supplemented *Slc5a6^{TnTCre}* mice.
A) Averaged longitudinal weight data of vitamin supplemented mice, *Slc5a6$^{+/+}$* (white), *Slc5a6$^{+/F;TnTCre}$* (Black) and *Slc5a6$^{F/F;TnTCre}$* (red), following weaning through to collection at 20 weeks. B) Body weight gain of each genotype calculated following collection at 20 weeks. n= 2 *Slc5a6$^{+/+}$*, 1 *Slc5a6$^{+/F;TnTCre}$*, 2 *Slc5a6$^{F/F;TnTCre}$*.

As mice continued to thrive under vitamin supplementation, ECGs were performed at 5, 8, 14 and 18 weeks to assess cardiac conduction throughout early adulthood.

7.2.1 Vitamin supplemented Slc5a6$^{F/F;TnTCre}$ show similar cardiac conductivity to littermate controls

As previously described in 6.1.7, ECG is performed to investigate the cardiac conduction cycle. This can be broken down into three stages; atrial contraction and depolarisation (P wave and PR interval), ventricular contraction (QRS interval) and repolarisation (ST height, T wave and QT interval). A representative ECG trace

recorded at 8 weeks for *Slc5a6*$^{+/+}$ (Figure 7.3A), *Slc5a6*$^{+/F;TnTCre}$ (Figure 7.3B) and *Slc5a6*$^{F/F;TnTCre}$ (Figure 7.3C). From this, there are observable changes apparent, including lengthening of PR interval, ST height and T wave depression in vitamin supplemented *Slc5a6*$^{F/F;TnTCre}$ mice compared to *Slc5a6*$^{+/+}$ and *Slc5a6*$^{+/F;TnTCre}$ mice, similar to conduction changes found in non-supplemented mice in Chapter 6. To enable characterisation of the effect of vitamin supplementation on cardiac conduction each parameter was quantified from recordings collected at 5, 8, 14 and 18 weeks.

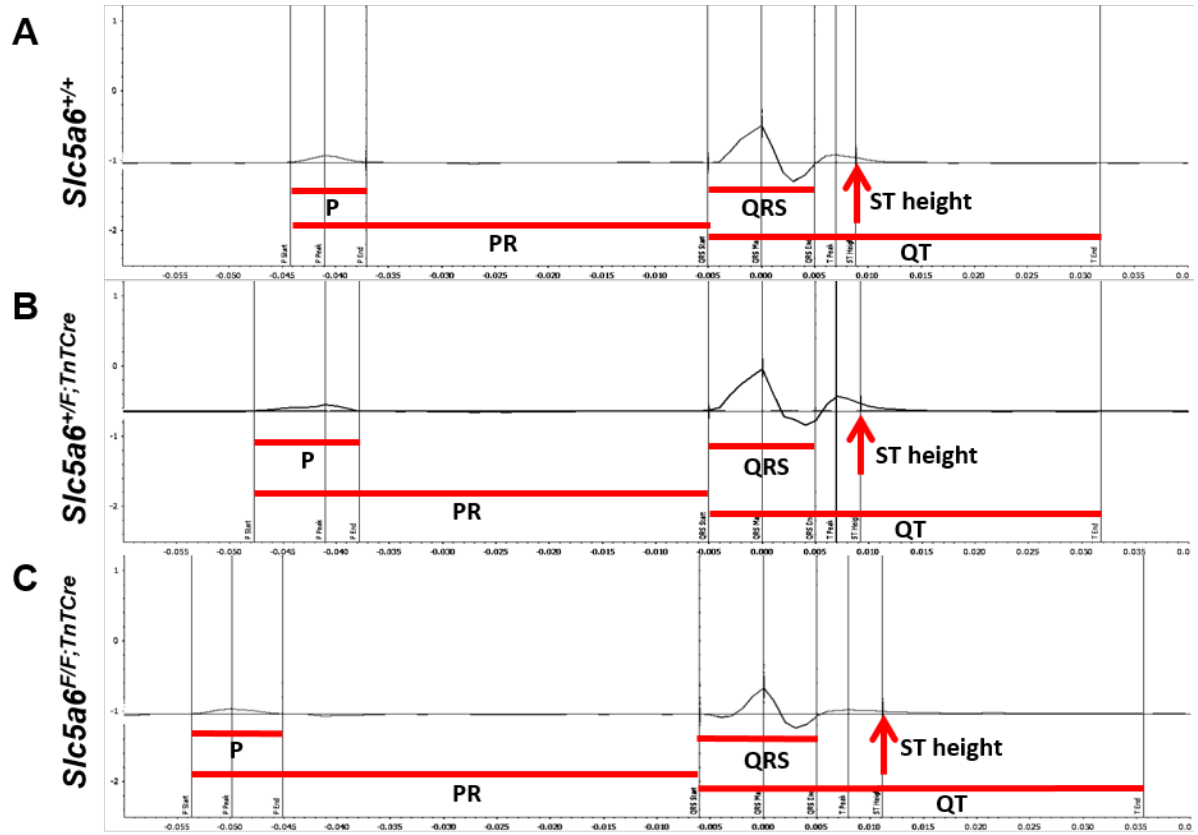

Figure 7.3. Representative averaged ECG trace of vitamin supplemented *Slc5a6*^{TnTCre} mice at 8 weeks.
ECGs were recorded for 3 minutes with data averaged over 60 seconds. Traces shown represent data from 60-120 second period for vitamin supplemented *Slc5a6*^{TnTCre} mice at 8 weeks. ECG parameters (red); P wave, PR interval, QRS interval, QT interval and ST height are shown on *Slc5a6*$^{+/+}$ (A), *Slc5a6*$^{+/F;TnTCre}$ (B) and *Slc5a6*$^{F/F;TnTCre}$ (C) traces. *n*= 2 *Slc5a6*$^{+/+}$, 1 *Slc5a6*$^{+/F;TnTCre}$, 2 *Slc5a6*$^{F/F;TnTCre}$.

ECG quantification of vitamin supplemented mice at 5 weeks shows comparable HR (Figure 7.4A), PR interval (Figure 7.4B), QRS interval (Figure 7.4C) and ST height (Figure 7.4E) between *Slc5a6*$^{+/+}$, *Slc5a6*$^{+/F;TnTCre}$ and *Slc5a6*$^{F/F;TnTCre}$. However, there is variation within *Slc5a6*$^{F/F;TnTCre}$ mice for T amplitude (Figure 7.4F), as well as a decreased QT interval (Figure 7.4D) in the vitamin supplemented *Slc5a6*$^{+/F;TnTCre}$

mouse compared to *Slc5a6*$^{+/+}$ and *Slc5a6*$^{F/F;TnTCre}$ mice at 5 weeks. An increased *n* is required to determine the statistical significance of data shown.

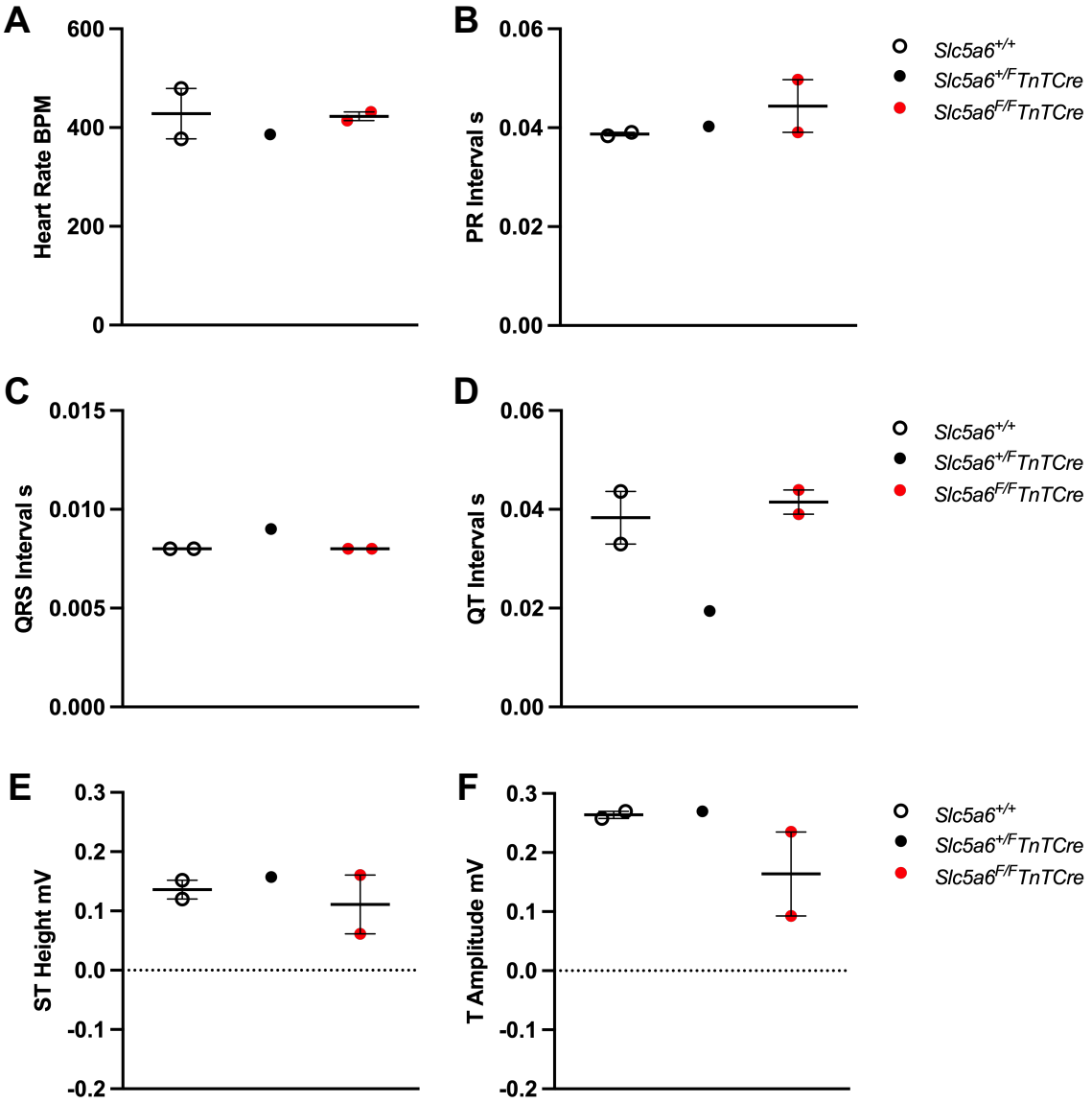

Figure 7.4. Quantification of ECG parameters for vitamin supplemented *Slc5a6*^{TnTCre} mice at 5 weeks.
No discernible differences were observed between *Slc5a6*$^{+/+}$ (white), *Slc5a6*$^{+/F;TnTCre}$ (black) or *Slc5a6*$^{F/F;TnTCre}$ mice (red) in HR (A), PR interval (B), QRS interval (C) or ST height (E). The *Slc5a6*$^{+/F;TnTCre}$ mouse did show a lower QT interval (D), than the other genotypes;however, only one *Slc5a6*$^{+/F;TnTCre}$ mouse was analysed. One vitamin supplemented *Slc5a6*$^{F/F;TnTCre}$ mouse showed a more prominent decrease in T wave amplitude (F) compared with *Slc5a6*$^{+/+}$ and *Slc5a6*$^{+/F;TnTCre}$ mice at 5 weeks. Data presented as mean±SEM. *n*= 2 *Slc5a6*$^{+/+}$, 1 *Slc5a6*$^{+/F;TnTCre}$ and 2 *Slc5a6*$^{F/F;TnTCre}$ mice.

Although the *n* is too small for statistical testing, the data collected from vitamin supplemented mice can be compared to ECG data from non-vitamin supplemented mice at 5 weeks (Figure 7.5).

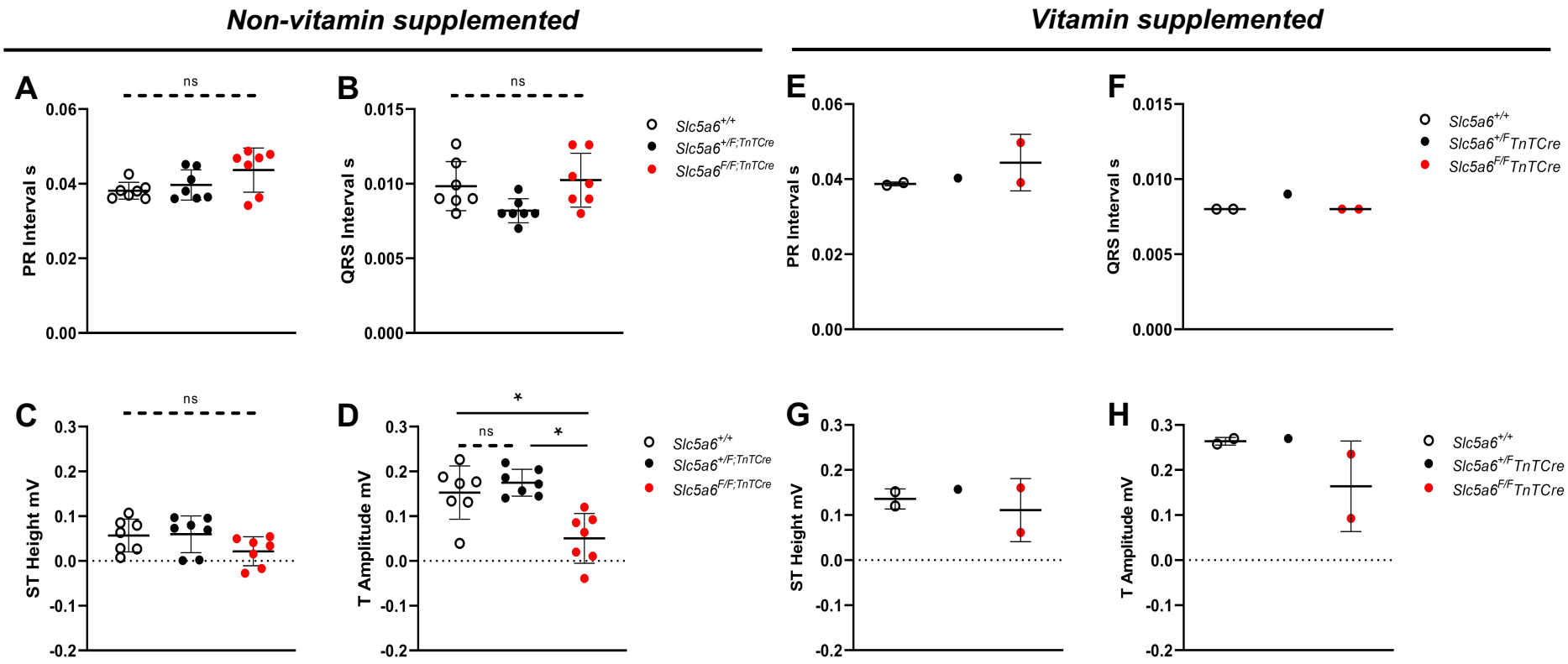

Figure 7.5. Comparison of ECG parameters for non-vitamin supplemented and vitamin supplemented *Slc5a6*^{TnTCre} mice at 5 weeks.

ECG parameters; PR interval (A, E), QRS interval (B, F), ST height (C, G) and T amplitude (D, H) are shown for each genotype; *Slc5a6*$^{+/+}$ (white), *Slc5a6*$^{+/F;TnTCre}$ (black) or *Slc5a6*$^{F/F;TnTCre}$ mice (red). A-D) ECG parameters of non-vitamin supplemented *Slc5a6*^{TnTCre} mice at 5 weeks from Figure 6.11. E-H) The same parameters are shown from vitamin supplemented *Slc5a6*^{TnTCre} mice. Vitamin supplemented mice show comparable PR (E) and QRS interval (F)values compared to those observed in non-vitamin supplemented PR (A) and QRS (B);however, vitamin supplemented mice have a higher average ST height (G) and T amplitude (H) compared to the ST height (C) and T amplitude (D) of non-vitamin supplemented mice. A-D) One-way ANOVA with multiple comparisons and Bonferroni correction was applied to non-vitamin supplemented datasets; n= 7 *Slc5a6*$^{+/+}$, 7 *Slc5a6*$^{+/F;TnTCre}$ and 7 *Slc5a6*$^{F/F;TnTCre}$ mice. * = p<0.05. E-H) Vitamin supplemented: n = 2 *Slc5a6*$^{+/+}$, 1 *Slc5a6*$^{+/F;TnTCre}$ and 2 *Slc5a6*$^{F/F;TnTCre}$ mice.

This comparison suggests that vitamin supplemented mice have a similar length of PR (Figure 7.5E) and QRS interval (Figure 7.5F) to the PR (Figure 7.5A) and QRS interval (Figure 7.5B) shown of non-vitamin supplemented mice. However, of note is the increase in the ST height of each genotype shown in Figure 7.5G of vitamin supplemented mice compared to Figure 7.5C. Here the average ST height of vitamin supplemented mice is ~0.1mV compared to ~0.05mV in non-supplemented mice. In addition to changes in ST height, there is also a noticeably higher T amplitude in vitamin supplemented *Slc5a6*$^{+/+}$ and *Slc5a6*$^{+/F;TnTCre}$ mice with a higher average T amplitude in *Slc5a6*$^{F/F;TnTCre}$ mice compared to non-supplemented mice (Figure 7.5D and Figure 7.5H, respectively). There appears to be no inversion of either ST height or T amplitude in vitamin supplemented *Slc5a6*$^{F/F;TnTCre}$ mice compared to no-vitamin supplemented mice. Together these changes suggest vitamin supplementation may be having a positive effect on cardiac conduction across all three genotypes at 5 weeks. Further investigation into cardiac conduction was performed in vitamin supplemented mice at 8 weeks (Figure 7.6).

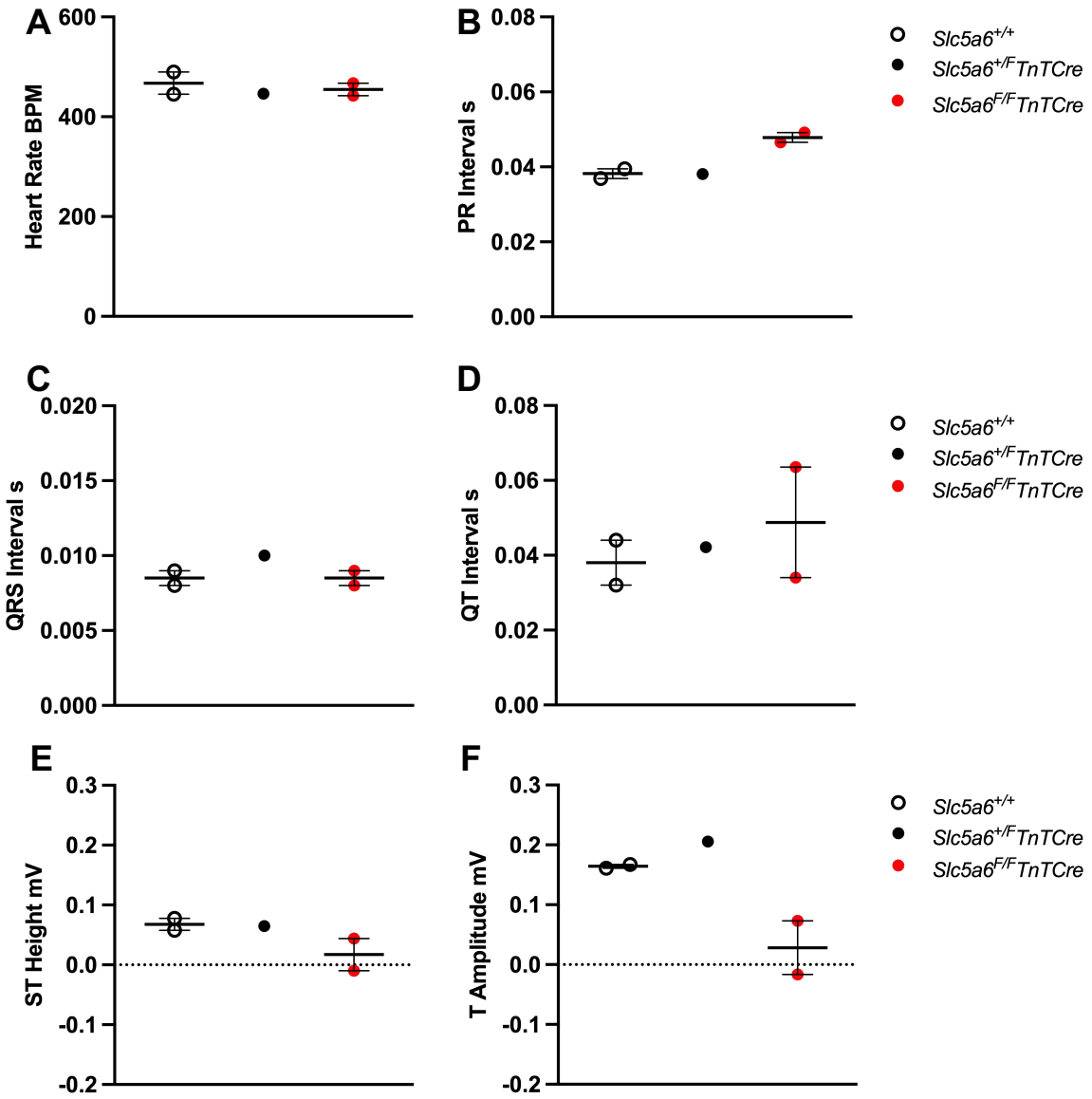

Figure 7.6. ECG quantification of parameters of vitamin supplemented *Slc5a6^{TnTCre}* mice at 8 weeks.
ECG parameters are shown for *Slc5a6$^{+/+}$* (white), *Slc5a6$^{+/F;TnTCre}$* (black) or *Slc5a6$^{F/F;TnTCre}$* mice (red). Similar values are observed across all three genotypes for HR (A), QRS interval (C) and QT interval (D). However, *Slc5a6$^{F/F;TnTCre}$* mice do have a longer PR interval (B) compared to littermate controls. The average ST height (E) and T amplitude (F) is lower in *Slc5a6$^{F/F;TnTCre}$* mice compared to *Slc5a6$^{+/+}$* and *Slc5a6$^{+/F;TnTCre}$* mice at 8 weeks. Data presented as mean±SEM. *n*= 2 *Slc5a6$^{+/+}$*, 1 *Slc5a6$^{+/F;TnTCre}$* and 2 *Slc5a6$^{F/F;TnTCre}$* mice.

Figure 7.6 shows quantification of ECG parameters at 8 weeks. From this data, no noticeable differences are observed in HR (Figure 7.6A), QRS interval (Figure 7.6C) or QT interval (Figure 7.6D) between each vitamin supplemented genotype, similar to ECG data at 5 weeks. However, there is an identifiable lengthening of the PR interval (Figure 7.6B) in *Slc5a6$^{F/F;TnTCre}$* mice at 8 weeks compared to *Slc5a6$^{+/+}$* and

Slc5a6$^{+/F;TnTCre}$ mice. Depolarisation changes are apparent in vitamin supplemented *Slc5a6*$^{F/F;TnTCre}$ mice at 8 weeks compared to *Slc5a6*$^{+/+}$ and *Slc5a6*$^{+/F;TnTCre}$ mice. Of the two *Slc5a6*$^{F/F;TnTCre}$ mice, one has a comparable ST height (Figure 7.6E) to *Slc5a6*$^{+/+}$ and *Slc5a6*$^{+/F;TnTCre}$ mice whereas the ST height in the second vitamin supplemented *Slc5a6*$^{F/F;TnTCre}$ mouse appears inverted. This is also shown in Figure 7.6.F, where the T amplitude is inverted in one vitamin supplemented *Slc5a6*$^{F/F;TnTCre}$ mouse compared to littermate controls. Again, a higher *n* is needed to investigate the changes identified in vitamin supplemented *Slc5a6*$^{F/F;TnTCre}$ mice; however, this data can be compared to data collected from non-vitamin supplemented mice at 8 weeks (Figure 7.7).

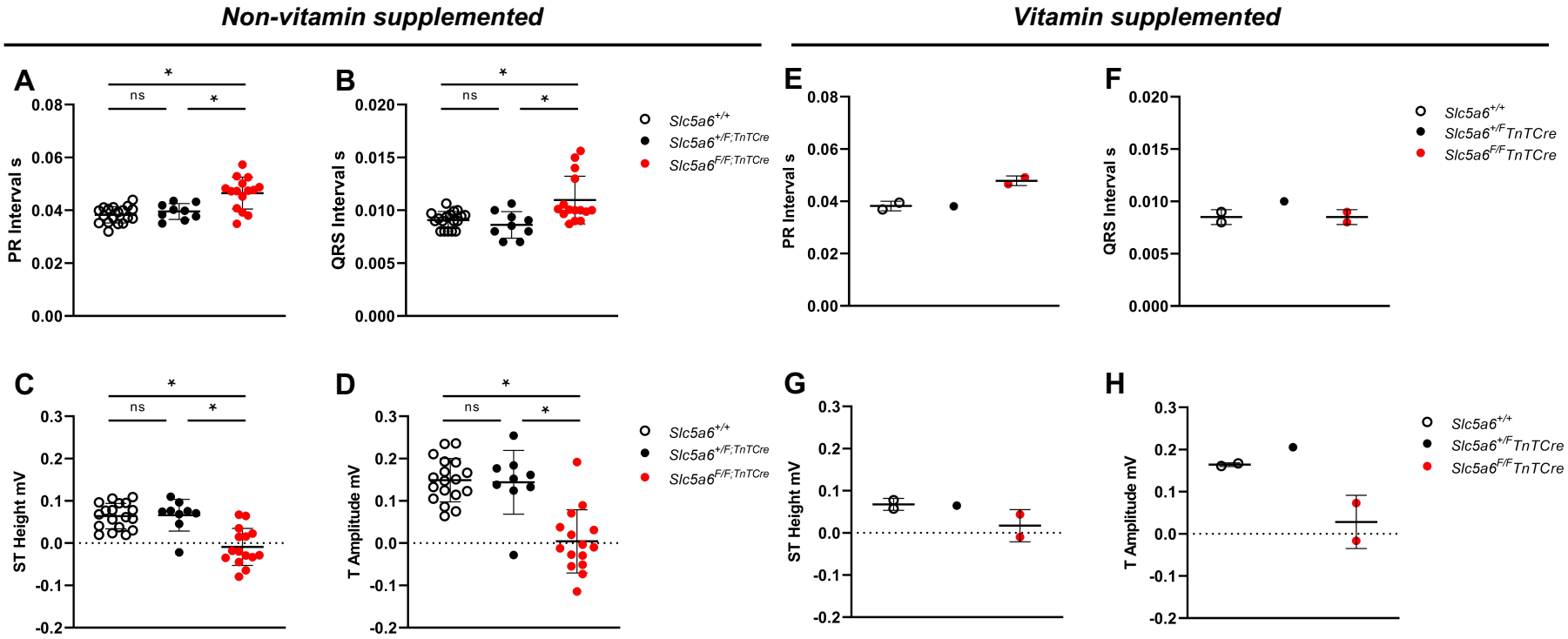

Figure 7.7. Comparison of non-vitamin supplemented and vitamin supplemented ECG parameters at 8 weeks.
ECG parameters; PR interval (A, E), QRS interval (B, F), ST height (C, G) and T amplitude (D, H) are shown for each genotype; *Slc5a6*$^{+/+}$ (white), *Slc5a6*$^{+/F;TnTCre}$ (black) or *Slc5a6*$^{F/F;TnTCre}$ mice (red). A-D) ECG data for non-vitamin supplemented *Slc5a6*^{TnTCre} mice at 8 weeks from Figure 6.12. E-H) ECG parameters are shown for vitamin supplemented *Slc5a6*^{TnTCre} mice at 8 weeks. Vitamin supplemented mice show comparable PR (E) and QRS interval (F) values per genotype to those observed in non-vitamin supplemented PR (A) and QRS interval (B). Repolarisation changes in vitamin supplemented *Slc5a6*$^{F/F;TnTCre}$; decreased ST height (G) and T amplitude (H) are also present in non-vitamin supplemented *Slc5a6*$^{F/F;TnTCre}$ ST height (C) and T amplitude (D). A-D) One-way ANOVA with multiple comparisons and Bonferroni correction was applied to non-vitamin supplemented dataset; n = 18 *Slc5a6*$^{+/+}$, 9 *Slc5a6*$^{+/F;TnTCre}$ and 15 *Slc5a6*$^{F/F;TnTCre}$ mice. * = p<0.05. E-H) Vitamin supplemented n = 2 *Slc5a6*$^{+/+}$, 1 *Slc5a6*$^{+/F;TnTCre}$ and 2 *Slc5a6*$^{F/F;TnTCre}$ mice.

Vitamin supplemented *Slc5a6*^{TnTCre} mice at 8 weeks appear comparable ECG parameters to those shown in non-vitamin supplemented *Slc5a6*^{TnTCre} mice. The average PR interval for non-vitamin supplemented *Slc5a6*$^{+/+}$ and *Slc5a6*$^{+/F;TnTCre}$ mice is ~0.04 (Figure 7.7A), similar to vitamin supplemented littermate controls (Figure 7.7.E). Vitamin supplemented *Slc5a6*$^{F/F;TnTCre}$ mice have an average PR interval of ~0.05 (Figure 7.7E) which is also seen in *Slc5a6*$^{F/F;TnTCre}$ mice without vitamin supplementation (Figure 7.7A). In non-vitamin supplemented *Slc5a6*^{TnTCre} mice, the QRS interval is significantly wider in *Slc5a6*$^{F/F;TnTCre}$ mice compared to *Slc5a6*$^{+/+}$ and *Slc5a6*$^{+/F;TnTCre}$ mice, with an average over 0.01s, indicative of myocardial fibrosis (Figure 7.7B). The QRS interval in vitamin supplemented *Slc5a6*$^{F/F;TnTCre}$ mice is the same as *Slc5a6*$^{+/+}$ mice, ~0.0085 (Figure 7.7F) suggesting myocardial fibrosis may not be present in vitamin supplemented *Slc5a6*$^{F/F;TnTCre}$ mice at 8 weeks. However, a decrease in the repolarisation of the ventricles can be observed in vitamin supplemented *Slc5a6*$^{F/F;TnTCre}$ mice, shown in Figure 7.7G (ST height) and Figure 7.7H (T amplitude) as seen in vitamin supplemented mice at 5 weeks. This is suggestive of LV strain pattern which is shown in *Slc5a6*$^{F/F;TnTCre}$ mice without vitamin supplementation, indicating that vitamin supplementation did not maintain or improve ventricular repolarisation in *Slc5a6*$^{F/F;TnTCre}$ mice. Although there are conduction changes observed in vitamin supplemented *Slc5a6*$^{F/F;TnTCre}$ compared to littermate controls, the assessment continued at 14 weeks (Figure 7.8).

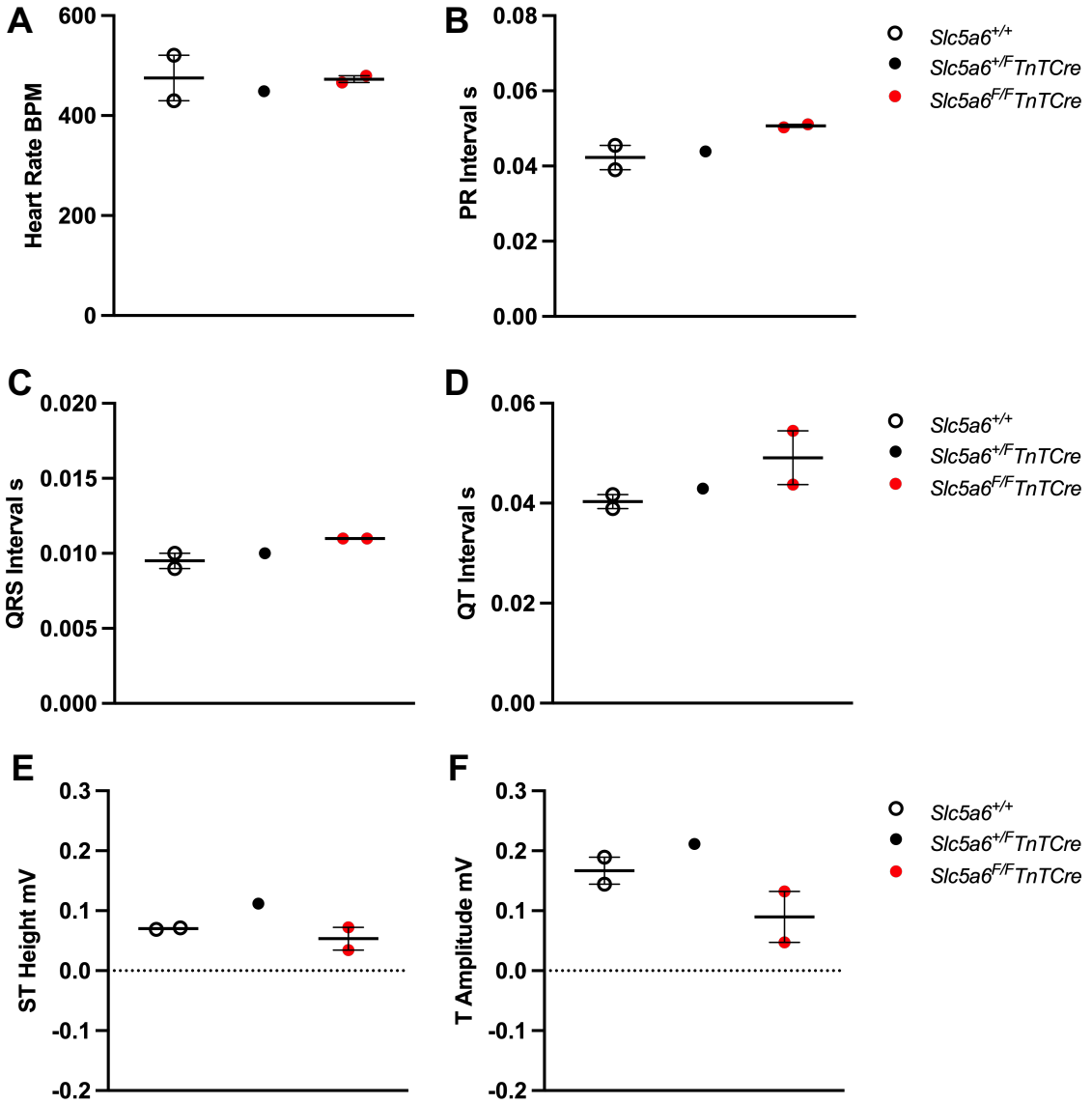

Figure 7.8. Quantification of ECG parameters of vitamin supplemented *Slc5a6^{TnTCre}* mice at 14 weeks.
There were no discernible differences were observed between *Slc5a6$^{+/+}$* (white), *Slc5a6$^{+/F;TnTCre}$* (black) or *Slc5a6$^{F/F;TnTCre}$* mice (red) in HR (A) at 14 weeks. PR (B), QRS (C) and QT interval (D) are slightly increased in *Slc5a6$^{F/F;TnTCre}$* mice compared to *Slc5a6$^{+/+}$* and *Slc5a6$^{+/F;TnTCre}$* mice. At 14 weeks, vitamin supplemented *Slc5a6$^{F/F;TnTCre}$* mice have a slightly lower ST height and T amplitude (F) compared to littermate controls. Data presented as mean±SEM. *n*= 2 *Slc5a6$^{+/+}$*, 1 *Slc5a6$^{+/F;TnTCre}$* and 2 *Slc5a6$^{F/F;TnTCre}$* mice.

Analysis of vitamin supplemented mice at 14 weeks reveals *Slc5a6$^{F/F;TnTCre}$* mice (*n* =2) appear to have a similar HR to *Slc5a6$^{+/+}$* and *Slc5a6$^{+/F;TnTCre}$* mice (Figure 7.8A). PR interval (Figure 7.8B) in *Slc5a6$^{F/F;TnTCre}$* mice also appears lengthened at 14 weeks, with *Slc5a6$^{F/F;TnTCre}$* mice revealing a potentially wider QRS (Figure 7.8C) and QT interval (Figure 7.8D) compared to littermate controls. Interestingly, no inversion of ST

(Figure 7.8E) or T amplitude (Figure 7.8F) is observed in vitamin supplemented *Slc5a6*$^{F/F;TnTCre}$ mice at 14 weeks. Due to low *n,* statistical significance cannot be performed on this data; however, this does suggest vitamin supplementation is now positively impacting the cardiac phenotype of *Slc5a6*$^{F/F;TnTCre}$ mice. Similar to 5 and 8 week ECG data, vitamin supplemented data can be compared to non-vitamin supplemented *Slc5a6*^{TnTCre} data at 14 weeks (Figure 7.9).

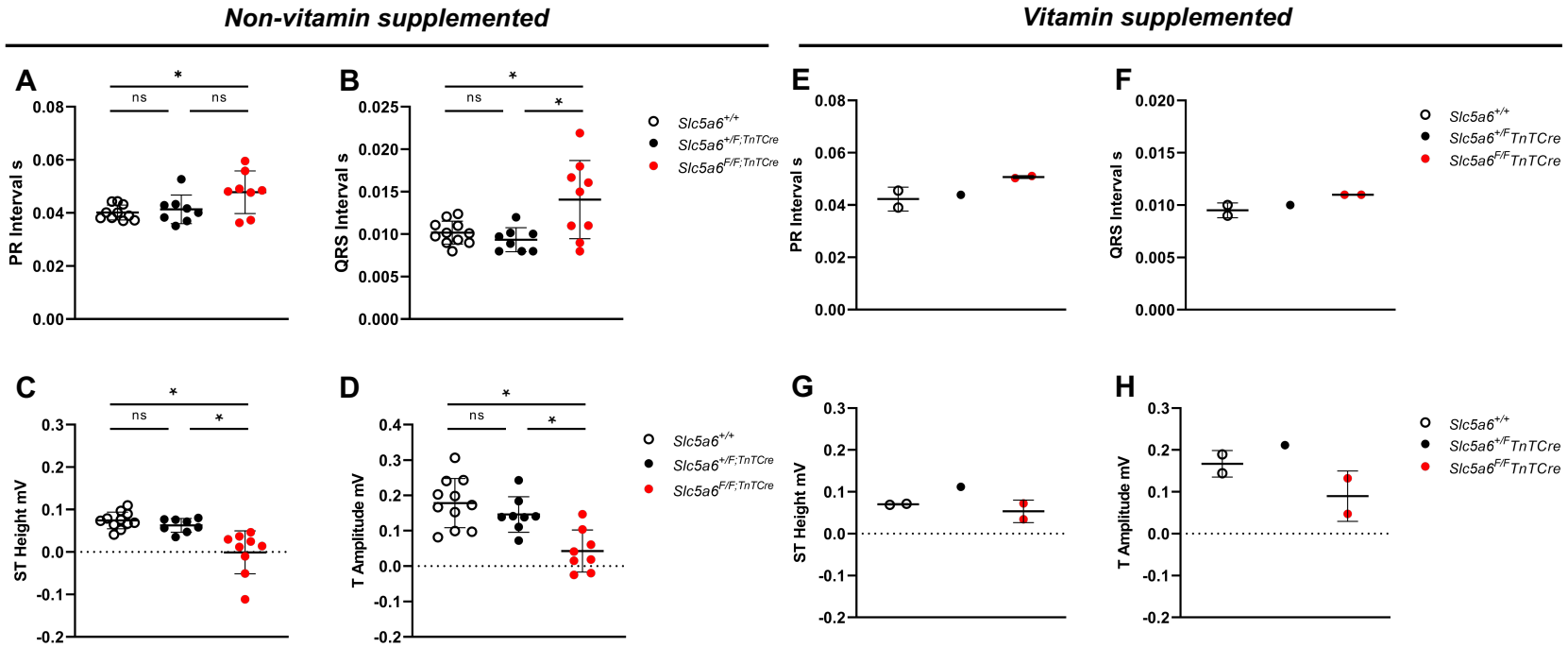

Figure 7.9. Comparison of ECG parameters between non-vitamin supplemented and vitamin supplemented *Slc5a6*^{TnTCre} mice at 14 weeks.

ECG parameters; PR interval (A, E), QRS interval (B, F), ST height (C, G) and T amplitude (D, H) are shown for *Slc5a6*$^{+/+}$ (white), *Slc5a6*$^{+/F;TnTCre}$ (black) or *Slc5a6*$^{F/F;TnTCre}$ mice (red). A-D) ECG parameters of non-vitamin supplemented *Slc5a6*^{TnTCre} mice at 14 weeks from Figure 6.13. E-H) Parameters are shown from vitamin supplemented *Slc5a6*^{TnTCre} mice from Figure 7.8. In non-vitamin supplemented mice, a significant increase in PR (A) and QRS interval (B) is seen in *Slc5a6*$^{F/F;TnTCre}$ mice compared to *Slc5a6*$^{+/+}$ and *Slc5a6*$^{+/F;TnTCre}$ mice. An increase in PR (E) and QRS interval (F) is also observed in vitamin supplemented *Slc5a6*$^{F/F;TnTCre}$ mice but to a lesser extent than seen in non-vitamin supplemented mice. ST (C) and T amplitude (D) is significantly reduced in non-vitamin supplemented *Slc5a6*$^{F/F;TnTCre}$ at 14 weeks; however, in vitamin supplemented mice ST height (G) is comparable between *Slc5a6*$^{+/+}$, *Slc5a6*$^{+/F;TnTCre}$ and *Slc5a6*$^{F/F;TnTCre}$ mice. T amplitude (H) is decreased in vitamin supplemented *Slc5a6*$^{F/F;TnTCre}$ mice. A-D) One-way ANOVA with multiple comparisons and Bonferroni correction was applied to non-vitamin supplemented datasets; n= 11 *Slc5a6*$^{+/+}$, 8 *Slc5a6*$^{+/F;TnTCre}$ and 9 *Slc5a6*$^{F/F;TnTCre}$ mice. * = p<0.05. E-H) Vitamin supplemented: n = 2 *Slc5a6*$^{+/+}$, 1 *Slc5a6*$^{+/F;TnTCre}$ and 2 *Slc5a6*$^{F/F;TnTCre}$ mice.

When comparing vitamin supplemented ECG data to non-vitamin supplemented data, some similarities and differences between the two groups can be seen at 14 weeks (Figure 7.9). The average PR interval for vitamin supplemented *Slc5a6*$^{F/F;TnTCre}$ is ~0.05 (Figure 7.9E) which is similar to non-supplemented *Slc5a6*$^{F/F;TnTCre}$ PR average (Figure 7.9A). Interestingly, although the QRS interval is slightly increased in vitamin supplemented *Slc5a6*$^{F/F;TnTCre}$ compared to *Slc5a6*$^{+/+}$ and *Slc5a6*$^{+/F;TnTCre}$ (Figure 7.9F), the interval is smaller than that seen in non-vitamin supplemented *Slc5a6*$^{F/F;TnTCre}$ (Figure 7.9B). ST height in vitamin supplemented mice is comparable across *Slc5a6*$^{+/+}$, *Slc5a6*$^{+/F;TnTCre}$ and *Slc5a6*$^{F/F;TnTCre}$ mice at 14 weeks (Figure 7.9G). This is in contrast to data from non-supplemented *Slc5a6*^{TnTCre} mice where *Slc5a6*$^{F/F;TnTCre}$ have a significantly reduced ST height (Figure 7.9C), with some mice having an inverted ST. Similarly, T amplitude in vitamin supplemented *Slc5a6*$^{F/F;TnTCre}$ is reduced compared to littermate controls (Figure 7.9H); however, not as reduced as non-vitamin supplemented *Slc5a6*$^{F/F;TnTCre}$ mice (Figure 7.9D). From this data, it is possible to suggest vitamin supplementation may have a positive impact on cardiac conduction of *Slc5a6*$^{F/F;TnTCre}$ mice.

In non-supplemented *Slc5a6*$^{F/F;TnTCre}$ mice at 18 weeks, data could not be quantified due to the severity of the cardiac phenotype (Figure 6.14). However, in contrast in vitamin supplemented mice, ECG parameters could be accurately determined. This initial data suggests a possible long-term improvement in cardiac function as a consequence of vitamin supplementation within this mouse line (Figure 7.10).

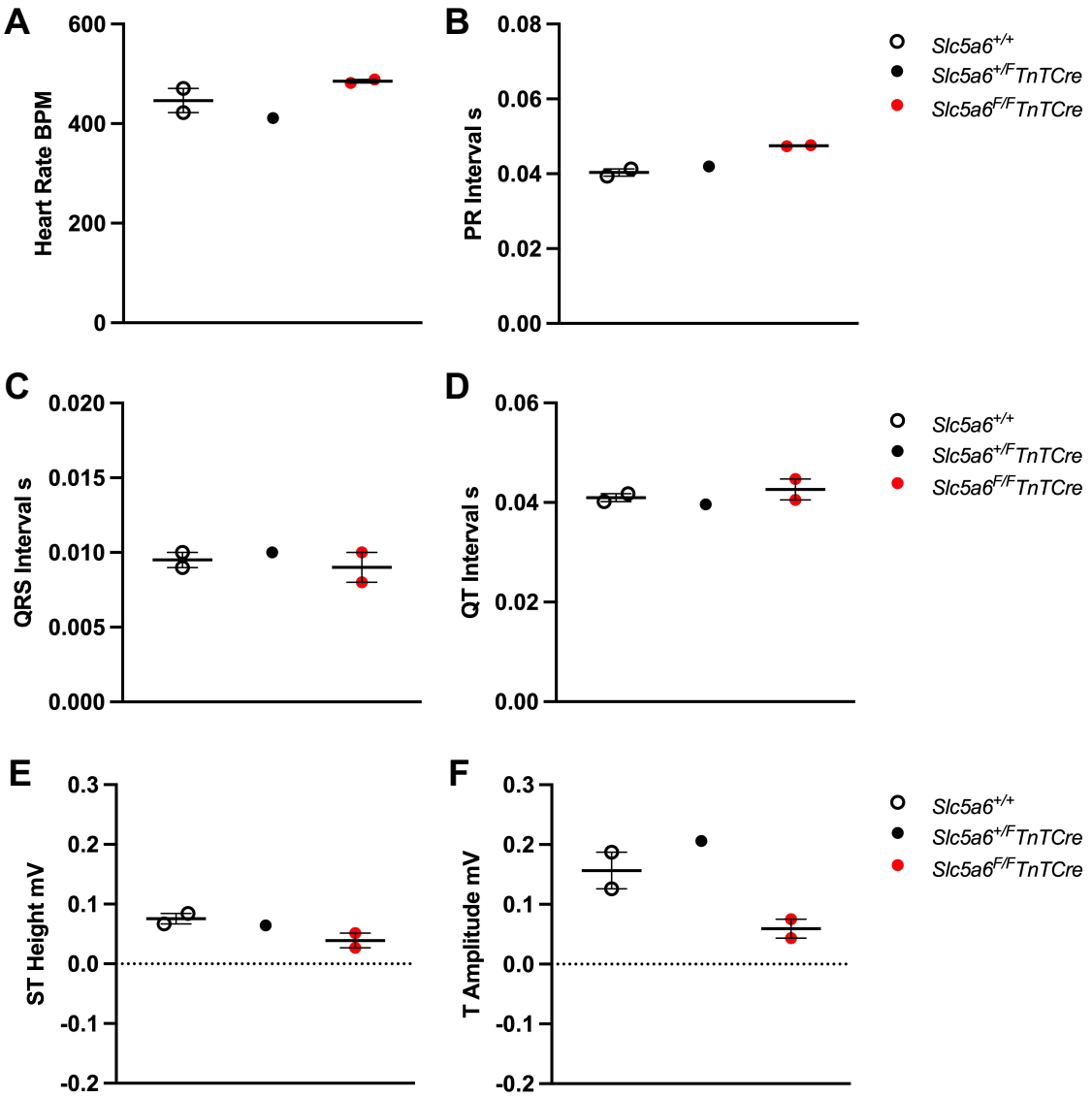

Figure 7.10. Quantification of ECG parameters of vitamin supplemented *Slc5a6*^{TnTCre} mice at 18 weeks.
ECG parameters shown for *Slc5a6*$^{+/+}$ (white), *Slc5a6*$^{+/F;TnTCre}$ (black) or *Slc5a6*$^{F/F;TnTCre}$ mice (red). Similar values are observed across all three genotypes for HR (A), QRS interval (C) and QT interval (D). However, vitamin supplemented *Slc5a6*$^{F/F;TnTCre}$ mice have a longer PR interval (B) compared to *Slc5a6*$^{+/+}$ and *Slc5a6*$^{+/F;TnTCre}$ mice. ST height (E) and T amplitude (F) is also lower in *Slc5a6*$^{F/F;TnTCre}$ mice compared to *Slc5a6*$^{+/+}$ and *Slc5a6*$^{+/F;TnTCre}$ mice at 18 weeks. Data presented as mean±SEM. *n*= 2 *Slc5a6*$^{+/+}$, 1 *Slc5a6*$^{+/F;TnTCre}$ and 2 *Slc5a6*$^{F/F;TnTCre}$ mice.

At 18 weeks, vitamin supplemented *Slc5a6*$^{+/+}$ and *Slc5a6*$^{+/F;TnTCre}$ mice appear comparable in all parameters; HR (Figure 7.10A), PR interval (Figure 7.10B), QRS interval (Figure 7.10C), QT interval (Figure 7.10D), ST height (Figure 7.10E) and T amplitude (Figure 7.10F). Interestingly, vitamin supplemented *Slc5a6*$^{F/F;TnTCre}$ mice have a visually comparable HR (Figure 7.10A), QRS (Figure 7.10C), and QT interval (Figure 7.10D) to littermate controls. This suggests that the duration of ventricular

contraction, depolarisation and repolarisation may be unaffected in vitamin supplemented *Slc5a6*$^{F/F;TnTCre}$ mice at 18 weeks. However, there appears to be a slight lengthening of PR interval observed (Figure 7.10B) and slight reduction in ST height (Figure 7.10E) and T amplitude (Figure 7.10A) in *Slc5a6*$^{F/F;TnTCre}$ mice, suggesting an atrioventricular block and LV strain pattern may be present even with vitamin supplementation.

Due to sudden death of the non-vitamin supplemented *Slc5a6*$^{F/F;TnTCre}$ mice at 26 weeks, restrictions on this mouse line meant vitamin supplemented mice had to be collected at 20 weeks for histological analysis.

7.2.2 Vitamin supplemented Slc5a6$^{F/F;TnTCre}$ *mice have enlarged hearts at 20 weeks*

At collection, all hearts were imaged and weighed for comparison (Figure 7.11). Images revealed that vitamin supplemented *Slc5a6*$^{F/F;TnTCre}$ hearts (Figure 7.11C) were enlarged compared to *Slc5a6*$^{+/+}$ (Figure 7.11A) and *Slc5a6*$^{+/F;TnTCre}$ (Figure 7.11B) hearts collected. Heart weight ratios to tibia length (Figure 7.11D) and body weight (Figure 7.11E) may suggest vitamin supplemented *Slc5a6*$^{F/F;TnTCre}$ heart weight is comparable to littermate controls, but due to low *n* and spread of data, conclusions could not be accurately drawn. However, it was hypothesised that, similar to non-supplemented *Slc5a6*$^{F/F;TnTCre}$ hearts, vitamin supplemented mice may have an enlarged heart due to ventricular dilation rather than an increase in ventricular wall hypertrophy.

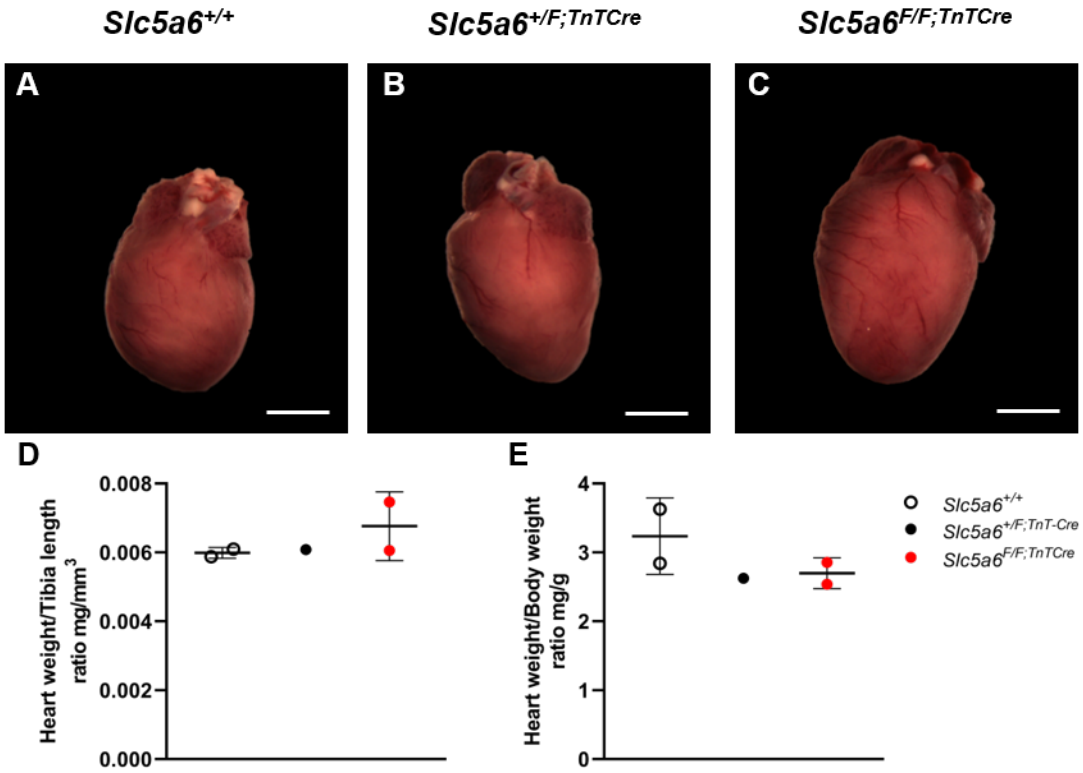

Figure 7.11. Representative whole heart images and heart weight data for vitamin supplemented *Slc5a6^{TnTCre}* mice at 20 weeks.
Whole heart images captured at 20 weeks for *Slc5a6$^{+/+}$* (A), *Slc5a6$^{+/F;TnTCre}$* (B) and *Slc5a6$^{F/F;TnTCre}$* (C) mice. Heart weight was normalised to tibia length (D) and body weight (E) for each genotype; *Slc5a6$^{+/+}$* (white), *Slc5a6$^{+/F;TnTCre}$* (black) and *Slc5a6$^{F/F;TnTCre}$* (red). *n*= 2 *Slc5a6$^{+/+}$*, 1 *Slc5a6$^{+/F;TnTCre}$ and 2 Slc5a6$^{F/F;TnTCre}$*.

To investigate this hypothesis, histological staining of vitamin supplemented mice at 20 weeks was performed and compared with histology from 14 week old non-vitamin supplemented *Slc5a6^{TnTCre}* mice (Figure 7.12).

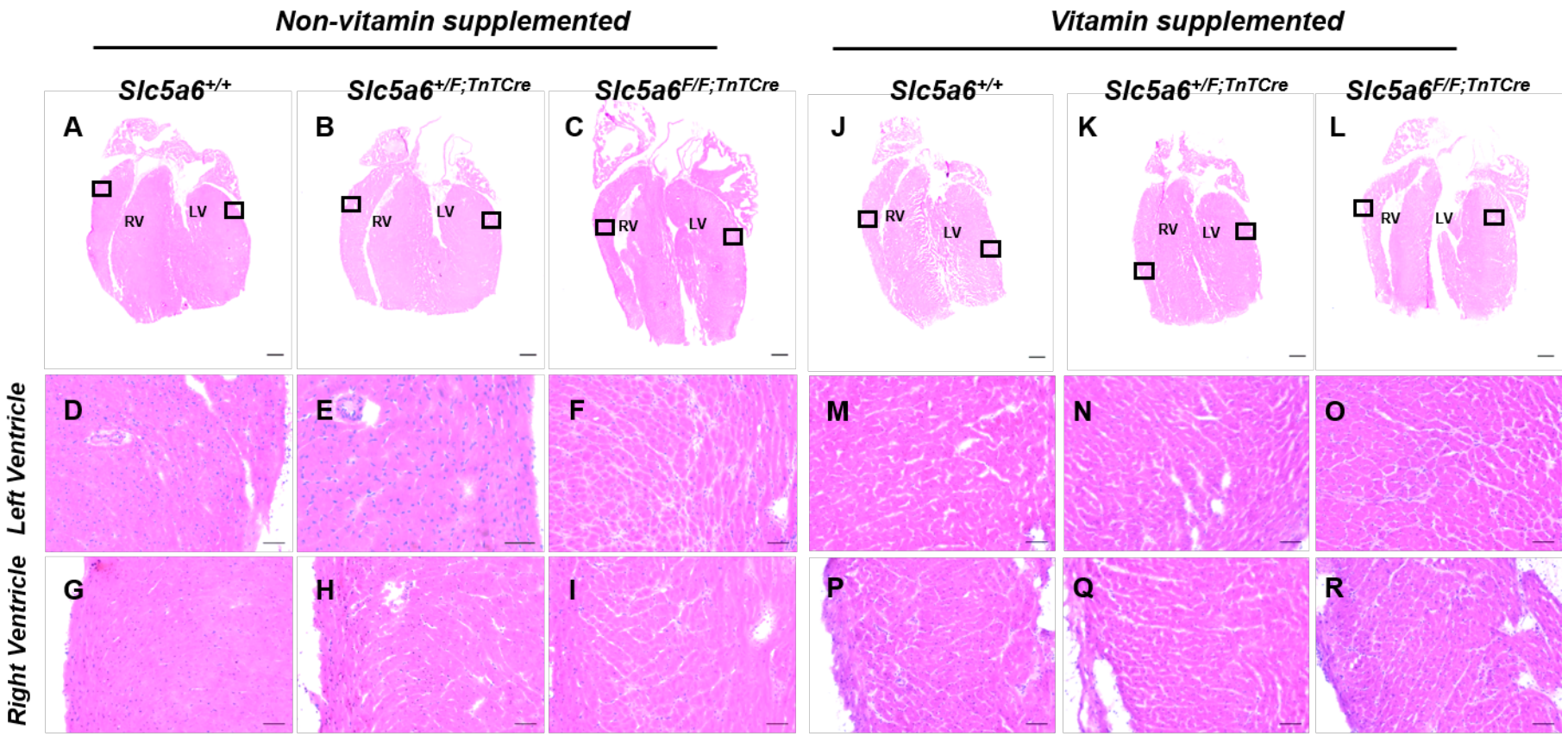

Figure 7.12. Histological images of non-vitamin supplemented and vitamin supplemented *Slc5a6^{TnTCre}* mice.
A-I) H&E images of non-vitamin supplemented *Slc5a6^{TnTCre}* mice at 14 weeks from Figure 6.19. J-R) H&E staining of vitamin supplemented *Slc5a6$^{+/+}$* (J,M,P), *Slc5a6$^{+/F;TnTCre}$* (K,N,Q) and *Slc5a6$^{F/F;TnTCre}$* (L,O,R) mice at 20 weeks. Low magnification (2.5x) images show both ventricles in vitamin supplemented *Slc5a6$^{F/F;TnTCre}$* hearts (L) are slightly dilated compared to *Slc5a6$^{+/+}$* (J), *Slc5a6$^{+/F;TnTCre}$* (K) hearts at 20 weeks. This is visually comparable to non-vitamin supplemented *Slc5a6$^{F/F;TnTCre}$* hearts (C) at 14 weeks. Representative higher powered images shown of the LV and RV for *Slc5a6$^{+/+}$* (M,P), *Slc5a6$^{+/F;TnTCre}$* (N,Q) and *Slc5a6$^{F/F;TnTCre}$* (O,R), respectively. 14 weeks *n* , 5 *Slc5a6$^{+/+}$*, 3 *Slc5a6$^{+/F;TnTCre}$* and 4 *Slc5a6$^{F/F;TnTCre}$*, 20 weeks *n* = 2 *Slc5a6$^{+/+}$*, 1 *Slc5a6$^{+/F;TnTCre}$* and 2 *Slc5a6$^{F/F;TnTCre}$* mice. A-C, J-L scale bar = 500μm, D-I, M-R scale bar = 50 μm.

Although collected at 20 weeks, all vitamin supplemented hearts appear smaller than their non-vitamin supplemented counterparts at 14 weeks. However, vitamin supplemented *Slc5a6*$^{F/F;TnTCre}$ (Figure 7.12L) mice do appear to have enlarged hearts in comparison to vitamin supplemented *Slc5a6*$^{+/+}$ (Figure 7.12J) and *Slc5a6*$^{+/F;TnTCre}$ (Figure 7.12K) hearts. Upon closer inspection of the myocardium of vitamin supplemented mice, more prominent myocardial spacing is apparent in *Slc5a6*$^{+/+}$ (LV Figure 7.12M; RV Figure 7.12P) and *Slc5a6*$^{+/F;TnTCre}$ (LV Figure 7.12N; RV Figure 7.12Q) compared to non-vitamin supplemented controls. Interestingly, vitamin supplemented *Slc5a6*$^{F/F;TnTCre}$ hearts still have an visible increase in the degree of interstitial space between cardiomyocytes in both the LV (Figure 7.12.O) and RV (Figure 7.12.R) compared to littermate controls. However, the amount of interstitial space seems to be reduced in vitamin supplemented 20 week old *Slc5a6*$^{F/F;TnTCre}$ compared to its 14 week old non-vitamin supplemented counterparts in both the LV (Figure 7.12F) and RV (Figure 7.12I), where widespread interstitial fibrosis was found to be increased. This suggests that the vitamin supplementation may be delaying the histological changes leading to the development of cardiomyopathy within *Slc5a6*$^{F/F;TnTCre}$ mice. To further confirm the presence of interstitial fibrosis, Picro-sirius red staining was performed.

7.2.3 Cardiac fibrosis appears reduced in vitamin supplemented compared to non-vitamin supplemented Slc5a6$^{F/F;TnTCre}$ *mice*

Cryosections of vitamin supplemented *Slc5a6*^{TnTCre} hearts were stained for fibrosis using Picro-sirius red and imaged for analysis. Figure 7.13 shows a comparison of Picro-sirius red staining of 14 week old non-vitamin supplemented *Slc5a6*^{TnTCre}, described in Figure 6.20, and 20 week old vitamin supplemented mice. It should be noted that staining of vitamin supplemented cardiac sections was not performed simultaneously with sections from Figure 6.20, and therefore variation in processing may have occurred. From H&E staining of vitamin supplemented littermate controls, there was a suggestion of increased myocardial space; however, from the Picro-sirius red staining of vitamin supplemented *Slc5a6*$^{+/+}$ (LV Figure 7.13I; RV Figure 7.13L) and *Slc5a6*$^{+/F;TnTCre}$ (LV Figure 7.13J; RV Figure 7.13M) this appears to be due to freezing artefact and not widespread interstitial fibrosis. As suggested by H&E staining, vitamin supplemented *Slc5a6*$^{F/F;TnTCre}$ mice still display increased levels of interstitial fibrosis

in both the LV (Figure 7.13K) and RV (Figure 7.13M); however, when compared to non-vitamin supplemented *Slc5a6*$^{F/F;TnTCre}$ mice (LV Figure 7.13C; RV Figure 7.13F) there seems to be a reduction in the spread of fibrosis throughout the myocardium, possibly due to vitamin supplementation. Quantification of the area of fibrosis in vitamin supplemented mice revealed *Slc5a6*$^{F/F;TnTCre}$ hearts have almost a two-fold increase in the area of myocardium in the LV (Figure 7.13O) and RV (Figure 7.13P) compared to the LV and RV of *Slc5a6*$^{+/+}$ mice with ~25% and ~30%, respectively. However, due to low *n,* statistical testing could not be applied to the vitamin supplemented dataset.

The area of fibrosis in the LV (Figure 7.13G) and RV (Figure 7.13H) of non-vitamin supplemented *Slc5a6*$^{F/F:TnTCre}$ hearts was significantly increased (~55%) compared to littermate controls (LV 10%, RV ~10-20%). However, vitamin supplemented *Slc5a6*$^{F/F;TnTCre}$ mice show a reduction in fibrosis compared the non-supplemented counterparts with an average area of ~40% fibrosis, in both LV (Figure 7.13O) and RV (Figure 7.13P) at 20 weeks. This provides further evidence that vitamin supplementation in *Slc5a6*$^{F/F;TnTCre}$ mice appears to have a positive effect by delaying the progression of cardiomyopathy within this mouse model.

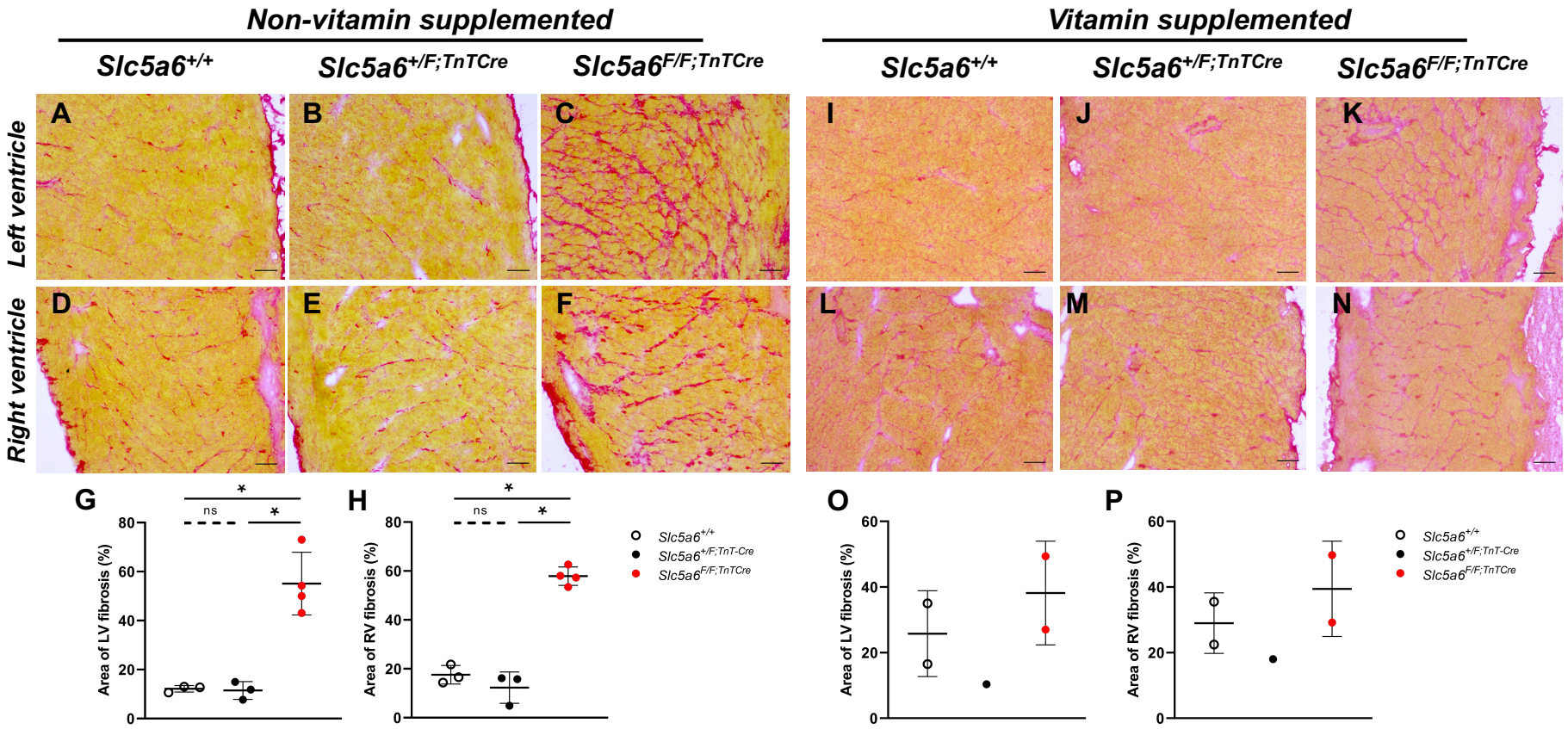

Figure 7.13. Quantification of myocardial fibrosis of non-vitamin supplemented and vitamin supplemented *Slc5a6*^{TnTCre} mice. A-H) Picro-sirius red images of non-vitamin supplemented *Slc5a6*^{TnTCre} mice at 14 weeks from Figure 6.20. I-P) Picro-sirius red staining of 20 week old vitamin supplemented *Slc5a6*$^{+/+}$ (I,L), *Slc5a6*$^{+/F;TnTCre}$ (J,M) and *Slc5a6*$^{F/F;TnTCre}$ (K,N) mice. Representative images are shown of the LV and RV for *Slc5a6*$^{+/+}$ (I,L), *Slc5a6*$^{+/F;TnTCre}$ (J,M) and *Slc5a6*$^{F/F;TnTCre}$ (K,N), respectively. Quantification of the area of fibrosis within the LV (O) and RV (P) is shown for *Slc5a6*$^{+/+}$ (white), *Slc5a6*$^{+/F;TnTCre}$ (black) and *Slc5a6*$^{F/F;TnTCre}$ (red) mice. 14 weeks n = 5 *Slc5a6*$^{+/+}$, 3 *Slc5a6*$^{+/F;TnTCre}$ and 4 *Slc5a6*$^{F/F;TnTCre}$, 20 weeks n = 2 *Slc5a6*$^{+/+}$ (72 LV cardiomyocytes and RV cardiomyocytes), 1 *Slc5a6*$^{+/F;TnTCre}$ (36 LV cardiomyocytes and RV cardiomyocytes) and 2 *Slc5a6*$^{F/F;TnTCre}$ mice (72 LV cardiomyocytes and RV cardiomyocytes). A-F,I-N scale bar = 50 μm.

7.2.4 Vitamin supplemented Slc5a6$^{F/F;TnTCre}$ mice show signs of cardiomyocyte hypertrophy

As previously described, characterisation of changes to the cardiomyocyte area within the heart of non-vitamin supplemented *Slc5a6^{TnTCre}* mice found that *Slc5a6$^{F/F;TnTCre}$* mice have significantly enlarged cardiomyocytes compared to littermate controls (Figure 6.21). To determine the effects of vitamin supplementation on cardiomyocyte area, WGA was performed on vitamin supplemented *Slc5a6^{TnTCre}* mice at 20 weeks and compared to images of non-vitamin supplemented *Slc5a6^{TnTCre}* mice at 14 weeks (Figure 7.14). From these images, enlarged cardiomyocytes were observed in both the LV and RV of vitamin supplemented *Slc5a6$^{F/F;TnTCre}$* hearts (LV Figure 7.14K; RV Figure 7.14N). This change is also noted in non-vitamin supplemented *Slc5a6$^{F/F;TnTCre}$* mice at 14 weeks (LV Figure 7.14C; RV Figure 7.14F).

For comparison, cardiomyocytes were manually traced, and area measurements collected for the LV (Figure 7.14O) and RV (Figure 7.14P) of each genotype. Here it can be seen thay vitamin supplemented *Slc5a6$^{+/+}$* and *Slc5a6$^{+/F;TnTCre}$* mice have an average cardiomyocyte area ~200μm in both ventricles. Compared to these controls, vitamin supplemented *Slc5a6$^{F/F;TnTCre}$* mice have slightly enlarged cardiomyocytes with an average area of ~300μm in LV and ~250μm in RV. Although cardiomyocytes are enlarged in *Slc5a6$^{F/F;TnTCre}$* hearts compared to littermate controls in the vitamin supplemented cohort, when compared to non-vitamin supplemented *Slc5a6$^{F/F;TnTCre}$* mice, which have an average cardiomyocyte area of 400μm in the LV (Figure 7.14.G) and 375μm in the RV (Figure 7.14.H), it can be seen that vitamin supplemented *Slc5a6$^{F/F;TnTCre}$* mice have smaller cardiomyocytes in both ventricles at a more advanced age. This also suggests that vitamin supplementation is potentially delaying the progression of cardiomyopathy in *Slc5a6$^{F/F;TnTCre}$* mice; however, the *n* should to be increased to enable application of statistical tests to the vitamin supplemented dataset.

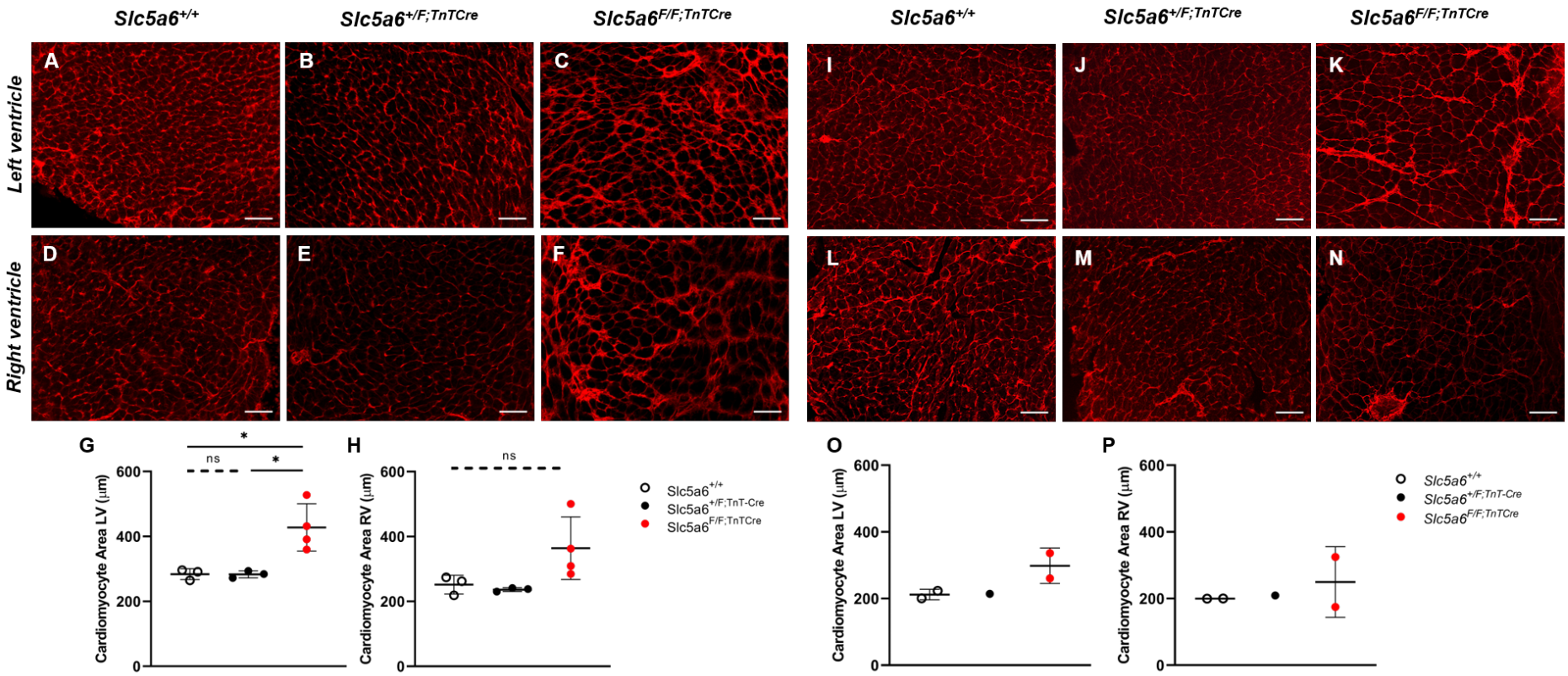

Figure 7.14. WGA staining and quantification of non-vitamin supplemented and vitamin supplemented *Slc5a6^{TnTCre}* mice. A-H) Representative WGA staining and cardiomyocyte area measurements for non-vitamin supplemented *Slc5a6^{TnTCre}* mice at 14 weeks (Figure 6.21). I-P) WGA staining and quantification of vitamin supplemented *Slc5a6^{TnTCre}* mice at 20 weeks. Representative images are shown for the LV and RV of *Slc5a6$^{+/+}$* (I,L), *Slc5a6$^{+/F;TnTCre}$* (J,M) and *Slc5a6$^{F/F;TnTCre}$* (K,N) mice. Cardiomyocyte area measurements are shown for the LV (O) and RV (P) of *Slc5a6$^{+/+}$* (white), *Slc5a6$^{+/F;TnTCre}$* (black) and *Slc5a6$^{F/F;TnTCre}$* (red) mice. 14 weeks *n* = 3 *Slc5a6$^{+/+}$*, 3 *Slc5a6$^{+/F;TnTCre}$* and 4 *Slc5a6$^{F/F;TnTCre}$*, 20 weeks *n* = 2 *Slc5a6$^{+/+}$*(1440 LV cardiomyocytes and RV cardiomyocytes) 1 *Slc5a6$^{+/F;TnTCre}$* (720 LV cardiomyocytes and RV cardiomyocytes) and 2 *Slc5a6$^{F/F;TnTCre}$* mice (1440 LV cardiomyocytes and RV cardiomyocytes). A-F, I-N scale bar = 50 µm.

7.3 Discussion

This chapter aimed to present the initial data from the investigation into the effect of biotin and PA supplementation on the development of cardiomyopathy in *Slc5a6*^{TnTCre} mice. Due to low *n* the vitamin supplemented data was qualitatively compared to age-matched non-vitamin supplemented *Slc5a6*^{TnTCre} mice previously analysed. ECG analysis of vitamin supplemented *Slc5a6*$^{F/F;TnTCre}$ mice suggested a comparable decrease in conduction at 8 weeks as observed in non-vitamin supplemented mice; however, these changes appear to recover in vitamin supplemented *Slc5a6*$^{F/F;TnTCre}$ mice at 14 weeks. Interestingly, cardiac conduction was too severe for quantification in non-vitamin supplemented *Slc5a6*$^{F/F;TnTCre}$ mice at 18 weeks; however, in vitamin supplemented mice, conduction at 18 weeks appears to be maintained from 14 week data. Cardiac histology at 20 weeks showed evidence of slight cardiac remodelling in vitamin supplemented *Slc5a6*$^{F/F;TnTCre}$ mice compared to the extent of cardiac phenotype observed in their non-vitamin supplemented counterparts at 14 weeks. From the pilot data shown in this chapter, it is possible to suggest that vitamin supplementation in *Slc5a6*$^{F/F;TnTCre}$ mice may have a beneficial effect on the development of pathological cardiac features as observed in non-supplemented *Slc5a6*$^{F/F;TnTCre}$ mice.

The initial hypothesis that vitamin supplementation may have an effect on the phenotype of cardiomyocyte specific *Slc5a6* knockout mice, was prompted from a study reported by Sabui *et al.* (2018). Here, they provided biotin and PA to their intestinal specific *Slc5a6* knockout mouse model, and found a complete reversal of the disease phenotype which included severe inflammation, altered gut permeability and growth retardation leading to premature death (Ghosal *et al.*, 2012). In addition, clinical reports of the success of biotin, PA and LA supplementation in patients with deleterious mutations in *SLC5A6* also provided the framework for considering a vitamin supplementation study on *Slc5a6*^{TnTCre} mice. A report by Subramanian *et al.* (2017) described vast clinical improvement in a boy with neurological and growth defects (Table 4.2) following oral supplementation. Following this publication, additional case studies have reported the success of treating patients with SLC5A6 mutations with biotin, PA and LA via various administration routes. Although the precise effect on Slc5a6 protein synthesis and function in *Slc5a6*^{TnTCre} mice has yet to be fully established and confirmed, it is possible that i) the protein has been degraded by non-

sense mediated decay or is a non-functional truncated protein, ii) a truncated protein is formed which retains partial functionality, In the former scenario where Slc5a6 is not present/functional only within the cardiomyocyte population, vitamins supplemented may, as previously described, passively diffuse through the plasma membrane of cardiomyocytes bypassing entry into the cell by the absent/non-functional Slc5a6. o Although the cardiomyopathy phenotype is not completely rescued in vitamin supplemented *Slc5a6*$^{F/F;TnTCre}$ mice, this data does show a delay in the progression of cardiomyopathy. This is apparent in the longitudinal ECG analysis of vitamin supplemented mice. In their non-vitamin supplemented counterparts, *Slc5a6*$^{F/F;TnTCre}$ mice show depolarisation changes as early as 5 weeks, whereas the cardiac conduction cycle in vitamin supplemented *Slc5a6*$^{F/F;TnTCre}$ mice is not altered until 8 weeks. This suggests that vitamin supplementation throughout development and postnatally has potentially delayed the onset of conduction defects due to cardiomyopathy within the *Slc5a6* cardiomyocyte knockout mice. Interestingly, at 14 weeks repolarisation of the ventricles improves in vitamin supplemented *Slc5a6*$^{F/F;TnTCre}$ mice and is maintained up to 18 weeks. This provides evidence that the cardiac phenotype is less severe in *Slc5a6*$^{F/F;TnTCre}$ with vitamin supplementation at 18 weeks, as the ECGs recorded in the non-vitamin supplemented counterparts at the same age were too severe to perform analysis. Although there are no published studies which investigate the effect of biotin and PA supplementation on the heart, patients with *SLC5A6* mutations presenting with severe growth and brain abnormalities (without cardiac involvement) have responded extremely well to vitamin supplementation throughout life. In all reported cases, normal growth resumed, and developmental milestones were reached (Subramanian *et al.*, 2017; Byrne *et al.*, 2019; Schwantje *et al.*, 2019). This suggests that prolonged vitamin supplementation of *Slc5a6*$^{F/F;TnTCre}$ mice may correct or maintain sufficient cardiac function throughout life. However, further studies to examine the effect of vitamin supplementation after 20 weeks are needed to fully investigate this hypothesis.

The evidence of cardiac remodelling in vitamin supplemented mice at 20 weeks suggests cardiomyopathy is present. This includes slight ventricular dilation shown by H&E as well as increased interstitial fibrosis between cardiomyocytes and cardiomyocyte hypertrophy in vitamin supplemented *Slc5a6*$^{F/F;TnTCre}$ mice which are absent in littermate controls. However, when compared to histological analysis performed on non-vitamin supplemented *Slc5a6*$^{F/F;TnTCre}$ mice at 14 weeks the

phenotype is less severe in vitamin supplemented mice 6 weeks older. Strongly suggesting that the progression of cardiomyopathy has been delayed in *Slc5a6*$^{F/F;TnTCre}$ given vitamin supplementation. This is likely due to the maintained supply and availability of biotin and PA for energy metabolism within the cardiomyocytes in the absence of SMVT.

Due to the COVID-19 pandemic, the effect of vitamin supplementation on the expression of mitochondrial OXPHOS complexes, and mitochondrial morphology remains to be established. Previous work performed on *Slc5a6*^{TnTCre} mice investigated the ultrastructure of cardiomyocytes and showed marked changes in mitochondrial morphology of *Slc5a6*$^{F/F;TnTCre}$ mice by EM. To assess the effect of vitamin supplementation on mitochondrial morphology, TEM analysis should be performed to assess any changes to the mitochondria. In addition to TEM, SBF-SEM could be performed to 3D reconstruct the cardiac myofibres to investigate morphological changes. This tool could also be used to calculate volumetric data to quantify any changes observed to mitochondrial morphology as demonstrated by Faitg *et al.* (2020). Additional investigation into the effect of vitamin supplementation on complexes involved in OXPHOS should be undertaken. As discussed in section 6.5, *Slc5a6*$^{F/F;TnTCre}$ mice show a marked reduction in CIV expression compared to littermate controls. It is hypothesised that providing excess amounts of biotin and PA should increase bioavailability of these substrates intracellularly by passive diffusion and therefore, help to maintain the cellular processes which are required for energy metabolism, including sufficient generation of intermediates from the TCA for production heme, which would then be used in the assembly of CIV of OXPHOS (Figure 7.15). As similarly discussed in chapter 6.5, heme synthesis could also be assessed in the vitamin supplemented *Slc5a6*$^{F/F;TnTCre}$ mice to establish any beneficial effect of vitamin supplementation.

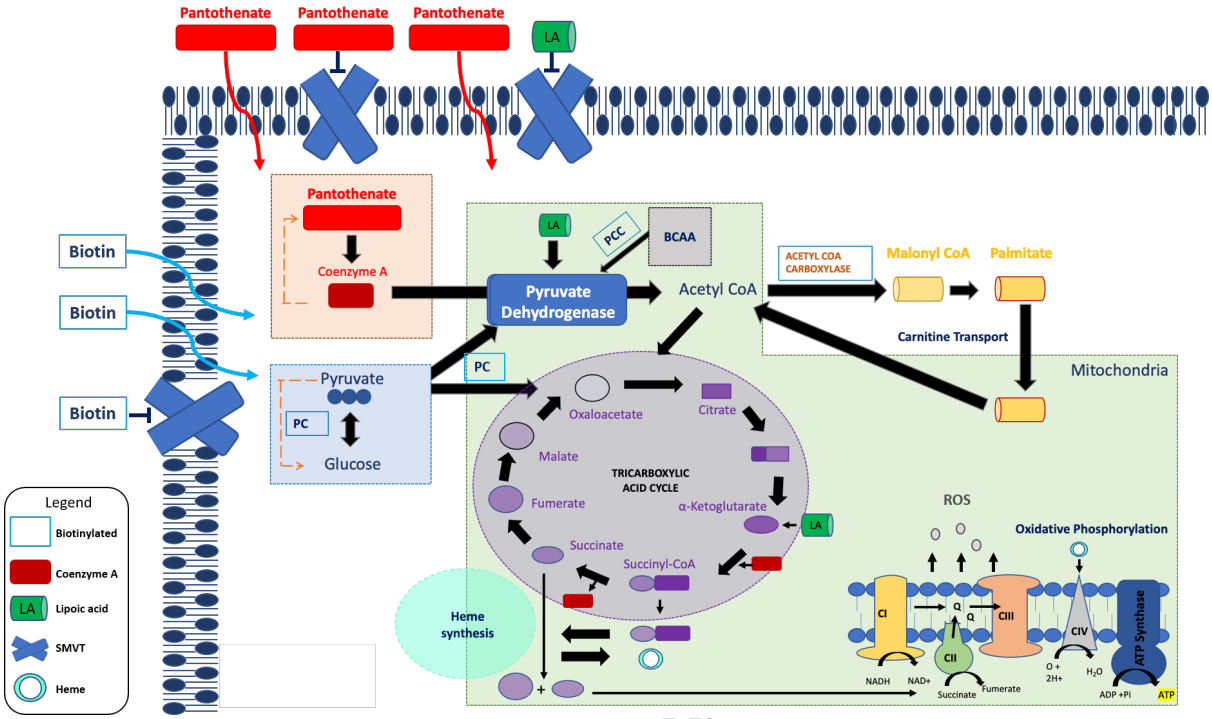

Figure 7.15. Hypothesis of providing *Slc5a6*^{TnTCre} mice with biotin and PA vitamin supplementation on energy metabolism pathways.
Modified from Figure 6.29. Providing mice with excess amounts of biotin and PA would increase the availability of both vitamin substrates to be passively diffused across the plasma membrane. This would then provide energy metabolism pathways including glycolysis, coenzyme A synthesis and TCA cycle with the intermediates required to produce ATP by OXPHOS.

Chapter 8 General discussion and future directions

8.1 Summary of findings and future directions

Heart disease is a leading cause of death, annually accounting for ~18 million deaths around the world. One of the most common forms of heart disease is cardiomyopathy, defined as a disease of the myocardium, with DCM characterised as dilation of the ventricle wall, resulting in poor cardiac function. DCM is commonly diagnosed as a result of systolic dysfunction by ECG, echocardiography or cardiac MRI in patients. There are currently no treatments for DCM, and as such many patients require transplantation or risk death. Siblings from a consanguineous family were diagnosed with DCM; the eldest sibling died at 2 years of age, while the second sibling survived infancy before presenting with poor cardiac output, leading to heart transplantation. WES was performed on both affected siblings and no pathogenic mutations were found in known DCM genes; however, a homozygous missense mutation in *SLC5A6* was identified and suggested as a novel candidate gene potentially causing DCM within the siblings. *In silico* analysis of the mutation predicted the amino acid substitution to be deleterious and disease causing, as well as being novel within the control population. *SLC5A6* encodes the sodium multi-vitamin transporter (SMVT) located at the plasma membrane, and is responsible for the transport of three substrates essential for energy metabolism and homeostasis; biotin, pantothenic acid (PA) and lipoic acid (LA) (Figure 8.1). It was hypothesised that the homozygous missense *SLC5A6* mutation identified in the affected siblings may reduce the functionality of the transporter to transport these substrates potentially leading to the development of DCM. The overall aim of this project was to understand the importance of *Slc5a6* in relation to the heart using genome editing technologies including CRISPR-Cas9 to insert the patient mutation into mice and, Cre-loxP to conditionally delete *Slc5a6* globally using *Sox2Cre* and within cardiomyocytes using *TnTCre* mouse lines.

.

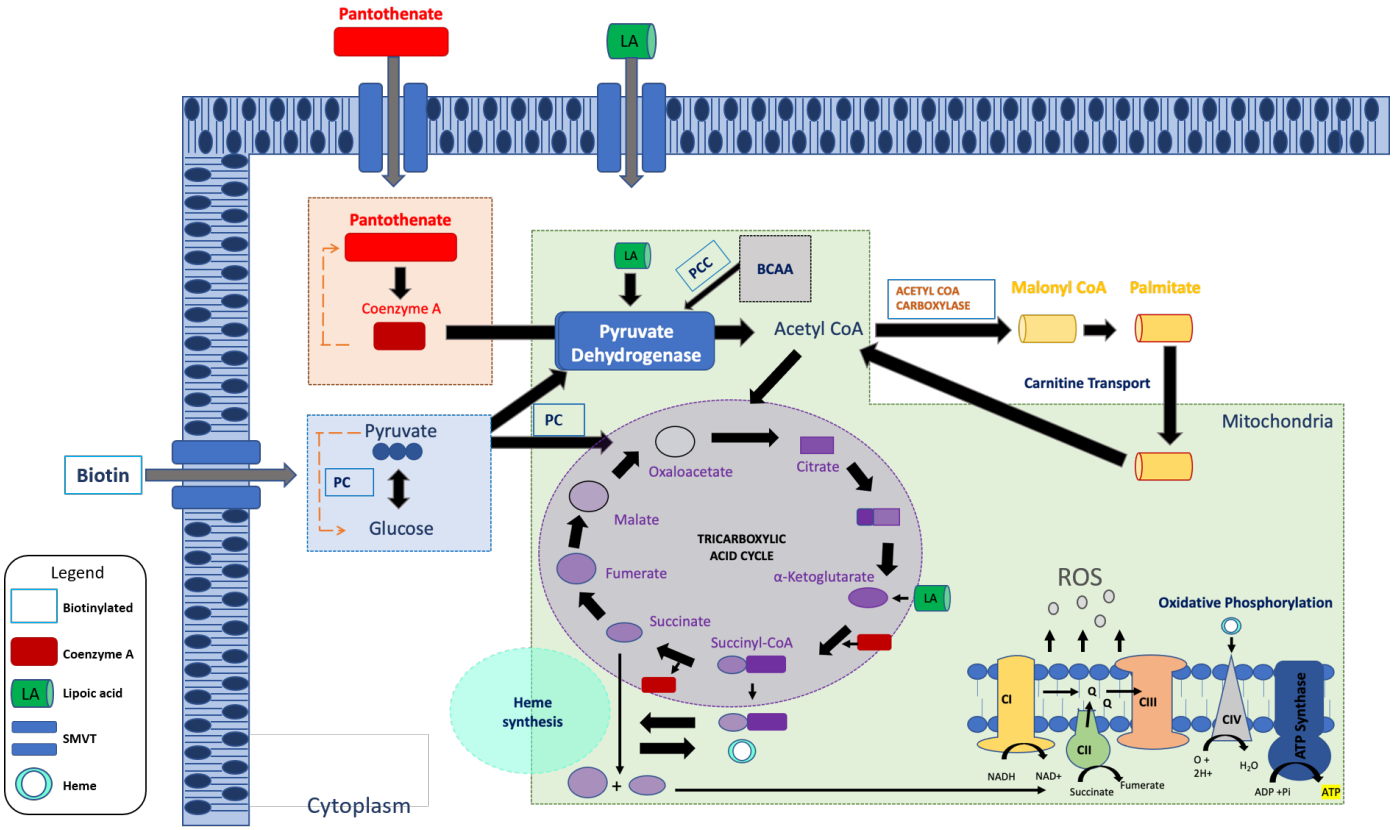

Figure 8.1. Transport of biotin, PA and LA into the cell by sodium-dependent multivitamin transporter.
Also shown in Figure 6.28. Biotin (blue box) once transported, is used for the biotinylation of pyruvate carboxylase (PC); involved in conversion of pyruvate to i) glucose (gluconeogenesis) ii) oxaloacetate (TCA), acetyl CoA carboxylase; conversion of acetyl CoA to malonyl CoA, and propionyl-CoA carboxylase (PCC); conversion of branched chain amino acids (BCAA) to intermediates for acetyl CoA production. Pantothenate (red), once transported is converted to coenzyme A and used in the production of acetyl CoA by pyruvate dehydrogenase. Acetyl CoA is an important intermediate in the TCA cycle and in the formation of fatty acid palmitate. Lipoic acid (green), once transported is used in the pyruvate dehydrogenase complex for the generation of acetyl CoA and in α-ketoglutarate dehydrogenase complex for the generation of succinyl CoA, important for heme synthesis and generation of succinate, both of which are essential for oxidative phosphorylation (OXPHOS). OXPHOS uses these substrates to drive the electron transport chain generating ATP and a small amount of reactive oxygen species (ROS) as a by-product.

The hypothesis of generating the *Slc5a6*^{R252W} mouse line, was that the alteration of the amino acid at 252 would result in altered vitamin transport by the Slc5a6 protein. Interestingly, work performed by Ghosal and Said (2011) investigated the effect of altering several histidines throughout Slc5a6, including H254, in ARPE19 cells on carrier-mediated biotin uptake. Their data showed that only H254 and H115 alterations caused a significant inhibition of biotin uptake within the cells, with a significant decrease in the maximal uptake rate (Vmax), suggesting the mutations severely affected Slc5a6 protein function. However, the binding affinity (Km) of the transporter was not affected, it is suggested that the Vmax and Km data may indicate a decrease in the number of Slc5a6 transporters at the plasma membrane. As the targeted mutation investigated in this study is the adjacent, highly conserved, amino acid to H254, the effect on the protein function is predicted to be the same, however carrier-mediated biotin uptake studies should be performed within a suitable cell line in order to confirm this hypothesis, in addition to IF to localise Slc5a6 cellular expression, should a suitable Slc5a6 antibody become available, compatible with mouse sections. The investigation using the *Slc5a6*^{R252W} mouse line, revealed *Slc5a6*$^{R252W/R252W}$ mice survived embryogenesis into early adulthood; however, sudden death occurred at 6.5 weeks without cardiac involvement. To eliminate any off-target effects affecting the CRISPR-Cas9 generated mice, *Slc5a6*$^{+/R252W}$ mice were backcrossed to C57BL/6N mice for four generations (F4). F4 *Slc5a6*$^{R252W/R252W}$ mice survived embryogenesis but died during the first week of life from an unidentified cause. Ultrastructural analysis at P0 showed mitochondrial abnormalities including cristae defects in F4 *Slc5a6*$^{R252W/R252W}$ hearts, suggesting the R252W mutation has affected mitochondrial structure which may relate to cause of death within these mice. However, further work is needed to characterise perinatal death within this mouse line. Additionally, the effect of the R252W mutation on the protein transporter's ability to contribute to Na^+ flux should be considered. It is hypothesised that the amino acid substitution has the potential to directly affect the transporter's ability to actively transport substrates across the plasma membrane via the LeuT fold. Therefore, Na^+ influx would be altered depending on the functionality of Slc5a6. Intracellular Na^+ levels are key to the modulation of contractility within the heart and therefore changes to the concentration of Na^+ by dysfunctional Slc5a6 may have a detrimental effect on the cardiac conduction of cardiomyocytes (Bers *et al.*, 2003; Despa and Bers, 2013). As previously discussed in section 6.5, an increase in intracellular Na^+ has been identified in both human and

guinea pig models of HCM. Additionally, high intracellular Na^+ is also observed in models of HF where Na^+ transporter imbalance has been implicated in the development of contractile dysfunction leading to the development of mitochondrial abnormalities and ultimately HF (Despa *et al.*, 2002; Despa and Bers, 2013; Aksentijević and Shattock, 2021). To investigate the effect of the mutated transporter on intracellular Na^+ flux, primary cardiomyocytes could be isolated from wild type and mutated Slc5a6 mice and for real time confocal imaging of Na^+ flux as described by Lee *et al.* (2016). Here, they describe the protocol for utilising CoroNa Green, which is a fluorescent dye to allow measurement of intracellular Na^+ in intact live cells.

Similarly to F4 *Slc5a6*$^{R252W/R252W}$ mice, the conditional global Slc5a6 knockout mice (*Slc5a6*$^{F/F;Sox2Cre}$) survived embryogenesis with normal heart development noted, but died following birth. It could be hypothesised that physiological changes which occur following birth, such as breathing, feeding or energy metabolism are affected by the global loss of Slc5a6. Ultrastructural analysis revealed gross structural abnormalities in *Slc5a6*$^{F/F;Sox2Cre}$ hearts at P0, including severe mitochondrial degradation and possible mitophagy, suggesting that loss of Slc5a6 is affecting mitochondrial structure which will negatively impact cardiac energy metabolism. Histological analysis needs to be performed on hearts collected at P0 to correlate changes at the ultrastructural level with any changes to the overall cardiac structure. The deletion of Slc5a6 with cardiomyocytes (*Slc5a6*$^{F/F;TnTCre}$) did not affect cardiac development; however, *Slc5a6*$^{F/F;TnTCre}$ suddenly died in adulthood (26 weeks), with clear ventricular dilation and increased myocardial fibrosis, suggestive of DCM. Functional and histological analysis of *Slc5a6*$^{F/F;TnTCre}$ mice at 14 and 20 weeks, revealed cardiac structural abnormalities and dysfunction, with ultrastructural changes observed within the mitochondria (Figure 8.2). From this data, it was suggested that the removal of Slc5a6 within the cardiomyocytes decreases CIV expression, which may affect energy metabolism resulting in mitochondrial structural abnormalities noted in *Slc5a6*$^{F/F;TnTCre}$ cardiomyocytes. A reduction in the functional capacity of mitochondria to produce energy may cause cardiac stress, resulting in conduction abnormalities as observed in *Slc5a6*$^{F/F;TnTCre}$ mice. These abnormalities would cause the heart to undergo pathological remodelling, compensating for reduced energy production by increasing myocardial mass by cardiomyocyte hypertrophy and would prompt an increase in the production of interstitial fibrosis. The increase in fibrosis would further contribute to cardiac dysfunction by reducing the ability of the myocardial wall to contract through

alteration of the action potentials of the conductive cells causing reduced SV, CO and EF. Together, these functional and structural changes are suggestive of DCM, suggesting the deletion of *Slc5a6* within cardiomyocytes may recapitulate the patients DCM phenotype.

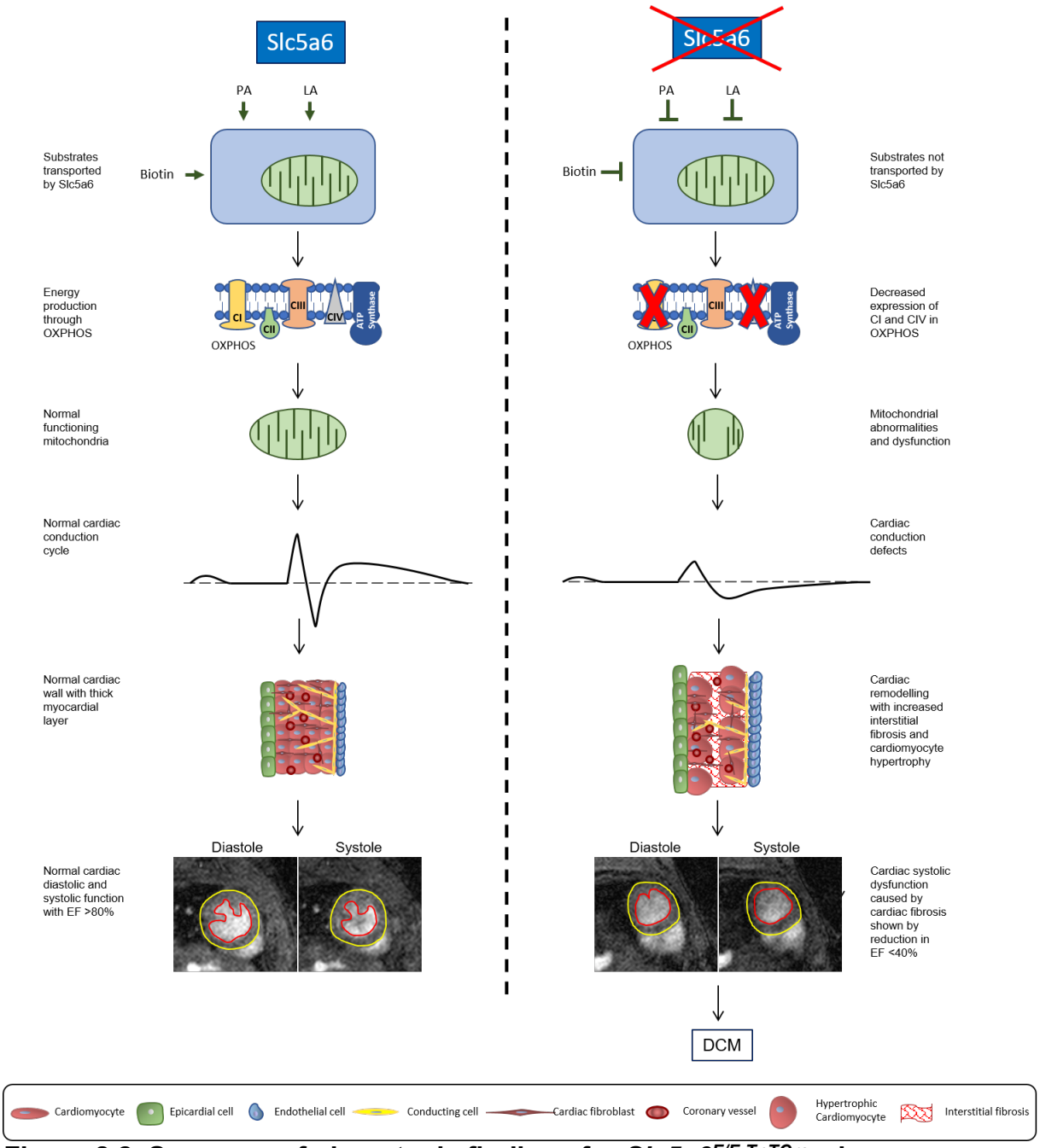

Figure 8.2. Summary of phenotypic findings for *Slc5a6*$^{F/F;TnTCre}$ mice.
When Slc5a6 is expressed, transport of biotin, PA and LA is facilitated into the cell and used to generate intermediates for energy metabolism with ATP produced by OXPHOS on the inner mitochondrial membrane. With the energy demand of the heart met by normal functioning mitochondria, normal cardiac conduction occurs with the electrical impulse travelling through the compact myocardium resulting in ventricular contraction to move blood throughout the body. In *Slc5a6*$^{F/F;TnTCre}$ mice, Slc5a6 is deleted in cardiomyocytes resulting in a reduction in the transport of vitamins into the cell. The lack of bioavailability of each substrate affects multiple processes within energy metabolism including the reduction in CI and CIV of OXPHOS previously shown. This has a detrimental effect on the structure of the mitochondria causing mitochondrial dysfunction and degradation. Mass mitochondrial dysfunction would affect energy production within the cell affecting the cells' ability to contract, which would result in conduction abnormalities as seen by lengthening of PR interval, widening of QRS and LV strain pattern by ECG. These abnormalities stress the heart

triggering pathological remodelling to compensate for reduced cardiac function causing an increase in interstitial fibrosis which was characterised by histological staining and CMR imaging. Together these changes are associated with DCM, as observed in both *SLC5A6* patients.

The final aim was to investigate the potential for vitamin supplementation as a treatment for cardiomyopathy. From this experiment, it was suggested that vitamin treatment in *Slc5a6*$^{F/F;TnTCre}$ mice delayed the progression of DCM within the model, with preserved cardiac structure and function at 20 weeks when compared to non-vitamin treated *Slc5a6*$^{F/F;TnTCre}$ mice at 14 weeks. It was also shown that expression of complex IV was increased in *Slc5a6*$^{F/F;TnTCre}$ cardiomyocytes compared to non-vitamin treated mice. This suggests vitamin supplementation facilitated sufficient substrate diffusion into the cell to enable and maintain energy metabolism. However, further investigation into the pathomechanism is needed to confirm this hypothesis.

8.1.1 Slc5a6 is important for postnatal survival

Mutations in *SLC5A6* were identified as a potential cause of cardiomyopathy within siblings affected by DCM; however, there is very little known about the expression of Slc5a6 within the heart. Studies by Prasad *et al.* (1998) and Wang *et al.* (1999a) first reported *Slc5a6* expression in rat and human tissues by Northern blot, showing faint expression of *Slc5a6* within the mammalian heart. This project confirmed expression of Slc5a6 within the heart as well as the brain and the gut during human development, as well as showing *Slc5a6* expression within the developing murine heart. It was hypothesised that Slc5a6 may play a role in the developing heart; however, when Slc5a6 was globally mutated (*Slc5a6*$^{R252W/R252W}$) or conditionally deleted (*Slc5a6*$^{F/F;Sox2Cre}$), embryos survived embryogenesis, and normal cardiac development was observed, suggesting that *Slc5a6* does not play a critical role in the development of the heart. There was; however, a loss of mutant *Slc5a6* pups following birth, suggesting the loss of *Slc5a6* affects postnatal survival. Turgeon and Meloche (2009) describe that during the first 24 hours following birth, three physiological processes are required for survival; respiratory capacity, energy metabolism and homeostasis, and suckling ability of the newborn. All *Slc5a6* mutants (*Slc5a6*$^{R252W/R252W}$ and *Slc5a6*$^{F/F;Sox2Cre}$) collected at P0 survived hours after birth and had milk spots present, suggesting that pups were capable of suckling and had the ability to breathe. From this, it was hypothesised energy metabolism may play a role in the postnatal death of mutant *Slc5a6* pups. Birth is an important process in energy metabolism; as oxygen

availability increases, metabolism shifts from glycolysis to OXPHOS in response to the increase in energy demand (Breckenridge *et al.*, 2013; Kolwicz *et al.*, 2013; de Carvalho *et al.*, 2017; Cerychova and Pavlinkova, 2018). As *Slc5a6* transports essential substrates vital for the contribution of intermediates for energy metabolism, it is possible that the global alteration of *Slc5a6* (*Slc5a6*$^{R252W/R252W}$ and *Slc5a6*$^{F/F;Sox2Cre}$) within newborn pups is severely affecting this process, which is essential for postnatal survival. Further investigation into the expression of genes involved in the metabolic switch, such as *Hif1a* and *PGC1a,* should be undertaken in late embryonic and postnatal *Slc5a6* mutants to help to understand the underlying cause of perinatal death.

Death in early adulthood was noted in F1 *Slc5a6*$^{R252W/R252W}$ mice without apparent cardiac involvement; however, a decrease in body weight was also observed. Previous studies by Ghosal *et al.* (2012) described a similar occurrence of sudden death in an intestinal specific knockout of *Slc5a6* similar to the F1 *Slc5a6*$^{R252W/R252W}$ mouse model. This suggests that the decline in weight gain may be related to the dysfunction of Slc5a6 within the intestinal tract, as biotin, PA and LA may not be absorbed in sufficient levels to maintain energy homeostasis. To bypass the effect of the removing Slc5a6 within the intestine and other organs which may preclude the development of cardiomyopathy, Slc5a6 was conditionally deleted within the cardiomyocytes. *Slc5a6*$^{F/F;TnTCre}$ mice survived embryogenesis without any cardiac abnormalities and survived postnatally with no decline in body weight observed. However, sudden death occurred at 26 weeks with a strong cardiac phenotype including ventricular dilation and an increase in interstitial fibrosis observed throughout the myocardium. Together this suggests that vitamin absorption at the intestinal tract is vital, and, when Slc5a6 is expressed normally within the heart, vitamin absorption is important to maintain normal cardiac structure and function. Therefore, investigation into vitamin uptake within cardiomyocytes, intestinal epithelial cells and hepatocytes would be important to determine the amount of biotin, PA and LA transported in F4 *Slc5a6*$^{R252W/R252W}$, *Slc5a6*$^{F/F;Sox2Cre}$ and *Slc5a6*$^{F/F;TnTCre}$ primary cells. Previously, Prasad *et al.* (1997) characterised vitamin uptake by SMVT using radioactively labelled substrates to determine uptake in human placental cells. Alternatively, fluorescently labelled substrates, such Atto-Biotin (Sigma) could be added to cultured cells to quantify uptake across the plasma membrane.

8.1.2 Slc5a6 is required for normal cardiac function

In this project it has been shown that deleting *Slc5a6* specifically within cardiomyocytes (*Slc5a6*$^{F/F;TnTCre}$) did not affect cardiac development or survival of pups postnatally. However, it has been shown that cardiac conduction and function progressively declines in adult hearts of *Slc5a6*$^{F/F;TnTCre}$ mice. This was initially observed by changes to ventricular repolarisation at 5 weeks by ECG which progressed to signs of atrioventricular block, myocardial fibrosis and LV strain pattern, all well-known markers of cardiomyopathy both in mouse models and patients with cardiomyopathy (Wang *et al.*, 1999b; Elliott, 2000; Aoki *et al.*, 2005; Du *et al.*, 2007; Jefferies and Towbin, 2010; Sweet *et al.*, 2015; Mathew *et al.*, 2017). Additionally, CMR imaging showed reduced SV and CO, with significantly decreased EF <40% at 20 weeks. This is often associated with severe DCM as well as heart failure (Yilmaz *et al.*, 2008; Francone, 2014; Mathew *et al.*, 2017). However, it is worth discussing the differences in electrophysiology between mice and humans. One startling difference between species is the HR, the mouse HR is ~ 10x faster than human, this is due to the lack of plateau in the mouse action potential resulting in a shorter duration of the action potential compared to humans (Ahrens-Nicklas and Christini, 2009). These differences in action potentials prove challenging when attempting to translate cardiac conduction defects in mouse to pathological changes in human patients (Boukens *et al.*, 2014). To circumvent this, novel techniques have been developed to assess the electrophysiology of a single mouse cardiac cell and convert that behaviour into a human cardiac cell with the use of computational modelling called cell-type transforming clamp (Ahrens-Nicklas and Christini, 2009). Although this technique may not be possible within the Phillips/Bamforth research group, similar techniques should be considered as to aid in the translation of mouse ECG findings to human.

The functional features, supported by histological findings of cardiomyocyte hypertrophy and increased interstitial fibrosis suggests that removing *Slc5a6* within the heart results in the development of characteristic cardiac abnormalities associated with DCM (Figure 8.2). As previously discussed, *Slc5a6* is responsible for the transport of three essential substrates required in energy metabolism located within the mitochondria, therefore the study then focused on characterising the effect of removing *Slc5a6* on the mitochondria.

8.1.3 Loss of Slc5a6 results in mitochondrial defects

Mitochondrial homeostasis is essential to maintain life (Pizzorno, 2014). As previously described, mitochondrial morphology is vitally linked to their overall functional capacity, and therefore structural abnormalities can have a detrimental effect of the survival of the cell (Cogliati *et al.*, 2013). Mitochondrial dysfunction can occur for a number of reasons, including insufficient mitochondrial number, electron transport defects, or a reduction in substrate required for energy metabolism (Nicolson, 2014). The presence of dysfunctional mitochondria; however, can prompt activation of three processes to mitigate any detrimental effects on overall cell function; mitochondrial fusion, fission and mitophagy (Scott and Youle, 2010; Twig and Shirihai, 2011; Nicolson, 2014). When these regulatory mechanisms fail or are inundated with defective mitochondria, this can contribute to the pathophysiology of disease phenotypes including mitochondrial disease and cardiomyopathies (Chung and Kang, 2015; Vincent *et al.*, 2016). In all mouse models of *Slc5a6* described in this study, mitochondrial abnormalities have been identified within the heart including F4 *Slc5a6*$^{R252W/R252W}$, *Slc5a6*$^{F/F;Sox2Cre}$ and *Slc5a6*$^{F/F;TnTCre}$. Specifically, mitochondrial cristae fragmentation with increased mitochondrial degradation without autophagosome involvement in *Slc5a6*$^{F/F;Sox2Cre}$. These abnormalities are suggestive of unbalanced mitochondrial dynamics possibly due to metabolic insult leading to mitochondrial apoptosis and activation of the BAK-BAX pathway. To confirm this hypothesis, apoptosis could be investigated by either cleaved caspase3 IF to determine levels of activated apoptotic caspases in *Slc5a6* mutants compared to controls or TUNEL assay which detects apoptotic DNA fragmentation in tissue and cells (Martínez-Lagunas *et al.*, 2020).

As well as global *Slc5a6* knockouts (*Slc5a6*$^{F/F;Sox2Cre}$), cardiomyocyte-specific *Slc5a6* knockout mice (*Slc5a6*$^{F/F;TnTCre}$) also show mitochondrial abnormalities within cardiomyocytes. Cristae degradation and mitochondrial degradation is again noted; however, a marked increase in mitochondrial proliferation is observed in mice at 14 weeks. Increased mitochondrial proliferation has been previously described in mouse models such as *Ant1* knockout mice, which also show cardiomyocyte hypertrophy, and *Mfn2* knockout mice which show decreased mitochondrial size, reduced ATP production and increased ROS in DCM. It would therefore be of interest to investigate levels of ATP produced in *Slc5a6*$^{F/F;TnTCre}$ mice as well as oxygen consumption and ROS within the heart. To determine ATP levels, hearts can be perfused and ATP measured using NMR spectroscopy (Luptak *et al.*, 2018), alternatively ATP production

can also be determined using luciferin luminescence assay as described by Wang *et al.* (2017). To measure oxygen consumption rates within the heart a number of methodologies can be utilised, including *in situ* luminescence imaging fiber oxygen sensor measurements which determine oxygen consumption from perfused hearts (Zhao *et al.*, 1999) or Seahorse assay which can be used to measure oxygen consumption rate (OXPHOS) and extracellular acidification rate (glycolysis) from isolated cardiac mitochondria as described by Sakamuri *et al.* (2018). To determine ROS levels in *Slc5a6* knockout mice, Starkov (2010) describes a reliable fluorescence based assay which measures H_2O_2 from isolated mitochondria which could be utilised. From data shown in this project, it is hypothesised that the amount of observed disruption to mitochondria may have a negative impact upon energy production within the heart, resulting in abnormal cardiac function. Many mitochondrial defects reported in association with cardiomyopathies affect complexes within the electron transport chain, responsible for ATP generation via oxidative phosphorylation (Meyers *et al.*, 2013; El-Hattab and Scaglia, 2016c). As severe abnormalities of cristae structure were identified within cardiac specific *Slc5a6* knockout hearts, investigation into the presence of OXPHOS complexes; I and IV was performed. It was shown that CIV of the ETC in OXPHOS was significantly reduced, providing evidence of an energy metabolism defect caused by loss of *Slc5a6* within the heart. Only two complexes were investigated in these mice, and therefore analysis should be expanded to include all complexes within the ETC including ATP synthase (CV). Western blot analysis could be performed using the total OXPHOS rodent antibody cocktail (abcam) which detects all 5 mitochondrial complexes in protein lysates which has been used by Visavadiya *et al.* (2021). Interestingly, this group also investigated mitochondrial proteins by proteomic analysis using a mitochondrial panel including proteins involved in mitochondrial dynamics and mitophagy, which may offer a more comprehensive analysis of mitochondrial status within *Slc5a6* cardiomyocyte-specific knockout hearts. From the data shown within this project, it is possible to hypothesise that the loss of *Slc5a6* may cause energy metabolism dysfunction which, when globally deleted (*Slc5a6*$^{F/F;Sox2Cre}$) results in perinatal death, and, when deleted only within cardiomyocytes (*Slc5a6*$^{F/F;TnTCre}$) causes cardiac dysfunction leading to DCM. Although further work is needed to unpick the mechanism in which energy metabolism defects occur, a mechanism can be hypothesised (Figure 8.3). Briefly, the loss of *Slc5a6* may result in a reduction of biotin, PA and LA across the plasma membrane. This could

result in decreased biotinylation of carboxylases involved in gluconeogenesis, oxaloacetate production, BCAA catabolism and FAS. Additionally, coenzyme A synthesis could not occur due to the lack of precursor PA, and therefore acetyl CoA would not be produced. Similarly, the lack of LA transport would also impact acetyl CoA synthesis as it plays a major role in the pyruvate dehydrogenase complex. Without acetyl CoA, the TCA cycle cannot generate intermediates, including NADH and succinate, which are essential for OXPHOS and succinyl CoA utilised in heme synthesis this is required for the assembly of CIV of the ETC within OXPHOS. Together these changes could have a detrimental effect of the amount of ATP produced from OXPHOS, as well as the negative effect of increased ROS levels within the cell, which may contribute to the development of DCM and ultimately death within our mouse models. To further investigate this mechanism, biochemical assays could be used to measure ATP production, in addition to determining the activity of key complexes within energy metabolism where each of the three substrates are required; pyruvate dehydrogenase (PDH) and α-ketoglutarate dehydrogenase (αKGDH) complex. Interestingly, a study by Ke *et al.* (2014) describes a new accurate measurement of PDH complex using phenazine methosulfate-3-(4,5-dimethylthiazol-2-yl)-2,5-diphenyltetrazolium bromide (PMS–MTT) compared to previously published methods, and uses spectrophotometry to determine PDH activity. Alternatively, commercially produced assay kits are available which simplify the quantification of PDH and αKGDH activity by offering colorimetric quantification by plate reader (abcam). Investigation of heme status and levels of ROS within *Slc5a6*$^{F/F;TnTCre}$ mice could be performed. An indicator of heme status which can be measured using a fluorometric assay, is succinyl-CoA, which is involved in the production of porphyrins, a heme synthesis intermediate (Atamna *et al.*, 2007; Tretter *et al.*, 2016). Smith *et al.* (1973) describe a methodology for detecting succinyl CoA levels in mitochondrial isolations from rat heart and liver which may be of interest when attempting to unpick the pathomechanism in *Slc5a6* mutants. If succinyl-CoA levels are decreased in *Slc5a6*$^{F/F;TnTCre}$, *Slc5a6*$^{F/F;Sox2Cre}$ or *Slc5a6*$^{R252W/R252W}$, it suggests that heme synthesis is also decreased, further confirming the hypothesis that mice without functional Slc5a6 cannot generate the energy metabolism intermediates needed throughout the energy metabolism pathways, as well as in the formation of mitochondrial complexes to produce energy for the cell.

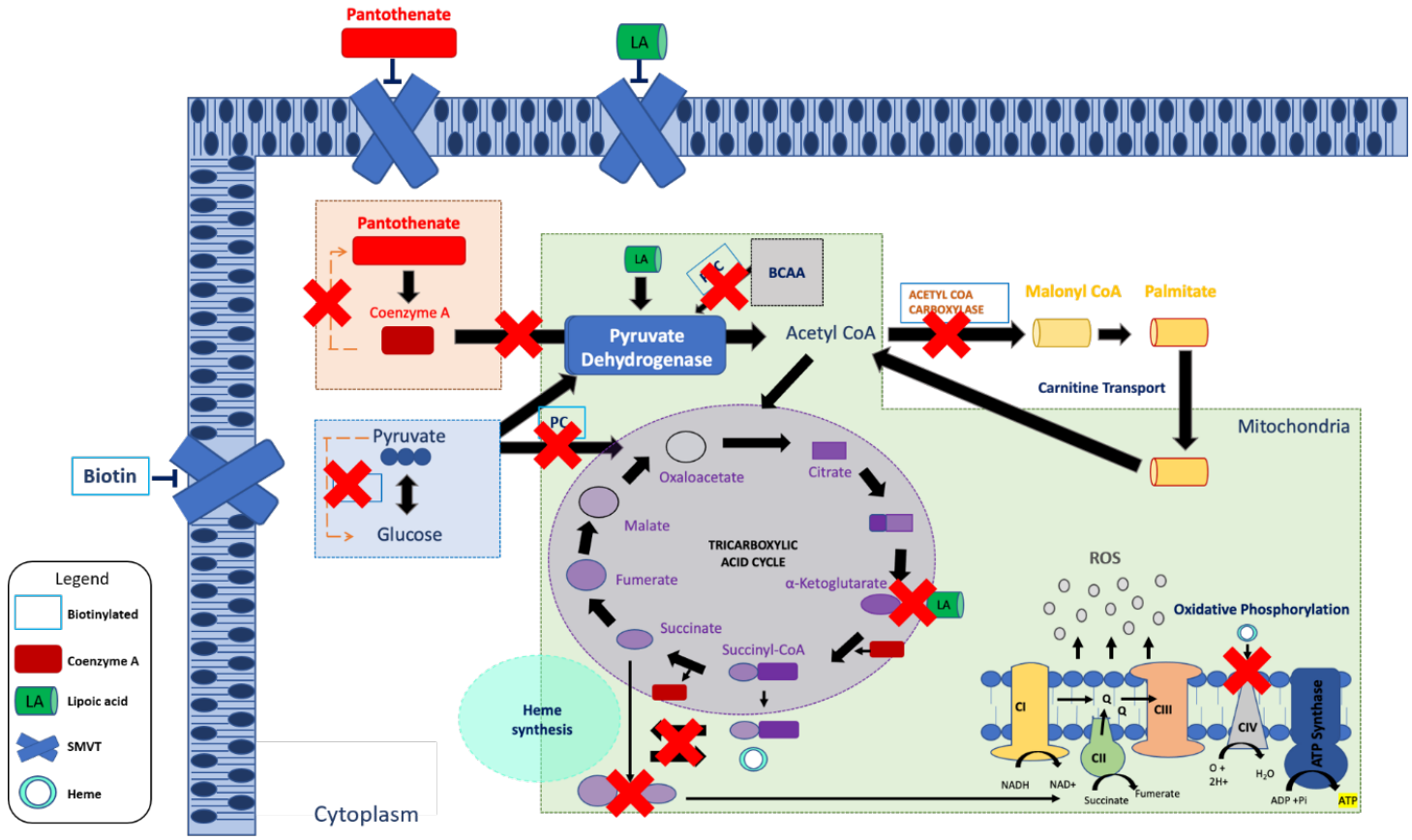

Figure 8.3. Hypothesised mechanism of disrupted vitamin transport by loss of Slc5a6.
Also shown in Figure 6.29. The loss of Slc5a6 (SMVT) could severely reduce biotin, PA (pantothenate) and LA transport. Reduction in the bioavailability of these substrates could affect i) biotinylation of carboxylases involved in gluconeogenesis, oxaloacetate generation, BCAA conversion and fatty acid synthesis. ii) coenzyme A synthesis which is essential for the generation of acetyl CoA involved in FAS and the TCA cycle, as well as the formation of succinyl CoA. iii) The function of PDH and αKGDH complexes which require LA, and intermediates produced using biotin and PA. Together these affected processes may have a detrimental effect on the production of essential intermediates generated by the TCA cycle which are required for generation of NADH and succinate for OXPHOS and heme synthesis; essential for CIV, without which oxygen cannot be reduced to water causing an increase in ROS generation and a decrease in ATP production.

8.1.4 Vitamin supplementation shows promise in delaying DCM phenotype

It is well known that a small amount of substrate, ie. vitamins, can passively diffuse across the plasma membrane (Cooper, 2000b). Therefore, it was hypothesised that vitamin supplementation may influence the phenotype of cardiomyocyte-specific *Slc5a6* knockout (*Slc5a6*$^{F/F;TnTCre}$) mice. This work was prompted by a study reported by Sabui *et al.* (2018) where they provided biotin and PA to their intestinal-specific *Slc5a6* knockout mouse model, and found a complete reversal of the disease phenotype described by Ghosal *et al.* (2012). Although the cardiomyopathy phenotype is not completely rescued in vitamin supplemented *Slc5a6*$^{F/F;TnTCre}$ mice, we do observe a delay in the progression of cardiomyopathy.

Non-vitamin supplemented *Slc5a6*$^{F/F;TnTCre}$ mice show depolarisation changes at 5 weeks, whereas the vitamin supplemented *Slc5a6*$^{F/F;TnTCre}$ mice do not appear to have altered conduction until 8 weeks. This suggests that vitamin supplementation throughout development and postnatally may have a positive effect on the development of conduction defects within *Slc5a6*$^{F/F;TnTCre}$ mice. Although there are no published studies which investigate the effect of biotin and PA supplementation on the heart, other studies have shown the importance of vitamin supplementation in cardiomyopathies, including L-carnitine. L-carnitine plays an essential role in the transport of long chain fatty acids into the mitochondria, and therefore deficiency in this substrate results in cardiac and musculoskeletal dysfunction as well as the development of severe neurological defects. Treatment with L-carnitine supplementation; however, has been demonstrated to maintain cardiac function in ischemic canine models, shown by preserved LV systolic function compared to the non-supplemented group (Silverman *et al.*, 1985). Interestingly, a study by Schönekess *et al.* (1995) investigated the effect of carnitine supplementation on a rat model of cardiac hypertrophy, which showed a significant increase in ATP production and cardiac function; however, this was due to an increase in carbohydrate metabolism not FAS and β-oxidation. They hypothesise that this is due to activation of PDH to moderate the levels of coenzyme A to acetyl CoA, which adds further to the previous suggestion of investigating the activity of PDH in *Slc5a6* mutant mice.

Future work on vitamin supplementation should continue to characterise changes observed in the cardiac function and structure in vitamin supplemented *Slc5a6*$^{F/F;TnTCre}$ mice. Additionally, refinement of this vitamin supplementation study would be to provide vitamin supplementation to F4 *Slc5a6*^{R252W} pups to determine whether the over

supplementation of biotin, PA and LA would prevent perinatal death within this mouse line.

This project is based on a consanguineous family with two affected daughters with DCM. Unfortunately, the first child died of DCM at 2 years with the second child presenting with cardiac abnormalities at 9 months of age. With continued poor cardiac output, the second child received a cardiac transplant. Following transplantation, the child recovered well but still suffered from left-sided paralysis, absent seizures and developmental delay, potentially caused by the homozygous missense mutation in *SLC5A6.* The generation of the *Slc5a6*^{R252W} mouse model showed that postnatal *Slc5a6*$^{R252W/R252W}$ mice failed to gain weight and died, potentially due to nutritional insufficiency as a result of the mutation within the intestinal tract. Similarly, the patient also suffered from poor feeding and suspected intestinal tract abnormalities which resulted in the administration of intravenous TPN, and later the insertion of a nasogastric tube to help with feeding and nutritional intake. The characterisation of the cardiomyocyte-specific Slc5a6 knockout (*Slc5a6*$^{F/F;TnTCre}$) revealed mice recapitulated the patient's DCM phenotype. It was shown that *Slc5a6*$^{F/F;TnTCre}$ mice developed characteristic cardiac abnormalities associated with DCM including pathological remodelling, presence of widespread interstitial fibrosis and cardiomyocyte hypertrophy, as well as reduced cardiac function; two-fold decrease in EF (<40%), significantly decreased SV and CO, with conduction defects including atrioventricular block and LV strain pattern. This mouse model was then used to determine the effect of vitamin supplementation on the development of cardiomyopathy, and showed *Slc5a6*$^{F/F;TnTCre}$ still developed cardiac abnormalities; however, the progression of the disease was delayed. During the course of this project, discussions with the consultants in charge of the patients care resulted in the patient being administered biotin, PA and LA, and being monitored for signs of clinical improvement. Although the patient received a heart transplant, the outcome measures were to assess the effect of the treatment on the frequency of absent seizures and developmental delay. In the last year of the project the clinicians involved with patient follow up have reported that the patient now experiences fewer seizures and has improved attention span and engagement. The results from this work have shown a clear clinical impact and the importance of vitamin supplementation not only in patients with mutations in *SLC5A6,* but also for conditions which may affect the availability of biotin, PA and LA within the body.

8.2 Conclusion

The data presented in this thesis has shown the potential importance of sodium dependent multivitamin transport of biotin, PA and LA to both heart function indicated by cardiac specific knockout and postnatal survival demonstrated by the global modification of *Slc5a6.* This work has characterised the novel effect which is caused by loss of *Slc5a6* within the heart, suggestive as a phenotype similar to the patient DCM phenotype. Further study into the effect on mitochondrial complexes has suggested an essential role the three substrates play in maintaining energy metabolism and homeostasis in the production of intermediates for the ETC and mitochondrial complex assembly. Most importantly, the data within this thesis has shown the potential of vitamin supplementation to delay the progression of cardiomyopathy within cardiac specific *Slc5a6* knockout mice, which presents a novel treatment for future patients with DCM which is caused by mutations in *SLC5A6.*

References

(NICE), N.I.f.H.a.C.E. (2021) *Intravenous nutrition* [Online reference]. Available at: https://bnfc.nice.org.uk/treatment-summary/intravenous-nutrition.html#PHP187 (Accessed: 28th June 2021).

Abdulhag, U.N., Soiferman, D., Schueler-Furman, O., Miller, C., Shaag, A., Elpeleg, O., Edvardson, S. and Saada, A. (2015) 'Mitochondrial complex IV deficiency, caused by mutated COX6B1, is associated with encephalomyopathy, hydrocephalus and cardiomyopathy', *European journal of human genetics : EJHG*, 23(2), pp. 159-164.

Abu-Elheiga, L., Matzuk, M.M., Abo-Hashema, K.A.H. and Wakil, S.J. (2001) 'Continuous Fatty Acid Oxidation and Reduced Fat Storage in Mice Lacking Acetyl-CoA Carboxylase 2', *Science*, 291(5513), p. 2613.

Ahrens-Nicklas, R.C. and Christini, D.J. (2009) 'Anthropomorphizing the Mouse Cardiac Action Potential via a Novel Dynamic Clamp Method', *Biophysical Journal*, 97(10), pp. 2684-2692.

Aksentijević, D. and Shattock, M.J. (2021) 'With a grain of salt: Sodium elevation and metabolic remodelling in heart failure', *Journal of Molecular and Cellular Cardiology*, 161, pp. 106-115.

Aleksova, A., Merlo, M., Zecchin, M., Sabbadini, G., Barbati, G., Vitrella, G., Di Lenarda, A. and Sinagra, G. (2010) 'Impact of atrial fibrillation on outcome of patients with idiopathic dilated cardiomyopathy: data from the Heart Muscle Disease Registry of Trieste', *Clinical medicine & research*, 8(3-4), pp. 142-149.

Allard, M.F., Schönekess, B.O., Henning, S.L., English, D.R. and Lopaschuk, G.D. (1994) 'Contribution of oxidative metabolism and glycolysis to ATP production in hypertrophied hearts', *Am J Physiol*, 267(2 Pt 2), pp. H742-50.

Anderson, R.H., Yanni, J., Boyett, M.R., Chandler, N.J. and Dobrzynski, H. (2009) 'The anatomy of the cardiac conduction system', *Clinical Anatomy*, 22(1), pp. 99-113.

Andrés-Delgado, L. and Mercader, N. (2016) 'Interplay between cardiac function and heart development', *Biochimica et Biophysica Acta (BBA) - Molecular Cell Research*, 1863(7, Part B), pp. 1707-1716.

Aoki, J., Ikari, Y., Nakajima, H., Mori, M., Sugimoto, T., Hatori, M., Tanimoto, S., Amiya, E. and Hara, K. (2005) 'Clinical and pathologic characteristics of dilated cardiomyopathy in hemodialysis patients', *Kidney International*, 67(1), pp. 333-340.

Araujo, L.F., Siena, A.D.D., Plaça, J.R., Brotto, D.B., Barros, I.I., Muys, B.R., Biagi, C.A.O., Peronni, K.C., Sousa, J.F., Molfetta, G.A., West, L.C., West, A.P., Leopoldino, A.M., Espreafico, E.M. and Silva, W.A. (2018) 'Mitochondrial transcription factor A (TFAM) shapes metabolic and invasion gene signatures in melanoma', *Scientific Reports*, 8(1), p. 14190.

Ashrafian, H., Docherty, L., Leo, V., Towlson, C., Neilan, M., Steeples, V., Lygate, C.A., Hough, T., Townsend, S., Williams, D., Wells, S., Norris, D., Glyn-Jones, S., Land, J., Barbaric, I., Lalanne, Z., Denny, P., Szumska, D., Bhattacharya, S., Griffin, J.L., Hargreaves, I., Fernandez-Fuentes, N., Cheeseman, M., Watkins, H. and Dear, T.N. (2010) 'A mutation in the mitochondrial fission gene Dnm1l leads to cardiomyopathy', *PLoS genetics*, 6(6), pp. e1001000-e1001000.

Atamna, H. (2004) 'Heme, iron, and the mitochondrial decay of ageing', *Ageing Res Rev*, 3(3), pp. 303-18.

Atamna, H., Liu, J. and Ames, B.N. (2001) 'Heme deficiency selectively interrupts assembly of mitochondrial complex IV in human fibroblasts: revelance to aging', *J Biol Chem*, 276(51), pp. 48410-6.

Atamna, H., Newberry, J., Erlitzki, R., Schultz, C.S. and Ames, B.N. (2007) 'Biotin Deficiency Inhibits Heme Synthesis and Impairs Mitochondria in Human Lung Fibroblasts', *The Journal of Nutrition*, 137(1), pp. 25-30.
Azevedo, P.S., Polegato, B.F., Minicucci, M.F., Paiva, S.A.R. and Zornoff, L.A.M. (2016) 'Cardiac Remodeling: Concepts, Clinical Impact, Pathophysiological Mechanisms and Pharmacologic Treatment', *Arquivos brasileiros de cardiologia*, 106(1), pp. 62-69.
Báez-Saldaña, A. and Ortega, E. (2004) 'Biotin Deficiency Blocks Thymocyte Maturation, Accelerates Thymus Involution, and Decreases Nose-Rump Length in Mice', *The Journal of Nutrition*, 134(8), pp. 1970-1977.
Bailey, S.M., Udoh, U.S. and Young, M.E. (2014) 'CIRCADIAN REGULATION OF METABOLISM', *The Journal of endocrinology*, 222(2), pp. R75-R96.
Bartlett, K., Ghneim, H.K., Stirk, J.H., Dale, G. and Alberti, K.G.M.M. (1984) 'Pyruvate carboxylase deficiency', *Journal of Inherited Metabolic Disease*, 7(1), pp. 74-78.
Baur, B., Wick, H. and Baumgartner, E.R. (1990) 'Na(+)-dependent biotin transport into brush-border membrane vesicles from rat kidney', *American Journal of Physiology-Renal Physiology*, 258(4), pp. F840-F847.
Bean, W.B., Hodges, R.E. and Daum, K. (1955) 'Pantothenic acid deficiency induced in human subjects', *The Journal of clinical investigation*, 34(7, Part 1), pp. 1073-1084.
Berg JM, T.J., Stryer L. (2002a) 'Fatty Acids Are Synthesized and Degraded by Different Pathways', in *Biochemistry*. Freeman, WH. Available at: https://www.ncbi.nlm.nih.gov/books/NBK22554/.
Berg JM, T.J., Stryer L. (2002b) 'Oxidative Phosphorylation', in *Biochemistry*. 5 edn. New York: W H Freeman.
Berg JM, T.J., Stryer L. (2002c) 'The Transport of Molecules Across a Membrane May Be Active or Passive', in *Biochemistry*. Freeman W H Available at: https://www.ncbi.nlm.nih.gov/books/NBK22454/.
Berg, J.M., Tymoczko, J.L. and Stryer, L. (2007) *Biochemistry*. W. H. Freeman.
Bers, D.M., Barry, W.H. and Despa, S. (2003) 'Intracellular Na+ regulation in cardiac myocytes', *Cardiovascular Research*, 57(4), pp. 897-912.
Bhan, A.K. and Brody, C. (2001) 'Propionic Acidemia: A Rare Cause of Cardiomyopathy', *Congestive Heart Failure*, 7(4), pp. 218-222.
Bindels, R.J.M. and Wagner, C.A. (2014) 'Sodium-dependent transporters in health and disease—a special issue', *Pflügers Archiv - European Journal of Physiology*, 466(1), pp. 1-2.
Birling, M.-C., Herault, Y. and Pavlovic, G. (2017) 'Modeling human disease in rodents by CRISPR/Cas9 genome editing', *Mammalian genome : official journal of the International Mammalian Genome Society*, 28(7-8), pp. 291-301.
Boukens, B.J., Rivaud, M.R., Rentschler, S. and Coronel, R. (2014) 'Misinterpretation of the mouse ECG: 'musing the waves of Mus musculus'', *The Journal of physiology*, 592(21), pp. 4613-4626.
Brand, T. (2003) 'Heart development: molecular insights into cardiac specification and early morphogenesis', *Developmental Biology*, 258(1), pp. 1-19.
Breckenridge, R.A., Piotrowska, I., Ng, K.-E., Ragan, T.J., West, J.A., Kotecha, S., Towers, N., Bennett, M., Kienesberger, P.C., Smolenski, R.T., Siddall, H.K., Offer, J.L., Mocanu, M.M., Yelon, D.M., Dyck, J.R.B., Griffin, J.L., Abramov, A.Y., Gould, A.P. and Mohun, T.J. (2013) 'Hypoxic Regulation of Hand1 Controls the Fetal-Neonatal Switch in Cardiac Metabolism', *PLOS Biology*, 11(9), p. e1001666.
Brooks, G.A., Dubouchaud, H., Brown, M., Sicurello, J.P. and Butz, C.E. (1999) 'Role of mitochondrial lactate dehydrogenase and lactate oxidation in the intracellular lactate shuttle', *Proceedings of the National Academy of Sciences*, 96(3), p. 1129.

Brower, G.L. and Janicki, J.S. (2001) 'Contribution of ventricular remodeling to pathogenesis of heart failure in rats', *American Journal of Physiology-Heart and Circulatory Physiology*, 280(2), pp. H674-H683.
Burr, S.P., Costa, A.S., Grice, G.L., Timms, R.T., Lobb, I.T., Freisinger, P., Dodd, R.B., Dougan, G., Lehner, P.J., Frezza, C. and Nathan, J.A. (2016) 'Mitochondrial Protein Lipoylation and the 2-Oxoglutarate Dehydrogenase Complex Controls HIF1α Stability in Aerobic Conditions', *Cell Metab*, 24(5), pp. 740-752.
Byrne, A.B., Arts, P., Polyak, S.W., Feng, J., Schreiber, A.W., Kassahn, K.S., Hahn, C.N., Mordaunt, D.A., Fletcher, J.M., Lipsett, J., Bratkovic, D., Booker, G.W., Smith, N.J. and Scott, H.S. (2019) 'Identification and targeted management of a neurodegenerative disorder caused by biallelic mutations in SLC5A6', *npj Genomic Medicine*, 4(1), p. 28.
Cerychova, R. and Pavlinkova, G. (2018) 'HIF-1, Metabolism, and Diabetes in the Embryonic and Adult Heart', *Frontiers in endocrinology*, 9, pp. 460-460.
Chatterjee, N.S., Kumar, C.K., Ortiz, A., Rubin, S.A. and Said, H.M. (1999) 'Molecular mechanism of the intestinal biotin transport process', *American Journal of Physiology-Cell Physiology*, 277(4), pp. C605-C613.
Chen, H., Chomyn, A. and Chan, D.C. (2005) 'Disruption of fusion results in mitochondrial heterogeneity and dysfunction', *J Biol Chem*, 280(28), pp. 26185-92.
Chen, Y. and Dorn, G.W., 2nd (2013) 'PINK1-phosphorylated mitofusin 2 is a Parkin receptor for culling damaged mitochondria', *Science (New York, N.Y.)*, 340(6131), pp. 471-475.
Christoffels, V.M., Habets, P.E.M.H., Franco, D., Campione, M., de Jong, F., Lamers, W.H., Bao, Z.-Z., Palmer, S., Biben, C., Harvey, R.P. and Moorman, A.F.M. (2000) 'Chamber Formation and Morphogenesis in the Developing Mammalian Heart', *Developmental Biology*, 223(2), pp. 266-278.
Chung, Y.W. and Kang, S.-M. (2015) 'An experimental approach to study the function of mitochondria in cardiomyopathy', *BMB reports*, 48(10), pp. 541-548.
Cocks, E., Taggart, M., Rind, F. and White, K. (2018) *A guide to analysis and reconstruction of serial block face scanning electron microscopy data: A GUIDE TO ANALYSIS AND RECONSTRUCTION*.
Cogliati, S., Frezza, C., Soriano, M.E., Varanita, T., Quintana-Cabrera, R., Corrado, M., Cipolat, S., Costa, V., Casarin, A., Gomes, L.C., Perales-Clemente, E., Salviati, L., Fernandez-Silva, P., Enriquez, J.A. and Scorrano, L. (2013) 'Mitochondrial cristae shape determines respiratory chain supercomplexes assembly and respiratory efficiency', *Cell*, 155(1), pp. 160-171.
Cong, L., Ran, F.A., Cox, D., Lin, S., Barretto, R., Habib, N., Hsu, P.D., Wu, X., Jiang, W., Marraffini, L.A. and Zhang, F. (2013) 'Multiplex Genome Engineering Using CRISPR/Cas Systems', *Science*, 339(6121), p. 819.
Cooper, G. (2000a) 'Metabolic Energy', in *The Cell: A Molecular Approach*. Sinauer Associates. Available at: https://www.ncbi.nlm.nih.gov/books/NBK9903/.
Cooper, G. (2000b) 'Transport of Small Molecules', in *The Cell: A Molecular Approach*. Sinauer Associates. Available at: https://www.ncbi.nlm.nih.gov/books/NBK9847/.
Cronan, J.E. (2014) 'Biotin and Lipoic Acid: Synthesis, Attachment, and Regulation', *EcoSal Plus*, 6(1), pp. 10.1128/ecosalplus.ESP-0001-2012.
Czumaj, A., Szrok-Jurga, S., Hebanowska, A., Turyn, J., Swierczynski, J., Sledzinski, T. and Stelmanska, E. (2020) 'The Pathophysiological Role of CoA', *International Journal of Molecular Sciences*, 21(23).
Dai, W. and Jiang, L. (2019) 'Dysregulated Mitochondrial Dynamics and Metabolism in Obesity, Diabetes, and Cancer', *Frontiers in Endocrinology*, 10(570).

Darin, N., Andersen, O., Wiklund, L.-M., Holmgren, D. and Holme, E. (2007) '3-Methylcrotonyl-CoA Carboxylase Deficiency and Severe Multiple Sclerosis', *Pediatric Neurology*, 36(2), pp. 132-134.
Das, A.M., Steuerwald, U. and Illsinger, S. (2010) 'Inborn errors of energy metabolism associated with myopathies', *Journal of biomedicine & biotechnology*, 2010, pp. 340849-340849.
de Carvalho, A.E.T.S., Bassaneze, V., Forni, M.F., Keusseyan, A.A., Kowaltowski, A.J. and Krieger, J.E. (2017) 'Early Postnatal Cardiomyocyte Proliferation Requires High Oxidative Energy Metabolism', *Scientific reports*, 7(1), pp. 15434-15434.
de Carvalho, F.D. and Quick, M. (2011) 'Surprising Substrate Versatility in SLC5A6: Na+-COUPLED I− TRANSPORT BY THE HUMAN Na+/MULTIVITAMIN TRANSPORTER (hSMVT)', *Journal of Biological Chemistry*, 286(1), pp. 131-137.
De La Cruz, M.V., Sánchez-Gómez, C. and Palomino, M.A. (1989) 'The primitive cardiac regions in the straight tube heart (Stage 9) and their anatomical expression in the mature heart: An experimental study in the chick embryo', *Journal of anatomy*, 165, pp. 121-131.
Dellefave, L. and McNally, E.M. (2010) 'The genetics of dilated cardiomyopathy', *Current Opinion in Cardiology*, 25(3), pp. 198-204.
Deltcheva, E., Chylinski, K., Sharma, C.M., Gonzales, K., Chao, Y., Pirzada, Z.A., Eckert, M.R., Vogel, J. and Charpentier, E. (2011) 'CRISPR RNA maturation by trans -encoded small RNA and host factor RNase III', *Nature*, 471(7340), pp. 602-607.
Dengler, V.L., Galbraith, M. and Espinosa, J.M. (2014) 'Transcriptional regulation by hypoxia inducible factors', *Critical reviews in biochemistry and molecular biology*, 49(1), pp. 1-15.
Dennis, E.P., Edwards, S.M., Jackson, R.M., Hartley, C.L., Tsompani, D., Capulli, M., Teti, A., Boot-Handford, R.P., Young, D.A., Piróg, K.A. and Briggs, M.D. (2020) 'CRELD2 Is a Novel LRP1 Chaperone That Regulates Noncanonical WNT Signaling in Skeletal Development', *Journal of Bone and Mineral Research*, 35(8), pp. 1452-1469.
Depeint, F., Bruce, W.R., Shangari, N., Mehta, R. and O'Brien, P.J. (2006) 'Mitochondrial function and toxicity: Role of the B vitamin family on mitochondrial energy metabolism', *Chemico-Biological Interactions*, 163(1), pp. 94-112.
Despa, S. and Bers, D.M. (2013) 'Na^+ transport in the normal and failing heart - remember the balance', *Journal of molecular and cellular cardiology*, 61, pp. 2-10.
Despa, S., Islam, M.A., Weber, C.R., Pogwizd, S.M. and Bers, D.M. (2002) 'Intracellular Na+ Concentration Is Elevated in Heart Failure But Na/K Pump Function Is Unchanged', *Circulation*, 105(21), pp. 2543-2548.
Di Meo, I., Carecchio, M. and Tiranti, V. (2019) 'Inborn errors of coenzyme A metabolism and neurodegeneration', *Journal of Inherited Metabolic Disease*, 42(1), pp. 49-56.
Di Pierro, E. and Granata, F. (2020) 'Nutrients and Porphyria: An Intriguing Crosstalk', *International journal of molecular sciences*, 21(10), p. 3462.
Diamandis, E.P. and Christopoulos, T.K. (1991) 'The biotin-(strept)avidin system: principles and applications in biotechnology', *Clinical Chemistry*, 37(5), p. 625.
Doenst, T., Nguyen, T.D. and Abel, E.D. (2013) 'Cardiac Metabolism in Heart Failure', *Circulation Research*, 113(6), p. 709.
Du, C.-K., Morimoto, S., Nishii, K., Minakami, R., Ohta, M., Tadano, N., Lu, Q.-W., Wang, Y.-Y., Zhan, D.-Y., Mochizuki, M., Kita, S., Miwa, Y., Takahashi-Yanaga, F., Iwamoto, T., Ohtsuki, I. and Sasaguri, T. (2007) 'Knock-In Mouse Model of Dilated Cardiomyopathy Caused by Troponin Mutation', *Circulation Research*, 101(2), pp. 185-194.

Dupuis, L., Campeau, E., Leclerc, D. and Gravel, R.A. (1999) 'Mechanism of Biotin Responsiveness in Biotin-Responsive Multiple Carboxylase Deficiency', *Molecular Genetics and Metabolism*, 66(2), pp. 80-90.
Eckle, T., Brodsky, K., Bonney, M., Packard, T., Han, J., Borchers, C.H., Mariani, T.J., Kominsky, D.J., Mittelbronn, M. and Eltzschig, H.K. (2013) 'HIF1A Reduces Acute Lung Injury by Optimizing Carbohydrate Metabolism in the Alveolar Epithelium', *PLOS Biology*, 11(9), p. e1001665.
Edhouse, J., Thakur, R.K. and Khalil, J.M. (2002) 'Conditions affecting the left side of the heart', *BMJ : British Medical Journal*, 324(7348), pp. 1264-1267.
El-Hattab, A.W. and Scaglia, F. (2016a) 'Mitochondrial Cardiomyopathies', *Frontiers in Cardiovascular Medicine*, 3, p. 25.
El-Hattab, A.W. and Scaglia, F. (2016b) 'Mitochondrial Cardiomyopathies', *Frontiers in cardiovascular medicine*, 3, pp. 25-25.
El-Hattab, A.W. and Scaglia, F. (2016c) 'Mitochondrial Cardiomyopathies', *Frontiers in Cardiovascular Medicine*, 3(25).
Eldjarn, L., Jellum, E., Stokke, O., Pande, H. and Waaler, P. (1970) 'β-HYDROXYISOVALERIC ACIDURIA AND β-METHYLCROTONYLGLYCINURIA: A NEW INBORN ERROR OF METABOLISM', *The Lancet*, 296(7671), pp. 521-522.
Elliott, P. (2000) 'Diagnosis and management of dilated cardiomyopathy', *Heart*, 84(1), p. 106.
Eltzschig, H.K. and Carmeliet, P. (2011) 'Hypoxia and inflammation', *The New England journal of medicine*, 364(7), pp. 656-665.
England, J. and Loughna, S. (2013) 'Heavy and light roles: myosin in the morphogenesis of the heart', *Cellular and Molecular Life Sciences*, 70(7), pp. 1221-1239.
Facucho-Oliveira, J.M. and St. John, J.C. (2009) 'The Relationship Between Pluripotency and Mitochondrial DNA Proliferation During Early Embryo Development and Embryonic Stem Cell Differentiation', *Stem Cell Reviews and Reports*, 5(2), pp. 140-158.
Faitg, J., Davey, T., Turnbull, D.M., White, K. and Vincent, A.E. (2020) 'Mitochondrial morphology and function: two for the price of one!', *Journal of Microscopy*, 278(2), pp. 89-106.
Fatkin, D., Johnson, R., McGaughran, J., Weintraub, R.G. and Atherton, J.J. (2017) 'Position Statement on the Diagnosis and Management of Familial Dilated Cardiomyopathy', *Heart, Lung and Circulation*, 26(11), pp. 1127-1132.
Finocchiaro, G., Merlo, M., Sheikh, N., De Angelis, G., Papadakis, M., Olivotto, I., Rapezzi, C., Carr-White, G., Sharma, S., Mestroni, L. and Sinagra, G. (2020) 'The electrocardiogram in the diagnosis and management of patients with dilated cardiomyopathy', *European Journal of Heart Failure*, 22(7), pp. 1097-1107.
Fleming, R.E., Britton, R.S., Waheed, A., Sly, W.S. and Bacon, B.R. (2005) 'Pathophysiology of hereditary hemochromatosis', *Seminars in liver disease*, 25(4), pp. 411-419.
Foglia, M.J. and Poss, K.D. (2016) 'Building and re-building the heart by cardiomyocyte proliferation', *Development*, 143(5), p. 729.
Folmes, C.D.L., Nelson, T.J., Martinez-Fernandez, A., Arrell, D.K., Lindor, J.Z., Dzeja, P.P., Ikeda, Y., Perez-Terzic, C. and Terzic, A. (2011) 'Somatic oxidative bioenergetics transitions into pluripotency-dependent glycolysis to facilitate nuclear reprogramming', *Cell metabolism*, 14(2), pp. 264-271.
Fonseca, H., Azevedo, L., Serrano, C., Sousa, C., Marcão, A. and Vilarinho, L. (2016) '3-Methylcrotonyl-CoA carboxylase deficiency: Mutational spectrum derived from comprehensive newborn screening', *Gene*, 594(2), pp. 203-210.

Forrest, L.R., Krämer, R. and Ziegler, C. (2011) 'The structural basis of secondary active transport mechanisms', *Biochimica et Biophysica Acta (BBA) - Bioenergetics*, 1807(2), pp. 167-188.
Francone, M. (2014) 'Role of cardiac magnetic resonance in the evaluation of dilated cardiomyopathy: diagnostic contribution and prognostic significance', *ISRN radiology*, 2014, pp. 365404-365404.
Ghosal, A., Lambrecht, N., Subramanya, S.B., Kapadia, R. and Said, H.M. (2012) 'Conditional knockout of the Slc5a6 gene in mouse intestine impairs biotin absorption', *American Journal of Physiology-Gastrointestinal and Liver Physiology*, 304(1), pp. G64-G71.
Ghosal, A., Lambrecht, N., Subramanya, S.B., Kapadia, R. and Said, H.M. (2013) 'Specific knockout of the Slc5a6 gene in mouse intestine via Cre/lox technology leads to impairment in biotin (and pantothenic acid) absorption', *The FASEB Journal*, 27(1_supplement), pp. 732.6-732.6.
Ghosal, A. and Said, H.M. (2011) 'Structure-function activity of the human sodium-dependent multivitamin transporter: role of His(115) and His(254)', *American Journal of Physiology - Cell Physiology*, 300(1), pp. C97-C104.
Ginoux, J.-M. and Rossetto, B. (2014) 'Slow invariant manifold of heartbeat model', *arXiv preprint arXiv:1408.4988*.
Goulbourne, C.N., Gin, P., Tatar, A., Nobumori, C., Hoenger, A., Jiang, H., Grovenor, C.R., Adeyo, O., Esko, J.D., Goldberg, I.J., Reue, K., Tontonoz, P., Bensadoun, A., Beigneux, A.P., Young, S.G. and Fong, L.G. (2014) 'The GPIHBP1-LPL complex is responsible for the margination of triglyceride-rich lipoproteins in capillaries', *Cell Metab*, 19(5), pp. 849-60.
Graham, B.H., Waymire, K.G., Cottrell, B., Trounce, I.A., MacGregor, G.R. and Wallace, D.C. (1997) 'A mouse model for mitochondrial myopathy and cardiomyopathy resulting from a deficiency in the heart/muscle isoform of the adenine nucleotide translocator', *Nature Genetics*, 16(3), pp. 226-234.
Grassl, S.M. (1992) 'Human placental brush-border membrane Na(+)-biotin cotransport', *J Biol Chem*, 267(25), pp. 17760-5.
Gray, R.P., McIntyre, H., Sheridan, D.S. and Fry, C.H. (2001) 'Intracellular sodium and contractile function in hypertrophied human and guinea-pig myocardium', *Pflügers Archiv*, 442(1), pp. 117-123.
Grossman, W. and Paulus, W.J. (2013) 'Myocardial stress and hypertrophy: a complex interface between biophysics and cardiac remodeling', *The Journal of clinical investigation*, 123(9), pp. 3701-3703.
Grünert, S.C., Stucki, M., Morscher, R.J., Suormala, T., Bürer, C., Burda, P., Christensen, E., Ficicioglu, C., Herwig, J., Kölker, S., Möslinger, D., Pasquini, E., Santer, R., Schwab, K.O., Wilcken, B., Fowler, B., Yue, W.W. and Baumgartner, M.R. (2012) '3-methylcrotonyl-CoA carboxylase deficiency: clinical, biochemical, enzymatic and molecular studies in 88 individuals', *Orphanet journal of rare diseases*, 7, pp. 31-31.
Guo, Y. and Pu, W.T. (2020) 'Cardiomyocyte Maturation', *Circulation Research*, 126(8), pp. 1086-1106.
Habarou, F., Brassier, A., Rio, M., Chrétien, D., Monnot, S., Barbier, V., Barouki, R., Bonnefont, J.P., Boddaert, N., Chadefaux-Vekemans, B., Le Moyec, L., Bastin, J., Ottolenghi, C. and de Lonlay, P. (2015) 'Pyruvate carboxylase deficiency: An underestimated cause of lactic acidosis', *Molecular Genetics and Metabolism Reports*, 2, pp. 25-31.
Hackman, P., Vihola, A., Haravuori, H., Marchand, S., Sarparanta, J., de Seze, J., Labeit, S., Witt, C., Peltonen, L., Richard, I. and Udd, B. (2002) 'Tibial Muscular

Dystrophy Is a Titinopathy Caused by Mutations in TTN, the Gene Encoding the Giant Skeletal-Muscle Protein Titin', *American Journal of Human Genetics*, 71(3), pp. 492-500.
Hagdorn, Q.A.J., Bossers, G.P.L., Koop, A.-M.C., Piek, A., Eijgenraam, T.R., van der Feen, D.E., Silljé, H.H.W., de Boer, R.A. and Berger, R.M.F. (2019) 'A novel method optimizing the normalization of cardiac parameters in small animal models: the importance of dimensional indexing', *American Journal of Physiology-Heart and Circulatory Physiology*, 316(6), pp. H1552-H1557.
Hamburger, V. and Hamilton, H.L. (1951) 'A series of normal stages in the development of the chick embryo', *Journal of Morphology*, 88(1), pp. 49-92.
Hanna, M.G. and Nelson, I.P. (1999) 'Genetics and molecular pathogenesis of mitochondrial respiratory chain diseases', *Cellular and Molecular Life Sciences CMLS*, 55(5), pp. 691-706.
Hassanpour, S.H., Dehghani, M.A. and Karami, S.Z. (2018) 'Study of respiratory chain dysfunction in heart disease', *Journal of cardiovascular and thoracic research*, 10(1), pp. 1-13.
Hayashi, S., Lewis, P., Pevny, L. and McMahon, A.P. (2002) 'Efficient gene modulation in mouse epiblast using a Sox2Cre transgenic mouse strain', *Mechanisms of Development*, 119, pp. S97-S101.
He, L., Hamm, J.A., Reddy, A., Sams, D., Peliciari-Garcia, R.A., McGinnis, G.R., Bailey, S.M., Chow, C.-W., Rowe, G.C., Chatham, J.C. and Young, M.E. (2016a) 'Biotinylation: a novel posttranslational modification linking cell autonomous circadian clocks with metabolism', *American Journal of Physiology - Heart and Circulatory Physiology*, 310(11), pp. H1520-H1532.
He, L., Hamm, J.A., Reddy, A., Sams, D., Peliciari-Garcia, R.A., McGinnis, G.R., Bailey, S.M., Chow, C.-W., Rowe, G.C., Chatham, J.C. and Young, M.E. (2016b) 'Biotinylation: a novel posttranslational modification linking cell autonomous circadian clocks with metabolism', *American journal of physiology. Heart and circulatory physiology*, 310(11), pp. H1520-H1532.
Hediger, M.A., Clémençon, B., Burrier, R.E. and Bruford, E.A. (2013) 'The ABCs of membrane transporters in health and disease (SLC series): Introduction()()', *Molecular Aspects of Medicine*, 34(2-3), pp. 95-107.
Hill, G.E. (2014) 'Cellular Respiration: The Nexus of Stress, Condition, and Ornamentation', *Integrative and Comparative Biology*, 54(4), pp. 645-657.
Hill, M.C., Kadow, Z.A., Li, L., Tran, T.T., Wythe, J.D. and Martin, J.F. (2019) 'A cellular atlas of Pitx2-dependent cardiac development', *Development*, 146(12), p. dev180398.
Horton, J.L., Martin, O.J., Lai, L., Riley, N.M., Richards, A.L., Vega, R.B., Leone, T.C., Pagliarini, D.J., Muoio, D.M., Bedi, K.C., Margulies, K.B., Coon, J.J. and Kelly, D.P. (2016) 'Mitochondrial protein hyperacetylation in the failing heart', *JCI Insight*, 1(2), p. e84897.
Horváth, Z. and Vécsei, L. (2011) 'Treatment With Pantethine', *Journal of Evidence-Based Complementary & Alternative Medicine*, 16(1), pp. 21-28.
Hroudová, J. and Fišar, Z. (2013) 'Control mechanisms in mitochondrial oxidative phosphorylation', *Neural Regeneration Research*, 8(4), pp. 363-375.
Huskisson, E., Maggini, S. and Ruf, M. (2007) 'The Role of Vitamins and Minerals in Energy Metabolism and Well-Being', *Journal of International Medical Research*, 35(3), pp. 277-289.
Huxley, H. and Hanson, J. (1954) 'Changes in the Cross-Striations of Muscle during Contraction and Stretch and their Structural Interpretation', *Nature*, 173(4412), pp. 973-976.

Ittner, L.M. and Götz, J. (2007) 'Pronuclear injection for the production of transgenic mice', *Nat Protoc*, 2(5), pp. 1206-15.
Ivanovitch, K., Esteban, I. and Torres, M. (2017) 'Growth and Morphogenesis during Early Heart Development in Amniotes', *Journal of cardiovascular development and disease*, 4(4), p. 20.
Iyer, N.V., Kotch, L.E., Agani, F., Leung, S.W., Laughner, E., Wenger, R.H., Gassmann, M., Gearhart, J.D., Lawler, A.M., Yu, A.Y. and Semenza, G.L. (1998) 'Cellular and developmental control of O2 homeostasis by hypoxia-inducible factor 1 alpha', *Genes Dev*, 12(2), pp. 149-62.
Jack, D.L., Paulsen, I.T. and Saier, M.H. (2000) 'The amino acid/polyamine/organocation (APC) superfamily of transporters specific for amino acids, polyamines and organocations', *Microbiology*, 146 (Pt 8), pp. 1797-814.
Jacot, J.G., Martin, J.C. and Hunt, D.L. (2010a) 'Mechanobiology of Cardiomyocyte Development', *Journal of biomechanics*, 43(1), p. 93.
Jacot, J.G., Martin, J.C. and Hunt, D.L. (2010b) 'Mechanobiology of cardiomyocyte development', *Journal of Biomechanics*, 43(1), pp. 93-98.
Jefferies, J.L. and Towbin, J.A. (2010) 'Dilated cardiomyopathy', *The Lancet*, 375(9716), pp. 752-762.
Jia, G., Aroor, A.R., Hill, M.A. and Sowers, J.R. (2018) 'Role of Renin-Angiotensin-Aldosterone System Activation in Promoting Cardiovascular Fibrosis and Stiffness', *Hypertension*, 72(3), pp. 537-548.
Jiao, K., Kulessa, H., Tompkins, K., Zhou, Y., Batts, L., Baldwin, H.S. and Hogan, B.L.M. (2003) 'An essential role of Bmp4 in the atrioventricular septation of the mouse heart', *Genes & Development*, 17(19), pp. 2362-2367.
Jiao, K., Langworthy, M., Batts, L., Brown, C.B., Moses, H.L. and Baldwin, H.S. (2006) 'Tgfbeta signaling is required for atrioventricular cushion mesenchyme remodeling during in vivo cardiac development', *Development*, 133(22), pp. 4585-93.
Joukar, S. (2021) 'A comparative review on heart ion channels, action potentials and electrocardiogram in rodents and human: extrapolation of experimental insights to clinic', *Laboratory Animal Research*, 37(1), p. 25.
Ke, C.-J., He, Y.-H., He, H.-W., Yang, X., Li, R. and Yuan, J. (2014) 'A new spectrophotometric assay for measuring pyruvate dehydrogenase complex activity: a comparative evaluation', *Analytical Methods*, 6(16), pp. 6381-6388.
Kilic, M., Ozgül, R.K., Coşkun, T., Yücel, D., Karaca, M., Sivri, H.S., Tokatli, A., Sahin, M., Karagöz, T. and Dursun, A. (2011) 'Identification of mutations and evaluation of cardiomyopathy in Turkish patients with primary carnitine deficiency', *JIMD reports*, 3, pp. 17-23.
Kircher, M., Witten, D.M., Jain, P., O'Roak, B.J., Cooper, G.M. and Shendure, J. (2014) 'A general framework for estimating the relative pathogenicity of human genetic variants', *Nature Genetics*, 46(3), pp. 310-315.
Knowles, J.R. (1989) 'The Mechanism of Biotin-Dependent Enzymes', *Annual Review of Biochemistry*, 58(1), pp. 195-221.
Knowles, R.L., Ridout, D., Crowe, S., Bull, C., Wray, J., Tregay, J., Franklin, R.C., Barron, D.J., Cunningham, D., Parslow, R.C. and Brown, K.L. (2017) 'Ethnic and socioeconomic variation in incidence of congenital heart defects', *Archives of Disease in Childhood*, 102(6), p. 496.
Kolwicz, S.C., Purohit, S. and Tian, R. (2013) 'Cardiac Metabolism and Its Interactions with Contraction, Growth, and Survival of the Cardiomyocte', *Circulation research*, 113(5), p. 10.1161/CIRCRESAHA.113.302095.
Kong, P., Christia, P. and Frangogiannis, N.G. (2014) 'The pathogenesis of cardiac fibrosis', *Cellular and molecular life sciences : CMLS*, 71(4), pp. 549-574.

Koopman, W.J., Visch, H.J., Smeitink, J.A. and Willems, P.H. (2006) 'Simultaneous quantitative measurement and automated analysis of mitochondrial morphology, mass, potential, and motility in living human skin fibroblasts', *Cytometry A*, 69(1), pp. 1-12.
Kramer, C.M. (2015) 'Role of Cardiac MR Imaging in Cardiomyopathies', *Journal of nuclear medicine : official publication, Society of Nuclear Medicine*, 56 Suppl 4(0 4), pp. 39S-45S.
Krier, J.B., Kalia, S.S. and Green, R.C. (2016) 'Genomic sequencing in clinical practice: applications, challenges, and opportunities', *Dialogues in Clinical Neuroscience*, 18(3), pp. 299-312.
Kuo, C.T., Morrisey, E.E., Anandappa, R., Sigrist, K., Lu, M.M., Parmacek, M.S., Soudais, C. and Leiden, J.M. (1997) 'GATA4 transcription factor is required for ventral morphogenesis and heart tube formation', *Genes & Development*, 11(8), pp. 1048-1060.
Lee, J.A., Collings, D.A. and Glover, C.N. (2016) 'A model system using confocal fluorescence microscopy for examining real-time intracellular sodium ion regulation', *Analytical Biochemistry*, 507, pp. 40-46.
Lee, T.M., Hsu, D.T., Kantor, P., Towbin, J.A., Ware, S.M., Colan, S.D., Chung, W.K., Jefferies, J.L., Rossano, J.W., Castleberry, C.D., Addonizio, L.J., Lal, A.K., Lamour, J.M., Miller, E.M., Thrush, P.T., Czachor, J.D., Razoky, H., Hill, A. and Lipshultz, S.E. (2017) 'Pediatric Cardiomyopathies', *Circulation Research*, 121(7), pp. 855-873.
Lehman, J.J., Barger, P.M., Kovacs, A., Saffitz, J.E., Medeiros, D.M. and Kelly, D.P. (2000) 'Peroxisome proliferator–activated receptor γ coactivator-1 promotes cardiac mitochondrial biogenesis', *The Journal of Clinical Investigation*, 106(7), pp. 847-856.
León-Del-Río, A. (2005) 'Biotin-dependent regulation of gene expression in human cells', *The Journal of Nutritional Biochemistry*, 16(7), pp. 432-434.
Leonardi, R. and Jackowski, S. (2007) 'Biosynthesis of Pantothenic Acid and Coenzyme A', *EcoSal Plus*, 2(2), p. 10.1128/ecosalplus.3.6.3.4.
Leone, M., Magadum, A. and Engel, F.B. (2015) 'Cardiomyocyte proliferation in cardiac development and regeneration: a guide to methodologies and interpretations', *American Journal of Physiology-Heart and Circulatory Physiology*, 309(8), pp. H1237-H1250.
Li, A.-H., Liu Peter, P., Villarreal Francisco, J. and Garcia Ricardo, A. (2014) 'Dynamic Changes in Myocardial Matrix and Relevance to Disease', *Circulation Research*, 114(5), pp. 916-927.
Liao, X., Zhang, R., Lu, Y., Prosdocimo, D.A., Sangwung, P., Zhang, L., Zhou, G., Anand, P., Lai, L., Leone, T.C., Fujioka, H., Ye, F., Rosca, M.G., Hoppel, C.L., Schulze, P.C., Abel, E.D., Stamler, J.S., Kelly, D.P. and Jain, M.K. (2015) 'Kruppel-like factor 4 is critical for transcriptional control of cardiac mitochondrial homeostasis', *J Clin Invest*, 125(9), pp. 3461-76.
Lipshultz, S.E., Cochran, T.R., Briston, D.A., Brown, S.R., Sambatakos, P.J., Miller, T.L., Carrillo, A.A., Corcia, L., Sanchez, J.E., Diamond, M.B., Freundlich, M., Harake, D., Gayle, T., Harmon, W.G., Rusconi, P.G., Sandhu, S.K. and Wilkinson, J.D. (2013) 'Pediatric cardiomyopathies: causes, epidemiology, clinical course, preventive strategies and therapies', *Future cardiology*, 9(6), pp. 817-848.
Litviňuková, M., Talavera-López, C., Maatz, H., Reichart, D., Worth, C.L., Lindberg, E.L., Kanda, M., Polanski, K., Heinig, M., Lee, M., Nadelmann, E.R., Roberts, K., Tuck, L., Fasouli, E.S., DeLaughter, D.M., McDonough, B., Wakimoto, H., Gorham, J.M., Samari, S., Mahbubani, K.T., Saeb-Parsy, K., Patone, G., Boyle, J.J., Zhang, H., Zhang, H., Viveiros, A., Oudit, G.Y., Bayraktar, O.A., Seidman, J.G., Seidman, C.E.,

Noseda, M., Hubner, N. and Teichmann, S.A. (2020) 'Cells of the adult human heart', *Nature*, 588(7838), pp. 466-472.
Lopaschuk, G.D., Belke, D.D., Gamble, J., Toshiyuki, I. and Schönekess, B.O. (1994) 'Regulation of fatty acid oxidation in the mammalian heart in health and disease', *Biochimica et Biophysica Acta (BBA) - Lipids and Lipid Metabolism*, 1213(3), pp. 263-276.
Lopaschuk, G.D. and Jaswal, J.S. (2010) 'Energy Metabolic Phenotype of the Cardiomyocyte During Development, Differentiation, and Postnatal Maturation', *Journal of Cardiovascular Pharmacology*, 56(2).
Lopaschuk, G.D. and Kelly, D.P. (2008) 'Signalling in cardiac metabolism', *Cardiovascular Research*, 79(2), pp. 205-207.
Lopaschuk, G.D., Spafford, M.A. and Marsh, D.R. (1991) 'Glycolysis is predominant source of myocardial ATP production immediately after birth', *American Journal of Physiology-Heart and Circulatory Physiology*, 261(6), pp. H1698-H1705.
Lu, D., Xia, Y., Chen, Z., Chen, A., Wu, Y., Jia, J., Sun, A., Zou, Y., Qian, J. and Ge, J. (2019) 'Cardiac Proteome Profiling in Ischemic and Dilated Cardiomyopathy Mouse Models', *Frontiers in Physiology*, 10(750).
Luptak, I., Sverdlov, A.L., Panagia, M., Qin, F., Pimentel, D.R., Croteau, D., Siwik, D.A., Ingwall, J.S., Bachschmid, M.M., Balschi, J.A. and Colucci, W.S. (2018) 'Decreased ATP production and myocardial contractile reserve in metabolic heart disease', *Journal of Molecular and Cellular Cardiology*, 116, pp. 106-114.
Lyon, A., Ariga, R., Mincholé, A., Mahmod, M., Ormondroyd, E., Laguna, P., de Freitas, N., Neubauer, S., Watkins, H. and Rodriguez, B. (2018) 'Distinct ECG Phenotypes Identified in Hypertrophic Cardiomyopathy Using Machine Learning Associate With Arrhythmic Risk Markers', *Frontiers in physiology*, 9, pp. 213-213.
Mailloux, R.J., Bériault, R., Lemire, J., Singh, R., Chénier, D.R., Hamel, R.D. and Appanna, V.D. (2007) 'The Tricarboxylic Acid Cycle, an Ancient Metabolic Network with a Novel Twist', *PLOS ONE*, 2(8), p. e690.
Mali, P., Yang, L., Esvelt, K.M., Aach, J., Guell, M., DiCarlo, J.E., Norville, J.E. and Church, G.M. (2013) 'RNA-Guided Human Genome Engineering via Cas9', *Science*, 339(6121), p. 823.
Mannella, C.A. (2020) 'Consequences of Folding the Mitochondrial Inner Membrane', *Frontiers in Physiology*, 11(536).
Marshall, C.R., Chowdhury, S., Taft, R.J., Lebo, M.S., Buchan, J.G., Harrison, S.M., Rowsey, R., Klee, E.W., Liu, P., Worthey, E.A., Jobanputra, V., Dimmock, D., Kearney, H.M., Bick, D., Kulkarni, S., Taylor, S.L., Belmont, J.W., Stavropoulos, D.J., Lennon, N.J. and Medical Genome, I. (2020) 'Best practices for the analytical validation of clinical whole-genome sequencing intended for the diagnosis of germline disease', *npj Genomic Medicine*, 5(1), p. 47.
Martínez-Lagunas, K., Yamaguchi, Y., Becker, C., Geisen, C., DeRuiter, M.C., Miura, M., Fleischmann, B.K. and Hesse, M. (2020) 'In vivo detection of programmed cell death during mouse heart development', *Cell Death & Differentiation*, 27(4), pp. 1398-1414.
Martínez-Reyes, I. and Chandel, N.S. (2020) 'Mitochondrial TCA cycle metabolites control physiology and disease', *Nature Communications*, 11(1), p. 102.
Mashiko, D., Fujihara, Y., Satouh, Y., Miyata, H., Isotani, A. and Ikawa, M. (2013) 'Generation of mutant mice by pronuclear injection of circular plasmid expressing Cas9 and single guided RNA', *Scientific Reports*, 3(1), p. 3355.
Massoud, A.F. and Leonard, J.V. (1993) 'Cardiomyopathy in propionic acidaemia', *European Journal of Pediatrics*, 152(5), pp. 441-445.

Mathew, T., Williams, L., Navaratnam, G., Rana, B., Wheeler, R., Collins, K., Harkness, A., Jones, R., Knight, D., O'Gallagher, K., Oxborough, D., Ring, L., Sandoval, J., Stout, M., Sharma, V., Steeds, R.P. and British Society of Echocardiography Education, C. (2017) 'Diagnosis and assessment of dilated cardiomyopathy: a guideline protocol from the British Society of Echocardiography', *Echo research and practice*, 4(2), pp. G1-G13.
Matzuk, M.M., Lu, N., Vogel, H., Sellheyer, K., Roop, D.R. and Bradley, A. (1995) 'Multiple defects and perinatal death in mice deficient in follistatin', *Nature*, 374(6520), pp. 360-363.
Mazzarotto, F., Olivotto, I. and Walsh, R. (2020) 'Advantages and Perils of Clinical Whole-Exome and Whole-Genome Sequencing in Cardiomyopathy', *Cardiovascular Drugs and Therapy*, 34(2), pp. 241-253.
McArthur, K., Whitehead, L.W., Heddleston, J.M., Li, L., Padman, B.S., Oorschot, V., Geoghegan, N.D., Chappaz, S., Davidson, S., San Chin, H., Lane, R.M., Dramicanin, M., Saunders, T.L., Sugiana, C., Lessene, R., Osellame, L.D., Chew, T.-L., Dewson, G., Lazarou, M., Ramm, G., Lessene, G., Ryan, M.T., Rogers, K.L., van Delft, M.F. and Kile, B.T. (2018) 'BAK/BAX macropores facilitate mitochondrial herniation and mtDNA efflux during apoptosis', *Science*, 359(6378), p. eaao6047.
McGarry, J.D. and Brown, N.F. (1997) 'The Mitochondrial Carnitine Palmitoyltransferase System — From Concept to Molecular Analysis', *European Journal of Biochemistry*, 244(1), pp. 1-14.
McKenna William, J., Maron Barry, J. and Thiene, G. (2017) 'Classification, Epidemiology, and Global Burden of Cardiomyopathies', *Circulation Research*, 121(7), pp. 722-730.
McNally, E.M. and Mestroni, L. (2017) 'Dilated Cardiomyopathy', *Circulation Research*, 121(7), p. 731.
Mestroni, L., Brun, F., Spezzacatene, A., Sinagra, G. and Taylor, M.R.G. (2014) 'GENETIC CAUSES OF DILATED CARDIOMYOPATHY', *Progress in pediatric cardiology*, 37(1-2), pp. 13-18.
Meyers, D.E., Basha, H.I. and Koenig, M.K. (2013) 'Mitochondrial cardiomyopathy: pathophysiology, diagnosis, and management', *Texas Heart Institute journal*, 40(4), pp. 385-394.
Minoche, A.E., Horvat, C., Johnson, R., Gayevskiy, V., Morton, S.U., Drew, A.P., Woo, K., Statham, A.L., Lundie, B., Bagnall, R.D., Ingles, J., Semsarian, C., Seidman, J.G., Seidman, C.E., Dinger, M.E., Cowley, M.J. and Fatkin, D. (2019) 'Genome sequencing as a first-line genetic test in familial dilated cardiomyopathy', *Genetics in medicine : official journal of the American College of Medical Genetics*, 21(3), pp. 650-662.
Mock, D.M., Mock, N.I., Johnson, S.B. and Holman, R.T. (1988) 'Effects of biotin deficiency on plasma and tissue fatty acid composition: evidence for abnormalities in rats', *Pediatr Res*, 24(3), pp. 396-403.
Mock, D.M., Quirk, J.G. and Mock, N.I. (2002) 'Marginal biotin deficiency during normal pregnancy', *The American journal of clinical nutrition*, 75(2), pp. 295-299.
Moorman, A., Webb, S., Brown, N.A., Lamers, W. and Anderson, R.H. (2003) 'DEVELOPMENT OF THE HEART: (1) FORMATION OF THE CARDIAC CHAMBERS AND ARTERIAL TRUNKS', *Heart*, 89(7), pp. 806-814.
Moorman, A.F.M. and Christoffels, V.M. (2003) 'Cardiac Chamber Formation: Development, Genes, and Evolution', *Physiological Reviews*, 83(4), pp. 1223-1267.
Morita Y, T.S. (2020) 'Metabolic Regulation of Cardiac Differentiation and Maturation in Pluripotent Stem Cells: A Lesson from Heart Development.', *JMA J.* , 3(3), pp. 193-200.

Morscher, R.J., Grünert, S.C., Bürer, C., Burda, P., Suormala, T., Fowler, B. and Baumgartner, M.R. (2012) 'A single mutation in MCCC1 or MCCC2 as a potential cause of positive screening for 3-methylcrotonyl-CoA carboxylase deficiency', *Molecular Genetics and Metabolism*, 105(4), pp. 602-606.
Nandi, D., Almond, C.S. and Rossano, J.W. (2018) 'Chapter 12 - Epidemiology and Economics of Pediatric Heart Failure', in *Heart Failure in the Child and Young Adult*. Boston: Academic Press, pp. 151-160.
Nathania, M., Hollingsworth, K.G., Bates, M., Eggett, C., Trenell, M.I., Velicki, L., Seferovic, P.M., MacGowan, G.A., Turnbull, D.M. and Jakovljevic, D.G. (2017) 'Impact of age on the association between cardiac high-energy phosphate metabolism and cardiac power in women', *Heart*.
Neckelmann, N., Li, K., Wade, R.P., Shuster, R. and Wallace, D.C. (1987) 'cDNA sequence of a human skeletal muscle ADP/ATP translocator: lack of a leader peptide, divergence from a fibroblast translocator cDNA, and coevolution with mitochondrial DNA genes', *Proceedings of the National Academy of Sciences*, 84(21), p. 7580.
Needleman, S.B. and Wunsch, C.D. (1970) 'A general method applicable to the search for similarities in the amino acid sequence of two proteins', *Journal of Molecular Biology*, 48(3), pp. 443-453.
Nerbonne, J.M. and Kass, R.S. (2005) 'Molecular physiology of cardiac repolarization', *Physiol Rev*, 85(4), pp. 1205-53.
Nicolson, G.L. (2014) 'Mitochondrial Dysfunction and Chronic Disease: Treatment With Natural Supplements', *Integrative medicine (Encinitas, Calif.)*, 13(4), pp. 35-43.
Oldfors, A. and Tulinius, M. (2003) 'Mitochondrial Encephalomyopathies', *Journal of Neuropathology & Experimental Neurology*, 62(3), pp. 217-227.
Olson, E.N. and Srivastava, D. (1996) 'Molecular Pathways Controlling Heart Development', *Science*, 272(5262), p. 671.
Organisation, W.H. (2017) *Cardiovascular disease* (Accessed: 29/05/2018).
Ostman-Smith, I., Brown, G., Johnson, A. and Land, J.M. (1994) 'Dilated cardiomyopathy due to type II X-linked 3-methylglutaconic aciduria: successful treatment with pantothenic acid', *British Heart Journal*, 72(4), pp. 349-353.
Owen, O.E., Kalhan, S.C. and Hanson, R.W. (2002) 'The key role of anaplerosis and cataplerosis for citric acid cycle function', *J Biol Chem*, 277(34), pp. 30409-12.
Pacheco-Alvarez, D., Solórzano-Vargas, R.S. and Del Río, A.L. (2002) 'Biotin in Metabolism and Its Relationship to Human Disease', *Archives of Medical Research*, 33(5), pp. 439-447.
Pacheco-Alvarez, D., Solórzano-Vargas, R.S., González-Noriega, A., Michalak, C., Zempleni, J. and León-Del-Río, A. (2005) 'Biotin availability regulates expression of the sodium-dependent multivitamin transporter and the rate of biotin uptake in HepG2 cells', *Molecular Genetics and Metabolism*, 85(4), pp. 301-307.
Packer, L. and Cadenas, E. (2010) 'Lipoic acid: energy metabolism and redox regulation of transcription and cell signaling', *Journal of Clinical Biochemistry and Nutrition*, 48(1), pp. 26-32.
Packer, L. and Cadenas, E. (2011) 'Lipoic acid: energy metabolism and redox regulation of transcription and cell signaling', *Journal of Clinical Biochemistry and Nutrition*, 48(1), pp. 26-32.
Papanicolaou, K.N., Kikuchi, R., Ngoh, G.A., Coughlan, K.A., Dominguez, I., Stanley, W.C. and Walsh, K. (2012) 'Mitofusins 1 and 2 are essential for postnatal metabolic remodeling in heart', *Circ Res*, 111(8), pp. 1012-26.
Pappenheimer, J.R. and Michel, C.C. (2003) 'Role of villus microcirculation in intestinal absorption of glucose: coupling of epithelial with endothelial transport', *The Journal of Physiology*, 553(Pt 2), pp. 561-574.

Park, S. and Sinko, P.J. (2005) 'THE BLOOD-BRAIN BARRIER SODIUM-DEPENDENT MULTIVITAMIN TRANSPORTER: A MOLECULAR FUNCTIONAL IN VITRO-IN SITU CORRELATION', *Drug Metabolism and Disposition*, 33(10), p. 1547.
Patel, D.P., Krausz, K.W., Xie, C., Beyoğlu, D., Gonzalez, F.J. and Idle, J.R. (2017) 'Metabolic profiling by gas chromatography-mass spectrometry of energy metabolism in high-fat diet-fed obese mice', *PLOS ONE*, 12(5), p. e0177953.
Peek, C.B., Affinati, A.H., Ramsey, K.M., Kuo, H.-Y., Yu, W., Sena, L.A., Ilkayeva, O., Marcheva, B., Kobayashi, Y., Omura, C., Levine, D.C., Bacsik, D.J., Gius, D., Newgard, C.B., Goetzman, E., Chandel, N.S., Denu, J.M., Mrksich, M. and Bass, J. (2013) 'Circadian Clock NAD(+) Cycle Drives Mitochondrial Oxidative Metabolism in Mice', *Science (New York, N.Y.)*, 342(6158), pp. 1243417-1243417.
Peirson, S.N., Butler, J.N. and Foster, R.G. (2003) 'Experimental validation of novel and conventional approaches to quantitative real-time PCR data analysis', *Nucleic Acids Research*, 31(14), pp. e73-e73.
Person, A.D., Klewer, S.E. and Runyan, R.B. (2005) 'Cell Biology of Cardiac Cushion Development', in *International Review of Cytology*. Academic Press, pp. 287-335.
Picard, M., White, K. and Turnbull, D.M. (2013) 'Mitochondrial morphology, topology, and membrane interactions in skeletal muscle: a quantitative three-dimensional electron microscopy study', *Journal of applied physiology (Bethesda, Md. : 1985)*, 114(2), pp. 161-171.
Pindolia, K., Jordan, M., Guo, C., Matthews, N., Mock, D.M., Strovel, E., Blitzer, M. and Wolf, B. (2011) 'Development and characterization of a mouse with profound biotinidase deficiency: a biotin-responsive neurocutaneous disorder', *Mol Genet Metab*, 102(2), pp. 161-9.
Pizzorno, J. (2014) 'Mitochondria-Fundamental to Life and Health', *Integrative medicine (Encinitas, Calif.)*, 13(2), pp. 8-15.
Plitzko, B. and Loesgen, S. (2018) 'Measurement of Oxygen Consumption Rate (OCR) and Extracellular Acidification Rate (ECAR) in Culture Cells for Assessment of the Energy Metabolism', *Bio-protocol*, 8(10), p. e2850.
Polina Sysa-Shah, Lars L Sørensen, M Roselle Abraham and Gabrielson, a.K.L. (2015) 'Electrocardiographic Characterization of Cardiac
Hypertrophy in Mice that Overexpress the ErbB2
Receptor Tyrosine Kinase', *Comparative Medicine*, 65(4), pp. 295-307.
Posey, J.E., Rosenfeld, J.A., James, R.A., Bainbridge, M., Niu, Z., Wang, X., Dhar, S., Wiszniewski, W., Akdemir, Z.H.C., Gambin, T., Xia, F., Person, R.E., Walkiewicz, M., Shaw, C.A., Sutton, V.R., Beaudet, A.L., Muzny, D., Eng, C.M., Yang, Y., Gibbs, R.A., Lupski, J.R., Boerwinkle, E. and Plon, S.E. (2016) 'Molecular Diagnostic Experience of Whole-Exome Sequencing in Adult Patients', *Genetics in medicine : official journal of the American College of Medical Genetics*, 18(7), pp. 678-685.
Prasad, P.D., Ramamoorthy, S., Leibach, F.H. and Ganapathy, V. (1997) 'Characterization of a sodium-dependent vitamin transporter mediating the uptake of pantothenate, biotin and lipoate in human placental choriocarcinoma cells', *Placenta*, 18(7), pp. 527-533.
Prasad, P.D., Srinivas, S.R., Wang, H., Leibach, F.H., Devoe, L.D. and Ganapathy, V. (2000) 'Electrogenic nature of rat sodium-dependent multivitamin transport', *Biochem Biophys Res Commun*, 270(3), pp. 836-40.
Prasad, P.D., Wang, H., Huang, W., Fei, Y.-J., Leibach, F.H., Devoe, L.D. and Ganapathy, V. (1999) 'Molecular and Functional Characterization of the Intestinal Na+-Dependent Multivitamin Transporter', *Archives of Biochemistry and Biophysics*, 366(1), pp. 95-106.

Prasad, P.D., Wang, H., Kekuda, R., Fujita, T., Fei, Y.-J., Devoe, L.D., Leibach, F.H. and Ganapathy, V. (1998) 'Cloning and Functional Expression of a cDNA Encoding a Mammalian Sodium-dependent Vitamin Transporter Mediating the Uptake of Pantothenate, Biotin, and Lipoate', *Journal of Biological Chemistry*, 273(13), pp. 7501-7506.
Quick, M. and Shi, L. (2015) 'The Sodium/Multivitamin Transporter (SMVT): a Multipotent System With Therapeutic Implications', *Vitamins and hormones*, 98, pp. 63-100.
Rahimov, F. and Kunkel, L.M. (2013) 'Cellular and molecular mechanisms underlying muscular dystrophy', *The Journal of Cell Biology*, 201(4), pp. 499-510.
Readnower, R.D., Brainard, R.E., Hill, B.G. and Jones, S.P. (2012) 'Standardized bioenergetic profiling of adult mouse cardiomyocytes', *Physiological genomics*, 44(24), pp. 1208-1213.
Riehle, C. and Bauersachs, J. (2019) 'Small animal models of heart failure', *Cardiovascular Research*, 115(13), pp. 1838-1849.
Ritterhoff, J. and Tian, R. (2017) 'Metabolism in cardiomyopathy: every substrate matters', *Cardiovascular research*, 113(4), pp. 411-421.
Rocha, M.C., Grady, J.P., Grünewald, A., Vincent, A., Dobson, P.F., Taylor, R.W., Turnbull, D.M. and Rygiel, K.A. (2015a) 'A novel immunofluorescent assay to investigate oxidative phosphorylation deficiency in mitochondrial myopathy: understanding mechanisms and improving diagnosis', *Scientific reports*, 5, pp. 15037-15037.
Rocha, M.C., Grady, J.P., Grünewald, A., Vincent, A., Dobson, P.F., Taylor, R.W., Turnbull, D.M. and Rygiel, K.A. (2015b) 'A novel immunofluorescent assay to investigate oxidative phosphorylation deficiency in mitochondrial myopathy: understanding mechanisms and improving diagnosis', *Scientific Reports*, 5(1), p. 15037.
Rodriguez-Gil, J.L., Watkins-Chow, D.E., Baxter, L.L., Elliot, G., Harper, U.L., Wincovitch, S.M., Wedel, J.C., Incao, A.A., Huebecker, M., Boehm, F.J., Garver, W.S., Porter, F.D., Broman, K.W., Platt, F.M. and Pavan, W.J. (2020) 'Genetic background modifies phenotypic severity and longevity in a mouse model of Niemann-Pick disease type C1', *Disease Models & Mechanisms*, 13(3), p. dmm042614.
Rodriguez-Melendez, R. and Zempleni, J. (2003) 'Regulation of gene expression by biotin☆ (review)', *The Journal of Nutritional Biochemistry*, 14(12), pp. 680-690.
Rodríguez-Rodríguez, D.R., Ramírez-Solís, R., Garza-Elizondo, M.A., Garza-Rodríguez, M.D.L. and Barrera-Saldaña, H.A. (2019) 'Genome editing: A perspective on the application of CRISPR/Cas9 to study human diseases (Review)', *International journal of molecular medicine*, 43(4), pp. 1559-1574.
Rogatzki, M.J., Ferguson, B.S., Goodwin, M.L. and Gladden, L.B. (2015) 'Lactate is always the end product of glycolysis', *Frontiers in Neuroscience*, 9, p. 22.
Rosenquist, G.C. (1970) 'Location and movements of cardiogenic cells in the chick embryo: The heart-forming portion of the primitive streak', *Developmental Biology*, 22(3), pp. 461-475.
Roth, G.A., Johnson, C., Abajobir, A., Abd-Allah, F., Abera, S.F., Abyu, G., Ahmed, M., Aksut, B., Alam, T., Alam, K., Alla, F., Alvis-Guzman, N., Amrock, S., Ansari, H., Ärnlöv, J., Asayesh, H., Atey, T.M., Avila-Burgos, L., Awasthi, A., Banerjee, A., Barac, A., Bärnighausen, T., Barregard, L., Bedi, N., Belay Ketema, E., Bennett, D., Berhe, G., Bhutta, Z., Bitew, S., Carapetis, J., Carrero, J.J., Malta, D.C., Castañeda-Orjuela, C.A., Castillo-Rivas, J., Catalá-López, F., Choi, J.-Y., Christensen, H., Cirillo, M., Cooper, L., Criqui, M., Cundiff, D., Damasceno, A., Dandona, L., Dandona, R., Davletov, K., Dharmaratne, S., Dorairaj, P., Dubey, M., Ehrenkranz, R., El Sayed Zaki, M., Faraon,

E.J.A., Esteghamati, A., Farid, T., Farvid, M., Feigin, V., Ding, E.L., Fowkes, G., Gebrehiwot, T., Gillum, R., Gold, A., Gona, P., Gupta, R., Habtewold, T.D., Hafezi-Nejad, N., Hailu, T., Hailu, G.B., Hankey, G., Hassen, H.Y., Abate, K.H., Havmoeller, R., Hay, S.I., Horino, M., Hotez, P.J., Jacobsen, K., James, S., Javanbakht, M., Jeemon, P., John, D., Jonas, J., Kalkonde, Y., Karimkhani, C., Kasaeian, A., Khader, Y., Khan, A., Khang, Y.-H., Khera, S., Khoja, A.T., Khubchandani, J., Kim, D., Kolte, D., Kosen, S., Krohn, K.J., Kumar, G.A., Kwan, G.F., Lal, D.K., Larsson, A., Linn, S., Lopez, A., Lotufo, P.A., El Razek, H.M.A., et al. (2017) 'Global, Regional, and National Burden of Cardiovascular Diseases for 10 Causes, 1990 to 2015', *Journal of the American College of Cardiology*, 70(1), pp. 1-25.
Sabui, S., Kapadia, R., Ghosal, A., Schneider, M., Lambrecht, N. and Said, H.M. (2018) 'Biotin and pantothenic acid over-supplementation to conditional SLC5A6 KO mice prevents the development of intestinal mucosal abnormalities and growth defects', *American journal of physiology. Cell physiology*.
Saggerson, D. (2008) 'Malonyl-CoA, a Key Signaling Molecule in Mammalian Cells', *Annual Review of Nutrition*, 28(1), pp. 253-272.
Said, H.M. (2002) 'Biotin: the forgotten vitamin', *The American Journal of Clinical Nutrition*, 75(2), pp. 179-180.
Said, H.M. (2004) 'Recent Advances in Carrier-Mediated Intestinal Absorption of Water-Soluble Vitamins', *Annual Review of Physiology*, 66(1), pp. 419-446.
Said, H.M. (2011) 'Intestinal absorption of water-soluble vitamins in health and disease', *The Biochemical journal*, 437(3), pp. 357-372.
Said, H.M. (2012) 'Biotin: Biochemical, Physiological and Clinical Aspects', in Stanger, O. (ed.) *Water Soluble Vitamins: Clinical Research and Future Application*. Dordrecht: Springer Netherlands, pp. 1-19.
Said, H.M., Ortiz, A., McCloud, E., Dyer, D., Moyer, M.P. and Rubin, S. (1998) 'Biotin uptake by human colonic epithelial NCM460 cells: a carrier-mediated process shared with pantothenic acid', *American Journal of Physiology-Cell Physiology*, 275(5), pp. C1365-C1371.
Sakabe, M., Matsui, H., Sakata, H., Ando, K., Yamagishi, T. and Nakajima, Y. (2005) 'Understanding heart development and congenital heart defects through developmental biology: A segmental approach', *Congenital Anomalies*, 45(4), pp. 107-118.
Sakamuri, S.S.V.P., Sperling, J.A., Sure, V.N., Dholakia, M.H., Peterson, N.R., Rutkai, I., Mahalingam, P.S., Satou, R. and Katakam, P.V.G. (2018) 'Measurement of respiratory function in isolated cardiac mitochondria using Seahorse XFe24 Analyzer: applications for aging research', *GeroScience*, 40(3), pp. 347-356.
Salehi, B., Berkay Yılmaz, Y., Antika, G., Boyunegmez Tumer, T., Fawzi Mahomoodally, M., Lobine, D., Akram, M., Riaz, M., Capanoglu, E., Sharopov, F., Martins, N., Cho, W.C. and Sharifi-Rad, J. (2019) 'Insights on the Use of α-Lipoic Acid for Therapeutic Purposes', *Biomolecules*, 9(8), p. 356.
Sander, J.D. and Joung, J.K. (2014) 'CRISPR-Cas systems for editing, regulating and targeting genomes', *Nature biotechnology*, 32(4), pp. 347-355.
Sawa, K., Uematsu, T., Korenaga, Y., Hirasawa, R., Kikuchi, M., Murata, K., Zhang, J., Gai, X., Sakamoto, K., Koyama, T. and Satoh, T. (2017) 'Krebs Cycle Intermediates Protective against Oxidative Stress by Modulating the Level of Reactive Oxygen Species in Neuronal HT22 Cells', *Antioxidants*, 6(1), p. 21.
Schönekess, B.O., Allard, M.F. and Lopaschuk, G.D. (1995) 'Propionyl l-Carnitine Improvement of Hypertrophied Heart Function Is Accompanied by an Increase in Carbohydrate Oxidation', *Circulation Research*, 77(4), pp. 726-734.

Schrick, J.J. and Lingrel, J.B. (2001) 'cDNA cloning, mapping and expression of the mouse Propionyl CoA Carboxylase Beta (pccb), the gene for human type II propionic acidaemia', *Gene*, 264(1), pp. 147-152.
Schulman, M.P. and Richert, D.A. (1957) 'Heme synthesis in vitamin B6 and pantothenic acid deficiencies', *J Biol Chem*, 226(1), pp. 181-9.
Schultheiss, H.-P., Fairweather, D., Caforio, A.L.P., Escher, F., Hershberger, R.E., Lipshultz, S.E., Liu, P.P., Matsumori, A., Mazzanti, A., McMurray, J. and Priori, S.G. (2019a) 'Dilated cardiomyopathy', *Nature reviews. Disease primers*, 5(1), pp. 32-32.
Schultheiss, H.-P., Fairweather, D., Caforio, A.L.P., Escher, F., Hershberger, R.E., Lipshultz, S.E., Liu, P.P., Matsumori, A., Mazzanti, A., McMurray, J. and Priori, S.G. (2019b) 'Dilated cardiomyopathy', *Nature Reviews Disease Primers*, 5(1), p. 32.
Schwantje, M., de Sain-van der Velden, M., Jans, J., van Gassen, K., Dorrepaal, C., Koop, K. and Visser, G. (2019) 'Genetic defect of the sodium-dependent multivitamin transporter: A treatable disease, mimicking biotinidase deficiency', *JIMD reports*, 48(1), pp. 11-14.
Schwarz, J.M., Rödelsperger, C., Schuelke, M. and Seelow, D. (2010) 'MutationTaster evaluates disease-causing potential of sequence alterations', *Nature Methods*, 7(8), pp. 575-576.
Scott, I. and Youle, R.J. (2010) 'Mitochondrial fission and fusion', *Essays in biochemistry*, 47, pp. 85-98.
Scuderi, G.J. and Butcher, J. (2017) 'Naturally Engineered Maturation of Cardiomyocytes', *Frontiers in Cell and Developmental Biology*, 5, p. 50.
Sharma, L.K., Lu, J. and Bai, Y. (2009) 'Mitochondrial respiratory complex I: structure, function and implication in human diseases', *Current medicinal chemistry*, 16(10), pp. 1266-1277.
Shi, L. and Tu, B.P. (2015) 'Acetyl-CoA and the regulation of metabolism: mechanisms and consequences', *Current opinion in cell biology*, 33, pp. 125-131.
Shihab, H.A., Gough, J., Cooper, D.N., Stenson, P.D., Barker, G.L., Edwards, K.J., Day, I.N. and Gaunt, T.R. (2013) 'Predicting the functional, molecular, and phenotypic consequences of amino acid substitutions using hidden Markov models', *Hum Mutat*, 34(1), pp. 57-65.
Silverman, N.A., Schmitt, G., Vishwanath, M., Feinberg, H. and Levitsky, S. (1985) 'Effect of Carnitine on Myocardial Function and Metabolism Following Global Ischemia', *The Annals of Thoracic Surgery*, 40(1), pp. 20-24.
Sim, N.-L., Kumar, P., Hu, J., Henikoff, S., Schneider, G. and Ng, P.C. (2012) 'SIFT web server: predicting effects of amino acid substitutions on proteins', *Nucleic Acids Research*, 40(W1), pp. W452-W457.
Smith, C.M., Bryla, J., Damon, S., Lanoue, K.F. and Williamson, J.R. (1973) 'Fluorometric assays for succinyl-CoA and propionyl-CoA in mitochondrial extracts', *Analytical Biochemistry*, 51(2), pp. 408-420.
Smith, S., Witkowski, A., Moghul, A., Yoshinaga, Y., Nefedov, M., de Jong, P., Feng, D., Fong, L., Tu, Y., Hu, Y., Young, S.G., Pham, T., Cheung, C., Katzman, S.M., Brand, M.D., Quinlan, C.L., Fens, M., Kuypers, F., Misquitta, S., Griffey, S.M., Tran, S., Gharib, A., Knudsen, J., Hannibal-Bach, H.K., Wang, G., Larkin, S., Thweatt, J. and Pasta, S. (2012) 'Compromised mitochondrial fatty acid synthesis in transgenic mice results in defective protein lipoylation and energy disequilibrium', *PLoS One*, 7(10), p. e47196.
Snell, E.E., Strong, F.M. and Peterson, W.H. (1937) 'Growth factors for bacteria: Fractionation and properties of an accessory factor for lactic acid bacteria', *The Biochemical journal*, 31(10), pp. 1789-1799.

Solmonson, A. and DeBerardinis, R.J. (2018) 'Lipoic acid metabolism and mitochondrial redox regulation', *The Journal of biological chemistry*, 293(20), pp. 7522-7530.
Song, M., Mihara, K., Chen, Y., Scorrano, L. and Dorn, G.W., 2nd (2015) 'Mitochondrial fission and fusion factors reciprocally orchestrate mitophagic culling in mouse hearts and cultured fibroblasts', *Cell metabolism*, 21(2), pp. 273-286.
Squire, J.M. (2016) 'Muscle contraction: Sliding filament history, sarcomere dynamics and the two Huxleys', *Global cardiology science & practice*, 2016(2), pp. e201611-e201611.
St-Pierre, J., Grégoire, J.-C. and Vaillancourt, C. (2017) 'A simple method to assess group difference in RT-qPCR reference gene selection using GeNorm: The case of the placental sex', *Scientific Reports*, 7(1), p. 16923.
Stanley, W.C., Recchia, F.A. and Lopaschuk, G.D. (2005) 'Myocardial Substrate Metabolism in the Normal and Failing Heart', *Physiological Reviews*, 85(3), pp. 1093-1129.
Starkov, A.A. (2010) 'Measurement of mitochondrial ROS production', *Methods in molecular biology (Clifton, N.J.)*, 648, pp. 245-255.
Subramanian, V.S., Constantinescu, A.R., Benke, P.J. and Said, H.M. (2017) 'Mutations in SLC5A6 associated with brain, immune, bone and intestinal dysfunction in a young child', *Human genetics*, 136(2), pp. 253-261.
Subramanya, S.B., Subramanian, V.S., Kumar, J.S., Hoiness, R. and Said, H.M. (2011) 'Inhibition of intestinal biotin absorption by chronic alcohol feeding: cellular and molecular mechanisms', *American journal of physiology. Gastrointestinal and liver physiology*, 300(3), pp. G494-G501.
Sweet, M., Taylor, M.R.G. and Mestroni, L. (2015) 'Diagnosis, prevalence, and screening of familial dilated cardiomyopathy', *Expert opinion on orphan drugs*, 3(8), pp. 869-876.
Sweetman, L., Nyhan, W.L., Sakati, N.A., Ohlsson, A., Mange, M.S., Boychuk, R.B. and Kaye, R. (1982) 'Organic aciduria in neonatal multiple carboxylase deficiency', *Journal of Inherited Metabolic Disease*, 5(1), pp. 49-53.
Sysa-Shah, P., Sørensen, L.L., Abraham, M.R. and Gabrielson, K.L. (2015) 'Electrocardiographic Characterization of Cardiac Hypertrophy in Mice that Overexpress the ErbB2 Receptor Tyrosine Kinase', *Comparative Medicine*, 65(4), pp. 295-307.
Talman, V., Teppo, J., Pöhö, P., Movahedi, P., Vaikkinen, A., Karhu, S.T., Trošt, K., Suvitaival, T., Heikkonen, J., Pahikkala, T., Kotiaho, T., Kostiainen, R., Varjosalo, M. and Ruskoaho, H. (2018) 'Molecular Atlas of Postnatal Mouse Heart Development', *Journal of the American Heart Association*, 7(20), p. e010378.
Tan, C.M.J. and Lewandowski, A.J. (2020) 'The Transitional Heart: From Early Embryonic and Fetal Development to Neonatal Life', *Fetal Diagnosis and Therapy*, 47(5), pp. 373-386.
Tang, B., Li, B., Gao, L.-D., He, N., Liu, X.-R., Long, Y.-S., Zeng, Y., Yi, Y.-H., Su, T. and Liao, W.-P. (2020) 'Optimization of in silico tools for predicting genetic variants: individualizing for genes with molecular sub-regional stratification', *Briefings in Bioinformatics*, 21(5), pp. 1776-1786.
Tarze, A., Deniaud, A., Le Bras, M., Maillier, E., Molle, D., Larochette, N., Zamzami, N., Jan, G., Kroemer, G. and Brenner, C. (2007) 'GAPDH, a novel regulator of the pro-apoptotic mitochondrial membrane permeabilization', *Oncogene*, 26(18), pp. 2606-2620.
Tiranti, V., Jaksch, M., Hofmann, S., Galimberti, C., Hoertnagel, K., Lulli, L., Freisinger, P., Bindoff, L., Gerbitz, K.D., Comi, G.P., Uziel, G., Zeviani, M. and Meitinger, T. (1999)

'Loss-of-function mutations of SURF-1 are specifically associated with Leigh syndrome with cytochrome c oxidase deficiency', *Annals of Neurology*, 46(2), pp. 161-166.
Tong, L. (2013) 'Structure and function of biotin-dependent carboxylases', *Cellular and molecular life sciences : CMLS*, 70(5), pp. 863-891.
Tretter, L., Patocs, A. and Chinopoulos, C. (2016) 'Succinate, an intermediate in metabolism, signal transduction, ROS, hypoxia, and tumorigenesis', *Biochimica et Biophysica Acta (BBA) - Bioenergetics*, 1857(8), pp. 1086-1101.
Turgeon, B. and Meloche, S. (2009) 'Interpreting Neonatal Lethal Phenotypes in Mouse Mutants: Insights Into Gene Function and Human Diseases', *Physiological Reviews*, 89(1), pp. 1-26.
Twig, G. and Shirihai, O.S. (2011) 'The interplay between mitochondrial dynamics and mitophagy', *Antioxidants & redox signaling*, 14(10), pp. 1939-1951.
Uchida, Y., Ito, K., Ohtsuki, S., Kubo, Y., Suzuki, T. and Terasaki, T. (2015) 'Major involvement of Na+-dependent multivitamin transporter (SLC5A6/SMVT) in uptake of biotin and pantothenic acid by human brain capillary endothelial cells', *Journal of Neurochemistry*, 134(1), pp. 97-112.
Ugarte, M., Pérez-Cerdá, C., Rodríguez-Pombo, P., Desviat, L.R., Pérez, B., Richard, E., Muro, S., Campeau, E., Ohura, T. and Gravel, R.A. (1999) 'Overview of mutations in the PCCA and PCCB genes causing propionic acidemia', *Human Mutation*, 14(4), pp. 275-282.
Vadlapudi, A.D., Vadlapatla, R.K. and Mitra, A.K. (2012) 'Sodium dependent multivitamin transporter (SMVT): a potential target for drug delivery', *Current drug targets*, 13(7), pp. 994-1003.
Vincent, A.E., Ng, Y.S., White, K., Davey, T., Mannella, C., Falkous, G., Feeney, C., Schaefer, A.M., McFarland, R., Gorman, G.S., Taylor, R.W., Turnbull, D.M. and Picard, M. (2016) 'The Spectrum of Mitochondrial Ultrastructural Defects in Mitochondrial Myopathy', *Scientific reports*, 6, pp. 30610-30610.
Visavadiya, N.P., Pena, G.S. and Khamoui, A.V. (2021) 'Mitochondrial dynamics and quality control are altered in a hepatic cell culture model of cancer cachexia', *Mol Cell Biochem*, 476(1), pp. 23-34.
Visser, G., Suormala, T., Smit, G.P.A., Reijngoud, D.-J., Bink-Boelkens, M.T.E., Niezen-Koning, K.E. and Baumgartner, E.R. (2000) '3-Methylcrotonyl-CoA carboxylase deficiency in an infant with cardiomyopathy, in her brother with developmental delay and in their asymptomatic father', *European Journal of Pediatrics*, 159(12), pp. 901-904.
Vlasova, T.I., Stratton, S.L., Wells, A.M., Mock, N.I. and Mock, D.M. (2005) 'Biotin deficiency reduces expression of SLC19A3, a potential biotin transporter, in leukocytes from human blood', *The Journal of nutrition*, 135(1), pp. 42-47.
Waldo, K.L., Kumiski, D.H., Wallis, K.T., Stadt, H.A., Hutson, M.R., Platt, D.H. and Kirby, M.L. (2001) 'Conotruncal myocardium arises from a secondary heart field', *Development*, 128(16), p. 3179.
Waldrop, G.L., Holden, H.M. and Maurice, M.S. (2012) 'The enzymes of biotin dependent CO(2) metabolism: What structures reveal about their reaction mechanisms', *Protein Science : A Publication of the Protein Society*, 21(11), pp. 1597-1619.
Wang, F., Flanagan, J., Su, N., Wang, L.-C., Bui, S., Nielson, A., Wu, X., Vo, H.-T., Ma, X.-J. and Luo, Y. (2012) 'RNAscope: a novel in situ RNA analysis platform for formalin-fixed, paraffin-embedded tissues', *The Journal of molecular diagnostics : JMD*, 14(1), pp. 22-29.
Wang, H., Huang, W., Fei, Y.-J., Xia, H., Yang-Feng, T.L., Leibach, F.H., Devoe, L.D., Ganapathy, V. and Prasad, P.D. (1999a) 'Human Placental Na+-dependent

Multivitamin Transporter: CLONING, FUNCTIONAL EXPRESSION, GENE STRUCTURE, AND CHROMOSOMAL LOCALIZATION', *Journal of Biological Chemistry*, 274(21), pp. 14875-14883.
Wang, J., Wilhelmsson, H., Graff, C., Li, H., Oldfors, A., Rustin, P., Brüning, J.C., Kahn, C.R., Clayton, D.A., Barsh, G.S., Thorén, P. and Larsson, N.-G. (1999b) 'Dilated cardiomyopathy and atrioventricular conduction blocks induced by heart-specific inactivation of mitochondrial DNA gene expression', *Nature Genetics*, 21, p. 133.
Wang, X., Zhang, X., Wu, D., Huang, Z., Hou, T., Jian, C., Yu, P., Lu, F., Zhang, R., Sun, T., Li, J., Qi, W., Wang, Y., Gao, F. and Cheng, H. (2017) 'Mitochondrial flashes regulate ATP homeostasis in the heart', *eLife*, 6, p. e23908.
Weber, K.T. (1989) 'Cardiac interstitium in health and disease: The fibrillar collagen network', *Journal of the American College of Cardiology*, 13(7), pp. 1637-1652.
Weber, K.T., Sun, Y., Bhattacharya, S.K., Ahokas, R.A. and Gerling, I.C. (2013) 'Myofibroblast-mediated mechanisms of pathological remodelling of the heart', *Nature Reviews Cardiology*, 10(1), pp. 15-26.
Weinstock, P.H., Bisgaier, C.L., Aalto-Setälä, K., Radner, H., Ramakrishnan, R., Levak-Frank, S., Essenburg, A.D., Zechner, R. and Breslow, J.L. (1995) 'Severe hypertriglyceridemia, reduced high density lipoprotein, and neonatal death in lipoprotein lipase knockout mice. Mild hypertriglyceridemia with impaired very low density lipoprotein clearance in heterozygotes', *J Clin Invest*, 96(6), pp. 2555-68.
Westermann, B. (2010) 'Mitochondrial fusion and fission in cell life and death', *Nature Reviews Molecular Cell Biology*, 11(12), pp. 872-884.
Wiedmann, S., Eudy, J.D. and Zempleni, J. (2003) 'Biotin Supplementation Increases Expression of Genes Encoding Interferon-γ, Interleukin-1β, and 3-Methylcrotonyl-CoA Carboxylase, and Decreases Expression of the Gene Encoding Interleukin-4 in Human Peripheral Blood Mononuclear Cells', *The Journal of Nutrition*, 133(3), pp. 716-719.
Williams, R.J., Lyman, C.M., Goodyear, G.H., Truesdail, J.H. and Holaday, D. (1933) 'Pantothenic acid," a growth determinant of universal occurrence', *Journal of the American Chemical Society*, 55, pp. 2912-2927.
Wong, F.H., Chen, J.S., Reddy, V., Day, J.L., Shlykov, M.A., Wakabayashi, S.T. and Saier, J.M.H. (2012) 'The Amino Acid-Polyamine-Organocation Superfamily', *Journal of Molecular Microbiology and Biotechnology*, 22(2), pp. 105-113.
Wüst, R.C.I., de Vries, H.J., Wintjes, L.T., Rodenburg, R.J., Niessen, H.W.M. and Stienen, G.J.M. (2016) 'Mitochondrial complex I dysfunction and altered NAD(P)H kinetics in rat myocardium in cardiac right ventricular hypertrophy and failure', *Cardiovascular Research*, 111(4), pp. 362-372.
Yilmaz, A., Gdynia, H.-J., Baccouche, H., Mahrholdt, H., Meinhardt, G., Basso, C., Thiene, G., Sperfeld, A.-D., Ludolph, A.C. and Sechtem, U. (2008) 'Cardiac involvement in patients with Becker muscular dystrophy: new diagnostic and pathophysiological insights by a CMR approach', *Journal of Cardiovascular Magnetic Resonance*, 10(1), p. 50.
Yoon, Y., Pitts, K.R. and McNiven, M.A. (2001) 'Mammalian dynamin-like protein DLP1 tubulates membranes', *Molecular biology of the cell*, 12(9), pp. 2894-2905.
Young, A., Oldford, C. and Mailloux, R.J. (2020) 'Lactate dehydrogenase supports lactate oxidation in mitochondria isolated from different mouse tissues', *Redox Biology*, 28, p. 101339.
Yu, A.Y., Shimoda, L.A., Iyer, N.V., Huso, D.L., Sun, X., McWilliams, R., Beaty, T., Sham, J.S.K., Wiener, C.M., Sylvester, J.T. and Semenza, G.L. (1999) 'Impaired physiological responses to chronic hypoxia in mice partially deficient for hypoxia-inducible factor 1α', *The Journal of Clinical Investigation*, 103(5), pp. 691-696.

Yuan, S.-M. (2018) 'Cardiomyopathy in the pediatric patients', *Pediatrics & Neonatology*, 59(2), pp. 120-128.
Zachari, M. and Ganley, I.G. (2017) 'The mammalian ULK1 complex and autophagy initiation', *Essays in biochemistry*, 61(6), pp. 585-596.
Zempleni, J., Hassan, Y.I. and Wijeratne, S.S. (2008) 'Biotin and biotinidase deficiency', *Expert review of endocrinology & metabolism*, 3(6), pp. 715-724.
Zempleni, J. and Mock, D.M. (2001) 'Biotin homeostasis during the cell cycle', *Nutrition Research Reviews*, 14(1), pp. 45-64.
Zempleni, J., Wijeratne, S.S.K. and Hassan, Y.I. (2009) 'Biotin', *BioFactors (Oxford, England)*, 35(1), pp. 36-46.
Zhang, X.-H., Tee, L.Y., Wang, X.-G., Huang, Q.-S. and Yang, S.-H. (2015) 'Off-target Effects in CRISPR/Cas9-mediated Genome Engineering', *Molecular Therapy - Nucleic Acids*, 4, p. e264.
Zhao, Q., Sun, Q., Zhou, L., Liu, K. and Jiao, K. (2019) 'Complex Regulation of Mitochondrial Function During Cardiac Development', *Journal of the American Heart Association*, 8(13), p. e012731.
Zhao, Y., Richman, A., Storey, C., Radford, N.B. and Pantano, P. (1999) 'In situ fiber-optic oxygen consumption measurements from a working mouse heart', *Anal Chem*, 71(17), pp. 3887-93.
Zheng, J.I.E. (2012) 'Energy metabolism of cancer: Glycolysis versus oxidative phosphorylation (Review)', *Oncology Letters*, 4(6), pp. 1151-1157.
Zhou, B. and Tian, R. (2018) 'Mitochondrial dysfunction in pathophysiology of heart failure', *The Journal of Clinical Investigation*, 128(9), pp. 3716-3726.

Conferences and courses

Biosciences Institute, NUBI Live! Newcastle [2020], Conference presentation ‘Disruption of sodium-dependent vitamin transport: a potential novel cause of cardiomyopathy’, Presentation prize

European Society of Cardiology; Development, Anatomy and Pathology Meeting, Malaga [2019]. Conference presentation ‘Disruption of sodium-dependent vitamin transport: a potential novel cause of cardiomyopathy’

Institute of Genetic Medicine Research Day, Newcastle [2019], ‘Disruption of sodium-dependent vitamin transport: a potential novel cause of cardiomyopathy’, Presentation prize

British Society for Cardiovascular Research Spring meeting, Manchester [2019]

Northern Cardiovascular Research group meeting, Newcastle [2018], Poster presentation ‘Disruption of sodium-dependent vitamin transport: a potential novel cause of cardiomyopathy’

Cardiovascular Research Centre Training Day, Newcastle [2018], Conference presentation ‘Disruption of sodium-dependent vitamin transport: a potential novel cause of cardiomyopathy’.